Theranostic Gold Nanoparticles for Enhanced Prostate Cancer Radiotherapy

by

Mohamed Aborig

A thesis
presented to the University of Waterloo
in fulfillment of the
thesis requirement for the degree of
Doctor of Philosophy
in
Pharmacy

Waterloo, Ontario, Canada, 2025

© Mohamed Aborig 2025

Examining Committee Membership

The following served on the Examining Committee for this thesis. The decision of the Examining Committee is by majority vote.

External Examiner:	Devika Chithrani Professor, Dept. of Physics and Astronomy, University of Victoria
Supervisor(s):	Shawn Wettig Professor, School of Pharmacy, University of Waterloo
Internal Member:	Emmanuel Ho Professor, School of Pharmacy, University of Waterloo
Internal-External Member:	Juewen Liu Professor, Dept. of Chemistry, University of Waterloo
Examiner:	Ernest Osei Adjunct Assistant Professor, School of Pharmacy, University of Waterloo

Author's Declaration

This thesis consists of material all of which I authored or co-authored: see Statement of Contributions included in the thesis. This is a true copy of the thesis, including any required final revisions, as accepted by my examiners.

I understand that my thesis may be made electronically available to the public.

Statement of Contributions

The work described in this thesis was carried out solely by Mohamed Aborig under the supervision of Dr. Shawn Wettig, with the following exceptions:

- In Chapter 3, Dr. Paul Malik contributed to experimental design of the Physiologically-Based Pharmacokinetic (PBPK) Model (Chapter 4.3.2: PBPK Model).
- Charly McKenna's contributions to Chapter 4, specifically section 4.4.4: Canine Study, included oversight and data collection for canine studies at the Ontario Veterinary College, managing biochemical samples (Table C.1CBC Results, C.2 Serum Biochemistry, C.3 Urinalysis) and CT imaging (Figure 4.15)

Abstract

Prostate cancer remains a leading cause of cancer-related mortality in men, but radiotherapy is often constrained by dose-limiting toxicity. To address this challenge, we developed dual functional theranostic gold nanoparticles (GNPs) that leverage both the photoelectric properties of gold and the anti-cancer effects of phytochemicals. Specifically, this research focused on synthesizing, characterizing, and evaluating EGCG-coated (EGCG-GNPs) and curcumin-coated gold nanoparticles (Curc-GNPs) for their efficacy as radiosensitizers in prostate cancer therapy.

In this study, four gold nanoparticle formulations (EGCG-GNPs, Curc-GNPs, Cit-GNPs, and PEG-GNPs) were synthesized and extensively characterized. Utilizing an eco-friendly, single-step green synthesis method, EGCG-GNPs and Curc-GNPs demonstrated superior stability, higher yield, and advantageous physicochemical properties relative to conventional citrate- and PEG-coated nanoparticles. Detailed analyses using Dynamic Light Scattering (DLS) and Transmission Electron Microscopy (TEM) revealed monodisperse, spherical nanoparticles with core diameters averaging approximately 10 nm and hydrodynamic diameters ranging from 20 to 25 nm. Colloidal stability studies showed negative zeta potentials for all formulations, with notably lower values observed for PEG-GNPs due to their polymeric coating. UV-Vis spectroscopy emphasized the enhanced stability of Curc-GNPs in biological media, particularly serum-supplemented RPMI, indicative of significant lipophilic protein affinity. Functional assays confirmed strong antioxidant activities for EGCG- and Curc-GNPs, surpassing both Cit- and PEG-coated nanoparticles. Further, FTIR spectroscopy and HPLC analyses validated robust curcumin attachment, achieving a drug loading efficiency of 20.8 wt%. Additionally, computed tomography (CT) imaging studies demonstrated a linear correlation between EGCG-GNP concentration and imaging contrast enhancement, suggesting their potential utility in clinical diagnostic imaging.

Subsequent in vitro investigations established the therapeutic efficacy of EGCG-GNPs and Curc-GNPs as radiosensitizers using PC-3 prostate cancer cells. Cytotoxicity assessments via the XTT assay revealed dose- and time-dependent toxicity across formulations at concentrations exceeding 100 μg/mL. EGCG-GNPs demonstrated the highest cytotoxic potential, reducing cell viability substantially at elevated concentrations. Conversely, Curc-GNPs uniquely displayed a biphasic hormetic response, promoting modest proliferation at lower doses but significant toxicity above 100 μg/mL. Cellular uptake quantified by ICP-MS was notably higher in serum-free media, indicating protein corona formation inhibited nanoparticle internalization. EGCG-GNPs exhibited superior uptake efficiency, potentially via receptor-mediated endocytosis pathways. Critically, clonogenic assays revealed substantial radiosensitization capabilities, with EGCG-GNPs achieving the highest

Sensitization Enhancement Ratio (SER) of 1.955 at 500 μg/mL, significantly reducing the necessary radiation dose to induce effective cancer cell apoptosis. Analyses of radiobiological parameters indicated that EGCG-GNPs primarily augmented single-track DNA damage.

In vivo studies utilizing murine models provided favorable biodistribution and toxicity profiles for EGCG-GNPs and Curc-GNPs. Predominant nanoparticle accumulation occurred in reticuloendothelial organs, particularly the liver, spleen, and stomach, consistent with macrophage-driven biodistribution. Hepatobiliary clearance was significant over a 56-day period, although spleen retention persisted, reflecting macrophage entrapment. Minimal renal clearance corroborated expectations of size-based renal exclusion. Importantly, both nanoparticle types exhibited benign toxicity profiles, demonstrated through normal physiological behaviors, weight gain, and absence of histopathological abnormalities in major organs. Pharmacokinetic modeling (PBPK) accurately predicted nanoparticle behavior across rat models, affirming translational potential despite minor deviations. Additionally, pilot canine studies validated technical feasibility and targeted intra-arterial nanoparticle delivery to the prostate, though imaging challenges indicated a need for enhanced visualization techniques.

Collectively, this thesis substantiates the robust synthesis, precise characterization, and significant therapeutic potential of EGCG-GNPs and Curc-GNPs as potent radiosensitizers. The promising preclinical outcomes support further optimization and development for clinical application in prostate cancer therapy.

Acknowledgements

I would like to sincerely acknowledge everyone from the University of Waterloo School of Pharmacy community who supported me throughout my thesis project. I was fortunate to have a supportive environment, beginning with my research lab group members who provided valuable insights and engaging discussions that greatly helped me navigate various research challenges.

Additionally, I extend my gratitude to the staff at the WRHN Cancer Centre, who generously shared their time and resources, granting me access to essential equipment for my studies. In particular, I would like to thank Dr. Ernest Osei for his invaluable expertise and guidance regarding the clinical aspects of my research. My appreciation also goes out to the animal facility staff at both the University of Waterloo and the Ontario Veterinary College. Their specialized knowledge, dedication, and contributions were instrumental in the successful completion of this project.

Above all, I would like to thank my supervisor, Dr. Shawn Wettig, whose continuous mentorship, guidance, and unwavering support throughout my research journey have been instrumental in my academic growth and the completion of this thesis. I am deeply grateful for the encouraging and collaborative community at the UW School of Pharmacy, WRHN Cancer Centre, and Ontario Veterinary College.

Dedication

I dedicate this thesis to my family, whose unwavering support has been my foundation throughout this journey. To my father, Amer Aborig, whose example inspired me to pursue a PhD and follow in his footsteps. To my mother, Naima, whose constant encouragement, love, and support have carried me through every moment. To my brothers, Siraj and Malek, and my sisters, Aya, Ala, and Esra, thank you for always standing by me. To my nieces, Alina, Meral, Aryam, Farah, Lena, Sarah, and Asia, and my nephews, Fahed and Emir, I love you all deeply. This achievement belongs to you as much as it does to me, and it truly would not have been possible without you.

Table of Contents

Examining Committee ii

Author's Declaration iii

Statement of Contributions iv

Abstract v

Acknowledgements vii

Dedication viii

List of Figures xiv

List of Tables xviii

List of Abbreviations xx

1 Introduction 1

1.1 Prostate Cancer 2

1.1.1 Stages of Prostate Cancer 3

1.1.2 Diagnosis of Prostate Cancer 4

1.2 Current Treatment Modalities 4

1.2.1 Radiation Therapy . . . 5
1.2.1.1 Types of Radiation Therapy . . . 6
1.2.2 Nutraceuticals . . . 8
1.2.2.1 Epigallocatechin gallate (EGCG) . . . 10
1.2.2.2 Curcumin . . . 11
1.2.2.3 Other Phytochemical-Capped Gold Nanoparticles . . . 13
1.3 Gold Nanoparticles (GNPs) . . . 15
1.3.1 Quantum Size Effects . . . 15
1.3.2 Inertness and Biocompatibility . . . 16
1.3.3 Ease of Synthesis and Functionalization . . . 16
1.3.4 High Atomic Number . . . 16
1.3.5 Synthesis of GNPs . . . 17
1.3.6 Mechanistic Approach . . . 19
1.3.7 Uptake of GNPs in Cells . . . 20
1.4 GNPs in Radiation Therapy . . . 22
1.4.1 Mechanisms of Radiosensitization . . . 23
1.4.1.1 Physical Process . . . 23
1.4.1.2 Chemical Processes . . . 26
1.4.1.3 Biological Processes . . . 26
1.5 Biodistribution and Toxicity of GNPs . . . 28
1.6 Research Gap and Rationale . . . 30
1.7 Aim and Objectives of Research Undertaken . . . 31

2 Synthesis and Characterization of EGCG-GNPs & CURC-GNPs 35
2.1 Introduction . . . 36
2.2 Materials . . . 40
2.2.1 Synthesis of EGCG Capped GNPs . . . 40
2.2.2 Synthesis of Curcumin Capped GNPs . . . 40

2.2.3 Synthesis of Citrate Capped GNPs . . . 41
2.2.4 Synthesis of PEG Capped GNPs . . . 41
2.3 Characterization . . . 42
2.3.1 UV-Vis Spectroscopy . . . 42
2.3.2 Dynamic Light Scattering (DLS) . . . 42
2.3.3 Transmission Electron Microscope (TEM) . . . 42
2.3.4 ICP-MS . . . 43
2.3.5 CT-Imaging . . . 43
2.3.6 Antioxidant Potential: DPPH Assay . . . 44
2.3.7 Fourier transform infrared spectroscopy (FTIR) . . . 45
2.3.8 High Performance Liquid Chromatography (HPLC) . . . 45
2.4 Results & Discussion . . . 46
2.4.1 UV-Vis Spectroscopic Analysis . . . 46
2.4.2 Dynamic Light Scattering (DLS) Analysis . . . 51
2.4.3 Transmission Electron Microscope (TEM) . . . 53
2.4.4 ICP-MS . . . 55
2.4.5 Antioxidant Capacity . . . 56
2.4.6 FTIR . . . 58
2.4.7 HPLC . . . 59
2.4.8 CT-Imaging . . . 61
2.5 Conclusion . . . 63

3 In Vitro Studies **65**
3.1 Introduction . . . 66
3.2 Materials . . . 71
3.3 Methods . . . 71
3.3.1 Cytotoxicity: XTT Assay . . . 71
3.3.2 Cellular Uptake-ICP-MS . . . 72

3.3.3 Clonogenic Assay . . . 74
3.4 Results & Discussion . . . 78
3.4.1 Cytotoxicity Assay . . . 78
3.4.2 Cellular Uptake . . . 82
3.4.3 Clonogenic Assay . . . 86
3.5 Conclusion . . . 93
References . . . 95

4 In Vivo Studies **98**
4.1 Introduction . . . 99
4.2 Materials . . . 104
4.3 Methods . . . 104
4.3.1 In vivo Mice studies . . . 104
4.3.1.1 Gold Quantification - Biodistribution . . . 105
4.3.1.2 GNP Toxicity- Organ weight Analysis . . . 106
4.3.1.3 Histopathology of Organs . . . 108
4.3.2 PBPK Model . . . 108
4.3.2.1 Software . . . 109
4.3.2.2 Model Structure . . . 109
4.3.2.3 Model Parameterization . . . 111
4.3.3 Canine Studies . . . 115
4.3.3.1 Beagle 1: Intra-Arterial Injection of EGCG-GNP . . . 116
4.3.3.2 Beagle 2: Prostatic Arterial Embolization . . . 117
4.3.3.3 Beagle 3: IA Injection of EGCG-GNP + Prostatic Arterial Embolization . . . 117
4.3.3.4 Clinical Case . . . 118
4.4 Results & Discussion . . . 118
4.4.1 Mice studies . . . 118

4.4.1.1 GNP Biodistribution in Mice . . . 119
4.4.2 GNP Toxicity-Organ Weight Analysis . . . 123
4.4.2.1 GNP Toxicity- Histology . . . 128
4.4.3 PBPK model . . . 129
4.4.4 Canine Study . . . 134
4.5 Conclusion . . . 138
References . . . 141

5 Conclusions & Future Directions **148**
5.1 Conclusions . . . 148
5.2 Challenges and Future Directions . . . 150
5.2.1 GNP stability in vivo relating to serum adsorption and aggregation in ionic solutions . . . 150
5.2.2 Investigating the Biphasic Effects of Curc-GNPs . . . 151
5.2.3 Ct-Imaging Challenges Following PAE Procedure . . . 152
5.2.4 Canine Clinical Trials . . . 153

References **155**

Appendices **167**
Appendix A . . . 167
Appendix B . . . 176
Appendix C . . . 183

List of Figures

1.1 Incidence and mortality rates (per 100,000) of prostate cancer by race/ethnicity in United States . . . 3

1.2 Conventional Radiotherapy, Intensity Modulated Radiotherapy (IMRT), Image-Guided Radiotherapy (IGRT), Stereotactic Radiosurgery (SRS) and Fractionated Stereotactic Radiotherapy (FSRT) w.r.t Fraction and Tumor Dose . . . 6

1.3 Chemical structures of commonly researched nutraceutical phytochemicals. 9

1.4 Therapeutic efficacy of Gum Arabic (GA), epigallocatechin gallage (EGCG) and mangiferin (MGF) conjugated GNPs in prostate tumor bearing mice . 14

1.5 Schematic illustration of gold nanoparticles synthesis by Turkevich method 18

1.6 Influence of cell size on cellular uptake of GNPs . . . 21

1.7 Physical, chemical and biological mechanisms of GNPs radiosensitization . 24

1.8 Mechanisms of ROS generation for apoptosis during radiosensitization . . . 26

2.1 Chemical structures of curcumin (top left), EGCG (top right), trisodium citrate (bottom left), and PEG-thiol (bottom right). . . . 39

2.2 1500 μg/ml of EGCG-GNPs imaged in an electron density phantom . . . 44

2.3 Comparing the UV-Vis spectra of different shaped GNPs . . . 46

2.4 UV-Vis Spectra of Cit-, EGCG-, Curcumin- and PEG- GNPs. . . . 47

2.5 UV-Vis spectra of Curc-GNP and Cit-GNP in RPMI or serum supplemented RPMI . . . 49

2.6 UV-Vis absorbance spectra of EGCG-GNPs at varying concentrations. . . 50

2.7 DLS Sizes and Apparent Zeta Potentials of EGCG-, PEG-, Curc- and Cit-GNPs 52

2.8 TEM Images of EGCG-GNP showing different shaped nanoparticles. Red boxes include irregular rod and triangular structures. 53
2.9 TEM Images and Calculated Diameters of Curc-GNPs (upper side) and EGCG-GNPs (lower side) 54
2.10 Curc-GNPs TEM Image with 92000X Magnification 54
2.11 DPPH inhibition of EGCG-GNP, Cit-GNP, Curc-GNP, PEG-GNP GNP structures and quercetin (Positive control) at varying concentrations (25 – 200 μg/mL). 58
2.12 FTIR spectra of Curc-GNPs (black) and pure curcumin (red). 59
2.13 HPLC analysis of curcumin loading. 60
2.14 The Measurement of mean HU Contrast of 1500 μg/ml EGCG-GNPs . . . 61
2.15 This figure shows a linear relationship between gold nanoparticle (EGCG-GNP) concentration and mean CT attenuation in Hounsfield Units (HU). . 63

3.1 A flowchart illustrating the steps of the clonogenic assay 75
3.2 Cytotoxicity graphs demonstrate the relationship between increasing GNP concentration and toxicity. 79
3.3 Cell viability graphs for all 4 types of GNP structures ranging from 0-1000 μg/mL. 81
3.4 GNP uptake metrics between EGCG/CIT/Curc GNP coated NPs in millions(M) 83
3.5 The cell survival curves illustrate the changes in surviving fraction due to the presence of GNPs. 88
3.6 The image illustrates the clonogenic assay results with EGCG-GNP (0-500 μg/mL) concentrations increasing left-right and radiation doses increasing top to bottom (0-6 Gy). 89
3.7 The cell survival curves illustrate the changes in surviving fraction due to the presence of GNPs. 91
3.8 The image illustrates the clonogenic assay results with Curc-GNP (0-500 μg/mL) concentrations increasing left-right and radiation doses increasing top to bottom (0-6 Gy). 92

4.1 Prostatic-artery embolization (PAE) as a platform for gold-nanoparticle delivery. . . . 101
4.2 Physiologically based pharmacokinetic (PBPK) modeling workflow. . . . 109
4.3 Schematic of GNP biodistribution . . . 110
4.4 IP Administration Pathway . . . 114
4.5 Weight fractions of injected AuNP dose found in select organs after acid digestion. . . . 120
4.6 Scatter plot of weight fraction of Au versus number of days in Liver . . . 122
4.7 Scatter plot of weight fraction of Au versus number of days in Spleen . . . 123
4.8 Mouse weight was recorded every 4 days . . . 124
4.9 Organ:body weight ratios to assess liver or spleen atrophy or dystrophy for EGCG-GNPs . . . 126
4.10 Organ:body weight ratios to assess liver or spleen atrophy or dystrophy for Curc-GNPs . . . 127
4.11 GNP Toxicity: Histological Examination of Liver, Lung, and Kidney Tissues 128
4.12 Model Simulation vs Observed Biodistribution . . . 131
4.13 Interspecies extrapolation from mouse to rat . . . 132
4.14 Sensitivity of liver (a) and spleen (b) exposures to relative perturbations in key parameters. . . . 133
4.15 Axial CT of Beagle 3 (red circle) . . . 136

A.1 Stepwise process of ImageJ Particle Size Analysis . . . 170
A.2 DLS graphs for size distribution (intensity%) and zeta potential of Curc-GNPs at 0, 24 and 48 hours in three different media. . . . 171
A.3 UV-Vis spectra and image of Curc-GNPs incubated in three different media for 24 hours. . . . 172
A.4 (Left) Image of ultra concentrated EGCG-GNP (approx. 10 mg/mL), (Centre) 1.5 mg/mL EGCG-GNP, and (Right) 200 mM $HAuCl_4$ stock solution as a comparison. . . . 175
B.1 XTT results exploring the biphasic dose of Curc-GNP. . . . 176

B.2 Cellular uptake of Curc-GNPs. 176
B.3 Curc-GNP time-dependent change in cell viability (%) of PC3 cells incubated with varying concentrations (25-1,000 μg/mL) of for 24, 48, 72 hours. . . . 177
B.4 EGCG-GNP time-dependent change in cell viability (%) of PC3 cells incubated with varying concentrations (25-1,000 μg/mL) of for 24, 48, 72 hours. 178
B.5 Cit-GNP time-dependent change in cell viability (%) of PC3 cells incubated with varying concentrations (25-1,000 μg/mL) of for 24, 48, 72 hours. . . . 179
B.6 PEG-GNP time-dependent change in cell viability (%) of PC3 cells incubated with varying concentrations (25-1,000 μg/mL) of for 24, 48, 72 hours. . . . 180
B.7 Image processing for colony count analysis. Minimum size cut-off for colony count was 0.044 mm^2. 181
C.1 Stomach purple discoloration caused by GNP injection in the intraperitoneal cavity. 185
C.2 Comparison of Model Simulations to Mouse Biodistribution Data from this Study. 188
C.3 Comparison of Model Simulations to Rat Biodistribution Data from Balasubramanian *et al.* 189
C.4 Comparison of Model Simulations to Rat Biodistribution Data from Fraga *et al.* 190

List of Tables

1.1 Literature reported GNPs employed for in vivo prostate cancer radiotherapy 24

2.1 DLS Parameters Calculated for Cit-, EGCG-, Curc- and PEG- GNPs . . . 53
2.2 ICP-MS Parameters for EGCG-GNPs . . . 55
2.3 ICP-MS Parameters for Curc-GNPs . . . 55
2.4 ICP-MS Parameters for Cit-GNPs . . . 56
2.5 ICP-MS Parameters for PEG-GNPs . . . 56
2.6 CT-Imaging Parameters (Electron Density Relative to Water and HU Contrast) Calculated for 1500 μg/ml EGCG-GNPs in Comparison to Other Materials . . . 62

3.1 EGCG Radiosensitization . . . 87
3.2 Curc-GNP Radiosensitization . . . 90

4.1 Number of mice sacrificed for each time point and study group . . . 105
4.2 Organ:Body Weight Ratio Utility in mouse IP injections. . . . 107
4.3 Experimental datasets from literature used for model evaluation . . . 115
4.4 Treatment protocols for the four different canine study groups. . . . 116
4.5 The fraction of Au that was detected in the liver is relative to the initial GNP dose. . . . 121
4.6 Summary of histopathology review for both EGCG-GNP and Curc-GNP treated organs. . . . 129

A.1 ICP-MS measurements. 167
A.2 The HPLC responses, calculated concentrations, and percent deviations for curcumin standards (0.1–50 ppm) used to derive the calibration equation (y = 1.17×10^5x + 3.04×10^4; $R^2 = 0.998$). 173
A.3 The CT-Images and Mean HU Contrast for Different EGCG-GNPs Concentrations. 174
C.1 CBC Results - Beagle Study (McKenna, C. J. (2021)) 183
C.2 Serum Biochemistry - Beagle Study (McKenna, C. J. (2021)) 183
C.3 Urinalysis Results - Beagle Study (McKenna, C. J. (2021)) 184
C.4 State, Variable and Parameter Notation 191
C.5 Anatomical Values for Mouse 193
C.6 Organ Volumes and Composition for Mouse 194
C.7 Fluid Flow Rates for Mouse 195
C.8 Extravasation Parameters 196
C.9 Macrophage Content 197
C.10 Model Constants 198
C.11 Anatomical Values for Rat 198
C.12 Organ Volumes and Composition for Rat 199
C.13 Fluid Flow Rates for Rat 200

List of Abbreviations

2D Two-Dimensiona

ADT Androgen Deprivation Therapy

AUC Area-Under-the-Curve

BPH Benign Prostatic Hyperplasia

BRCA2 Breast Cancer gene 2

CCAC Canadian Council on Animal Care

CKD Chronic Kidney Disease

CRPC Castration-Resistant Prostate Cancer

CT Computed Tomography

CTAB Cetyltrimethylammonium Bromide

Curc Curcumin

D50 Dose for 50% effect

DEF Dose Enhancement Factor

DLS Dynamic Light Scattering

DNA Deoxyribonucleic Acid

EBRT External Beam Radiotherapy

EGCG Epigallocatechin gallate

EPR Enhanced Permeation and Retention

FBS Fetal Bovine Serum

FSRT Fractionated Stereotactic Radiotherapy

FTIR Fourier Transform Infrared Spectroscopy

GNPs Gold Nanoparticles

HPLC High-Performance Liquid Chromatography

HU Hounsfield Unit

IA Intraarterial

ICP-MS Inductively Coupled Plasma Mass Spectrometry

IGRT Image-Guided Radiotherapy

IMRT Intensity-Modulated Radiotherapy

IV Intravenous

LOQ Limit of Quantification

LQ Linear-Quadratic

MDL Method Detection Limit

MRI Magnetic resonance imaging

OVC Ontario Veterinary College

PAE Prostatic Arterial Embolization

PBPK Physiologically Based Pharmacokinetic

PBS Phosphate-Buffered Saline

PDI Polydispersity Index

PE Plating Efficiency

PEG Polyethylene Glycol

RES Reticuloendothelial System

ROS Reactive Oxygen Species

SER Sensitization Enhancement Ratio

SF Surviving Fraction

SOP Standard Operating Procedure

SPECT Single Photon Emission Computed Tomography

SPR Surface Plasmon Resonance

SRS Stereotactic Radiosurgery

STP Society of Toxicologic Pathology

TEM Transmission Electron Microscopy

UV-Vis Ultraviolet-Visible

WRHN Waterloo Regional Health Network

Chapter 1

Introduction

Prostate cancer is one of the most prevalent cancers affecting the male population worldwide, with significant variations in incidence across regions. Globally, prostate cancer accounts for approximately 7.1% of all cancer cases and 3.8% of all cancer deaths among men [1]. In Canada, it is the most commonly diagnosed cancer in men, with about 1 in 9 Canadian men expected to develop prostate cancer during their lifetime [2]. While surgery, chemotherapy, and radiotherapy are the primary treatment modalities for prostate cancer, radiotherapy is limited by dose-related toxicity to organs near the prostate. This thesis explores the application of phytochemical-conjugated gold nanoparticles (GNPs) to enhance radiotherapy efficacy for prostate cancer. The unique properties of nano-gold, combined with the biological activity of phytochemicals derived from natural compounds, offer a novel approach to targeted prostate cancer therapy.

In this introductory chapter, we summarize the current state of prostate cancer treatment with an emphasis on the evolving role of nanomedicine, particularly the use of GNPs in enhancing radiotherapy efficacy. This overview begins with an examination of the prevalent radiotherapy approaches and their limitations, especially in the context of prostate cancer. We then transition to a detailed discussion on the emerging use of nanoparticles in therapeutic irradiation. This includes an in-depth exploration of the properties and mechanisms of GNPs, particularly those coated with plant-based extracts, and their potential as multi-functional theranostic platforms in cancer treatment. Crucially, the chapter also addresses the critical aspects of biodistribution and toxicity of GNPs, a vital consideration in their clinical application. This comprehensive chapter sets the stage for understanding the innovative integration of nanotechnology and natural compounds in the pursuit of more effective prostate cancer treatment.

1.1 Prostate Cancer

Cancer is defined as a disease caused by the uncontrollable division of cells and their spread into surrounding tissues. This abnormality arises from alterations in genes involved in DNA repair, cell cycle regulation, and proliferation. For example, the downregulation of tumor suppressor genes can lead to uncontrolled growth of abnormal cells that would otherwise be suppressed or undergo apoptosis [3]. Cancer is often considered a modern health challenge in the 21^{st} century, partly due to increased life expectancy. However, fossil evidence shows that cancer has affected humans and their ancestors for millions of years. For example, a 1.7- million-year-old toe bone from South Africa revealed the presence of osteosarcoma, a rare and aggressive form of bone cancer, in an ancient human [4].

Prostate cancer is considered the most commonly diagnosed male malignancy in the world and the 5^{th} highest cancer-related death rate in men. It is believed that by the age of 80, 80% of men will develop prostate cancer but it will most likely be slow-growing and have little impact on life expectancy [5]. Risk factors for prostate cancer include age, genetic predisposition, and lifestyle choices, with the highest incidence in older men and those with a family history of the disease [6]. Racial and ethnic disparities are also evident, with Black men having a higher risk and worse prognosis. The mortality rate for Black prostate cancer patients is significantly worse than the general population. According to 2022 estimates from the American Cancer Society, African Americans have a 72% higher mortality rate than White males [7]. The vast differences in incidence and mortality amongst demographic groups especially between Asian populations and Western populations lead credence to the idea that lifestyle plays a major role in prostate cancer. A meta-analysis by Discacciati *et al.* found the risk of prostate cancer diagnosis increased by 9% for overweight men and 15% for obese men compared to men of normal weight [8]. Incidence and mortality rates (per 100,000) of prostate cancer by race/ethnicity in United States as per literature is depicted in Figure 1.1.

While environmental factors play a role, the initiation and progression of prostate cancer are fundamentally driven by genetic alterations. These changes can range from mutations that affect gene function to variations in gene expression, all of which can contribute to the transformation of normal prostate cells into cancerous ones. The pathophysiology involves genetic and epigenetic changes leading to uncontrolled cell growth in the prostate gland. The prostate cancer predisposition gene BRCA2 is widely known for being aggressive and having a poor prognosis [10]. *TP53*, *ATM*, and *MSH2* genes are linked with DNA damage repair processes and are also associated with aggressive prostate cancer. Hormones, particularly androgens, play a critical role in prostate cancer development and progression, as they stimulate the growth of both normal and cancerous prostate cells [11].

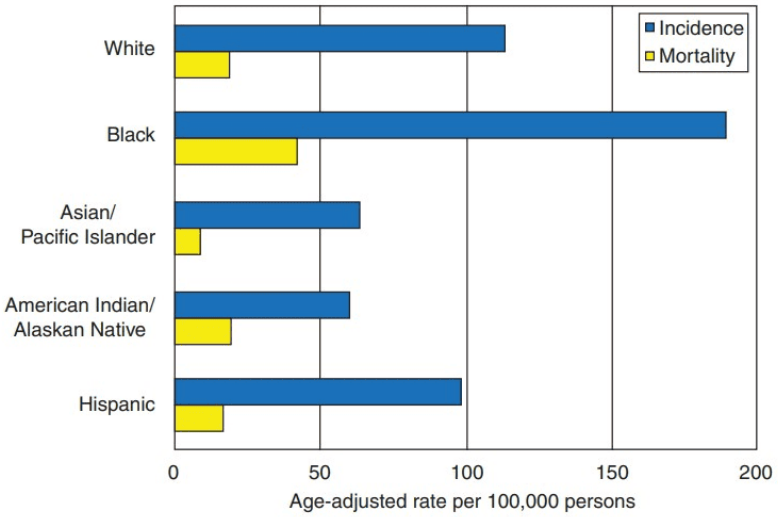


Figure 1.1: Incidence and mortality rates (per 100,000) of prostate cancer by race/ethnicity in United States [9]

1.1.1 Stages of Prostate Cancer

In the early stages, prostate cancer is often contained within the prostate gland, and the 5-year survival rate for men diagnosed with localized or regional prostate cancer is nearly 100%. However, for those with distant metastases, the 5-year survival rate falls to 30% [12]. The progression of prostate cancer is often gradual, and it may initially be asymptomatic or present with nonspecific lower urinary tract symptoms. The disease can evolve from a localized tumor, amenable to curative treatment, to locally advanced and metastatic disease [13]. The latter stages are characterized by spread to surrounding tissues, bones, or other organs and typically require systemic therapies. The natural history of prostate cancer is highly variable; some tumors may remain indolent for years, while others are aggressive and rapidly progressive [14].

The progression is influenced by both the biological behavior of the tumor and the hormonal environment of the host. The androgen receptor plays a central role in the development and progression of prostate cancer, and hence, androgen deprivation therapy (ADT) is an effective treatment for advanced disease. However, despite initial responsiveness, most prostate cancers eventually progress to a castration-resistant state (CRPC), where they no longer respond to ADT. In these advanced stages, radiation therapy emerges as a critical component of the treatment regimen [10].

1.1.2 Diagnosis of Prostate Cancer

If a patient is suspected of having prostate cancer, the treatment protocol typically follows a diagnostic and evaluation process before any treatment begins. Here's a simplified overview:

A. **Initial Screening:** If prostate cancer is suspected, usually based on a raised prostate-specific antigen (PSA) level or an abnormal digital rectal exam (DRE), further diagnostic tests are needed.

B. **Diagnostic Confirmation:** A biopsy is often the next step to confirm the presence of cancer. Imaging tests such as MRI, CT scans, or bone scans may be used to assess the extent of the disease.

C. **Risk Assessment:** Once diagnosed, the cancer is staged based on the TNM system (Tumor, Node, Metastasis) and graded based on the Gleason score. These evaluations help in determining the aggressiveness of the cancer.

D. **Treatment Decision:** Based on the stage and grade of the cancer, overall health, and patient preferences, a treatment plan is developed. For low-risk, localized cancer, options may include active surveillance, surgery or radiation therapy. For higher risk localized cancer, a combination of radiation therapy and prostatectomy may be recommended.

E. **Advanced Disease:** If cancer is advanced or has metastasized, the protocol typically involves systemic therapies such as hormone therapy, chemotherapy, immunotherapy, or newer targeted therapies such as radioligand therapy, or PARP-inhibitors.

F. **Follow-Up:** Regular follow-up is crucial to monitor the effectiveness of the treatment, manage side effects, and detect any signs of recurrence.

1.2 Current Treatment Modalities

The standard treatment protocol for prostate cancer is determined by the stage of the disease, the patient's overall health, age, potential side effects, and the likelihood of curing the disease or prolonging life. The most common treatment modalities for prostate cancer include surgery, radiation therapy, hormone therapy, and chemotherapy [15]. Prostate surgery, also referred to as prostatectomy, is the most commonly used treatment for localized prostate cancer, with radical prostatectomy (complete removal of the prostate) being the

standard surgical procedure [16]. Hormone therapy, or androgen deprivation therapy (ADT), aims to lower androgen levels to slow cancer growth and is commonly used for advanced stages [17]. Chemotherapy is typically reserved for advanced or aggressive metastatic prostate cancer that no longer responds to hormone therapy. Radiation therapy is a widely used treatment for both localized and locally advanced prostate cancer, offering cure rates comparable to surgery and serving as a key option for patients who are not surgical candidates or prefer a non-surgical approach [18]. Among these, radiation therapy stands out for its ability to precisely target prostate tumors, offering a non-invasive alternative to surgery and causing less systemic impact than androgen deprivation therapy (ADT) or chemotherapy [19]. It should be noted that treatment for prostate cancer often involves a combination of these therapies, tailored to the individual patient's disease characteristics and overall health. For example, combining radiation therapy with ADT reduced prostate cancer specific deaths by 48% compared to ADT alone, according to a meta-analysis of 18,456 patients [20].

1.2.1 Radiation Therapy

Radiation therapy utilizes electromagnetic waves or charged particles to target and eradicate malignant cancer cells. Approximately 50% of all cancer patients are subjected to receive radiation therapy during their course of illness [21]. Radiation therapy is a highly effective and widely used treatment for prostate cancer, offering cure rates comparable to surgery for localized disease [22]. Surgical options, such as prostatectomy, involve the physical removal of the prostate gland and carry significant risks of side effects, including urinary incontinence and erectile dysfunction. Hormone therapy suppresses the body's androgen production, which reduces prostate cancer growth, but does not directly kill cancer cells. In contrast, radiation therapy offers a non-invasive, targeted approach that preserves the surrounding tissues and organ function to a greater extent [23]. Its precision in targeting specific tissue makes it a strong tool, especially when the cancer is localized and has not spread, thereby providing effective treatment with a lower risk of side effects compared to more invasive treatments. A meta- analysis comparing quality of life differences between external beam radiotherapy (EBRT) and surgery found that patients who underwent the radical prostatectomy group had worse sexual function and urinary incontinence than EBRT patients, while the EBRT group had worse bowel function [24].

Radiation therapy plays a pivotal role in the management of prostate cancer across various stages of the disease. It can be used as a primary treatment for localized prostate cancer, offering an alternative to surgery with comparable outcomes in terms of cancer control and cure rates [22]. For locally advanced cancer, radiation therapy can be combined

with hormone therapy to improve survival outcomes. In the metastatic setting, it can provide palliative relief from symptoms such as bone pain. There are conventional and advanced approaches for radiotherapy as summarized in Figure 1.2. Advances in radiation technology, such as intensity- modulated radiation therapy (IMRT) and image-guided radiation therapy (IGRT), have significantly improved the precision of treatment delivery, maximizing the dose to the tumor while minimizing exposure to surrounding normal tissues, thereby reducing side effects and improving quality of life for patients [25].

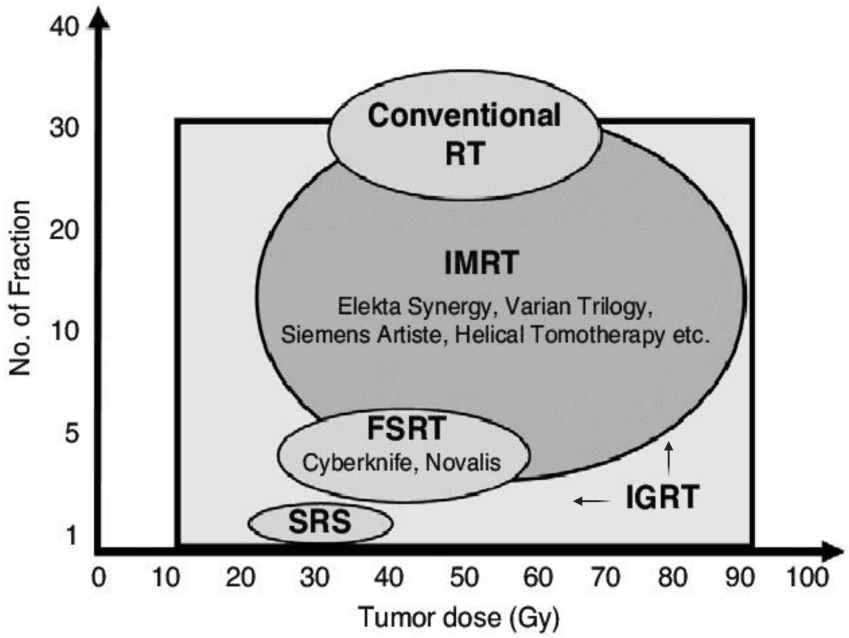


Figure 1.2: Conventional Radiotherapy, Intensity Modulated Radiotherapy (IMRT), Image-Guided Radiotherapy (IGRT), Stereotactic Radiosurgery (SRS) and Fractionated Stereotactic Radiotherapy (FSRT) w.r.t Fraction and Tumor Dose [26].

1.2.1.1 Types of Radiation Therapy

Modern radiotherapy for prostate cancer can be categorized into two main modalities: external beam radiation therapy (EBRT) and internal radiation therapy (brachytherapy) [14]. More recently, radioligand therapy, also called radiopharmaceutical therapy, has emerged as a promising option, particularly for advanced or metastatic prostate cancer. Radioligand therapy uses radioactive isotopes that specifically target prostate cancer cells, delivering radiation directly at the cellular level to destroy them.

A. External Beam and Advanced Radiation Techniques

Several EBRT techniques are available. Three-dimensional conformal radiation therapy shapes the radiation beams to match the tumor (3D-CRT), while intensity-modulated radiation therapy (IMRT) further refines this approach by varying the intensity of the beams from multiple angles, allowing for closer conformity to the tumor and better protection of nearby organs such as the rectum and bladder. Proton beam therapy uses positively charged protons that release most of their energy at a specific depth, known as the Bragg peak, which helps minimize radiation exposure to tissues beyond the tumor. Stereotactic body radiation therapy (SBRT) delivers very high doses of radiation in a small number of sessions with sub-millimeter precision, offering both convenience and accuracy, particularly for localized prostate cancer. These methods are selected based on the stage and characteristics of the cancer and aim to maximize tumor control while minimizing exposure to surrounding healthy tissue [27].

B. Brachy Therapy and Internal Radiation Therapy

Internal radiation therapy for prostate cancer primarily includes brachytherapy and, more recently, radioligand therapy for advanced prostate cancer. Brachytherapy delivers radiation directly within or adjacent to the prostate gland and is classified as either low-dose-rate (LDR) or high-dose-rate (HDR). LDR brachytherapy involves permanent implantation of radioactive seeds such as Iodine-125 (27–35 keV photons) or Palladium-103 (20–23 keV photons), commonly used in patients with low to intermediate-risk localized prostate cancer [28]. HDR brachytherapy uses a temporary placement of a high-activity source like Iridium-192 (average 380 keV photons) through trans-perineal catheters, typically delivered in multiple short sessions, and is often combined with EBRT in higher-risk cases for improved tumor control [28].

In addition to brachytherapy, radioligand therapy (RLT) has emerged as a promising systemic internal radiation approach for patients with metastatic castration-resistant prostate cancer (mCRPC). This therapy uses radioactive isotopes such as Lutetium-177 (^{177}Lu, β-emitter) or Actinium-225 (^{225}Ac, α-emitter) linked to small molecules that target prostate-specific membrane antigen (PSMA) on cancer cells, delivering radiation at the cellular level while sparing normal tissues [29]. RLT represents a major advancement for patients with advanced diseases who have progressed on prior treatments.

1.2.2 Nutraceuticals

The exploration of naturally sourced materials for the treatment of human diseases, particularly cancers, is an area of growing interest and research. Nutraceuticals, a fusion of 'nutrition' and 'pharmaceuticals,' are plant-derived products that provide both nutritional and therapeutic benefits [30]. Phytochemicals, which are naturally occurring chemical compounds in plants, contribute to their color, flavor, and structure (structures of select phytochemicals are shown in Figure 1.3). Although not classified as essential nutrients, phytochemicals are recognized for their significant health benefits. Epidemiological studies have shown that these compounds act through distinct and synergistic mechanisms to exert protective effects against infections and cancer. Many of the phytochemicals being studied for their health-promoting properties are polyphenols, flavonoids, terpenoids, alkaloids, and glucosinolates, which are molecules that help protect plants against microbial pathogens, insects, and UV damage [31, 32, 33]. For this reason, these compounds have demonstrated antimicrobial, antifungal, antiviral, and antioxidant activity, which explains why humans have recognized the medicinal properties of plants since ancient times and why they remain of high interest in modern medicine [31, 32, 33, 34, 35].

Nutraceuticals have been extensively studied in cancer therapy for their potential to prevent, manage, and treat various malignancies. However, only a small fraction of these products have demonstrated clinical efficacy, largely due to limitations such as low bioavailability and rapid degradation [37]. To address these challenges, nanotechnology has been employed to enhance the performance of nutraceuticals. Nanoparticle-based formulations improve bioavailability and stability by increasing surface area and shielding the compounds from phagocytic clearance or harsh gastrointestinal conditions. They also facilitate targeted delivery to specific sites in the body [38]. For example, Gholami *et al.* showed that liposomal encapsulation of curcumin significantly enhanced its bioavailability and therapeutic efficacy in cellular studies targeting the HTB9 bladder carcinoma cell line [39]. Similarly, chitosan-coated PLGA nanoparticles of resveratrol demonstrated superior stability, antioxidant activity, and cellular uptake in H1299 lung cancer cells compared to free resveratrol [40]. These advances highlight the potential of nanotechnology to overcome the inherent limitations of nutraceuticals and expand their clinical applications. In addition to serving as active pharmaceutical ingredients, nutraceuticals have also been used to enhance the biocompatibility, targeting efficiency, and stability of nanoparticles. For instance, conventional reducing agents like cetyltrimethylammonium bromide (CTAB) used in the synthesis of GNPs are known to cause toxicity [41]. To counter this, nutraceuticals have been applied as 'green' reducing and capping agents, offering a biocompatible alternative to synthetic chemicals. Multiple in vitro studies have shown that nutraceutical-coated GNPs

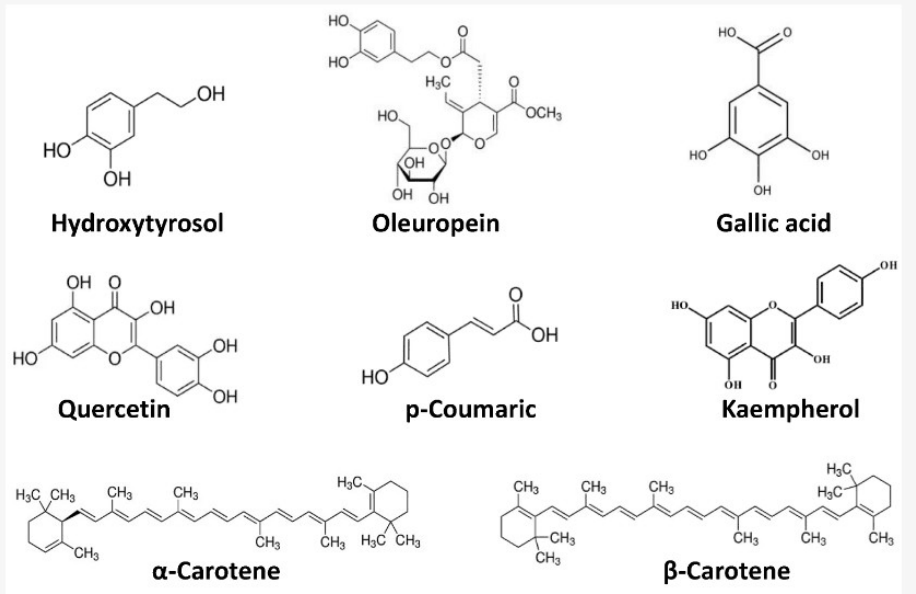


Figure 1.3: Chemical structures of commonly researched nutraceutical phytochemicals: polyphenols (hydroxytyrosol, oleuropein, gallic acid, quercetin, p-coumaric acid, kaempferol) and carotenoids (alpha carotene, beta carotene). Their conjugated aromatic systems confer antioxidant activity [36].

exhibit lower cytotoxicity and higher biocompatibility than their conventionally synthesized counterparts [42]. One proposed mechanism is the strong affinity of plant extracts for proteins, attributed to the presence of various bioactive compounds such as polyphenols, flavonoids, alkaloids, and other secondary metabolites [43].

In the green synthesis of nutraceutical capped GNPs, the plant extract molecules serve a dual purpose: firstly, as reducing agents, facilitating the conversion of gold ions (Au^{3+}) into elemental GNPs; and secondly, as stabilizing agents, preventing the agglomeration of these nanoparticles [44]. Many plant extracts serve as reducing agents due to their inherent chemical structure, which is rich in functional groups like hydroxyl, carboxyl, and ketones. The functional groups in plant extracts facilitate the reduction of metal ions to their elemental form in the synthesis of nanoparticles primarily by acting as electron donors to the Au atoms. The efficiency of this process is enhanced by the presence of multiple such functional groups, often found in the cyclic structures of natural compounds like flavonoids and phenolics. The topic of green synthesis is gaining attention due to its eco-friendly approach and its ability to produce inorganic nanoparticles with multifunctional properties, including stabilization, targeting, and therapeutic activity [31, 32, 33].

1.2.2.1 Epigallocatechin gallate (EGCG)

Epigallocatechin gallate (EGCG), a prominent catechin derived from green tea, has garnered significant attention in nutraceutical research. It is researched for its numerous health- benefiting properties, including anti-cancer, antioxidant, anti-inflammatory, and neuroprotective effects [34]. As a polyphenol, EGCG exhibits a complex chemical structure characterized by multiple phenol rings, which are responsible for its potent biological activities and strong reducing potential. These rings enable effective scavenging of free radicals, contributing to its antioxidant capacity. Specifically, EGCG has been shown to interfere with the NF-κB and Akt pathways, leading to the induction of apoptosis and inhibition of cell proliferation in breast cancer (MCF-7), prostate cancer (PC-3), and colorectal cancer (HT-29) cells [35]. These mechanisms contribute to its potent anti-cancer properties, effectively inhibiting tumor growth and progression. The neuroprotective effects of EGCG, particularly in the context of neurodegenerative diseases, are attributed to its ability to cross the blood-brain barrier and exert protective actions against neuronal damage [45]. Studies have shown that EGCG can modulate β-amyloid peptide damage in Alzheimer's disease and exert multiple neuroprotective effects through its biological, pharmacological, antioxidant, and metal chelation properties, suggesting its potential as a therapeutic agent in combating neurodegenerative conditions [46].

EGCG's application in prostate cancer therapy represents one of the most promising and dynamic areas of cancer research [47]. An epidemiologic study in Japan by Hirayama *et al.* investigated the relationship between diet and prostate cancer and found a significantly lower age-standardized death rate for prostate cancer in men who consumed green and yellow plants [48]. A similar study by Kurahashi *et al.* study found no strong association between green tea consumption and incidence of localized prostate cancer, but they did find a dose-dependent decrease in the risk of advanced prostate cancer. This study involved 49,920 men living in Japan aged 40-69 years. During the follow-up period, 404 men were diagnosed with prostate cancer, including 114 advanced cases and 271 localized cases. The relative risk for advanced prostate cancer was 0.52 for men consuming 5 or more cups of green tea per day compared to those consuming less than 1 cup per day [49]. Invitro data has also demonstrated the strong anti- cancer properties of EGCG. EGCG was found to effectively block the androgen receptor in PC- 3 cells, a critical pathway in prostate cancer progression. The study demonstrated that EGCG at concentrations of 10, 20, and 40 μM reduced the invasion of PC-3 cells by 25%, 38%, and 62%, respectively [50]. Additionally, EGCG inhibited vasculogenic mimicry (VM) tube formation of PC-3 cells by 15%, 31%, and 57% at the same concentrations (10, 20, and 40 μM, respectively). Notably, EGCG significantly decreased cell viability at 80 μM, but there was no effect on cell viability up to

40 μM, ensuring that the observed inhibitory effects on invasion and VM formation were not due to cytotoxicity [50]. In a separate study by Shukla *et al.*, EGCG-coated GNPs demonstrated enhanced uptake and binding affinity to PC-3 cells, primarily via the laminin receptor (67LR), which is overexpressed in prostate cancer cells [51]. The researchers found that blocking these receptors resulted in a significant reduction in gold concentration within the cells. This targeted approach enhances the delivery of therapeutic nanoparticles directly to prostate cancer cells, thereby maximizing efficacy and reducing toxicity. Moreover, EGCG has been observed to significantly suppress proliferation, impede invasion, and blunt metastatic potential in PC-3 cells, demonstrating its potent anti-tumorigenic capabilities [51].

In terms of EGCG's interaction with radiotherapy, studies have shown it predominantly amplifies cancer cell arrest [52, 53]. EGCG is a well-characterized NF-κB inhibitor: it blocks IKK activity (preventing IκBα phosphorylation), alkylates critical cysteine residues on the p65 subunit, and thereby prevents p65 nuclear translocation and DNA binding. This was demonstrated by Yang *et al.*, who showed that EGCG directly inhibits IκB kinase activity, thereby blocking IκB phosphorylation and preventing p65 nuclear translocation in IEC-6 cells [52]. Inhibition of NF-κB is strongly associated with reduced radioresistance due to its key role in promoting survival pathways during radiotherapy. Free EGCG (50 μg/mL) significantly sensitized DU145 prostate carcinoma cells to 4 Gy radiation, resulting in fewer surviving colonies, lower proliferation rates, and higher apoptosis indices compared to radiation alone. The combination treatment upregulated the cell cycle inhibitor $p16^{INK4A}$ and downregulated the anti-apoptotic Bcl-2 protein relative to irradiation alone. NF-κB acts as a transcriptional activator of anti-apoptotic genes such as Bcl-2, underscoring its critical role in promoting radioresistance in cancer cells.

1.2.2.2 Curcumin

Curcumin, a natural polyphenolic compound, is sourced from the rhizomes of the turmeric plant (Curcuma longa), predominantly cultivated in Asian regions. It has gained prominence in research for its anti-cancer, anti-inflammatory, antibacterial, and antioxidant properties. There have been over 9000 articles relating to curcumin and over 100 different clinical trials [54]. Research on the molecular mechanisms of actions of curcumin has established that it is a pleiotropic molecule affecting various signal transduction pathways associated with inflammation and cancer. At the cellular level it has been shown to express anti-inflammatory activity through interaction with cell signaling pathways such as NF-κB, STAT3, Nrf2, ROS, and COX-2 [55].

The inhibition of the NF-κB pathway is highly relevant to our project, as it has been

shown to increase cancer cell radiosensitivity. As mentioned in the previous section, NF-κB plays a key role in cancer cell survival, inflammation, and radioresistance. Upon irradiation, NF-κB is typically activated, promoting the expression of anti-apoptotic genes (Bcl-3, XIAP) that counteract radiation-induced damage [56]. However, curcumin can suppress NF-κB activation by a similar method to EGCG which is by interfering with IKK-mediated phosphorylation of the inhibitor protein IκBα [57, 58, 59, 56, 60]. This phosphorylation is normally required for IκBα degradation, which permits NF-κB translocation to the nucleus and activation of proinflammatory and survival genes. Curcumin's phenolic and α, β-unsaturated carbonyl groups can interact with cysteine residues in the catalytic domain of IKKβ, disrupting its kinase activity [59]. Additionally, curcumin has been reported to bind ATP-binding pockets of various kinases, thereby competing with ATP and limiting kinase-driven NF-κB activation [60]. Another mechanism by which curcumin induces radiosensitivity is through cell cycle arrest at the G2/M phase, where cells are intrinsically more sensitive to radiation due to highly condensed chromatin and reduced DNA repair capacity [58]. Recent studies have shown that curcumin can enhance radiotherapy efficacy in several cancer types, including prostate cancer, hepatocellular carcinoma, colorectal cancer, and glioblastoma [57, 58, 59].

However, like many nutraceuticals, curcumin's clinical application has been hindered by poor aqueous solubility, faster first-pass metabolism, and low bioavailability. Wahlstrom and Blennow reported that oral administration of curcumin (1 g/kg) to rats resulted in excretion of between 65%-85% in the feces within 3 days. The development of curcumin nanoparticles could notably enhance its bioavailability and therapeutic potential [61].

In the realm of anti-cancer research, curcumin nanoparticles have shown significant efficacy. A study by Yallapu *et al.* revealed that curcumin-loaded nanoparticles inhibited the proliferation of breast (MCF-7) and prostate (PC-3) cancer cells. The nanoparticles induced apoptosis in 70- 80% of MCF-7 cells and arrested the cell cycle in the G2/M phase in 60% of PC-3 cells, demonstrating a marked increase in anti-cancer activity as compared to free curcumin [62].

Nambiar *et al.* developed a robust and simple green synthesis method for fabricating curcumin- coated GNPs and in the same study demonstrated that cell medium containing serum proteins had lower cellular uptake but much higher nucleus uptake of Curc-GNPs in PC-3 cells than serum-free media. This study confirms many other reports that curcumin has a high affinity for protein thiols and the protein corona can be engineered to influence cellular uptake [63].

Specifically focusing on in vivo prostate cancer models, curcumin nanoparticles have demonstrated promising results. In a study by Mukherjee and Vishwanatha, PLGA-

encapsulated curcumin reduced tumor volume by up to 40% in a prostate cancer xenograft model. The study observed a dose-dependent response, with higher concentrations of nanoparticles yielding more significant tumor suppression [64].

1.2.2.3 Other Phytochemical-Capped Gold Nanoparticles

There have been over 70,000 published articles in Pubmed relating to nutraceuticals or dietary supplements. Plant extracts are especially useful in combination with metal nanoparticles because they can contain many bioactive molecules that facilitate the synthesis of metal nanoparticles from their salt form [65]. The list of nutraceutical-capped GNPs researched in the context of treating prostate cancer therapy are briefly discussed below.

Gum Arabic is a natural plant-derived substance obtained from the Acacia senegal and Acacia seyal trees. It consists of complex polysaccharides and glycoproteins. Gum Arabic has been used for various purposes, such as a thickening agent and stabilizer in the food industry and as a binder in the pharmaceutical industry [66]. In the context of gold nanoparticle synthesis, it is mainly used for its biocompatibility and stabilization. In 2010, Chanda *et al.* synthesized radioactive GA-^{198}AuNP to treat prostate tumor-bearing mice in a xenograft model. They reported significant tumor uptake and therapeutic efficacy with tumor volumes in the treated animals 82% smaller than the control group [67]. Researchers from the Katti group at the University of Missouri conducted a similar study in 9 canine patients with naturally occurring prostate cancer. Their study objective was to demonstrate the safety profile of radioactive GA-^{198}AuNP injected intratumorally. At 30 minutes post-injection, an average of 53% of the injected dose was found in the prostate with most elimination occurring through the bladder and urine. The authors suggested further research on retention, dosimetry, long-term toxicity, and efficacy before proceeding to Phase I trials in humans [67].

Mangiferin is a bioactive compound found in all parts of the mango plant. It is a promising antioxidant with strong health-related properties such as antiviral, anticancer, antidiabetic, antioxidative, antiaging, immunomodulatory, hepatoprotective, and analgesic effects [68]. Katti *et al.* synthesized radioactive MGF-^{198}GNPs and reported an over 85% reduction of tumor volume compared to untreated control groups in immunocompromised mice bearing prostate tumor xenografts and 90% of the dose was retained there for long periods. They claimed the high retention was due to increased tumor cell metabolism of glucose present in the lanthanoid functionality of mangiferin [69]. These promising results resulted in a pilot human clinical investigation based out of India (Figure 1.4). The results of the clinical study were published in 2020 in the Journal of Nanomedicine [67]. The clinical trial was a comparative study model with 6 breast cancer patients split randomly into two

treatment arms A (control) and B (treatment). Patients from the control group received the "Standard of Care Treatment," which included Doxorubicin injection (60 mg/m^2 every 3 weeks as a 1-hour intravenous infusion) and Cyclophosphamide injection (600 mg/m^2 every 3 weeks as a 1-hour intravenous infusion) for 12 weeks. The treatment group received standard-of-care treatment plus a capsule containing MGF-GNPs that was taken three times a day for the duration of the study (12 weeks). The authors reported 100% clinical benefit with two patients from both the control and treatment groups experiencing at least one adverse event. Most of the adverse events were reported to be mild but one severe adverse event was reported and it was claimed to not be related to treatment. Efficacy was assessed by radiographic evaluation of the size of lesions. Progressive disease response was observed in one patient (33.3%) of the control group, whereas none of the patients showed progressive disease in the treatment group [70].

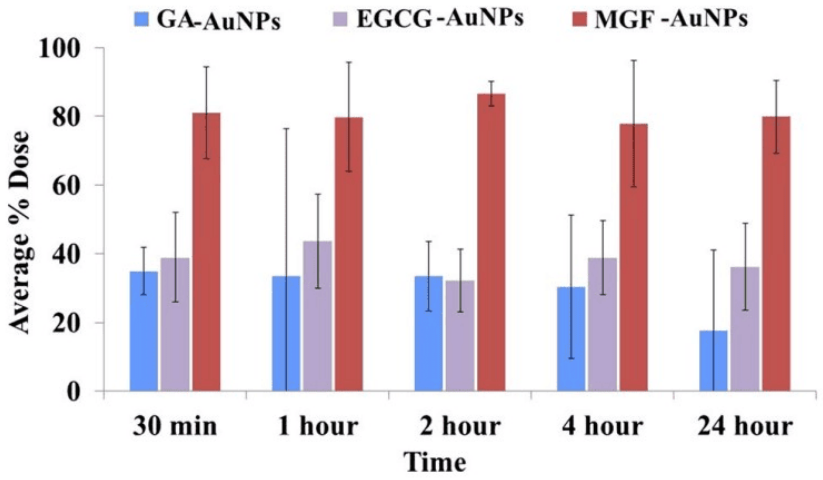


Figure 1.4: Therapeutic efficacy of Gum Arabic (GA), epigallocatechin gallage (EGCG) and mangiferin (MGF) conjugated GNPs in prostate tumor bearing mice [69]

Notably, it should be added that plant-derived medicines have a long history in oncology, and many FDA-approved chemotherapeutic treatments are derived from natural sources. For example, paclitaxel is a commonly used anti-cancer drug and was first extracted from the bark of the Pacific yew tree (Taxus brevifolia) [71]. This discovery marked a significant milestone in cancer treatment as paclitaxel demonstrated remarkable anti-cancer properties in leukemic mice in a study published in 1978 [72]. Paclitaxel belongs to a class of compounds known as taxanes, which are characterized by their ability to interfere with microtubule function, ultimately preventing cell division. This mechanism of action has made paclitaxel

an essential component in the treatment of various cancers including ovarian, breast, lung, bladder, prostate, melanoma, esophageal, and other types of solid tumors [73]. Although not plant-based, the widely used anti-cancer drug doxorubicin was also discovered from natural sources. It was discovered by the Italian research company, Farmitalia Research Laboratories after they began organizing an effort to discover anticancer molecules from soil-based microbes in 1950. The success of paclitaxel and doxorubicin underscores the importance of exploring and harnessing the therapeutic potential of natural compounds found in nature [74].

1.3 Gold Nanoparticles (GNPs)

Nanotechnology has seen a surge in research due to the unique quantum properties that emerge at the nanoscale. Gold, in particular, is a major focus in nanotechnology because of its distinctive atomic and electronic structure. Its unique properties stem from its electronic configuration: [Xe] $4f^{14}$ $5d^{10}$ $6s^{1}$. While a single outer electron typically increases reactivity, gold's 6s electron is unusually inert due to relativistic effects from its heavy nucleus [75]. This strong nuclear attraction contracts the 6s orbital, making it less reactive, yet the electron remains delocalized, allowing gold to be both a strong conductor and chemically inert [76]. In contrast, other elements with one valence electron, such as the Group 1 alkali metals (Li, Na, K, Rb, Cs, and Fr) are extremely reactive and readily lose their electron, reacting violently with water and air. This phenomenon is the basis of why gold is special: it is one of the few elements that contains delocalized electrons yet remains virtually unreactive and stable against corrosion or oxidation. The only comparable element is platinum, though it is still less inert than gold, as reflected by their ionization energies (9.23 eV for Au vs 8.96 eV for Pt). Some of the unique properties of GNPs are listed below.

1.3.1 Quantum Size Effects

One of the clearest examples of the power of nanotechnology is the quantum size effects in GNPs. These effects, particularly surface plasmon resonance (SPR), arise when the size of GNPs approaches the wavelength of light, altering their interaction with electromagnetic radiation. SPR in GNPs occurs due to their reduced size, enabling the electron cloud surrounding the nanoparticle to oscillate and resonate at specific wavelengths [77]. This resonance, particularly at around 520-550 nm for spherical GNPs, imparts a distinct ruby-red color, a unique optical signature resulting from these size-dependent oscillations. This phenomenon underlies their application in colorimetric biosensing, where GNPs SPR signal

changes based on particle binding on the surface. The size and shape of GNPs crucially influence these quantum size effects. For instance, the color variation due to GNP shape can vary drastically as well [78].

1.3.2 Inertness and Biocompatibility

The unreactivity and stability of gold contribute to the biocompatibility of GNPs, making them suitable for use in biological systems. However, there is ongoing debate about the toxicity of smaller GNPs <5 nm. This concern arises because smaller NPs are more likely to bypass biological barriers such as the liver sinusoids, kidney glomerular filtration, blood-brain barrier, or nuclear envelope [79, 80, 81, 82, 83, 79]. There is also a theory that the increased surface area of GNPs exposes more interfacial electrons compared to bulk gold [84]. These interfacial electrons can interact more readily with biomolecules, which might contribute to toxicity. These factors highlight the importance of surface coating on GNPs. There are studies demonstrating the vastly different biodistribution of GNPs based on size alone, with GNPs greater than 5 nm more likely to accumulate in the Liver and smaller than 5 nm more likely to be widely dispersed and excreted through the bladder [83]. While GNPs are generally considered non-toxic, their surface chemistry and size are crucial factors in determining their interaction with biological systems and more studies need to be conducted in this field [85].

1.3.3 Ease of Synthesis and Functionalization

Gold's ease of functionalization compared to other materials stems from the high concentration of delocalized electrons on the surface of GNPs. This high electron density facilitates strong interactions with sulfur-containing compounds, enabling the formation of self-assembled monolayers and attachment of functional groups [86]. This property makes GNPs highly versatile and desirable for various biomedical applications, allowing for efficient surface modification with biomolecules, drugs, and diagnostic agents. The ability to easily functionalize GNPs significantly expands their utility in the biomedical field [86].

1.3.4 High Atomic Number

Gold's high atomic number enhances its X-ray attenuation properties, making GNPs valuable in cancer therapy, particularly in radiological imaging and radiosensitization

of cancer cells. In diagnostic imaging, GNPs serve as effective contrast agents in X-ray computed tomography, improving image clarity and detail. In cancer therapy, their high atomic number allows for better absorption of high-energy photons, increasing the efficacy of radiation therapy [87]. This makes GNPs a potent tool in both diagnosing and treating cancer, offering enhanced visibility and treatment precision. This dual functionality, encompassing both diagnosis and treatment, is known as theranostics [87, 88, 89, 90].

1.3.5 Synthesis of GNPs

Due to size-dependent optical, electrical, and chemical characteristics, understanding GNP synthesis is crucial in producing nanoparticles fit for purpose. One of the most intriguing aspects of GNP synthesis is the sheer diversity of protocols available. The reason behind the multitude of synthesis protocols is the sensitivity of GNPs' properties to the conditions under which they are synthesized. Parameters like temperature, pH, pressure gold concentration, reducing agents, and stabilizers can all influence the outcome. This sensitivity allows for a high degree of customization but also necessitates a wide range of protocols to achieve the desired characteristics for specific applications [91].

The first synthesis of colloidal gold, often attributed to Michael Faraday in the 1850s, laid the groundwork for modern nanoparticle science. However, it was the work of Turkevich *et al.* in the 1950s that revolutionized the field. Turkevich's method involved reducing gold chloride using citrate, leading to the formation of small, spherical GNPs. This protocol was not only simple but also reproducible, paving the way for the standardized production of GNPs. The Turkevich method (Figure 1.5) remains a cornerstone in GNP synthesis, often serving as a starting point for developing new synthetic strategies [92].

Since the Turkevich method, there have been countless synthesis protocols proposed each with its advantages and disadvantages. Generally, they are broken down into two methodologies, known as the top-down approach or the bottom-up approach [93]. The bottom-up approach starts with the molecular interaction of metal salts to produce a structure, whereas the top-down approach starts with the bulk material being broken down until the required size/shape is obtained. The bottom-up techniques can be further divided into subcategories physical, biological, and chemical. The physical method can entail sonication, laser ablation, radiation, or electrodeposition [93]. The biological method can entail plant, bacteria, and fungi-mediated synthesis [94]. The chemical method can entail chemical reduction, condensation, or seed mediated [93]. Gold nanospheres are usually through the chemical reduction method whereas gold nanorods are through seed-mediated growth and gold nanowires are made through the electrochemical method. Interestingly,

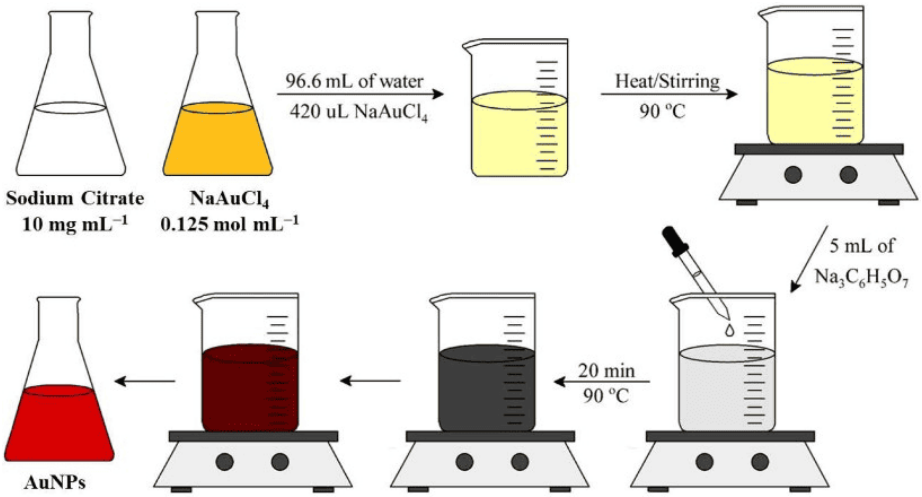


Figure 1.5: Schematic illustration of gold nanoparticles synthesis by Turkevich method [92]

there is an innovative method based on in vivo plant- based synthesis, where living plants can uptake gold nanoparticle precursors from the soil [95]. These precursors are then transported and synthesized into GNPs within different compartments of the plant. This natural process of nanoparticle formation within living plants represents a fascinating intersection of nanotechnology and plant biology [96, 97, 93].

The concept of green synthesis of GNPs started to emerge in the early 2000s as researchers sought more sustainable and environmentally friendly methods of nanoparticle production. More recently, they have been further studied to incorporate the medicinal properties of the green extract with the nanoparticle construct. One of the main advantages of the green synthesis method for GNPs is that it often uses a single substance that acts both as a reducing agent and a stabilizing agent [90]. This dual functionality is not typically found in other conventional methods of GNP synthesis, which generally require separate chemicals for reduction and stabilization [94]. In the synthesis of GNPs using sodium borohydride, the process typically involves two distinct components: the reducing agent and the stabilizing agent. Sodium borohydride serves as the reducing agent, responsible for the chemical reduction of gold ions into GNPs [91]. However, sodium borohydride alone cannot stabilize the newly formed nanoparticles, which are prone to aggregation. To prevent this, a separate stabilizing agent is required. Common stabilizers include citrate, polyvinyl alcohol (PVA), or polyvinylpyrrolidone (PVP), which adsorb onto the surface of the nanoparticles, providing steric or electrostatic stabilization [86, 91, 92, 96, 97]. Compare this to the green synthesis of EGCG, curcumin, and mangiferin-coated GNPs,

the polyphenols, flavonoids, and terpenoids present in these extracts effectively reduce gold ions and simultaneously adsorb onto the surface [98]. In summary, plant-based molecules can fulfill both roles because of their complex and multifunctional nature whereas synthetic chemicals are generally made for singular functionality. For example, sodium borohydride is primarily used in research and industrially as a nucleophilic reducing agent in reactions.

1.3.6 Mechanistic Approach

The mechanism of GNP synthesis has been thoroughly studied, and multiple models have been proposed. Adams *et al.* proposed a multistep mechanism for the quick reduction of Au (III) to Au (0) atoms that form clusters, followed by their assembly into larger polycrystalline particles and completed by further aggregation [99]. The mechanism of green synthesis of GNPs has also been studied in aqueous mediums containing polyphenols. The mechanism follows similar stages to conventional synthesis of GNP synthesis which is as follows:

A. Nucleation: This is the initial phase where gold ions in a solution begin to form tiny clusters. This phase is rapid, and the concentration of nanoparticles is the highest at this point. The process is initiated by the bioactive molecules that convert gold ions (Au^{3+}) into elemental gold (Au^0). This nucleation phase is critical because the conditions set here (like concentration, temperature, and pH) significantly influence the size, shape, and thickness of the green coating of GNPs [44]. In polyphenols such as EGCG the multiple phenolic hydroxyls act as binding centers and thus can bind Au^{3+} ions by forming stable chelating rings. Because of complexation, a redox reaction occurs, and the chelated Au^{3+} ions are reduced to Au^0 atoms, while a part of the phenolic hydroxyls is simultaneously oxidized to corresponding quinone. Thus, the phenolic molecules result in being physically adsorbed onto the surface of nanogold particles [44]. This attachment has been studied by Singh *et al.* who proposed through computational studies that the electron transfer of O from the hydroxyl group to the Au atom is what potentially causes the physical binding [44].

B. Growth: Once nucleation starts, the tiny gold clusters grow by accumulating more gold atoms or other gold clusters. The concentration of nanoparticles decreases indicating coalescence of gold clusters. This stage is controlled by factors like the concentration of green extracts, and the reaction conditions (temperature, pH, pressure) [44]. During the growth phase, the processes start to slow down as nanoclusters come together. According to Reiss *et al.* the growth rate of spherical

nanoparticles is controlled by monomer flux [100]. Therefore, the concentration ratio between green extract and gold ions will be a major factor in the growth and size of the GNPs. Generally, the greater the concentration of green extract the smaller the GNPs as the particle reaches electrostatic stability quicker. However, the balance of extract to Au ion concentration is important as demonstrated by Adlia *et al.* where they synthesized different- sized curcumin-GNPs using curcumin concentrations of 0.25, 0.5, 0.75, 1, 1.5 and, 2 mM [101]. Surprisingly, the largest concentration 2 mM did not result in the smallest GNPs because GNPs were not formed at that concentration. The smallest GNPs were found in 1.5 mM (62.3 nm) and not 2 mM. However, the authors did report a correlation between curcumin concentration and GNP size but only for concentrations where actual GNPs were formed [101].

C. **Stabilization:** The termination of the growth phase is influenced by many factors such as depletion of precursor Au^{3+} ions in the solution, adsorption of green extract onto the surface, and thermodynamic stability [100]. The first factor is self-explanatory, once the precursor gold ion is used up, the growth phase cannot occur. The adsorption of the green extract on the surface can also lead to the end of growth as the adsorbed molecules form a barrier on the nanoparticle surface, hindering further growth by preventing additional gold ions from accessing the nanoparticle surface [44]. Additionally, many biomolecules in green extracts carry a negative charge [44]. When these molecules coat the surface of GNPs, they impart a negative charge to the particles. This results in electrostatic repulsion between individual nanoparticles. From a thermodynamic perspective, smaller GNPs have higher surface energy, and this drives their tendency to grow [100]. However, as GNPs grow and reach a certain size, the thermodynamic driving force for further growth diminishes. The adsorption of green extract compounds further reduces the surface energy of the nanoparticles, contributing to their thermodynamic stability [94].

1.3.7 Uptake of GNPs in Cells

One of the most important features of GNP constructs is their cellular uptake, particularly in the context of GNP adjuvant radiotherapy. Effective uptake of GNPs in cancer cells is crucial as many studies have shown a correlation between GNP uptake and higher dose enhancement factors [102, 103, 87, 88, 89]. This objective, while seemingly straightforward, is complex to achieve because there is tremendous variability in the literature. A significant contribution to this field is the 2019 study by Carnovale *et al.*, which examined the influence

of various GNP nanoparticle parameters on uptake in PC-3 cells [104]. Their findings indicated that cellular uptake varied with the shape of the nanoparticles. Gold nanospheres exhibited the highest uptake, followed by gold nanocages, nanorods, and nanoprisms. Spherical particles were preferentially taken up due to their geometry, which have higher contacts with cell surface receptors and requires less energy for endocytosis [104].The variability in nanoparticle uptake across different studies can be attributed to differences in experimental conditions such as size, shape, concentration, cell line, surface charge, coating, serum, and protein corona. Changing any one of these parameters can have profound impacts on uptake as depicted in Figure 1.6

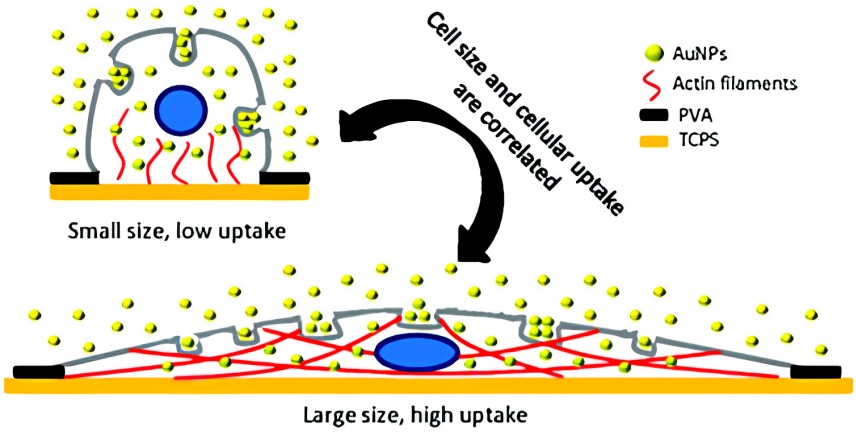


Figure 1.6: Influence of cell size on cellular uptake of GNPs [105]

Concerning size, smaller spherical GNPs were taken up in significantly higher numbers compared to their larger counterparts [104]. However, the total gold content internalized was lower for smaller particles. It is generally observed that nanoparticles in the 25-50 nm range have the higher cell uptake, a trend consistent with many studies [105, 106, 107, 108]. The mode of entry for smaller particles is typically through pinocytosis, while larger particles utilize receptor- mediated endocytosis. Additionally, larger GNPs tend to be retained within cells for longer durations as their size can prevent efficient exocytosis. Conversely, smaller GNPs may be more readily excreted from cells [106].

There have also been studies that investigated the effect of serum protein on nanoparticle uptake in PC-3 cells. In general, GNPs were taken up more abundantly in serum conditions compared to serum- The influence of serum protein on nanoparticle uptake in PC-3 cells reveals that GNPs are more readily internalized in serum-free conditions [107]. This was reported to be due to the formation of a protein corona on the nanoparticle surface in serum-supplemented media, which can hinder interactions with the cell membrane [104]. However,

the effect of serum varies with surface coatings: tyrosine-coated GNPs show increased cellular viability with serum pre-incubation, whereas citrate-coated, tryptophan-coated, CTAB/citrate-coated GNPs, AuNC (Gold nanocages), and AuNPr (Gold nanoprisms) exhibit no significant difference [107].

Surface coating plays a critical role, with tryptophan- and tyrosine-coated GNPs demonstrating higher uptake compared to those coated with citrate and CTAB/citrate. This highlights the importance of surface chemistry in mediating nanoparticle-cell interactions, particularly the influence of aromatic groups on affinity and binding to cell surface receptors [104].

Upon internalization, GNPs exhibit dynamic intracellular distribution, which critically influences their functionality. Studies show rapid internalization and distribution within various cellular compartments. For example, 57 nm and 84 nm GNPs in HeLa and MCF-7 cells were predominantly found in the cytoplasm, sparsely near the nucleus, and even within mitochondria, indicating their ability to traverse beyond initial endocytic pathways [108].

GNP size also dictates their intracellular fate. Smaller GNPs are more likely to escape endosomes and disperse into the cytoplasm, while larger ones tend to remain confined within endosomal or lysosomal compartments [109]. Furthermore, smaller GNPs more readily enter the nucleus, which is crucial for radiosensitization applications where nuclear localization enables short-range electrons to damage genomic structures [109]. Nativo *et al.* demonstrated enhanced endosomal escape and nuclear targeting by functionalizing GNP surfaces with cell-penetrating peptides and a nuclear localization sequence (NLS), leading to increased nuclear presence and disrupted perinuclear endosomes [110].

In summary, the intracellular fate of GNPs, including their distribution across the cytoplasm, perinuclear regions, endosomes, and potentially the nucleus, is influenced by size, surface chemistry, and cellular entry mechanisms. Understanding these complex GNP-cell interactions is vital for effective biomedical applications, particularly in designing GNPs for radiation therapy, where increased cellular and nuclear uptake has been linked to enhanced efficacy [102].

1.4 GNPs in Radiation Therapy

One of the most promising applications for GNPs lies within radiation therapy. Gold's high atomic number allows for photon energy absorption up to 100-fold greater than water, making GNPs attractive for X-ray contrast agents and radiosensitization [102]. Radiosensitization, a key oncological concept, enhances cancer cells' sensitivity to ionizing

radiation, enabling more effective radiation doses, especially for resistant cells [111]. This radio-enhancement typically involves high-energy particle bombardment of gold particles, releasing energy localized near the GNPs. The phenomenon of dose enhancement from high Z materials was initially observed in patients with metal implants undergoing radiotherapy for head and neck cancers [102]. Early research attempting to utilize gold as a radiosensitizer employed gold foil and microspheres, but their effectiveness was limited by insufficient tumor delivery [102].

Nanotechnology has since enabled the precise delivery of GNPs to tumor cells and even subcellular locations [108, 109, 110]. The pioneering work by Hainfeld *et al.* demonstrated the first use of GNPs as radiosensitizers in 2004. They observed complete tumor regression and a significant increase in survival (from 20% to 86%) in tumor-bearing mice systemically injected with 1.9 nm thiol-coated GNPs combined with 250 kVp X-rays [103]. Subsequent research indicated that the enhanced cell killing by GNPs surpassed predictions based solely on physical dose enhancement from computer models [112, 113, 114, 115, 116]. This discrepancy suggested more complex mechanisms of radiosensitization beyond simple increased energy deposition [117]. Table 1.1 presents some literature reporting GNPs synthesized through various methods and tested in vitro for prostate cancer treatment.

1.4.1 Mechanisms of Radiosensitization

Radiosensitization by GNPs was initially attributed solely to physical dose enhancement, primarily due to gold's high photoelectric absorption [112]. However, experimental data revealed additional chemical and biological contributions, suggesting GNPs influence all three phases of interactions with ionizing radiation (Figure 1.7) [112]. While the precise mechanisms remain to be fully elucidated, several modes of radiosensitization have been proposed [112]. These mechanisms are discussed in detail below.

1.4.1.1 Physical Process

The physical mechanisms behind enhanced cell killing by high-Z materials are well-defined. The primary process is the photoelectric effect, where incident photons interact with gold atoms in the nanoparticles. When photon energy approaches or exceeds the binding energy of K-shell electrons in gold (80.7 keV), these photoelectrons are ejected. This localized ionization and damage are particularly effective in tumor cells that have taken up the nanoparticles [113]. Following K-shell electron ejection, an electron from a higher energy level fills the vacancy, releasing excess energy either as a secondary photon or by ejecting

Table 1.1: Literature reported GNPs employed for in vivo prostate cancer radiotherapy

GNPs	Synthesis Method	Tumor Model	Radiation Type	Results	Ref
Glucose-capped GNPs	Chemical	MCF-7 cell line	200 kVp X-ray	Cancer cells take up functional Glu-GNPs significantly more than naked GNPs and cytotoxicity increased by 63.5% for them.	[87]
PSMA-1 targeted GNPs	Physical	PC3pip and PC3flu cells	6 Gy of X-ray	The targeting ligand PSMA-1 dramatically improved gold uptake by PSMA-expressing PC3pip cells.	[88]
Amine-pegylated GNPs	Turkevich	PC3, DU145, and LNCaP cell lines	2.5 Gy in 3 days, total radiation dose of 7.5 Gy	An increase in the sensitization enhancement ratio was observed by cells treated with GNPs and ionization radiation which was cell line dependent.	[89]
MGF-GNPs	Green	SCID mice implanted with prostate tumor (PC-3) xenografts	30 Gy to 120 Gy	Over 85% reduction of tumorvolume as compared to untreated control groups was observed with retention of over 90% of the injected dose within tumors for long periods of time.	[69]
Alhagi maurorum leaf-GNPs	Green	DU 145, NCI-H660, 22Rv1, and LNCaP clone FGC cell lines	200 kVp X-ray	The viability of malignant prostate cell lines reduced dose-dependency in the presence of GNPs. The IC50 of GNPs were 229, 368, 298, and 222 μg/mL for each cell line respectively.	[90]
BSA-GNPs	Biological	LnCaP and PC-3 cell lines	6 Gy	The therapeutic potential of the BSA based GNPs was significant with a focus on cases where there was complete regression of the tumor mass.	[118]

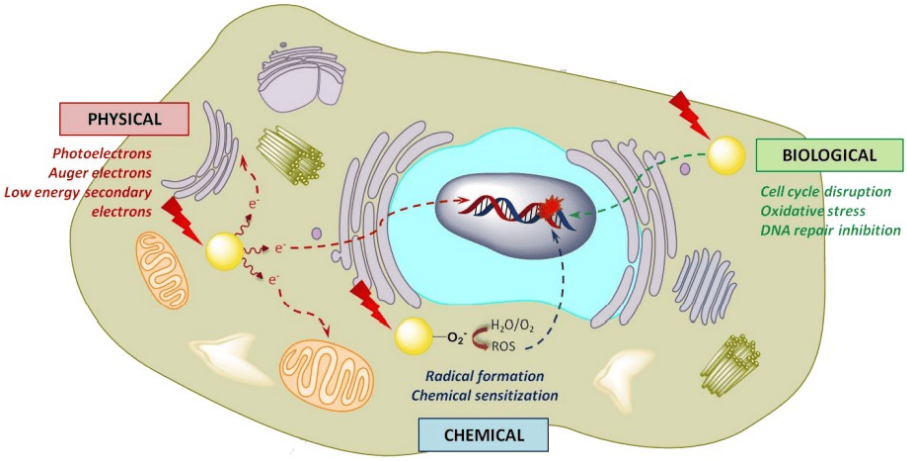


Figure 1.7: Phyical, chemical and biological mechanisms of GNPs radiosensitization [112]

another electron, known as an Auger electron. Despite their low energy, Auger electrons are highly effective at causing localized cellular damage due to their short range, and high local dose. significantly impacting DNA and other vital cellular components [113]. The efficiency of the photoelectric effect notably increases when photon energy is just above the gold K-edge, approximately 80 keV [113].

Complementing the photoelectric effect is Compton scattering. In this process, incident photons scatter off electrons within the GNPs, transferring part of their energy to these Compton electrons. These energized electrons further contribute to ionization and damage in tumor cells [114]. The effectiveness of Compton scattering depends on the incident radiation's energy and the GNPs' physical properties, such as size and concentration [114]. Compton interaction dominates in the higher photon energy range of 25 keV-25 MeV and is the most common interaction in cancer tissue during routine radiotherapy, which typically uses energy levels of 6-20 MeV [114].

The last reported physical mechanism is pair production, where a high-energy photon (typically exceeding 1.022 MeV) interacts with a nucleus's electromagnetic field, converting into an electron-positron pair [114, 115]. This 1.022 MeV threshold is twice the rest mass energy of an electron, providing the minimum energy required for the creation of an electron and a positron [113, 114, 115]. Once liberated, the electron and positron dissipate energy through successive interactions with nearby particles [114]. Pair production dominates above 25 MeV, so it only contributes a small fraction in routine radiation therapy [114].

Monte Carlo methods are highly effective for simulating radiation dose enhancement in-silico based on these physical interactions [116]. These simulations account for factors like beam attenuation, secondary particle distribution, and elemental variations in the irradiation field, leading to accurate dose predictions [116]. Hossain *et al.* utilized Monte Carlo methods for a comparative study on the dose enhancement capabilities of gold, platinum, and bismuth nanoparticles. By adjusting variables like nanoparticle size, concentration, and X-ray voltages, they calculated the production probabilities of photoelectrons, Auger electrons, and total Dose Enhancement Factors (DEFs) [116]. Their findings showed that smaller nanoparticles, lower energy X-rays, and nanoparticles positioned closer to the cell nucleus resulted in higher DEFs [116]. Intriguingly, they discovered that Auger electrons, despite their lower energy, had a more significant impact on dose improvement than photoelectrons. This is attributed to the higher linear energy transfer (LET) of Auger electrons, enabling them to transfer more energy to cells adjacent to the nanoparticles [116].

1.4.1.2 Chemical Processes

The chemical processes of radiosensitization by GNPs are crucial, especially concerning reactive oxygen species (ROS) production. The significantly increased biological effects observed under radiation in the presence of GNPs are largely attributed to ROS formation [117]. ROS, including superoxide anion (O_2^-), hydroxyl radical (OH ·), and hydrogen peroxide (H_2O_2), are the primary mediators of radiation-induced cell death [111]. These ROS are generated near GNPs by the emission of photoelectrons and Auger electrons. For instance, high-energy electrons can ionize water molecules, forming (OH ·), which leads to oxidative stress and subsequent DNA breakage. Auger electrons, specifically, are highly effective at localized ionization and excitation of molecules. Numerous studies, as illustrated in Figure 1.8, demonstrate increased ROS generation from the combination of ionizing radiation and GNPs [119].

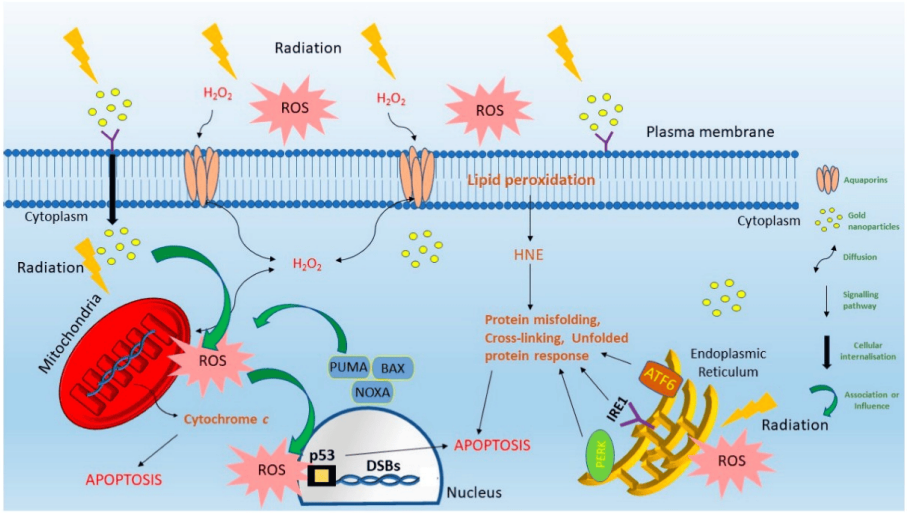


Figure 1.8: Mechanisms of ROS generation for apoptosis during radiosensitization [117]

1.4.1.3 Biological Processes

Understanding the biological processes of radiosensitivity is best framed within the context of the 5Rs of radiotherapy: repair, reoxygenation, repopulation, redistribution, and intrinsic radiosensitivity [120]. The 5Rs describe how tumor and normal cells respond to fractionated therapy, where radiotherapy is delivered in multiple treatments over a period, typically weeks. The following subsections discuss how GNPs can biologically affect each of the 5Rs.

A. **Repair:** After radiation therapy, cancer cells attempt to repair induced damage. Cells possess mechanisms to repair DNA damage from ionizing radiation [111, 117, 120, 121]. However, GNP exposure has been linked to a reduced DNA repair rate, evidenced by a higher ratio of unrepaired double-strand breaks (DSBs) in GNP-incubated cells compared to controls. This increase in unrepaired DSBs directly correlates with cell death, indicating that GNPs intrinsically impair cells' ability to repair sub-lethal damage. Studies have also shown downregulation of DNA repair genes like ATM, RAD21, and MRE11A [121].

B. **Reoxygenation:** Oxygen is vital for making cancer cells more susceptible to radiation. Tumors often contain hypoxic (low oxygen) regions, which are less responsive to treatment [113]. As radiotherapy progresses, these areas can reoxygenate, enhancing treatment efficacy [113, 121]. Studies demonstrate that GNP radiosensitization is more pronounced under normoxic (normal oxygen) conditions than hypoxic ($pO_2 < 1\%$) conditions, underscoring oxygen's critical role in GNP enhancement [120]. Interestingly, radical scavengers, which neutralize ROS, have been found to reduce the radiosensitization effect when GNP-containing cells are exposed to ionizing radiation [120]. GNPs have been shown to increase intracellular ROS levels even without radiation in numerous in vitro studies [119].

C. **Repopulation:** Cancer cell repopulation, or growth during radiation treatment, poses a major challenge in radiotherapy, often leading to treatment failure as rapidly dividing cells outpace radiation-induced damage [113]. GNPs can counteract this by inhibiting or slowing cellular growth and proliferation through their effect on the cell cycle [120]. Research indicates that citrate GNPs can induce overexpression of p21 and p27 proteins in various multiple myeloma cell lines, leading to G1 phase cell cycle arrest [120]. Additionally, a decrease in cells in the G2/M phase was observed when GNPs coated with a nuclear localization sequence were incubated with different cancer cell lines [120].

D. **Redistribution:** Cellular radiosensitivity varies significantly across cell cycle phases. S- phase cells are more resistant, possibly due to enhanced homologous recombination repair, while late G2 and M phases are more sensitive [113, 117]. Research on GNP effects on cell cycle distribution is mixed; some studies found no significant change in various cell lines with specific GNP sizes (1.4, 1.9, or 2.7 nm), while others reported GNP-induced cell-cycle arrest [115, 120]. Most findings indicate a G2/M phase arrest coupled with acceleration of G0/G1 or S phases. This suggests GNPs can influence cell cycle phases, potentially sensitizing cells to radiation at specific points, with observed

changes in gene and protein expression providing insights into this redistribution effect [115, 120].

E. Intrinsic Radiosensitivity: Different cancer cell types exhibit varying natural sensitivities to radiation [113]. Incubation of DU145 prostate cancer cells with 8 nm GNPs increased radiosensitivity through activation of CASP 3, 8, and 9 [84]. Similarly, 15 nm GNPs upregulated apoptosis-related genes like CASP3 and CASP7 [102]. GNPs have also been found to inhibit the TrxR protein, encoded by the TXNRD1 gene [122]. Overexpression of TXNRD1 in tumors correlates with treatment resistance and poor patient survival. Given varying basal TXNRD1 expression levels in cancer cells, GNP inhibition of TrxR suggests a role in reducing treatment resistance [122].

In the current clinical landscape, FDA-approved radiosensitizers are often based on cell cycle interactions, DNA crosslinking, and targeting tumor hypoxia [113, 111]. Examples include conventional chemotherapeutics like fluoropyrimidines, gemcitabine, and platinum analogs, which show synergistic effects with radiation therapy [123, 124]. Fluoropyrimidines increase radiosensitivity by disrupting S-phase cell cycle checkpoints [123]. Platinum-based chemotherapeutics, such as cisplatin, inhibit DNA repair by cross-linking DNA strands, thereby exacerbating radiation-induced DNA damage [124]. Hypoxic cell radiosensitizers, like misonidazole and metronidazole, are a distinct category designed to target hypoxic tumor cells by increasing their oxygen content [124].

1.5 Biodistribution and Toxicity of GNPs

The biodistribution of GNPs critically informs their biomedical applications, revealing their therapeutic potential and toxicity. Factors such as size, shape, surface charge, and coating significantly influence this distribution within the body, altering their biokinetics, biological interactions, and ultimate efficacy [79]. Early research by Oussoren *et al.* (1998) administering liposomes containing colloidal gold subcutaneously in mice found predominant GNP accumulation in the liver and spleen, primarily via phagocytic cells of the reticuloendothelial system (RES), highlighting organ-specific targeting [79].

GNP size is the most crucial factor dictating their biological interactions and biodistribution. Generally, larger GNPs tend to accumulate in the liver via the RES, while smaller GNPs exhibit prolonged blood circulation and broader systemic exposure [80, 81, 82, 83]. This trend holds across various shapes and surface coatings, as reported by Hirn *et al.* [80]. Their study, using ^{198}Au-radiolabeled negatively charged GNPs of various sizes

(1.4, 5, 18, 80, and 200 nm) and 2.8 nm GNPs with positive surface charges in rats, demonstrated that both size and surface charge significantly influenced biodistribution after 24 hours. Specifically, 99% of 200 nm GNPs were detected in the liver, whereas only 50% of 1.4 nm GNPs were found there, with the remaining 1.4 nm particles distributing to other organs like the kidney, brain, and lungs [80]. They also found size-dependent clearance routes: GNPs less than 10 nm were primarily cleared renally (urine), while larger GNPs were cleared through hepatobiliary route (feces) [80]. However, hepatobiliary excretion also depends on GNP stability, as agglomerated GNPs are excreted much slower and more prone to liver toxicity [125].

In summary, smaller GNPs tend to exhibit broad organ distribution regardless of administration route, owing to their ability to bypass biological barriers like cell membranes and phagocytic detection [79]. A size range of 10-60 nm is often considered ideal for prolonged blood circulation, as these particles are large enough to avoid rapid renal clearance but small enough to avoid immediate liver accumulation [81]. This aligns with the enhanced permeation and retention (EPR) effect and circulation passively accumulate in tumors due to their leaky vasculature [81]. Betzer *et al.* synthesized 20, 50, and 70 nm insulin-coated GNPs (INS-GNPs) and observed the most widespread biodistribution and highest brain accumulation in 20 nm INS-GNPs in BALB/c mice, with decreasing accumulation for larger GNPs [82]. A kinetic study by De Jong *et al.* on GNP biodistribution in rats found 10 nm particles in every tested tissue (blood, liver, spleen, kidney, testis, thymus, heart, lung, and brain), whereas larger particles (50, 100, 250 nm) were only detected in blood, liver, and spleen [83].

Beyond size, surface coating is another critical parameter influencing GNP biodistribution and toxicity [79, 125]. Polyethylene glycol (PEG)-coated GNPs are extensively studied for their ability to evade phagocytosis and RES uptake, leading to extended blood circulation times [79]. Hirn *et al.* confirmed that PEGylation of 5 nm GNPs prolongs their blood circulation compared to naked GNPs, which are more prone to agglomeration and protein binding [80]. The formation of a protein corona is increasingly recognized as a crucial factor altering their biological fate and, by extension, their biodistribution [80, 79].

Understanding GNP toxicity remains a major barrier to clinical translation and has sparked ongoing debate since their introduction in nanomedicine [126]. Key questions about long-term effects, especially liver and kidney toxicity, remain unresolved. Despite extensive research, findings are often conflicting, largely due to a reliance on in vitro rather than in vivo studies and comparisons between GNPs with very different physico-chemical properties [126]. Grouping all GNPs together in toxicity discussions is problematic, as demonstrated in by Yan *et al.*, where they found GNPs varying by size, shape, or surface (e.g., 5 nm vs. 100 nm or rods vs. spheres) behave very differently in biological systems [71].

1.6 Research Gap and Rationale

Despite promising advances using phytochemicals or GNPs individually in cancer therapy, a critical gap remains in evaluating their combined potential as radiosensitizers for prostate cancer. Numerous studies have examined GNPs alone or natural compounds like EGCG and curcumin alone as enhancers of radiotherapy, but few have systematically explored GNPs conjugated with these phytochemicals. The potential synergistic benefits of such phytochemical-coated GNPs in radiotherapy thus remain largely uncharacterized in the literature. In particular, no head-to-head comparisons have been reported to determine which phytochemical coating (EGCG vs. curcumin) offers superior radiosensitization under identical nanoparticle conditions, especially under clinically relevant megavoltage (MV) X-rays. This represents a significant knowledge gap that this thesis aims to address.

There are strong indications that EGCG and curcumin could enhance the radiosensitizing efficacy of GNPs [57, 58, 59, 56, 60, 52, 53]. Both EGCG and curcumin exhibit intrinsic radiosensitization mechanisms, such as suppression of pro-survival pathways like NF-κB, induction of G_2/M cell-cycle arrest, and modulation of oxidative stress and apoptosis regulators, which could complement the physical dose-enhancing effects of high Z gold. Moreover, EGCG and curcumin have demonstrated favorable interactions with prostate cancer cells. EGCG, for instance, has a high affinity for the 67 kDa laminin receptor overexpressed on PC-3 prostate cancer cells, enabling targeted uptake of EGCG-coated nanoparticles by these cells [51]. Curcumin, being lipophilic, can readily integrate into lipid membranes and may facilitate nanoparticle internalization into tumor cells [64]. Additionally, both phytochemicals serve as robust reducing and capping agents for green synthesis of GNPs, yielding stable, biocompatible nanoparticles without the need for harsh chemicals [63]. Given these advantages, a direct comparative evaluation of Curcu-GNPs vs. EGCG-GNP formulations (with consistent particle size, shape, and concentration) is needed to isolate their mechanistic contributions to radiosensitization and determine which coating confers greater enhancement of radiation effects.

A second major gap exists in the in vivo delivery strategy for nanoparticle radiosensitizers. Nearly all preclinical studies delivering GNPs for radiosensitization have used intravenous (IV) injection and relied on the EPR effect for tumor accumulation. However, the EPR effect in solid tumors is highly heterogeneous and its clinical relevance is increasingly debated, with studies showing that only a small fraction of systemically injected nanoparticles actually localize to human tumors [127]. This raises concerns that IV delivery may not achieve sufficient intratumoral gold concentrations in prostate cancer for effective radiosensitization. Alternative delivery routes, such as intraperitoneal (IP) and intra-arterial (IA) injections, have been scarcely explored for nanoparticle-based therapy, yet they could potentially

improve targeting and distribution. IP administration, for example, may prolong circulation or favor uptake in pelvic tissues, while direct IA infusion into the prostatic artery could bypass systemic dilution and liver sequestration, delivering a higher payload of nanoparticles directly to the tumor site. Early clinical evidence already suggests that arterial infusion can dramatically increase local agent uptake in oral tumors compared to IV infusion [128]. Therefore, investigating IP and IA delivery of EGCG-GNPs and Curc-GNPs is crucial to determine whether these routes offer more favorable biodistribution profiles and to bridge the translational gap between promising in vitro results and practical clinical application in radiotherapy.

By directly comparing two phytochemical functionalizations side-by-side and evaluating novel delivery pathways beyond the conventional IV/EPR approach, this research will fill key knowledge voids. The findings will elucidate whether phytochemical-coated GNPs can provide enhanced, tumor-selective radiosensitization in prostate cancer and how best to deliver these nanotherapeutics in vivo, thereby laying groundwork for more effective and clinically translatable GNP-based radiosensitizers.

1.7 Aim and Objectives of Research Undertaken

Hypothesis 1: EGCG-GNPs and Curc-GNPs will be effectively taken up by prostate cancer cells and will act as potent radiosensitizers under clinically relevant X-ray energies. Coating GNPs with EGCG or curcumin is expected to increase their cellular internalization and augment increased cytotoxicity and radiation-induced cell killing in PC-3 prostate cancer cells.

Objective 1.1 (Synthesis & Characterization): Synthesize EGCG-GNPs and Curc-GNPs using a green, single-step method, and thoroughly characterize their physicochemical properties. This includes determining nanoparticle size (core diameter and hydrodynamic diameter), morphology, zeta potential, gold concentration and yield, and colloidal stability (in various media). The new formulations will be benchmarked against conventional GNPs (citrate-reduced and PEG-coated GNPs) to ensure comparable sizes and to assess enhancements due to the phytochemical coatings.

Objective 1.2 (Cellular Uptake & Cytotoxicity): Evaluate the in vitro interactions of EGCG-GNPs and Curc-GNPs with PC-3 prostate cancer cells. This involves quantifying cellular uptake of the nanoparticles (using ICP-MS for gold content) and assessing baseline cytotoxicity using XTT cell viability assays. GNP uptake is a crucial parameter, as many studies have shown a strong correlation between uptake and radiosensitization.

Objective 1.3 (Radiosensitization Efficacy in vitro): Determine the extent of radiation dose enhancement provided by EGCG-GNPs and Curc-GNPs in PC-3 cells under external beam X-ray irradiation. Clonogenic survival assays will be performed at various GNP concentrations to measure the radiation sensitization effect, quantified by metrics such as the Sensitization Enhancement Ratio (SER) and reduction in surviving fraction or radiotherapy dose (D_{50}) needed for a given cell kill. This objective will identify whether EGCG or curcumin coatings confer superior radiosensitizing potency and establish the optimal nanoparticle concentration that maximizes tumor cell killing.

Hypothesis 2: EGCG-GNPs and Curc-GNPs (of ~20–30 nm hydrodynamic size) will be well-tolerated in vivo, showing low signs of toxicity and achieve favorable biodistribution when administered via alternative routes (IP in mice and IA in canines). Specifically, IP delivery in mice will result in predominant accumulation in the reticuloendothelial organs (liver and spleen) with progressive clearance over time, whereas IA delivery in a large-animal model will yield higher local nanoparticle deposition in the prostate with lower systemic exposure, compared to traditional IV delivery. This hypothesis addresses the translational aspect that these phytochemical-coated GNPs can be safely delivered and targeted to the tumor site in vivo.

Objective 2.1 (Murine Biodistribution and Tolerance): Examine the in vivo fate of EGCG-GNPs and Curc-GNPs in a rodent model by administering the nanoparticles intraperitoneally to CD1 mice. At multiple time points post-injection (e.g. 1, 7, 14, 28, and 56 days), quantify gold biodistribution across major organs (liver, spleen, kidneys, lungs, etc.) using ICP-MS, and evaluate clearance kinetics (expecting decreasing hepatic gold levels over time if clearance occurs). Assess toxicity and tolerance by monitoring animal health (behavior, weight gain), calculating organ weight indices, and performing histopathological examination of tissues (with emphasis on liver and spleen) for any nanoparticle-induced lesions or inflammation. This objective will confirm whether the phytochemical-coated GNPs can be administered safely at therapeutic doses and will characterize how they distribute and persist in vivo over an extended period.

Objective 2.2 (Pharmacokinetic Modeling): Develop a physiologically based pharmacokinetic (PBPK) model to describe and predict the biodistribution of EGCG- and Curc-coated GNPs, using the experimental mouse data for model calibration. The model will incorporate major compartments (plasma, liver, spleen, etc.) and physiological parameters to simulate GNP kinetics after IP administration. Once validated in mice, the model will be extrapolated to rats. This computational objective provides a translational tool to anticipate how dosing or route modifications might impact organ distribution, thus guiding the design of future preclinical and clinical studies.

Objective 2.3 (Canine Prostatic Arterial Delivery Study): Evaluate the feasibility, safety, and localizing efficacy of intra-arterial (IA) nanoparticle delivery to the prostate in a large animal model. In a pilot study, EGCG-GNPs are delivered via selective prostatic arterial injection followed by arterial embolization (PAE). This includes a controlled study in healthy male beagle dogs to assess procedure tolerability, any acute toxicities, and imaging visibility of GNP deposition in the prostate when combined with arterial embolization. Additionally a clinical case in a client-owned Boston terrier with naturally occurring prostate cancer will be conducted to test procedure feasibility and explore EGCG-GNP efficacy. Safety monitoring (blood counts, serum chemistry, urine analysis) and imaging or post-mortem analyses of organs will be performed to detect any adverse effects or off-target distribution. This objective aims to demonstrate that IA administration of GNPs can concentrate the nanoparticles in the prostate tumor region, enhance CT-imaging contrast, and treat prostate cancer, providing a potential translational route for therapy.

Thesis Outline: The remainder of this dissertation is organized into six chapters, as outlined below:

Chapter 2 – Synthesis and Characterization of EGCG-GNPs & Curc-GNPs: After this introduction, Chapter 2 details the green synthesis of the EGCG- and curcumin-coated GNPs and their comprehensive physicochemical characterization. Key parameters such as particle size (by TEM and DLS), shape and morphology, zeta potential, antioxidant potential and colloidal stability in biological media are measured. The successful conjugation of the phytochemicals to the GNP surface is confirmed through techniques like UV-Vis spectroscopy, FTIR, and HPLC, including quantification of curcumin loading. Additionally, Chapter 2 compares the new formulations with conventional CIT-GNPs and PEG-GNPs (as benchmarks widely reported in the literature) to highlight improvements in stability or functionality.

Chapter 3 – In Vitro Studies (Radiosensitization in PC-3 Cells): Chapter 3 presents an in-depth investigation of the interactions between the synthesized nanoparticles and prostate cancer cells in vitro. It first examines the baseline cytotoxicity of EGCG-GNPs and Curc-GNPs on PC-3 cells over various concentrations (0–1000 μg/mL) and time points (24–72 h) using XTT viability assays, comparing results with control GNPs (Cit-GNP and PEG-GNP). The chapter then explores the cellular uptake of GNPs, quantified via ICP-MS to determine gold mass internalized per cell, with experiments assessing the influence of serum protein corona on uptake. The radiosensitization efficacy of EGCG-GNPs and Curc-GNPs is subsequently evaluated through clonogenic survival assays: PC-3 cells are irradiated with external-beam megavoltage X-rays in the presence or absence of nanoparticles, and radiation dose–response curves are generated. From these, metrics such

as the Sensitization Enhancement Ratio (SER) are calculated to quantify how much each nanoparticle formulation enhances cell killing compared to radiation alone. Collectively, the in vitro results in Chapter 3 demonstrate the degree of radiosensitization achieved by EGCG-GNP and Curc-GNP, identify the more potent radiosensitizer, and inform the nanoparticle concentrations to be used in subsequent in vivo experiments.

Chapter 4 – In Vivo Studies (Biodistribution and Pharmacokinetics): Chapter 4 investigates the in vivo performance of the phytochemical-coated GNPs, through mouse and canine models. Biodistribution studies in CD-1 mice are described, where animals receive IP injections of EGCG-GNPs or Curc-GNPs and are then sacrificed at designated time intervals (ranging from 1 day up to 56 days). The gold content in major organs are measured by ICP-MS to determine how the GNPs distribute and clear over time. Tissue sections are examined histologically by a veterinary pathologist to detect any toxicological effects or inflammation attributable to nanoparticle deposition. In addition, this chapter introduces a PBPK model that is constructed using the mouse data. The model's parameters are adjusted to fit the experimental biodistribution, and it is then extrapolated to predict nanoparticle kinetics under the larger rat model. Chapter 4 also describes pilot studies conducted in a canine model to evaluate the feasibility of intra-arterial GNP delivery to the prostate, a step toward translating the concept into a clinical scenario. A study involving three healthy male beagle dogs is presented, wherein EGCG-GNPs are intra-arterially injected into the prostatic artery followed by prostatic arterial embolization (PAE). This assesses the technical feasibility of catheter-based nanoparticle delivery, the acute safety/tolerance in a large animal, and the ability to visualize nanoparticle distribution in the prostate via imaging (CT or fluoroscopy) immediately after injection. Second, Chapter 4 presents a case study involving a client-owned Boston terrier with naturally occurring prostate cancer, in which the efficacy of our phytochemical GNPs will be evaluated in a realistic clinical setting.

Chapter 5 – Conclusion and Future Directions: This section synthesizes the thesis's key findings, explains their significance for prostate cancer nanoradiotherapy, highlights the challenges encountered, and proposes actionable steps to advance GNP-based therapy toward clinical application.

Chapter 2

Synthesis and Characterization of EGCG-GNPs & CURC-GNPs

This chapter presents the synthesis and physicochemical characterization of the gold nanoparticles (GNPs) used in this study. Characterization is a critical first step in any nanoparticle-based biomedical application, as physicochemical properties significantly influence biological interactions such as cellular signaling, protein corona formation, membrane association, intracellular uptake, toxicity, clearance, and organ biodistribution. **Method:** Four types of GNPs were evaluated: EGCG-GNPs, Curc-GNPs, Cit-GNPs, and PEG-GNPs. The properties analyzed included hydrodynamic size, zeta potential, shape, polydispersity index (PDI), surface coating, gold concentration, antioxidant potential and X-ray attenuation. Characterization techniques used were ultraviolet-visible (UV-Vis) spectroscopy, dynamic light scattering (DLS), transmission electron microscopy (TEM), inductively coupled plasma mass spectrometry (ICP-MS), Fourier transform infrared spectroscopy (FTIR), high-performance liquid chromatography (HPLC), and computed tomography X-ray imaging (CT). **Results:** All GNP formulations were monodisperse and stable in water. The green synthesis protocol yielded concentrations of 424.67 μg/mL for EGCG-GNPs and 329.57 μg/mL for Curc-GNPs, while the adapted Turkevich method yielded 87.56 μg/mL for Cit-GNPs and 75.39 μg/mL for PEG-GNPs. Hydrodynamic diameters ranged from 17.89 to 55.53 nm, with Cit-GNPs being the smallest and PEG-GNPs the largest. All samples showed sharp single peaks in their size distribution histograms, except PEG-GNPs, which exhibited a minor secondary peak (2.2%) at 3069 nm. All nanoparticles had negative zeta potentials, with EGCG-, Curc-, and Cit-GNPs ranging from -30 to -35 mV, and PEG-GNPs showing a reduced value of -11.2 mV. UV-Vis spectra revealed surface plasmon resonance (SPR) peaks near 525 nm for all samples,

characteristic of spherical GNPs. TEM confirmed spherical morphology, with gold core diameters of 7.78 nm for EGCG-GNPs and 6.21 nm for Curc-GNPs. The difference between hydrodynamic and core diameters corresponded to estimated coating thicknesses of ∼16.88 nm for EGCG and ∼14.62 nm for Curcumin. Both EGCG-GNP and Curc-GNP exhibited superior antioxidant activity compared to Cit-GNP and PEG-GNP. HPLC analysis of Curc-GNPs showed a drug loading of 20.8 wt.%. CT imaging of EGCG-GNPs showed strong contrast enhancement, reaching 119 HU at 1500 μg/mL gold concentration. **Conclusions:** The findings affirm the suitability of EGCG-GNPs and Curc-GNPs for further biomedical applications due to their advantageous synthesis methods, superior physicochemical stability, potent antioxidant properties, and imaging enhancement capabilities. Future investigations should leverage these optimized nanoparticle formulations in targeted drug delivery and therapeutic efficacy studies.

2.1 Introduction

The most common synthesis method for gold nanoparticles is the Turkevich method, first described by Turkevich in his publication in 1951 [33]. The fact that it is still the most common procedure for the synthesis of GNPs is a testament to how easily the method produces stable, spherical, and monodisperse GNPs with excellent reproducibility. The simplest description of the synthesis involves rapidly adding sodium citrate ($Na_3C_6H_5O_7$) to a boiling solution of auric acid ($HAuCl_4$). For precise control over GNP dimensions, synthesis conditions such as reactant concentrations ($HAuCl_4$ + $Na_3C_6H_5O_7$ + H_2O), pressure, and temperature must be carefully regulated. The main disadvantage of the Turkevich method is that it is energy intensive and produces low GNP concentrations. Many Turkevic variations have been proposed to address this, for example the addition of sodium borohydride results in reducing heat energy required to synthesize citrate capped gold nanoparticles (Cit-GNPs). The other challenges with Cit-GNPs are that they are very susceptible to aggregation in salt solutions and the citrate coating provides weak steric stability. This is especially important, as weak stability against physiological buffering salts weakens the use of Cit-GNPs for biomedical applications, since blood is an ionic medium that will promote aggregation and desorption of the citrate coating [129].

Polyethylene glycol (PEG) is a polymer composed of ethylene glycol that is widely used in nanomedicine to improve the pharmokinetics of nanoparticles. PEG has the unique properties of hydrophilicity and electric neutrality. These two properties allow PEG coated nanoparticles to reduce protein adherence and evade recognition from macrophages and the immune system. Proteins such as opsonins act as signalling molecules for immune cells to

recognize, engulf and clear foreign particles from circulation. As a result, PEG has become one of the most commonly used polymers in nano-drug delivery research [130].

There are 3 main synthesis strategies for PEG coating on the GNPs surface which are as follows:

a) PEG physically adheres to the surface of the GNPs through physical absorption which can include electrostatic or hydrophobic interaction.

b) PEG is chemically bonded to the surface of the GNPs

c) Self assembly through a block-copolymer

The method used in our study is the chemical reduction method as it is simple and results in strong covalent bonds between the GNP surface and a thiol-terminated PEG molecule. PEG-thiol is a polymer chain of PEG with the end unit containing a thiol SH group. The thiol group has a strong affinity for the Au surface of the nanoparticle due to the attraction between the lone pair of electrons on the sulfur atom and the partially filled d orbital of the gold atom. The resulting Au-S bond is relatively strong and stable. The PEG chain surrounds the GNPs like a "brush" and provides steric stability. There are many sizes of PEG chains that can be coated [131]. Depending on the density of the PEG coating, the nanoparticle can still have targeting ligands for a balance of stability and targeting functionality. By balancing the ratio of PEG to targeting ligand, it is possible to optimize both the nanoparticle's resistance to nonspecific protein adsorption and its ability to selectively bind to target cells or tissues. For example, Hak *et al.* synthesized PEG-coated nanoemulsions with RGD peptides for tumor targeting. They found that the optimal PEG surface density for 100 nm peptide ligand nanoemulsions was 10:90 PEG: RGD mol% or lower. In fact, they reported that increasing the PEG content above 20 mol% removed any targeting benefit in vivo [132].

In this study, we utilize PEG6000-thiol to synthesize PEG-GNPs with no targeting moieties—only full PEG coverage. The number 6000 denotes the average molecular weight of the polymer. It is reported that larger PEG molecules confer greater steric repulsion on the GNP surface, thereby enhancing stability. The synthesis protocol used here is adapted from Manson *et al.* and builds on the Turkevich method for forming Cit-GNPs [132]. PEG6000-thiol is added to Cit-GNPs, and over time, a ligand exchange occurs in which PEG displaces citrate ions. PEG-thiol replaces citrate due to the stronger Au–S bond (40–50 kcal/mol) compared to the Au–citrate interaction (5–10 kcal/mol). According to the authors, a PEG concentration of 16.8 μg/mL achieves $\sim$14 wt% PEG loading, corresponding to 1,140 thiol-terminated PEG molecules per 17.9 nm Cit-GNPs. Among the concentrations

tested (3.6, 8.4, 16.8, and 25.2 μg/mL), 16.8 μg/mL yielded the highest PEG seeding density of 1.13 chains per nm^2 of GNP surface [132]. For this reason, 16.8 μg/mL PEG6000-thiol was selected for our experiments. If we were incorporating a targeting component, we would reduce the PEG coverage to allow sufficient space for the targeting ligands to attach and remain accessible.

The synthesis of EGCG-GNPs and Curcumin-GNPs were carried out through a single-step, one pot, green synthesis method. One pot meaning the entire synthesis occurs in one vessel and "green synthesis" meaning it is an eco-friendly method that requires relatively low energy and uses naturally derived molecules as reducing and stabilizing agents. Unlike traditional synthesis methods that may involve toxic chemicals or high energy consumption, green synthesis aims to make the process safer, more sustainable, and less harmful to both the environment and living organisms. Another advantage of our green synthesis method is that it can be easily upsized into large scale production, and it is relatively cheap. The solvent system used in green synthesis and in our study synthesis is ultrapure water with no chemical solvents used. Lastly, our green synthesis protocol can produce high concentrations of GNPs while still maintaining monodispersity. Having control of GNP size and the range of sizes is crucial for our in vivo and in vitro experiments. The green synthesis using curcumin and EGCG are very similar although they are from different classes of phytochemicals. Chemically, curcumin is a diarylheptanoid composed of two aromatic rings, each bearing methoxy and hydroxy groups, connected by a seven-carbon chain featuring two α,β-unsaturated carbonyl groups. EGCG is a polyphenolic flavonoid with a flavan-3-ol core, consisting of two aromatic rings and a third gallate group attached via an ester bond, resulting in a molecule with many hydroxyl groups Figure 2.1. The hydroxyl groups play a major role in EGCG's antioxidant potential by donating hydrogen atoms or electrons, while the aromatic rings act as scaffolds that stabilize the resulting negative charge through resonance.

The synthesis protocol for both EGCG-GNPs and Curcumin-GNPs begins by deprotonating their multiple phenolic and enolic groups using a dilute concentration of NaOH added to an aqueous solution containing either EGCG or curcumin. Both EGCG and curcumin have numerous phenolic hydroxyl (OH) groups, and the ionization of these groups is pH dependent. Deprotonation of the hydroxyl groups enhances the nucleophilic character of the oxygen atoms, making them more reactive toward Au^{3+} ions in $HAuCl_4$ and facilitating both reduction and binding to the gold surface.

In the following sections of this chapter, we provide a breakdown of the synthesis and characterization of each GNP structure. We begin with describing the step-by-step synthesis method of each GNP structure, followed by characterization using UV-Vis spectroscopy, transmission electron microscopy (TEM), Zetasizer analysis, ICP-MS, and CT imaging. In

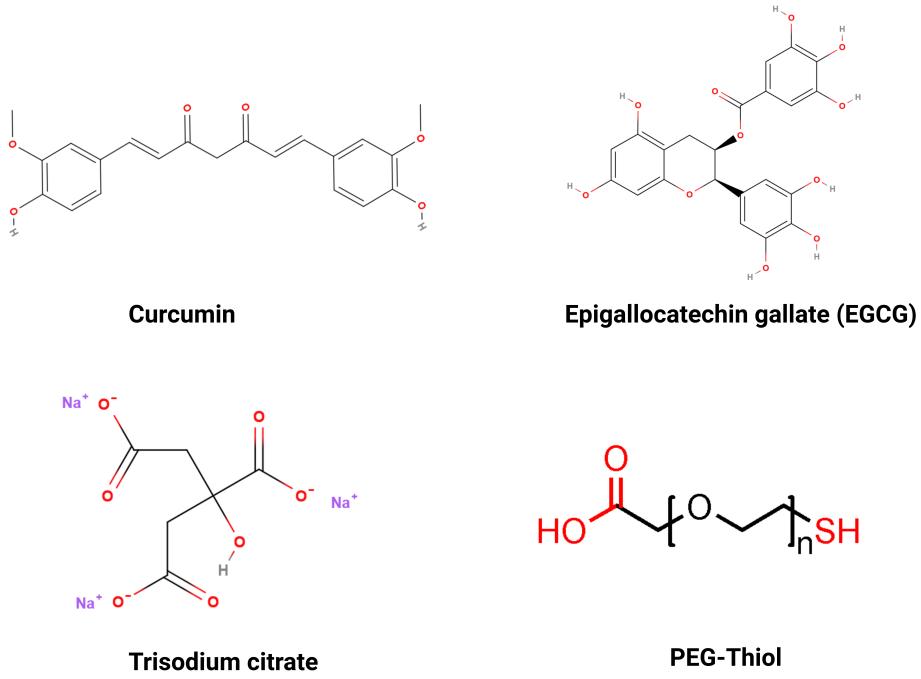


Figure 2.1: Chemical structures of curcumin (top left), EGCG (top right), trisodium citrate (bottom left), and PEG-thiol (bottom right). Reactive centers are highlighted in red. These include phenolic hydroxyls, enolic or carbonyl groups, and terminal thiol group. These functional groups mediate strong interactions with the Au nanoparticle surface through coordination, reduction, and adsorption.

the UV-Vis spectroscopy section, we identify the surface plasmon resonance (SPR) peak for each nanostructure and determine the minimum detectable concentration of EGCG-GNPs. The Zetasizer section will present data on the average diameter, polydispersity, mean peak intensity, and zeta potential of each GNP structure. Next, we present TEM images of Curc-GNP and EGCG-GNP, along with corresponding graphs of Au-core diameter distributions. The ICP-MS section details the yield concentration of each synthesis protocol, while the CT imaging section presents X-ray images of EGCG-GNPs submerged in conical vials and reports the mean X-ray contrast (HU) for these particles. Lastly, we provide surface characterization of Curc-GNPs using FTIR spectroscopy to confirm the presence of curcumin on the nanoparticle surface and identify the reactive moieties bound to gold. HPLC analysis is then used to quantify drug loading and calculate synthesis yield based on the initial reagent input. This information is crucial for guiding and optimizing our in vivo

approach, ensuring reliable and interpretable results.

2.2 Materials

Curcumin (≥98% purity, Alexis Biochemicals, San Diego, CA, USA), sodium citrate dihydrate (S25545-Fisher Scientific, Waltham, MA, USA), and gold(III) chloride trihydrate ($HAuCl_4 \cdot 3H_2O$, 520918-Aldrich, St. Louis, MO, USA), Epigallocatechin gallate (≤95% purity, E4143–Aldrich, St. Louis, MO, USA) and PEG-thiol (Mn 6,000), 729159-Aldrich, St. Louis, MO, USA) were used as supplied for the synthesis of GNPs. 2,2-Diphenyl-1-picrylhydrazyl (DPPH, ≥97%, Sigma-Aldrich, Cat. No. D9132) was used for antioxidant experiment. Formvar/Carbon coated nickel grids, 200 mesh, 3.05 mm diameter (Polysciences, Inc., Cat. No. 24916) was used for TEM imaging. All synthesis protocols utilized ultrapure Milli-Q water derived from the Millipore Gradient A10 water purification system (Merck Millipore, MA, USA). Milli-Q water will be referred to as ultrapure water.

2.2.1 Synthesis of EGCG Capped GNPs

The synthesis of EGCG-GNPs was adapted from the Curc-GNP protocol described by Nambiar *et al.* [63] A stock solution of 100 mM $HAuCl_4 \cdot 3H_2O$ was prepared in ultrapure water. Next, 10 mL of a 1 mM EGCG solution was prepared, and 1 mL of 5 mM NaOH was added to adjust the pH and promote deprotonation of the phenolic groups. The EGCG solution was placed in a water bath sonicator at 44 °C, and 200 μL of 100 mM $HAuCl_4 \cdot 3H_2O$ was added dropwise. The formation of EGCG-GNPs was confirmed by a distinct color change from clear to ruby red. To remove any unreacted components, the solution was transferred to 3.5 kDa dialysis tubing and dialyzed against 2 L of water for 48 hours, with frequent water changes.

2.2.2 Synthesis of Curcumin Capped GNPs

A stock solution of 100 mM $HAuCl_4 \cdot 3H_2O$ was prepared in ultra-pure water. Next, 10 mL of a 1.0 mM curcumin solution was prepared, and 1 mL of 5 mM NaOH was added to adjust the pH and promote deprotonation of the phenolic and enolic groups. The curcumin solution was placed in a water bath sonicator at 44 °C, and 200 μL of 100 mM $HAuCl_4 \cdot 3H_2O$ was added dropwise. The formation of Curc-GNPs was indicated by a distinct color change from clear to ruby red. To remove any unreacted components, the solution was transferred

to 3.5 kDa dialysis tubing and dialyzed against 2 L of water for 48 hours, with frequent water changes [133].

2.2.3 Synthesis of Citrate Capped GNPs

A stock solution of 1 mM $HAuCl_4 \cdot 3H_2O$ was prepared in ultra-pure water. Then, 300 mL of this 1 mM $HAuCl_4 \cdot 3H_2O$ solution was transferred to a round-bottom flask, heated to a rolling boil, and maintained under reflux with vigorous stirring. Separately, a 40 mM sodium citrate solution was prepared in ultra-pure water. Once the gold solution was boiling, 6 mL of the 40 mM sodium citrate solution was quickly added. Heating and stirring were continued under reflux for 15 minutes to ensure complete reaction. During this time, the solution gradually changed color from yellow to brown to ruby red, indicating the formation of gold nanoparticles. The ruby-red solution was then allowed to cool to room temperature with continuous stirring, yielding Cit-GNPs [134].

2.2.4 Synthesis of PEG Capped GNPs

A stock solution of 1 mM $HAuCl_4 \cdot 3H_2O$ was prepared in ultra-pure water. Then, 300 mL of this solution was transferred to a round-bottom flask, heated to a rolling boil, and maintained under reflux with vigorous stirring. Separately, a 40 mM trisodium citrate solution was prepared in ultra-pure water. Once the gold solution reached boiling, 6 mL of the 40 mM trisodium citrate solution was quickly added. Heating and stirring were continued under reflux for 15 minutes to ensure complete reaction. During this time, the solution gradually changed color from yellow to brown to ruby red, indicating the formation Cit-GNPs. The ruby-red solution was then allowed to cool to room temperature with continuous stirring.

To produce PEG-GNPs, 16.8 μg/mL of 6,000 Mw PEG-thiol was added to the as-synthesized Cit-GNP solution at room temperature. After the required amount of PEG was added, the solution was stirred at room temperature for 2 hours to allow for complete exchange of citrate with PEG. The PEG-GNP solutions were then centrifuged at 10,000 rpm for 30 minutes in 10 mL batches. A PEG-GNP pellet formed at the bottom, and 9.9 mL of the supernatant was removed. Finally, 9.9 mL of ultrapure water was re-added to the PEG-GNP pellet and the particles were redispersed using a sonicator and vortex [135].

2.3 Characterization

2.3.1 UV-Vis Spectroscopy

Formation of GNPs was confirmed using UV-Vis absorption measurements. A single strong absorbance band between 500–550 nm indicates successful GNP formation. UV-Vis spectra were recorded with a Molecular Devices SpectraMax M5 Plate Reader over the 300–800 nm range at 0.5 nm intervals, using 1 mL of GNP sample in a 1.5 mL PMMA cuvette. Three UV-Vis studies were conducted: (i) identification of the SPR peak for EGCG-GNP, Curc-GNP, Cit-GNP, and PEG-GNP; (ii) comparison of colloidal stability between Curc-GNP and Cit-GNP in RPMI and RPMI supplemented with 10% FBS; and (iii) determination of the lowest EGCG-GNP concentration detectable by SPR peak on the SpectraMax M5 Plate Reader.

2.3.2 Dynamic Light Scattering (DLS)

The hydrodynamic diameter, size distribution (polydispersity index, PDI), and zeta potential of the dialyzed or centrifuged GNP samples were measured using a Malvern Zetasizer Ultra ZS (Malvern Instruments Ltd., Malvern, UK). DLS provides information on the hydrodynamic size and size distribution of nanoparticles, as indicated by the PDI. For size measurements, 1 mL of each sample was transferred to a disposable PMMA cuvette. Measurements were performed in triplicate, and the average diameter (nm), PDI, and intensity-weighted mean peak were recorded. For zeta potential measurements, 0.75 mL of each sample was transferred to a DTS1070 disposable zeta potential cell. Each sample was analyzed three times at 25°C, and the average zeta potential (in mV) was recorded.

2.3.3 Transmission Electron Microscope (TEM)

Core size distribution and shape of the EGCG-GNPs and Curc-GNPs was obtained from TEM analysis. Dialyzed Curc-GNPs and EGCG-GNPs samples were drop casted on a 200-mesh Formvar/Carbon-coated copper grid and TEM images were acquired at 60 kV with a Philips CM10 electron microscope. TEM size measurements display only the size of the Au core, and exclude the outer coating of EGCG or curcumin. Image processing was carried out on computer using the software ImageJ.

2.3.4 ICP-MS

The concentration of GNPs was measured after completion of dialysis or centrifugation using an inductively coupled plasma optical emission spectrometer (ICP-OES, Teledyne Leeman Labs, USA). Each sample was divided into three vials to obtain triplicate measurements, and each vial was analyzed three times per ICP run. To dissolve the GNPs and convert the gold back to its ionic form ($HAuCl_4$), 1 mL of freshly prepared aqua regia (3:1 ratio of HCl to HNO_3) was added to each vial. A calibration curve for quantifying Au content was generated using a blank and five gold standards ranging from 1 to 800 μg/mL. All calibration curves had correlation coefficients > 0.995. The calibration was verified using a standard prepared from a different source of gold and was considered acceptable if results were within $\pm 10\%$ of the expected value. The method detection limit (MDL) for Au was 1 ppm, and the limit of quantitation (LOQ) was 10 ppm. Instrument analysis was performed on ^{197}Au, with ^{195}Pt and ^{205}Pt used as internal standards to correct for variations in plasma conditions.

2.3.5 CT-Imaging

Computed tomography (CT) was used to quantify the imaging contrast of EGCG-GNPs and Curc-GNPs. Scans were acquired using a Siemens SOMATOM Definition AS 64-slice scanner with settings optimized for phantom imaging: a collimation of 64 $\times$ 0.6 mm, reconstructed slice thickness of 0.625 mm, helical mode scanning with a rotation time of 0.8 s, pitch of 1.0, tube voltage of 120 kV, and an effective tube current–time product of 200 mAs. Attenuation values of GNP suspensions were determined by measuring Hounsfield Units (HU) in conical tubes containing at least 2 mL of sample submerged in water. Five gold concentrations, ranging from 0 to 1500 μg/mL, were evaluated for X-ray contrast. Each tube was held upright in a Styrofoam holder to maintain consistent positioning during scanning. Additionally, 1500 μg/mL of EGCG-GNPs was placed into an empty insert slot of the Electron Density CT Phantom to evaluate its X-ray attenuation properties in comparison to standardized tissue-equivalent materials (Figure 2.2).

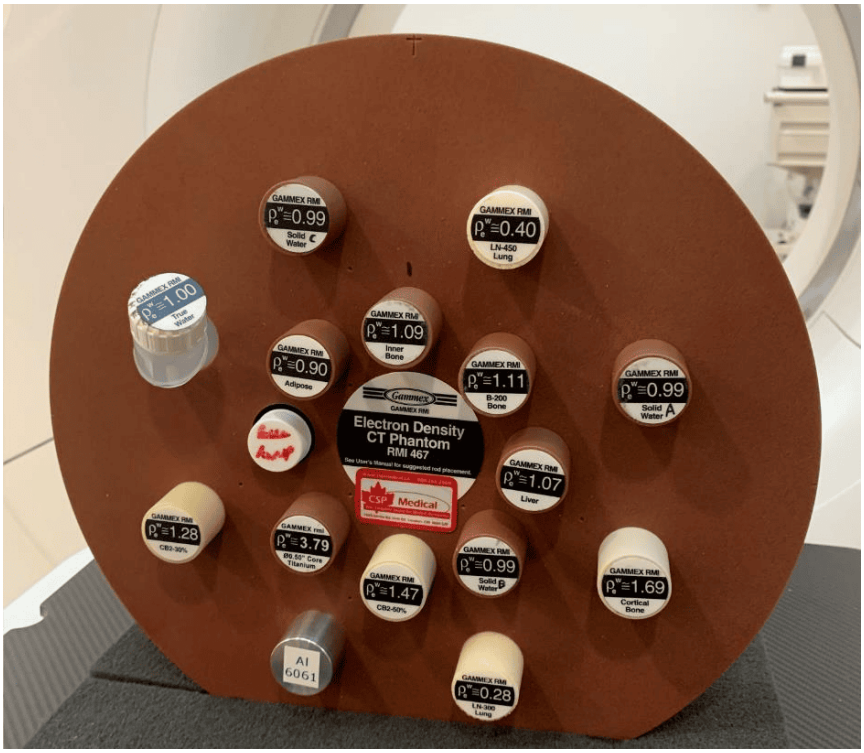


Figure 2.2: 1500 μg/ml of EGCG-GNPs imaged in an electron density phantom

2.3.6 Antioxidant Potential: DPPH Assay

The antioxidant potential of Curc-GNP, EGCG-GNP, PEG-GNP, and Cit-GNP was measured based on the (DPPH) 2,2-diphenyl-1-picrylhydrazyl radical scavenging assay adapted from Gulcin et al [136], whereby the antioxidant activity of a compound correlates with the spectrometric shift caused by DPPH reduction. Briefly, a 0.1 mM DPPH stock solution was prepared by dissolving 3.94 mg of DPPH powder in 100 mL ethanol. Four different concentrations (25, 50, 100, and 200 μg/mL) were tested for DPPH activity. 2 mL of each GNP solution was mixed with 2 mL of the DPPH stock solution, vortexed, and incubated in the dark for 30 minutes. Afterward, the samples were centrifuged at 3,000 g for 10 minutes, and the supernatant was used for analysis. Absorbance was recorded at 517 nm on a Molecular Devices SpectraMax M5 plate reader. The absorbance readings were converted to antioxidant activity based on Equation (2.1):

$$DPPH\ Inhibition(\%) = \left[\frac{Abs_{control} - (Abs_{sample} - Abs_{blank})}{Abs_{control}}\right] \times 100\% \qquad (2.1)$$

where $Abs_{control}$, Abs_{sample}, and Abs_{blank} are the absorption readings of the DPPH control, the DPPH-treated samples, and the blank samples, respectively.

2.3.7 Fourier transform infrared spectroscopy (FTIR)

FTIR spectroscopy was conducted to compare the characteristic absorption peaks of powdered curcumin (≥98% purity) with those of the freeze-dried Curc-GNPs. Analyses were performed on a Thermo Nexus 670 FTIR spectrometer equipped with a Continuum microscope, with spectra recorded in the solid state over the wavenumber range of 700–2500 cm^{-1}. Transmission peaks were examined to confirm the presence of curcumin on the gold nanoparticle surface and identify any shifts in functional group absorption relative to free curcumin.

2.3.8 High Performance Liquid Chromatography (HPLC)

Curcumin loading onto gold nanoparticles was quantified using a Waters Alliance HPLC system. Chromatographic separation was achieved on a C18 column using an isocratic mobile phase composed of aqueous 0.1% formic acid and 0.1% formic acid in acetonitrile (50:50, v/v) at a flow rate of 1.5 mL/min. Detection was carried out at 425 nm. A calibration curve was established using 6 curcumin standards (≥98% purity) at concentrations of 0.1 - 54.25 μg/mL. To determine curcumin loading, curcumin was desorbed from the GNP surface by treating the Curc-GNP suspension with acidified ethanol (0.1 mL formic acid per 100 mL ethanol). The mixture was sonicated, vortexed thoroughly, and centrifuged at 10,000 × g for 10 minutes. The resulting supernatant was filtered through a 0.2 μm GHP syringe filter and analyzed via HPLC to determine the desorbed curcumin concentration. The GNP pellet was resuspended in acidified ethanol and the process was repeated again. Curcumin loading was calculated using the equation:

$$\omega_{Curc} = \frac{m_{Curc}}{m_{Au}} \tag{2.2}$$

where ω_{Curc} is the Curcumin loading in mg Curc/mg Au, m_{Curc} is the desorbed Curcumin content detected in the supernatant and m_{Au} is the mass of gold in the Curc-GNP suspension. Gold content was quantified by resuspending the nanoparticle pellet in ultrapure water and measuring the gold concentration using ICP-MS (Agilent Technologies).

2.4 Results & Discussion

2.4.1 UV-Vis Spectroscopic Analysis

UV-Visible spectroscopy is a widely used technique for characterizing the optical properties of GNPs, as their absorption bands are directly influenced by particle size, shape, and aggregation state (Figure 2.3). GNPs exhibit distinctive optical behavior in the UV-Vis region due to surface plasmon resonance (SPR). Many biosensing applications utilizing GNPs are based on this property, where the binding of target molecules induces a shift in the SPR signal. For example, Walter *et al.* developed an SPR biosensor to detect C-reactive protein binding onto aptamer-functionalized GNPs, with sensitivity down to 12.46 nM [137]. In our study, we used UV-Vis analysis as a post-synthesis test to observe the SPR peak at ∼525 nm, indicative of spherical GNPs, and to assess peak width for insights on monodispersity or aggregation.

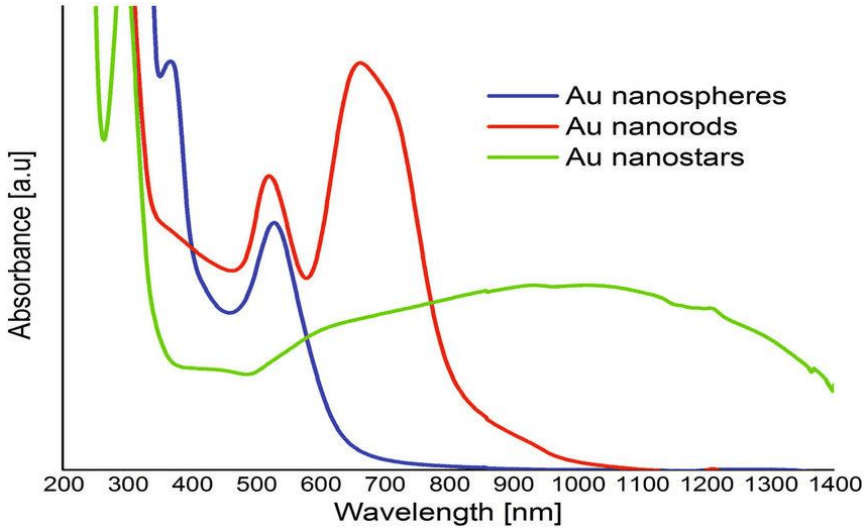


Figure 2.3: Comparing the UV-Vis spectra of different shaped GNPs [138].

The SPR peak for Cit-GNPs, EGCG-GNPs, Curc-GNPs, and PEG-GNPs was recorded at approximately ∼517 nm, ∼520 nm, ∼525 nm, and ∼540 nm, respectively, as shown in Figure 2.4. The optical properties of GNPs are highly dependent on their size and shape. Smaller, spherical gold nanoparticles tend to absorb light and exhibit peaks near 525 nm, while larger or irregularly shaped nanoparticles scatter light, resulting in broader

peaks and red shifts toward longer wavelengths. Figure 2.3 shows the UV-Vis spectra of gold nanospheres, nanorods, and nanostars. All GNPs in our study displayed the UV-Vis signature characteristic of gold nanospheres. PEG-GNPs exhibited the highest SPR peak at 540 nm with a broad absorbance range spanning approximately 500 to 600 nm. The slight differences in SPR peaks among the samples may reflect variations in nanoparticle size and monodispersity. It is important to note that differences in absorbance intensity at the SPR peak primarily reflect the concentration (number of particles) in the nanoparticle suspension, assuming particle size and aggregation state are similar. Therefore, as shown in Figure 2.4, Cit-GNP exhibited the lowest absorbance peak because it was the most dilute sample. GNP shape is important in drug delivery design, as it significantly influences membrane-mediated uptake, intracellular localization, and toxicity [104]. In a study by Carnovale *et al.*, gold nanospheres demonstrated the highest uptake in prostate cancer cells (PC-3) compared to nanostars, nanocages, and nanorods of similar size and concentration [104]. Gold nanospheres also showed the lowest cytotoxicity among the shapes, but only when intracellular gold concentration was used as the baseline for comparison. This is relevant to our study, as our objective is to maximize uptake and cytotoxicity in prostate cancer cells while minimizing toxicity to non-targeted cells [104].

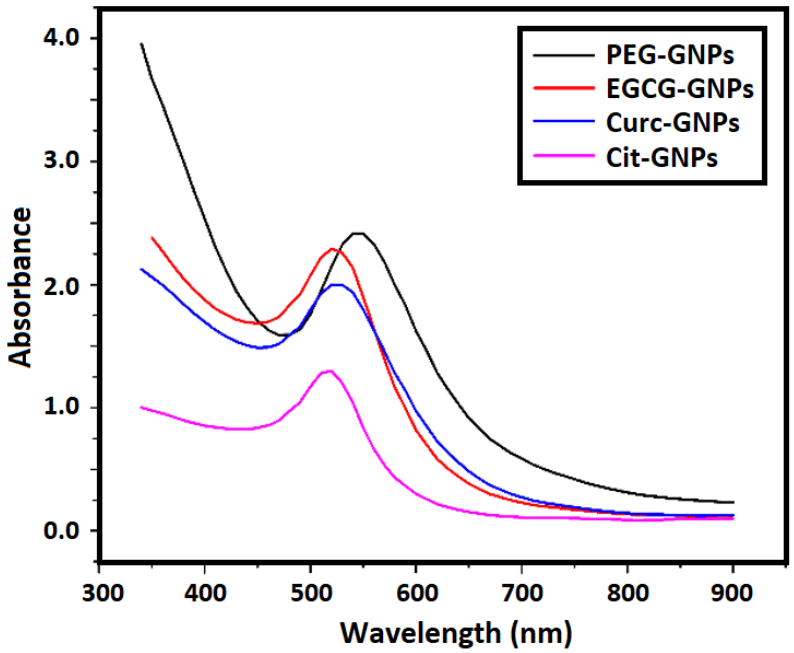


Figure 2.4: UV-Vis Spectra of Cit-, EGCG-, Curcumin- and PEG- GNPs.

These previous UV-Vis spectra were carried out in ultrapure water under ideal conditions; however, they do not reflect the complex environments in vivo, where GNPs may encounter high ionic strength, serum proteins, and biomolecular coronas that can alter their aggregation state, surface properties, and optical behavior. When Curc-GNPs and Cit-GNPs were placed in RPMI medium and RPMI supplemented with 10% FBS, their UV-Vis spectra showed drastic differences. Both GNP structures appear to aggregate in RPMI; however, the Cit-GNP peak broadens significantly with a pronounced red shift. Curc-GNPs still retain a visible SPR peak, though shifted to 560 nm. In serum-supplemented RPMI, Curc-GNPs show much greater stability than Cit-GNPs, as their spectra remain nearly unchanged after 48 hours. In contrast, the Cit-GNP peak broadens over time and shifts to 550 nm, while Curc-GNPs remain stable. This may be due to the stronger binding affinity of curcumin to gold via its β-diketone moiety, which acts as a strong chelator. Additionally, curcumin is lipophilic and has high affinity for albumin which is the most abundant serum protein. This likely contributes to a corona formation and protects the nanoparticle from the ionic medium.

The final component of the UV-Vis study was to determine the lowest concentration of EGCG-GNPs that could produce a detectable SPR peak using the SpectraMax M5 Plate Reader. This test was conducted in collaboration with the RiverLabs Institute, which was developing a graphene water filter and needed a simple method to identify GNPs in aqueous solutions. The Au concentrations tested were 0.1, 0.25, 0.5, 1, 2, 3, 4, and 5 μg/mL. It was found that the lowest concentration of EGCG-GNPs that produced a noticeable SPR peak was 0.25 μg/mL; however, the signal exhibited high noise (Figure 2.6B). A concentration of 1 μg/mL showed a broader, more distinct peak and was selected as the reference (Figure 2.6A). Four water samples potentially containing GNPs were sent by the institute at various stages of filtration (pre- and post-filtration) for Au detection. None of the unknown samples showed an SPR peak based on their UV-Vis spectra (Figure 2.6C). All spectra closely resembled that of tap water, indicating that the GNP concentration was likely below 1 μg/mL or that GNPs were absent altogether.

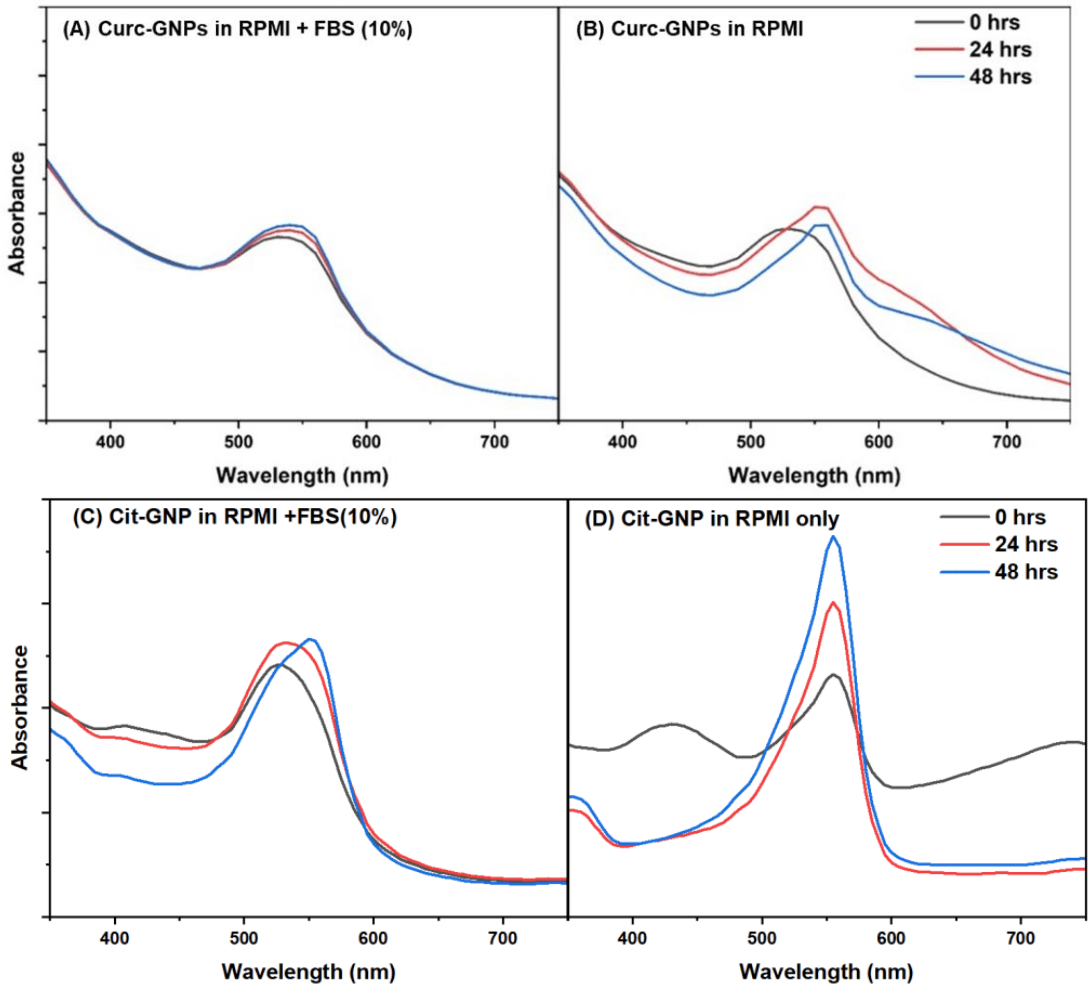


Figure 2.5: UV-Vis spectra of Curc-GNP and Cit-GNP in RPMI or serum supplemented RPMI. Both GNP spr peaks shifted to ∼550 nm in RPMI however the Cit-GNP is much broader.

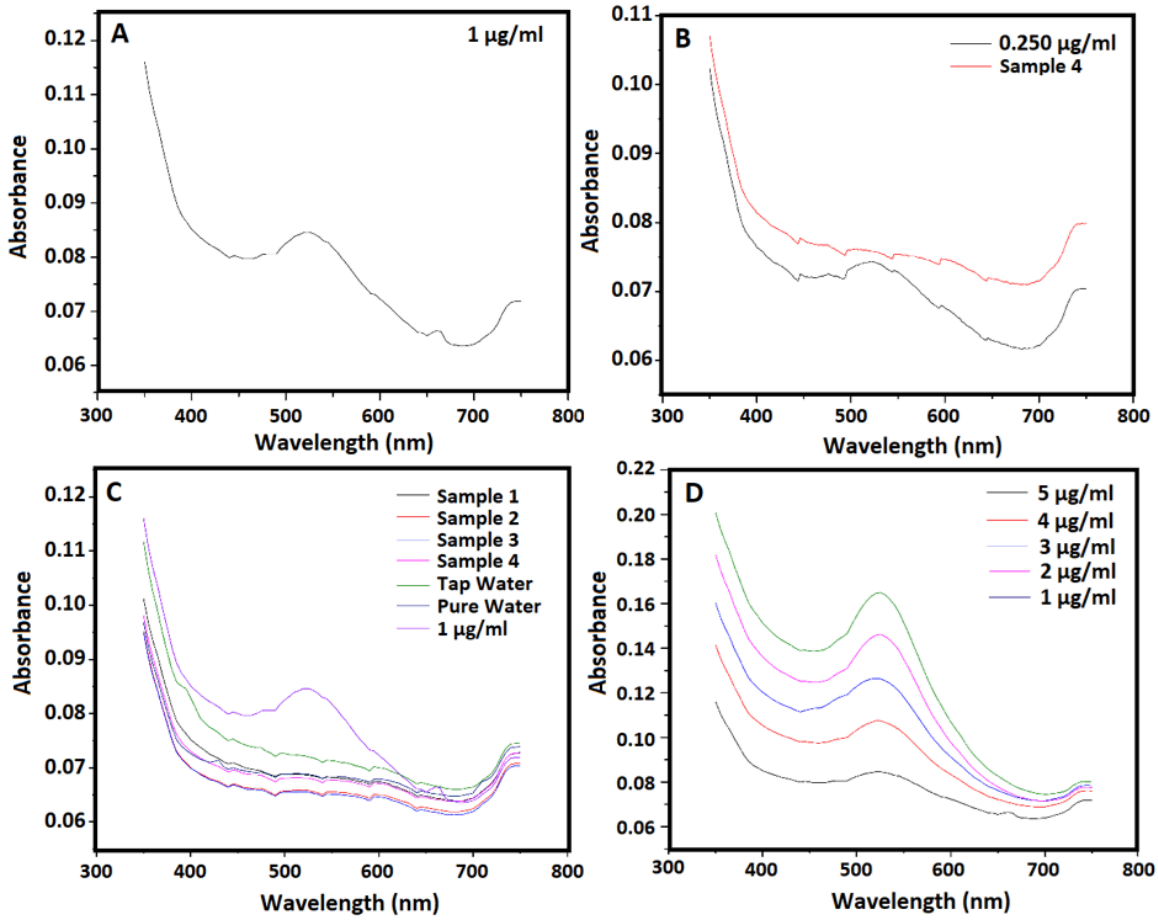


Figure 2.6: UV-Vis absorbance spectra of EGCG-GNPs at varying concentrations. *(A)* A clear SPR peak is visible at 1 μg/mL. *(B)* The 0.25 μg/mL sample shows a weak, noisy SPR signal, similar to Sample 4. *(C)* Samples 1–4, received from RiverLabs at various filtration stages, show no detectable SPR peak and resemble tap and pure water spectra. *(D)* Increasing EGCG-GNP concentrations from 1 to 5 μg/mL show a dose-dependent rise in SPR peak intensity, centered near 525 nm.

2.4.2 Dynamic Light Scattering (DLS) Analysis

Dynamic light scattering (DLS) is a routine analytical tool for measuring the hydrodynamic size of nanoparticles and colloids in liquid environments. GNPs are strong light scatterers at or near their surface plasmon resonance wavelength [139]. DLS measurements are summarized in Table 2.1. The hydrodynamic diameters of EGCG-GNPs, Curc-GNPs, PEG-GNPs, and Cit-GNPs are 24.66 ± 0.23 nm, 20.83 ± 0.01 nm, 55.53 ± 0.20 nm, and 17.89 ± 0.07 nm, respectively. The diameter and peak intensities for each sample are shown in Figure 2.7. PEG-GNPs, which are coated with 6,000 Mw PEG, exhibited the largest measured hydrodynamic size.

However, this data is slightly skewed as the DLS results for PEG-GNPs indicate some aggregation, with a secondary particle population around 3069 nm. All GNP structures exhibited negative zeta potentials ranging from –11.2 mV to –34.4 mV, with PEG-GNPs having the lowest recorded value. This lower zeta potential is expected due to the nature of the PEG polymer and the high molecular weight (6000 Da) PEG-thiol used for coating. In contrast, the molecular weights of EGCG, curcumin, and citrate are 458.37 g/mol, 368.38 g/mol, and 258.06 g/mol, respectively. The observed aggregation in PEG-GNPs may be attributed to the more rigorous purification process involving repeated centrifugation, unlike the other GNPs, which were purified via passive diffusion using dialysis tubing.

One of the most important parameters provided by DLS is the polydispersity index (PDI), which estimates the size uniformity of nanoparticles in solution. The PDI values for EGCG-GNP, Curc-GNP, PEG-GNP, and Cit-GNP were 0.194, 0.134, 0.236, and 0.097, respectively. For pharmaceutical nanoparticles, a PDI of 0.3 or less is generally considered acceptable. In our study, all GNPs were well below this threshold, with PEG-GNPs showing the highest PDI at 0.236. This parameter is critical for our project, as even small variations in NP size can cause significant changes in biological interactions. A narrow size distribution ensures consistency in experimental outcomes, particularly in in vitro and in vivo studies. Hirn *et al.* demonstrated that minor size differences can dramatically alter biodistribution: 1.4 nm GNPs exhibited a serum-to-blood cell concentration ratio of 75:25, whereas 5 nm GNPs showed a 50:50 ratio [80]. This 3.6 nm size difference significantly impacted nanoparticle clearance, immune uptake, renal filtration, and vascular permeability. These findings underscore the importance of achieving low PDI values for reliable and reproducible nano-drug delivery systems, as heterogeneous populations may result in distinct biological behaviors between smaller and larger nanoparticle fractions.

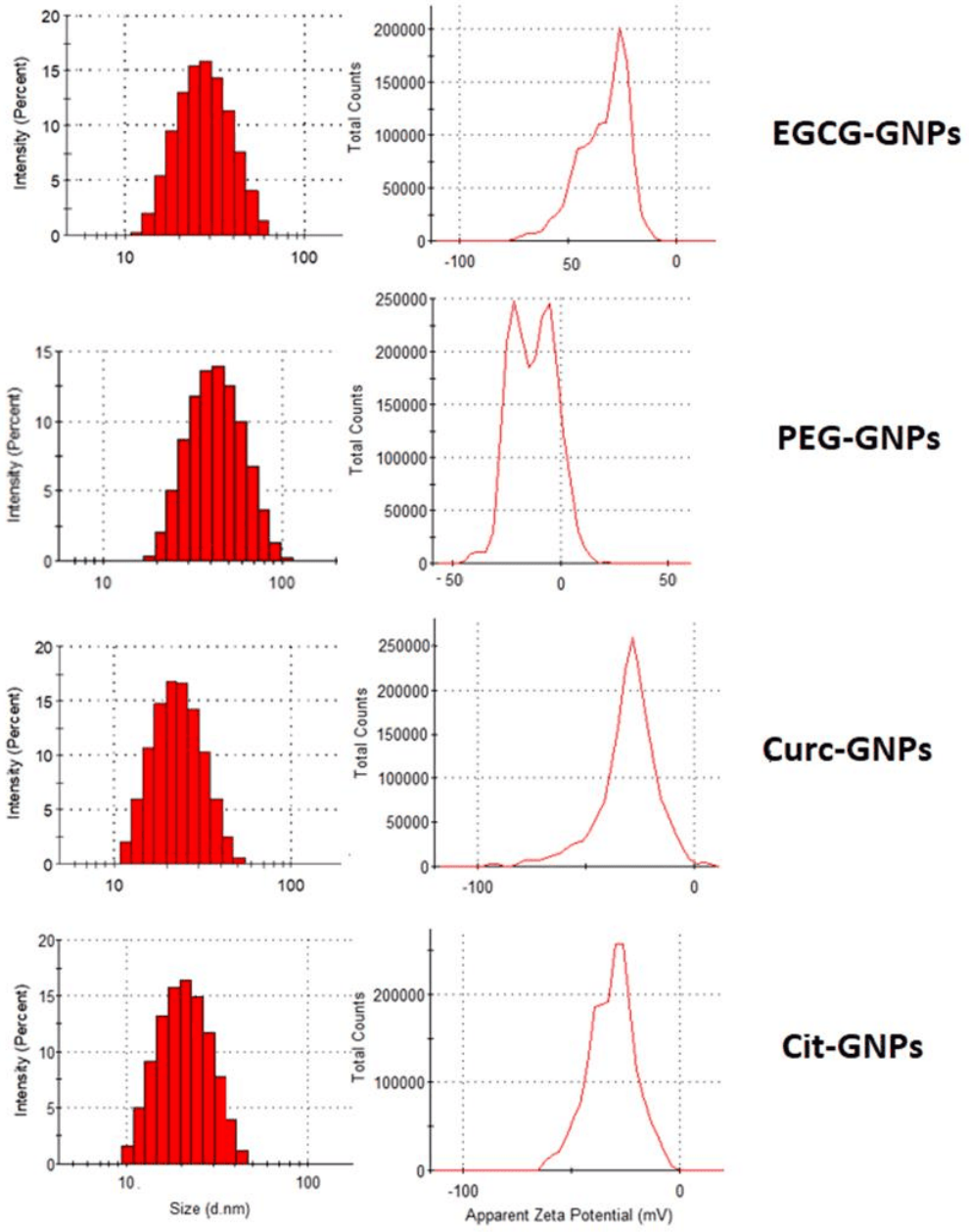


Figure 2.7: DLS Sizes and Apparent Zeta Potentials of EGCG-, PEG-, Curc- and Cit-GNPs

Table 2.1: DLS Parameters Calculated for Cit-, EGCG-, Curc- and PEG- GNPs

GNPs	diameter (nm)	PDI	Peak 1 mean Intensity	Peak 2 mean Intensity	Peak 3 mean Intensity	Peak 1 Area Intensity	Peak 2 Area Intensity	Zeta potential (mV)
EGCG-GNPs	24.66 ± 0.23	0.194	29.96	0	0	100	0	-30.8 mV ± 1.82
Curc-GNPs	20.83 ± 0.096	0.134	23.74	0	0	100	0	-30.8 mV ± 0.551
PEG-GNPs	55.53 ± 0.203	0.236	69.05	3069	0	97.8%	2.2%	-11.2 mV ± 0.404
Cit-GNPs	17.89 ± 0.07	0.097	19.82	0	0	100	0	-34.4 mV ± 0.651

2.4.3 Transmission Electron Microscope (TEM)

TEM images of Curc-GNPs and EGCG-GNPs are shown in Figure 2.9, and both structures exhibited similar shapes and sizes. The nanoparticles were predominantly spherical, with occasional rod- or triangular-shaped particles also observed (Figure 2.8). Maximum magnification was 130,000× for EGCG-GNPs and 92,000× for Curc-GNPs (Figure 2.10); the lower magnification for Curc-GNPs was due to lighting issues and insufficient contrast at higher settings. The average gold core sizes were 7.78 ± 2.59 nm for EGCG-GNPs and 6.21 ± 3.36 nm for Curc-GNPs. The difference between the hydrodynamic diameter and core size was used to estimate the thickness of the green coating and associated solvent layer, calculated to be approximately 16.88 nm for EGCG and 14.62 nm for curcumin.

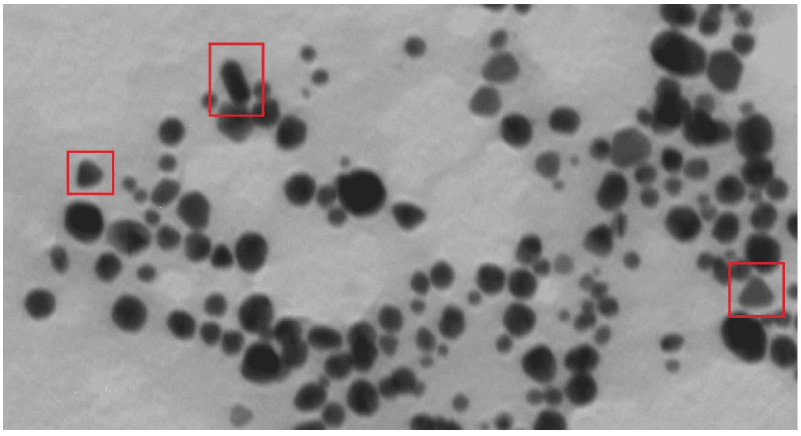


Figure 2.8: TEM Images of EGCG-GNP showing different shaped nanoparticles. Red boxes include irregular rod and triangular structures.

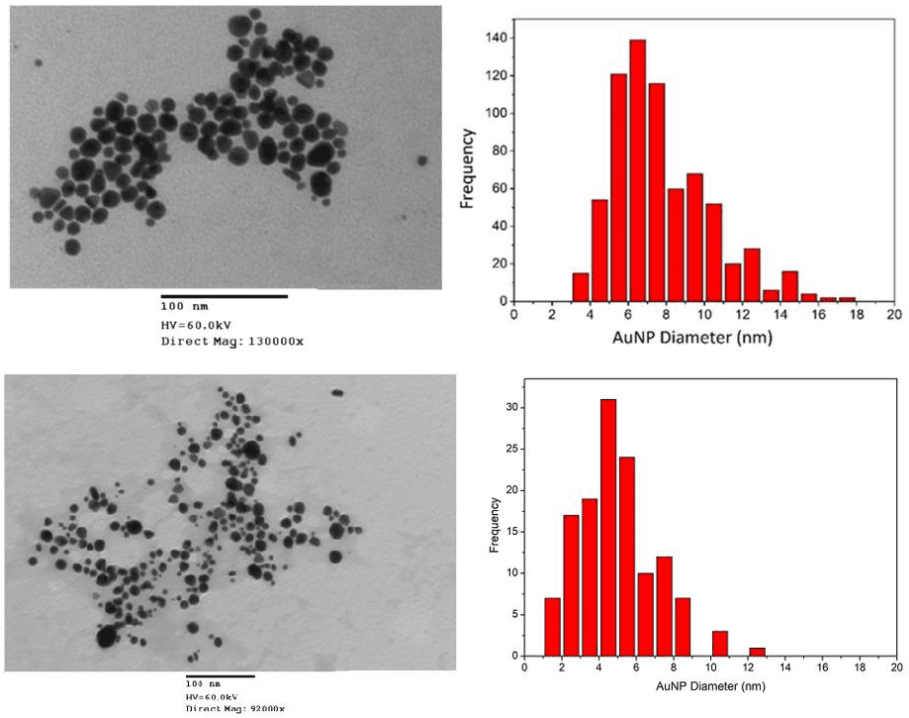


Figure 2.9: TEM Images and Calculated Diameters of Curc-GNPs (upper side) and EGCG-GNPs (lower side)

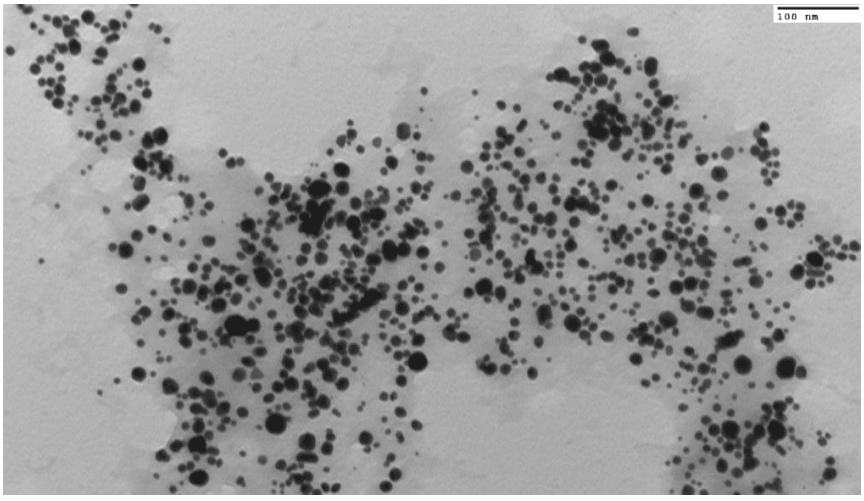


Figure 2.10: Curc-GNPs TEM Image with 92000X Magnification

2.4.4 ICP-MS

The concentration yield from each synthesis protocol was determined by ICP measurements, with data listed in Tables 2.2–2.5 for each GNP sample. EGCG-GNP and Curc-GNP concentrations were similar, as both were synthesized using the protocol described by Nambiar *et al.* [63]. Cit-GNPs and PEG-GNPs yielded lower concentrations but could be easily concentrated using centrifugation. While increasing the concentration of starting precursors such as $HAuCl_4$ and the reducing agent could theoretically enhance GNP yield, Dong *et al.* reported that doing so, while maintaining a constant molar ratio, resulted in increased polydispersity [140]. This was attributed to higher ionic strength and reduced electrostatic repulsion between GNPs.

Table 2.2: ICP-MS Parameters for EGCG-GNPs

Volume of EGCG-GNPs (mL)	**ICP Concentration (mg/L)**	**Dilution Factor**	**Final Concentration (μg/ml)**
0.5	19.7478	20	430.73
1.0	42.7830	10	429.11
1.5	62.7028	6.666	414.20
			Avg: 424.67 ± 7.44

Table 2.3: ICP-MS Parameters for Curc-GNPs

Volume of Curc-GNPs (mL)	**ICP Concentration (mg/L)**	**Dilution Factor**	**Final Concentration (μg/ml)**
0.5	15.8513	20	317.03
1.0	33.9559	10	339.56
1.5	49.8189	6.667	332.13
			Avg: 329.57 ± 9.37

Table 2.4: ICP-MS Parameters for Cit-GNPs

Volume of Cit-GNPs (mL)	ICP Concentration (mg/L)	Dilution Factor	Final Concentration (μg/ml)
0.5	4.5356	20	90.71
1.0	8.8900	10	88.89
1.5	12.4602	6.667	83.07
			Avg: 87.56 ± 3.26

Table 2.5: ICP-MS Parameters for PEG-GNPs

Volume of PEG-GNPs (mL)	ICP Concentration (mg/L)	Dilution Factor	Final Concentration (μg/ml)
0.5	3.7885	20	72.713
1.0	5.3330	10	76.39
1.5	11.1839	6.667	77.07
			Avg: 75.39 ± 1.91

2.4.5 Antioxidant Capacity

The free radical scavenging activity of different types of GNPs was assessed by DPPH scavenging. All GNP structures showed a dose-dependent response (Figure 2.11), meaning DPPH inhibition increased with increasing GNP concentration. This trend was statistically significant for all GNP structures (EGCG-GNP ($p = 0.02$), Curc-GNP ($p = 0.01$), PEG-GNP ($p = 0.02$), and Cit-GNP ($p = 0.003$). It was observed for all structures that the gradient of DPPH activity appears to decrease and flatten between 100-200 μg/ml, this could be a sign of saturation. For example, EGCG-GNP showed an increase of 71.6 % in DPPH inhibition between 50 μg/mL and 100 μg/mL, but only a 31.7% increase between 100 μg/mL and 200 μg/mL suggesting that the availability of active antioxidant molecules may be reaching a limit at higher concentrations. The highest DPPH inhibition was recorded for Curc-GNP at 200 μg/ml, which was 63.36% ± 9.75. It is worth noting that both

green GNPs (EGCG-GNP and Curc-GNP) demonstrated similar free-radical scavenging potential and were considerably higher than both Cit-GNP and PEG-GNP. It was not possible to assess which one was a better antioxidant as all comparison p-values were well above statistical significance ($p>0.05$). For the 25 μg/mL concentration, Curc-GNP demonstrated almost 3.80-fold increased scavenging activity versus PEG-GNP, which was 11.10% ($p<0.01$). This drastic difference arises because the 6000 Da polyethylene glycol (PEG) molecule is a relatively long chain, with only the terminal thiol group expected to quench free radicals, limiting its overall antioxidant capacity compared to curcumin, which contains multiple phenolic and enolic groups that actively scavenge reactive species (Figure 2.1).

Mechanistically, these findings suggest that the intrinsic antioxidant properties of EGCG and curcumin coatings, combined with their interaction with the GNP matrix and the resulting increase in surface area, significantly enhance their scavenging potential. This is especially relevant for curcumin, which is both hydrophobic and lipophilic. Upon binding to the GNP surface, or any nanoparticle, the nanoparticle will act as a dispersing carrier, preventing hydrophobic molecules from aggregating or precipitating. The lower activity of PEG and citrate coatings may reflect their primarily stabilizing roles rather than direct contributions to free radical scavenging. Citrate lacks easily ionizable hydrogens, electron delocalization, and resonance stabilization, unlike curcumin and EGCG. And PEG-6000, due to its large molecular weight and neutral backbone, lacks the redox-active functional groups required for hydrogen or electron donation.

Sanna *et al.* carried out a study exploring different polyphenol-coated GNPs and their antioxidant activity. The GNPs synthesized were coated with EGCG, resveratrol (RSV), and fisetin (FS). All polyphenol-coated GNPs exhibited significant antioxidant activity, as assessed by the DPPH assay. They demonstrated a dose-dependent radical-scavenging effect, with EGCG-GNPs and FS-GNPs showing higher antioxidant potential compared to RSV-GNPs [141]. Specifically, the inhibition of DPPH radicals ranged from 16–19% at 25 μg/mL to 60–66% at 200 μg/mL for EGCG-GNPs and FS-GNPs, whereas RSV-GNPs achieved a maximum inhibition of 26% at 200 μg/mL. However, in the ABTS scavenging assay, RSV-GNPs showed much higher activity, comparable to FS-GNPs and EGCG-GNPs (46%, 51%, and 55% for EGCG-GNP, RSV-GNP, and FS-GNP, respectively). The authors attributed this mismatch in resveratrol's antioxidant performance to the distinct chemical mechanisms of the two assays: ABTS is more responsive to electron transfer-based antioxidants like resveratrol, whereas DPPH favors compounds with stronger hydrogen-donating capacity [141]. This study highlights the importance of evaluating antioxidant potential through multiple mechanisms, as a single assay may yield misleading or incomplete results.

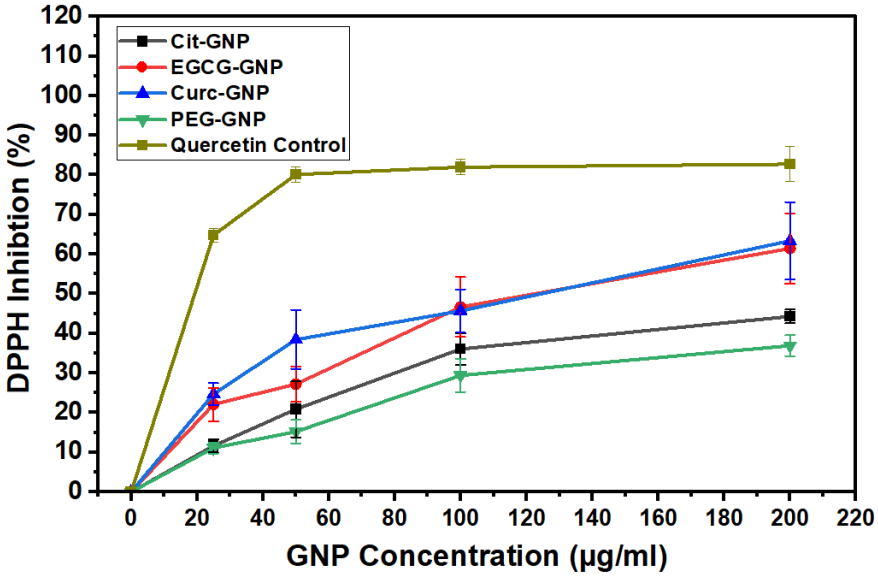


Figure 2.11: DPPH inhibition of EGCG-GNP, Cit-GNP, Curc-GNP, PEG-GNP GNP structures and quercetin (Positive control) at varying concentrations (25 – 200 μg/mL).

2.4.6 FTIR

FTIR spectra (Figure 2.12) of ≥98% purity curcumin showed a strong, conjugated carbonyl (C=O) stretch near 1625–1628 cm^{-1} that overlaps with aromatic C=C signals. Upon binding to GNPs, this band diminished in intensity and partially shifted to a higher frequency around 1700– 1740 cm^{-1}. This upward shift suggests that curcumin's β-diketone moiety was converted to a less hydrogen-bonded carbonyl, consistent with coordination to the gold surface. Conversely, the aromatic ring vibrations around 1500–1600 cm^{-1} remained largely unaltered, indicating that the phenyl rings do not participate greatly in binding with GNPs. Additionally, a notable decrease or disappearance of the enolic =C-OH bending peak near 960 cm^{-1} further supports the involvement of the β-diketone/enol functional group in anchoring curcumin to the gold surface. Altogether, these spectral changes confirm that curcumin was successfully coated onto the GNPs primarily via its polar β-diketone/enol while the aromatic rings remain structurally intact.

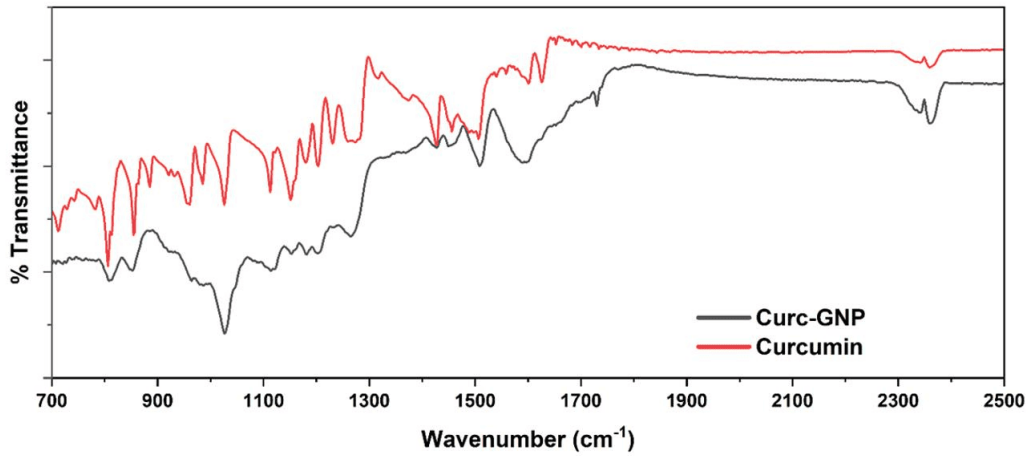


Figure 2.12: FTIR spectra of Curc-GNPs (black) and pure curcumin (red). Characteristic absorption bands of curcumin, including peaks corresponding to aromatic C=C stretching (1627 cm^{-1}), enolic –OH (1275 cm^{-1}), and C=O stretching vibrations (1601 cm^{-1}), are observed in the red spectrum.

2.4.7 HPLC

The HPLC method exhibited strong linearity for curcumin standards in the range of 0.1–54.25 μg/mL, with an R^2 value of 0.996. Standard measurements between 5.425 - 54.25 μg /mL were especially accurate as they all yielded % deviations of less than 5% of expected value (Figure 2.13C). Curcumin consistently eluted at approximately 4.03 $\pm$ 0.01 minutes for all samples analyzed, including both standards and Curc-GNP desorbate (Figure 2.13A, B). The first desorption cycle yielded an average curcumin concentration of 7.011 $\pm$ 0.014 μg/mL . As the solution was diluted 10-fold for HPLC analysis, the actual supernatant concentration was 70.11 μg/mL. With a total supernatant volume of 25 mL, this corresponds to 1.75 mg of curcumin recovered. A second desorption cycle was performed to capture any remaining curcumin on the GNPs however, the measured value was extremely small <0.5 μg/mL, below the quantification limit of 3.60 ppm. Thus, it can be concluded that the first desorption cycle removed >97% of the curcumin from the GNPs, demonstrating the effectiveness of the acidic ethanol method. ICP analysis of the resuspended pellet revealed a gold concentration of 336.54 $\pm$ 0.12 μg/mL, equivalent to 8.41 mg of gold in the 25 mL suspension. Using Equation 2.2, the curcumin loading is calculated as follows:

$$\omega_{Curc} = \frac{m_{Curc}}{m_{Au}} = \frac{1.75\ mg}{8.41\ mg} = 0.208\ mg\ Curcumin/mg\ Au$$

This corresponds to a curcumin loading of 20.8 wt%. The Curc-GNP synthesis initially used 9.21 mg of curcumin, so the 1.75 mg detected on the GNPs represents a ∼19% encapsulation efficiency. Quantification of curcumin loading on GNPs is crucial, as curcumin is the active therapeutic agent. Accurate loading data provide essential context for interpreting in vitro results in terms of therapeutic efficacy. Furthermore, precise quantification ensures reproducibility and facilitates comparison between different formulations.

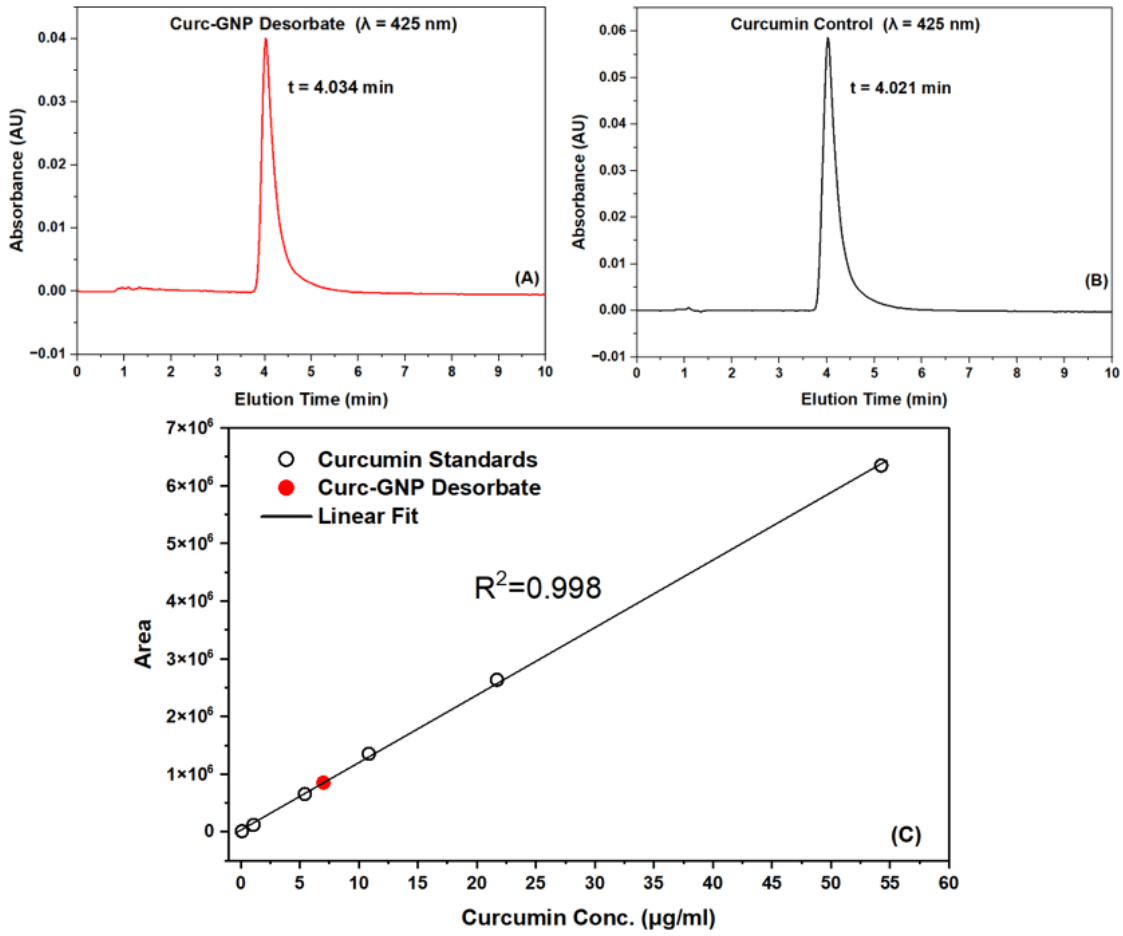


Figure 2.13: *HPLC analysis of curcumin loading.* *(A)* Chromatogram of Curc-GNP desorbate (t = 4.034 min). *(B)* Chromatogram of curcumin control (t = 4.02 min). *(C)* Calibration curve for curcumin (0.1 – 55 μg/mL; $R^2 = 0.998$) with Curc-GNP desorbate plotted in red

2.4.8 CT-Imaging

CT images of EGCG-GNPs revealed clear contrast across various gold concentrations and environments. 1500 μg/mL EGCG-GNPs was imaged in an electron density phantom. The mean Hounsfield Unit (HU) contrast at this concentration was measured as 109 HU (Figure 2.14), with additional values listed in Table 2.6. EGCG-GNPs were imaged within an electron density phantom to assess CT contrast performance under standardized, tissue-mimicking conditions and to benchmark their attenuation relative to clinically relevant reference materials. The ${\rho_e}^w$ of the GNP solution was calculated based on Au concentration. Despite a nearly identical electron density to water (${\rho_e}^w \approx 1.001$), the 1500 μg/mL EGCG-GNP solution exhibited a HU contrast of +109, highlighting that X-ray attenuation in CT imaging is strongly influenced by the high atomic number of gold rather than bulk electron density. This confirms the suitability of GNPs as effective low-dose contrast agents in CT-based applications. The main objective of this study was to generate a line of best fit correlating gold concentration with HU contrast. A tube voltage of 120 kVp was selected to maximize contrast near the K-edge of gold, which is approximately 80.7 keV. CT scanners emit a broad X-ray spectrum; a setting of 120 kVp corresponds to a maximum photon energy of 120 keV. However, the average photon energy typically falls between 40–70% of the peak, placing the mean energy close to the gold K-edge. The line of best fit yielded a slope of 57.56 HU per mg/mL Au ($R^2 = 0.972$), indicating a strong linear correlation (Figure 2.15). This high slope confirms that even small increases in Au concentration produce substantial gains in CT contrast, supporting the utility of EGCG-GNPs for dose-sensitive imaging applications (Figure 2.15).

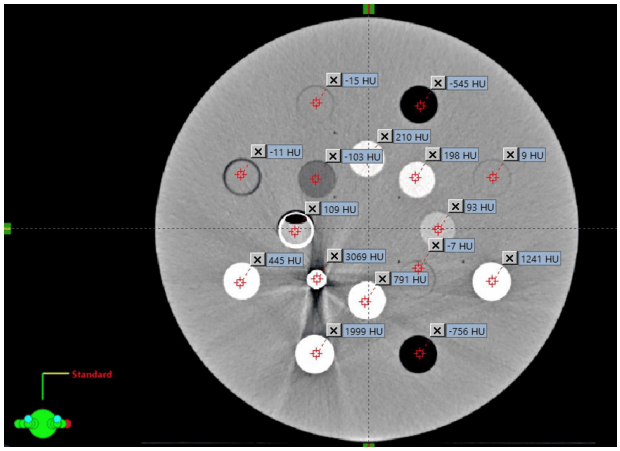


Figure 2.14: The Measurement of mean HU Contrast of 1500 μg/ml EGCG-GNPs

Table 2.6: CT-Imaging Parameters (Electron Density Relative to Water and HU Contrast) Calculated for 1500 μg/ml EGCG-GNPs in Comparison to Other Materials

Materials	**Electron Density Relative to Water ($\rho_e{}^w$)**	**HU Contrast**
Solid Water C	0.99	-15 HU
Lung LN-450	0.40	-545 HU
True Water	1.00	-11 HU
Adipose	0.90	-103 HU
Inner Bone	1.09	210 HU
Bone B-200	1.11	198 HU
Solid Water A	0.99	9 HU
CB2-30%	1.28	445 HU
Titanium	3.79	3069 HU
CB2-50%	1.47	791 HU
Liver	1.07	93 HU
Solid Water B	0.99	-7 HU
Cortical Bone	1.69	-1241 HU
Lung LN-300	0.28	-756 HU
Aluminum	2.34	1999 HU
1500 μg/ml EGCG-GNPs	**1.001**	**109 HU**

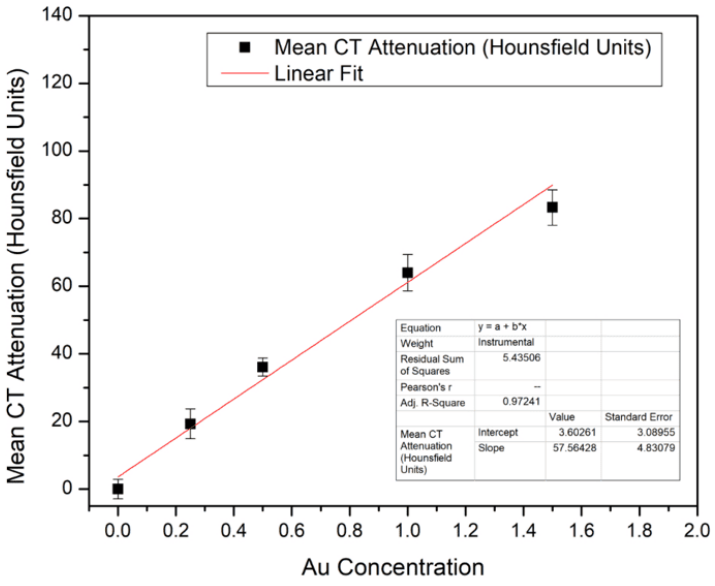


Figure 2.15: This figure shows a linear relationship between gold nanoparticle (EGCG-GNP) concentration and mean CT attenuation in Hounsfield Units (HU). The black squares represent experimental mean HU values at different gold concentrations (0–1.5 mg/mL), with error bars indicating standard deviation. The red line represents the linear regression fit, demonstrating a strong correlation (Adjusted $R^2 = 0.97241$) between increasing gold concentration and CT contrast. The equation of the line is provided in the inset, with a slope of 57.56 and an intercept of 3.60.

2.5 Conclusion

This chapter explored the physico-chemical properties of different GNP constructs. This is a crucial first step in the success of the project because of the massive implications that the physical properties of our nanostructures will have on the biological systems they are tested in. In conclusion, this chapter presented the successful synthesis and detailed physicochemical characterization of four distinct GNP formulations: EGCG-GNPs, Curc-GNPs, Cit-GNPs, and PEG-GNPs. Utilizing both traditional (Turkevich) and innovative green synthesis methods, the GNPs demonstrated desirable attributes, including monodispersity, colloidal stability, spherical morphology, and controlled hydrodynamic sizes. EGCG- and Curc-conjugated GNPs were synthesized using a one-pot, eco-friendly approach, yielding higher

concentrations and superior stability compared to the citrate-based methods. DLS and TEM analyses confirmed the narrow size distributions, with core diameters averaging around 7 nm and hydrodynamic diameters ranging from approximately 18 nm for Cit-GNPs to 56 nm for PEG-GNPs. Zeta potential measurements highlighted substantial surface charges necessary for colloidal stability, notably lower for PEG-GNPs, reflective of their dense polymer coating.

The antioxidant studies demonstrated significantly enhanced DPPH radical scavenging capacities for EGCG- and Curc-GNPs compared to Cit- and PEG-GNPs, confirming the beneficial effects of phytochemical surface functionalization. FTIR spectroscopy and HPLC further validated the efficient and robust attachment of curcumin to the GNP surface, with a quantified drug loading of 20.8 wt%. Additionally, computed tomography (CT) imaging demonstrated the strong contrast capabilities of EGCG-GNPs, with 57.6 HU/mg Au, highlighting their effectiveness as imaging contrast agents at clinically relevant concentrations.

Importantly, UV-Vis spectroscopy analyses revealed that Curc-GNPs maintained significantly greater stability in biological media compared to Cit-GNPs, highlighting their enhanced suitability for biomedical applications. Overall, the findings presented here affirm the suitability of EGCG-GNPs and Curc-GNPs for further biomedical applications, particularly due to their advantageous synthesis methods, superior physicochemical stability, potent antioxidant properties, and imaging enhancement capabilities. Future investigations should leverage these optimized nanoparticle formulations in targeted drug delivery and therapeutic efficacy studies, emphasizing their translation into clinical nanomedicine.

Chapter 3

In Vitro Studies

This Chapter evaluates and compares EGCG-GNP and Curc-GNP to conventional GNPs (Cit-GNP and PEG-GNP) in prostate cancer PC-3 cells in vitro. **Method:** Cytotoxicity was quantified with XTT assays over 24–72 h at 0–1000 μg/mL, gold uptake was measured by ICP-MS at 50 and 100 μg/mL (10 h and 24 h; $\pm$ serum), and radiosensitization was determined by clonogenic survival after 0–6 Gy X-irradiation. Linear–quadratic modelling yielded α, β, median lethal dose (D_{50}) and sensitization-enhancement ratio (SER). **Results:** All coatings were well tolerated $\leq$ 100 μg mL^{-1}, but viability declined sharply above this threshold. EGCG-GNPs were most cytotoxic, falling to 16.9% viability at 1000 μg mL^{-1} (72 h), whereas PEG-GNPs were least toxic. Curc-GNPs exhibited a biphasic response: modest proliferation at 0–100 μg/mL yet marked toxicity above 100 μg/mL. Uptake increased with dose, time and serum removal; EGCG-GNP uptake (83.7 pg cell^{-1}, 24 h, no serum) exceeded Cit-GNP by 1.5-fold, while Curc-GNP matched EGCG-GNP and surpassed Cit-GNP. In radiosensitization studies, EGCG-GNPs reduced D_{50} from 2.48 Gy (control) to 1.26 Gy at 500 μg mL^{-1} and raised SER to 1.96; Curc-GNPs achieved SER = 1.82. α rose steadily with EGCG-GNP concentration, indicating enhanced single-track DNA breaks, whereas β changed modestly, shifting cell kill toward indirect damage. **Conclusion:** Collectively, the data identify EGCG-GNPs as the most cytotoxic and potent radiosensitizer to PC-3 cells. Curc-GNPs biphasic cytotoxicity requires further investigation, but it demonstrated similar radiosensitization and cellular uptake to EGCG-GNPs. Reduced uptake under serum supplemented medium underscore the importance of nanoparticle design.

3.1 Introduction

The starting point for many nanodrug delivery research projects typically involves in vitro studies. These are ideal because they are cost-effective, allow high-throughput experimentation, and establish proof of principle. In our project, the goal of in vitro studies is to investigate the interactions of PC-3 cell colonies exposed to different GNP structures. This controlled environment enables us to analyze cellular responses without the challenges of in vivo studies. In vitro experiments also allow precise control over conditions such as dosage, exposure time, and cellular environment, which is essential for isolating the specific effects of GNPs. They provide early insights into key parameters such as cytotoxicity, cellular uptake, intracellular localization, cell signaling biomarkers, and drug release dynamics which are critical factors for optimizing GNP design. This information forms a solid foundation for understanding the efficacy and mechanisms of our GNP structures before progressing to in vivo studies. The data generated here, together with the physicochemical properties from the previous chapter, will guide the selection of the most promising GNP structures and help predict optimal parameters for in vivo applications, such as GNP concentration, surface coating, size, and X-ray dose.

Despite the advantages of in vitro studies, there are notable limitations that must be discussed. Firstly, cellular experiments are highly simplistic compared to the complex and dynamic conditions present in living organisms. One of the most evident shortcomings is that static, planar, two-dimensional (2D) cell cultures fail to replicate the dynamic environment of three-dimensional tissue structures, often leading to significant discrepancies in translational studies. In vivo factors such as blood flow, mechanical forces, immune surveillance, and systemic hormonal and neural signals, all greatly influence nanoparticle behavior and response, and these are entirely missing from 2D in vitro studies. For this reason, results can deviate greatly when progressing from cellular to animal studies. Another major challenge, particularly relevant to nanodrug delivery research, is the inconsistency in the scientific literature regarding in vitro and in vivo results. As we discussed in the previous chapter regarding the impact of physicochemical properties on nanoparticles, studies investigating the same topic often report widely divergent outcomes due to variations in physicochemical properties (surface, size, shape, charge) [1]. Additionally, the variability in experimental conditions such as cell medium, cell density, temperature, pH, exposure time, and concentration can also impact nanoparticle behavior, uptake, and bioactivity [2]. These factors collectively contribute to inconsistent results across studies and underscore the need for standardized reporting of both nanoparticle descriptors and experimental conditions to improve reproducibility and comparability. Therefore, making blanket statements about GNP toxicity is difficult and each structure should be studied and tested individually.

Comparisons would require experimental conditions to be as identical as possible. Sani *et al.* addressed this topic in their highly cited systematic review paper, "Toxicity of Gold Nanoparticles (AuNPs): A Review," which conducted a systematic analysis of sixty-nine studies that explored in vitro and in vivo GNP toxicity [2]. They found a strong correlation between studies using smaller GNPs and toxicity in both cell and in vivo models, however, GNPs with inert surface ligands (PEG, GSH, albumin) showed comparable toxicity measurements to larger GNPs. Additionally, they stated that variability was driven by cell lines and assays, as some studies reported significantly different cytotoxicities even with the same GNP construct and animal/cell model. Their findings highlighted that drawing definitive conclusions about GNP toxicity is challenging.

Therefore, our project aims to generate consistent and reproducible data by ensuring that the physical properties of each GNP structure are recorded and remain as identical as possible across experiments, along with controlled experimental conditions such as medium, cell seeding, temperature, and pH. To ensure accuracy and reproducibility, we have developed the following strategy: **(1)** incorporate Good Laboratory Practices, including record management, standardizing protocols, and authoring SOPs for each synthesis and cell testing method; **(2)** optimize cell culture conditions to remain identical across all GNP structures and studies; **(3)** minimize assay interference; and **(4)** implement robust data analysis and collection methods. By focusing on these approaches, we aim to reduce variability and establish a more reliable foundation for understanding GNP toxicity.

(i) Standardizing Experimental Protocols

To ensure consistency, we aimed to make each round of in vitro experiments as uniform and identical as possible. This required synthesizing monodisperse GNPs with precisely known properties, including size, shape, zeta potential, and coating. We used dynamic light scattering (DLS) and UV-vis measurements before each in vitro experiment to assess GNP properties and ensure they met thresholds. Our property thresholds were that the GNPs needed to be spherical, have negative surface charge, and a polydispersity index (PDI) below 0.3. Size thresholds were defined as 15–25 nm for CIT-GNP, Curc-GNP, and EGCG-GNP, and 45–70 nm for PEG-GNP. Any GNPs outside these thresholds were discarded, resynthesized, and recharacterized to ensure compliance. Each synthesis method was documented in a detailed Standard Operating Procedure (SOP), stored electronically and in laboratory notebooks along with water bath temperatures, solution pH, reaction times, reagent concentrations, volumes of gold precursor, and post-synthesis storage conditions. Additionally, batches were labelled with synthesis dates, analyst initials, and characterization results to maintain detailed batch histories and ensure traceability.

(ii) Optimizing Cell Culture Conditions

Consistency in cell culture was maintained by using well-documented and standardized media formulations. All experiments utilized RPMI-1640 medium (Sigma-Aldrich), supplemented with 1% (v/v) Gibco Penicillin-Streptomycin. For serum-supplemented studies, 10% (v/v) Gibco Fetal Bovine Serum (FBS) was added. The pH of the medium was routinely measured and maintained within a narrow range of 7.0 to 7.4; any medium falling outside this range was discarded. PC-3 prostate cancer cells were exclusively used at early passages to ensure genetic and phenotypic consistency. Cells were passaged using standardized protocols, and once a line exceeded 20 passages, a new cryovial from liquid nitrogen storage was thawed and expanded. All culture conditions, including incubation temperature (37 °C), CO_2 concentration (5%), and passage ratios, were kept consistent across all experimental replicates. All cell culture procedures were performed using standardized protocols documented in SOPs and recorded in laboratory notebooks and transferred to electron lab-notebook according to Good Lab Procedure (GLP) guidelines.

(iii) Minimizing Assay Interference

Assay interference is a common challenge in in vitro studies, particularly when the absorption spectra of dyes overlap with the characteristic optical properties of nanoparticles. Gold nanoparticles exhibit strong surface plasmon resonance near 525 nm, which can interfere with dye-based assays. To mitigate this, we selected the XTT cell viability assay, which measures absorbance at 450 nm and 660 nm—wavelengths with minimal spectral overlap. To further control for potential interference, we utilized two types of blank controls which are GNP+media blanks and media-only blanks which were subtracted from all sample measurements. Additionally, negative and positive controls were included to further ensure the precision of the assay procedure.

(iv) Implementing Robust Data Analysis and Collection

To ensure reproducibility, all in vitro experiments were repeated at least three times ($n = 3$). Experimental parameters, including nanoparticle synthesis and characterization data, were recorded both digitally and in laboratory notebooks. Statistical analysis was conducted to validate results, with calculations for p-values, standard deviations and standard error. P-values comparing the mean of two groups used the paired t-test, and p-values comparing the mean of three or more groups were calculated based on the method “one way ANOVA”.

Trend p-values were calculated using the linear regression test method. P-values stated from this point will refer to treatment relative to control unless explicitly stated in the text.

By addressing these challenges, we are able to produce reliable and reproducible data that can be presented to the scientific community for comparison and analysis. The in vitro methods used in this project were the XTT reduction assay for measuring cytotoxicity, ICP-MS for measuring gold cellular uptake, and the clonogenic assay for measuring the colony forming potential of cells after exposure to radiation and GNPs.

The first in vitro method presented in this chapter is the XTT (2,3-bis(2-methoxy-4-nitro-5-sulfophenyl)-5-carboxanilide-2H-tetrazolium) cell viability study, which explored the cytotoxicity of each GNP structure (EGCG, Curc, Cit, PEG) as a function of concentration (0 to 1000 μg/ml) and incubation time (24, 48, and 72 hours). The XTT assay is a widely used method for assessing cell viability and cytotoxicity. It works on the principle that metabolically active cells reduce the XTT reagent, a tetrazolium salt, into a water soluble formazan dye through the activity of mitochondrial dehydrogenases [3]. This reduction occurs only in living cells, making the intensity of the colored formazan directly proportional to the number of viable cells. The absorbance of the formazan product can then be measured spectrophotometrically, providing a quantitative assessment of cell viability. XTT was chosen over the commonly used MTT assay because it has higher sensitivity and the formazan product is water soluble, allowing for higher throughput unlike MTT which requires an extra solubilization step [4]. Cytotoxicity studies are valuable to this project because they allow us to evaluate whether the GNPs induce toxic effects in prostate cancer cells and if so at what concentration and to what extent. Once we have this data, we can create a dose response curve, which is crucial for selecting the best dose for maximizing PC-3 cell death while minimizing GNP exposure to healthy tissues. This information will serve as the baseline for establishing a therapeutic window for radiation treatment and guiding our in vivo animal studies.

The third in vitro experiment involves measuring GNP uptake in PC-3 cells using inductively coupled plasma mass spectrometry (ICP-MS). GNP uptake is a crucial design parameter for our GNP constructs, as numerous studies have demonstrated a strong correlation between GNP uptake and enhanced radiosensitization and cell killing [5, 6]. Understanding and optimizing this parameter is essential for improving the therapeutic efficacy of GNP-based treatments. Furthermore, it is well documented that the surface coating of GNPs significantly influences their cellular uptake [5, 6, 7]. This is particularly relevant in the case of EGCG-GNP, where molecular docking studies have shown that EGCG binds to the active cavity of the 67LR receptor, which is overexpressed on prostate cancer cells, such as LNCaP, DU145 and PC-3 cell lines [8]. This suggests that EGCG-GNPs are internalized via 67LR-mediated endocytosis, offering a targeted mechanism of uptake.

Our desired endpoints from this experiment are to gain insight into the uptake mechanics of GNPs relative to their surface coating, concentration, exposure time, and the effects of serum versus non-serum supplemented medium. The non-serum uptake of our GNPs will allow us to assess the surface coating effect on cell membranes, and the serum supplemented condition will better reflect the in vivo environment and allow us to observe the effect of protein adsorption on cell uptake.

Finally, our last in vitro experiment involves the clonogenic assay, which is designed to evaluate the combined effect of radiation and GNPs on PC-3 cells. The clonogenic assay is a well-established method for assessing the ability of cells to survive and proliferate following radiation treatment [9]. It measures long-term reproductive viability, allowing us to determine how effectively a treatment, such as radiation or GNPs, inhibits sustained cell growth. Colorimetric assays such as XTT and MTT often rely on mitochondrial function to represent apoptosis; in the case of radiation therapy, the cell killing potential may not be realized immediately, as cells can undergo mitotic death over several divisions [10]. This makes long-term assays like the clonogenic assay essential for accurately capturing treatment outcomes. While the assay is highly informative for radiotherapy studies, its broader use across other therapies is limited due to its time-intensive nature and specific focus on proliferative capacity.

In our radiosensitization study, cells are plated at low densities and exposed to GNPs at varying concentrations (0 to 500 μg/mL), followed by irradiation at different doses (0 to 6 Gy). After a suitable incubation period, typically 14 to 28 days, surviving cells form visible colonies. These colonies are stained and counted using image capture software. The number of colonies relative to the number of cells seeded post-treatment represents the fraction of cells that survived and were able to form a colony. If we divide this number by the initial number of cells seeded, we obtain the surviving fraction. To quantify radiosensitization, the surviving fractions are plotted against radiation doses to generate survival curves. The degree of radiosensitization is determined by comparing the survival curves of cells treated with radiation alone to those treated with GNP alone and with radiation combined with GNPs [9]. The survival data are fitted to the linear-quadratic (LQ) equation, which models the synergistic effect of GNPs on radiation-induced DNA damage by altering the α and β coefficients that define the curve [9]. An increase in α or β indicates radiosensitization, a decrease suggests a radioprotective effect, and no change implies that the observed cell death is purely additive. A common metric used to express radiosensitization is the sensitization enhancement ratio (SER), calculated as the ratio of the radiation dose required to achieve a specific surviving fraction in the control group to the dose required in the GNP-treated group [11]. An SER greater than 1 indicates enhanced radiosensitivity due to the GNPs. By analyzing the clonogenic survival data, this experiment will help us understand how different

GNP coatings, concentrations, and cellular uptake influence their ability to enhance the effects of radiation on PC-3 cells. This detailed assessment of radiosensitization will be crucial for optimizing GNP-based strategies for radiotherapy in animal studies.

3.2 Materials

Reagents for GNP synthesis were as follows: Curcumin (≥98% purity; Alexis Biochemicals, San Diego, CA, USA), sodium citrate dihydrate (S25545; Fisher Scientific, Waltham, MA, USA), gold(III) chloride trihydrate ($HAuCl_4 \cdot 3H_2O$, 520918; Sigma-Aldrich, St. Louis, MO, USA), epigallocatechin gallate (≤95% purity; E4143; Sigma-Aldrich, St. Louis, MO, USA), and PEG-thiol (Mn 6,000; 729159; Sigma-Aldrich, St. Louis, MO, USA). All synthesis protocols utilized ultrapure Milli-Q water from a Millipore Gradient A10 water purification system (Merck Millipore, Burlington, MA, USA). Reagents for in vitro studies included RPMI 1640 medium (R8758; Sigma-Aldrich), fetal bovine serum (FBS; A3160702; Fisher Scientific), penicillin-streptomycin (15140122; Fisher Scientific), Dulbecco's phosphate-buffered saline (PBS; SH30028.02; Fisher Scientific), trypsin-EDTA (25200072; Fisher Scientific), dimethyl sulfoxide (DMSO; MT25950CQ; Fisher Scientific), and crystal violet (C0775-100G; Sigma-Aldrich).

3.3 Methods

3.3.1 Cytotoxicity: XTT Assay

The cytotoxicity of PC-3 prostate cancer cells following treatment with EGCG-GNP, Curc-GNP, Cit-GNP, and PEG-GNP was assessed using the colorimetric XTT assay [3]. This assay is based on the reduction of XTT to a soluble formazan product by metabolically active cells, which serves as an indicator of cell proliferation and viability.

DAY ONE: PC-3 cells were seeded into 96-well plates at a density of 5,000 cells per well and incubated in RPMI-1640 medium supplemented with 10% fetal bovine serum (FBS) and 1% penicillin-streptomycin at 37 °C in a 5% CO_2 incubator for 24 hours to allow cell adherence and stabilization.

DAY TWO: Seven concentrations of each GNP structure (25, 50, 75, 100, 200, 500, and 1000 μg/mL) were prepared in serum supplemented RPMI medium using 15 mL conical tubes. The experimental groups were as follows:

- *Treated Wells:* PC-3 cells treated with different concentrations of GNPs.
- *Negative Control:* PC-3 cells incubated with medium only (no GNPs).
- *Blank Control:* Wells containing medium and GNPs (no cells).
- *Positive Control:* PC-3 cells incubated with hydrogen peroxide (H_2O_2)

Cells were exposed to each GNP concentration for treatment durations of 24, 48, and 72 hours. Separate 96-well plates were used for each treatment duration and GNP structure, resulting in a total of 12 plates. Each concentration and treatment condition was performed in quintuplicate (5 wells per condition) and the final volume was 100 μL per well.

DAY THREE: A 5.1 mL XTT working solution was prepared by combining 5 mL XTT reagent with 0.1 mL of XTT activator. At the end of each treatment time point, medium was pipetted out and wells were gently rinsed with 100 μL of PBS before 50 μL of XTT working solution was added to each well, and the plates were incubated for an additional 4 hours at 37 °C in a 5% CO_2 incubator. Following incubation, absorbance was measured at a wavelength of 450 nm with a reference wavelength of 650 nm using a microplate (ELISA) reader. Cell viability for each treatment group was calculated using Equation (3.1), accounting for both the negative and blank controls to normalize data. The results were used to evaluate the cytotoxicity of each GNP structure in PC-3 cells over the defined concentrations and time points.

$$\%\ Viability = \frac{Abs\ of\ Treated\ Wells - Abs\ of\ Blank}{Abs\ of\ Control - Abs\ of\ Blank} \times 100 \tag{3.1}$$

$$\%\ Cytotoxicity = 100 - \%\ Viability \tag{3.2}$$

3.3.2 Cellular Uptake-ICP-MS

The cellular uptake of EGCG-GNP, Curc-GNP, and Cit-GNP by PC-3 cells was quantified by measuring gold (Au) concentrations using ICP-MS [1]. The experiment was designed to assess the effect of incubation time (10 hours vs 24 hours) and medium composition (serum-supplemented vs. non-serum-supplemented medium) on GNP uptake at two concentrations (50 vs 100 μg/mL).

Stage One: Cell Seeding: PC-3 cells were seeded into six-well plates at a density of 0.3×10^6 cells per well in growth medium. For serum-supplemented medium, the growth

medium consisted of RPMI-1640 supplemented with 10% fetal bovine serum (FBS) and 1% penicillin-streptomycin. For non-serum-supplemented medium, RPMI-1640 with 1% penicillin-streptomycin was used. Cells were incubated at 37 °C in a 5% CO_2 atmosphere until they reached 75% confluency.

Stage Two: GNP Treatment: At 75% confluency, the medium was removed, and 3 mL of fresh medium containing 50 or 100 μg/mL of GNPs was added to each well. Cells were incubated for 10 or 24 hours at 37 °C, with one experimental group maintained in serum-supplemented medium and the other in non-serum-supplemented medium. Each concentration and condition consisted of triplicate wells.

Stage Three: Cell Harvesting and Gold Quantification:

1. After the designated incubation period, the medium containing GNPs was removed, and each well was washed gently with PBS three times to remove unbound nanoparticles.

2. A volume of 1.5 mL of trypsin was added to each well to detach the PC-3 cells, and the detached cells from three wells were transferred collectively into a 15 mL conical tube.

3. To neutralize the trypsin, 10.5 mL of medium was added to each tube. Cell suspensions were counted using a hemocytometer in triplicate for accurate cell quantification.

4. Cell suspensions were centrifuged at 1200 rpm for 10 minutes, and the supernatant was carefully discarded. The remaining pellet was resuspended in 4 mL of Mili-Q water.

5. The resuspended cells were transferred to a DigiTUBE acid digestion tube. A volume of 1 mL of aqua regia (1:3 mixture of HNO_3 and HCl) was added for acid digestion. Tubes were placed on an EHD36 Digiblock Digester at 150 °C for 20 minutes.

6. After digestion, the solution was diluted to 10 mL with Milli-Q water and thoroughly mixed before analysis.

ICP-MS Analysis: Gold concentrations in the digested samples were analyzed using an ICP-MS instrument (Agilent Technologies). Measurements were performed for ^{197}Au, while ^{89}Y was used as the internal standard to correct for variations in plasma conditions. External calibration was performed using a 5-point calibration curve (1–100 ppm), and curve correlation coefficients were all >0.995. Calibration was validated using a 10 ppm or 50 ppm Au standard from a different source, with acceptable results within $\pm 10\%$ of the

expected value. The Method Detection Limit (MDL) and Limit of Quantification (LOQ) for gold in solution were calculated as 0.408 ppm and 1.300 ppm, respectively.

Gold Uptake Calculation: Gold measurements obtained from the ICP-MS were used to estimate the gold content per cell using the following formula:

$$Au\ per\ cell = \frac{Total\ Au\ concentration\ (from\ 3\ wells)}{Total\ cell\ count\ (from\ 3\ wells)} \tag{3.3}$$

3.3.3 Clonogenic Assay

The workflow for the clonogenic assay is depicted in Figure 3.1 and was carried out in four parts, described below [9]. PC-3 cells were cultured in RPMI-1640 medium supplemented with 10% fetal bovine serum (FBS) (v/v) and 1% penicillin-streptomycin (v/v). Additional materials used during the assay included phosphate-buffered saline (PBS, pH 7.2), trypsin-EDTA (0.5%), and a colony staining solution consisting of 6.0% glutaraldehyde (v/v) and 0.5% crystal violet (w/v) prepared in ultrapure water.

PART ONE: PC-3 cells were harvested from a donor culture and seeded into six-well plates at a density of $3x10^5$ cells per well, with each well containing 3 mL of growth medium. The cells were allowed to grow until they reached approximately 75% confluency, at which point green-coated GNPs (EGCG-GNP and Curc-GNP) were applied at six different concentrations: 0, 25, 50, 100, 200, and 500 μg/mL. Following a 24-hour incubation, the GNP-containing medium was discarded, and the cells were thoroughly rinsed three times with PBS to remove unbound nanoparticles.

Radiation treatment was then applied at Waterloo Regional Health Network using a medical linear accelerator (Varian LINAC). Radiation doses of 0, 2, 4, and 6 Gy were administered. Each GNP concentration was performed in triplicate wells for consistency. For each radiation dose, 6 six-well plates were required: one set of 3 for the treatment group (GNP + radiation) and another set of 3 for the control group (GNP only, no radiation).

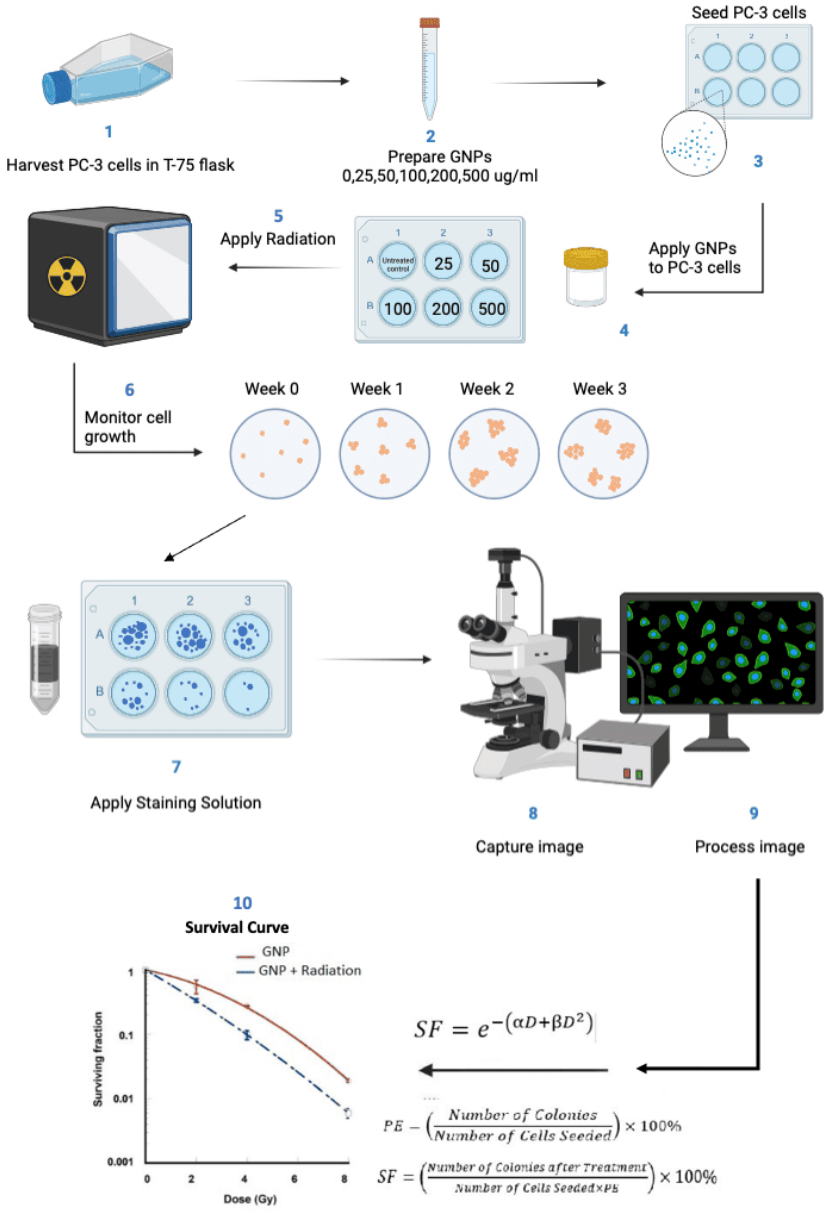


Figure 3.1: A flowchart illustrating the steps of the clonogenic assay, starting with PC-3 cell seeding, GNP treatment, and radiation exposure, followed by colony formation, staining, imaging, and data analysis. The final outputs include survival curves and Sensitizer Enhancement Ratio (SER).

PART TWO: Following treatment, the medium was removed from all wells, and the cells were rinsed thoroughly with PBS. The cells were then trypsinized to detach them from the plates and counted using a hemocytometer with trypan blue staining to identify viable cells. The resuspended cells were seeded into new plates at a density tailored to achieve approximately 100 colonies per well. This density was estimated based on our previous XTT cytotoxicity studies, which evaluated the inhibitory effects of GNP exposure. Higher seeding densities were required for conditions with high GNP potency, while lower densities were used for less potent GNP concentrations.

PART THREE: After seeding, the plates were incubated for up to three weeks to allow colony formation. The incubation period varied depending on the cell growth rate, with the endpoint determined by the size of colonies in the control plates. Plates were removed from the incubator once the colonies had grown sufficiently large but before they began to overlap or aggregate. At the end of the incubation period, the medium was removed, and cells were washed with PBS. A total of 2 mL of crystal violet staining solution was added to each well and left to incubate for 30 minutes. The staining solution was then removed, and the wells were rinsed with tap water. Plates were placed on a rack to air dry overnight at room temperature. The next day, circular purple stains were visible, representing the locations of individual colonies.

PART FOUR: Images of each plate were captured and uploaded to a computer for processing using ImageJ software. Images of each well were taken and processed in ImageJ using the ColonyCount plugin to standardize colony counting and reduce bias [12]. Once the images were processed, the colony count data was exported to Microsoft Excel for further analysis. **Plating Efficiency (PE)** (Equation 3.4) and **Surviving Fraction (SF)** (Equation 3.5) were calculated to evaluate the effects of GNPs and radiation treatment on PC-3 cells.

Plating Efficiency was determined as the ratio of the number of colonies formed to the number of cells originally seeded. This metric reflects the proportion of cells capable of adhering to the plate and forming colonies following GNP exposure in the absence of radiation treatment. In this study, plating efficiency was calculated for each GNP concentration (25, 50, 100, 200, and 500 μg/mL) using control plates that did not receive any radiation. The formula used for PE was:

$$PE = \left(\frac{Number\ of\ Colonies}{Number\ of\ Cells\ Seeded} \right) \times 100\% \tag{3.4}$$

This calculation served as the baseline for subsequent analyses involving the effects of radiation treatment on colony formation and survival.

Surviving Fraction (SF) was calculated to determine the proportion of cells that retained their ability to form colonies after exposure to radiation treatment. This metric is essential for evaluating the combined effect of GNPs and radiation therapy in inhibiting PC-3 cell proliferation and survival. Surviving Fraction was computed using the formula:

$$SF = \left(\frac{Number\ of\ Colonies\ after\ radiotherapy}{Number\ of\ Cells\ Seeded \times PE} \right) \times 100\% \tag{3.5}$$

PART FIVE: After determining the plating efficiency (PE) and surviving fraction (SF) for each treatment group, the next step involved creating radiation survival curves. These curves plotted the radiation dose on the x-axis and the surviving fraction (in logarithmic form) on the y-axis, providing a visual representation of the dose-response relationship.

The survival curves were fitted to the data points using weighted, stratified linear regression based on the **linear-quadratic (LQ) model**, which is described by the equation:

$$SF = e^{-(\alpha D + \beta D^2)} \tag{3.6}$$

Where:

- *SF:* Surviving Fraction.
- *D:* Radiation dose.
- α: Represents the linear component of cell killing (single-track DNA damage).
- β: Represents the quadratic component of cell killing (double-track DNA damage).

This non-linear regression model allowed for the identification of trends in radiation sensitivity and the synergistic effects of GNPs and radiation in reducing cell viability. By fitting the survival curves to the LQ model, key parameters such as α, β, and dose-response relationships were quantified for each treatment group.

To determine the linear parameters α and β of the linear-quadratic (LQ) model, a separate **.csv file** was generated for each radiation-survival experiment. The data was then transferred to Python for analysis using Jupyter Notebook. In Python, the necessary libraries imported were **NumPy**, **Pandas**, **Matplotlib**, and **SciPy**. The LQ model function was defined as shown in Equation 3.6, where SF (surviving fraction) was input as the dependent variable, and radiation dose (D) and its square (D^2) were the independent variables. The curve fitting function from SciPy was used to perform nonlinear regression,

minimizing the sum of squared residuals between the experimental data and the model predictions. From this data, the software is able to compute the best-fit values for α and β, as well as generate the Sensitizer Enhancement Ratio (SER), Dose for 50% effect (D_{50}), R^2 values, standard error, and p-values.

Sensitizer Enhancement Ratio (SER): Quantifies the radiosensitizing effect of GNPs.

$$SER = \frac{Dose\ with\ GNP}{Dose\ without\ GNP} \tag{3.7}$$

This metric reflects the relative enhancement in radiation efficacy due to the presence of GNPs. By analyzing the survival curves and associated parameters, the synergistic effects of GNPs and radiation on cell survival were measured.

3.4 Results & Discussion

3.4.1 Cytotoxicity Assay

In our study, we used the XTT assay to assess the cytotoxicity of four different GNP structures on PC-3 cells across three incubation time points: 24, 48, and 72 hours. Analyzing the general data for all GNP structures, a clear trend emerges showing increased cytotoxicity above 100 μg/mL GNP concentration, a pattern observed consistently across all time points (Figure 3.2). This finding is supported by statistical analysis, which demonstrates a significant increase in cytotoxicity for all GNP structures above 100 μg/mL and across all time points ($p < 0.01$). For GNP concentrations below 100 μg/mL, the data suggest these concentrations are largely tolerable to the PC-3 cells, with cell viability remaining near or above 80%. However, an exception to this trend was observed in the 72-hour time point for EGCG-GNP, where cell viability for 25, 50, 75, and 100 μg/mL concentrations was recorded at 71.40%, 76.50%, 73.05%, and 67.04% (all $p < 0.05$), respectively, demonstrating cytotoxicity even at lower concentrations for extended exposure times. Additionally, Curc-GNPs were the only structure to show a statistically significant increase in cell viability at the 24-hour time point for 0 to 100 μg/mL dose. At the 72-hour time point, all GNP structures showed high cytotoxicity at 0 to 100 μg/mL, however Curc-GNP did not show a statistically significant difference from control cells.

A general trend of increased cytotoxicity with prolonged exposure time was observed for all GNP structures, particularly pronounced at higher concentrations of 200, 500, and 1000 μg/mL. Among the individual trends, PEG-GNP exhibited the lowest change in

cell viability across the 200, 500, and 1000 μg/mL concentrations, indicating minimal cytotoxicity. For instance, cell viability decreased steadily with PEG-GNP concentration but maintained 64.06% viability at 1000 μg/mL ($p < 0.01$), whereas EGCG-GNP showed a sharper decline, dropping to 29.41% viability at 1000 μg/mL ($p < 0.01$). Curc-GNP demonstrated negative cytotoxicity at 25, 50, and 75 μg/mL concentrations, particularly during the 24-hour incubation, where cell viability was recorded as 111.05% ($p < 0.05$), 113.62% ($p < 0.05$), and 111.56% ($p < 0.05$), respectively. This negative cytotoxicity may signify a protective effect that promotes cell proliferation, which warrants further mechanistic investigation.

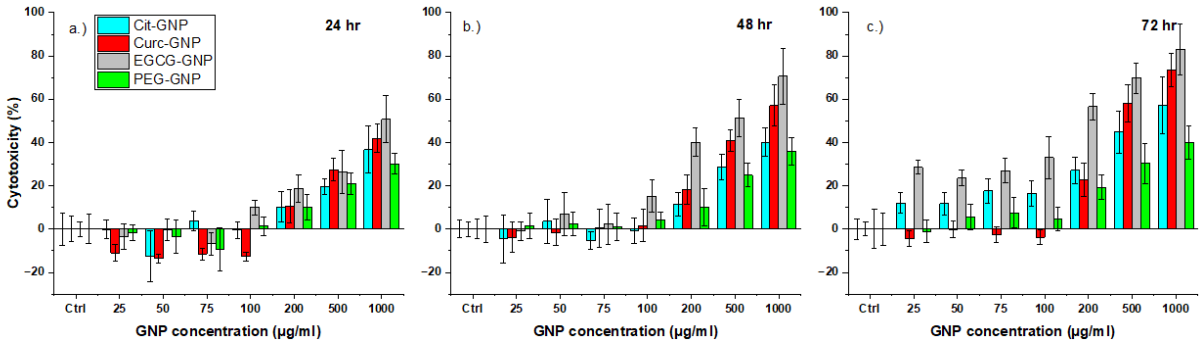
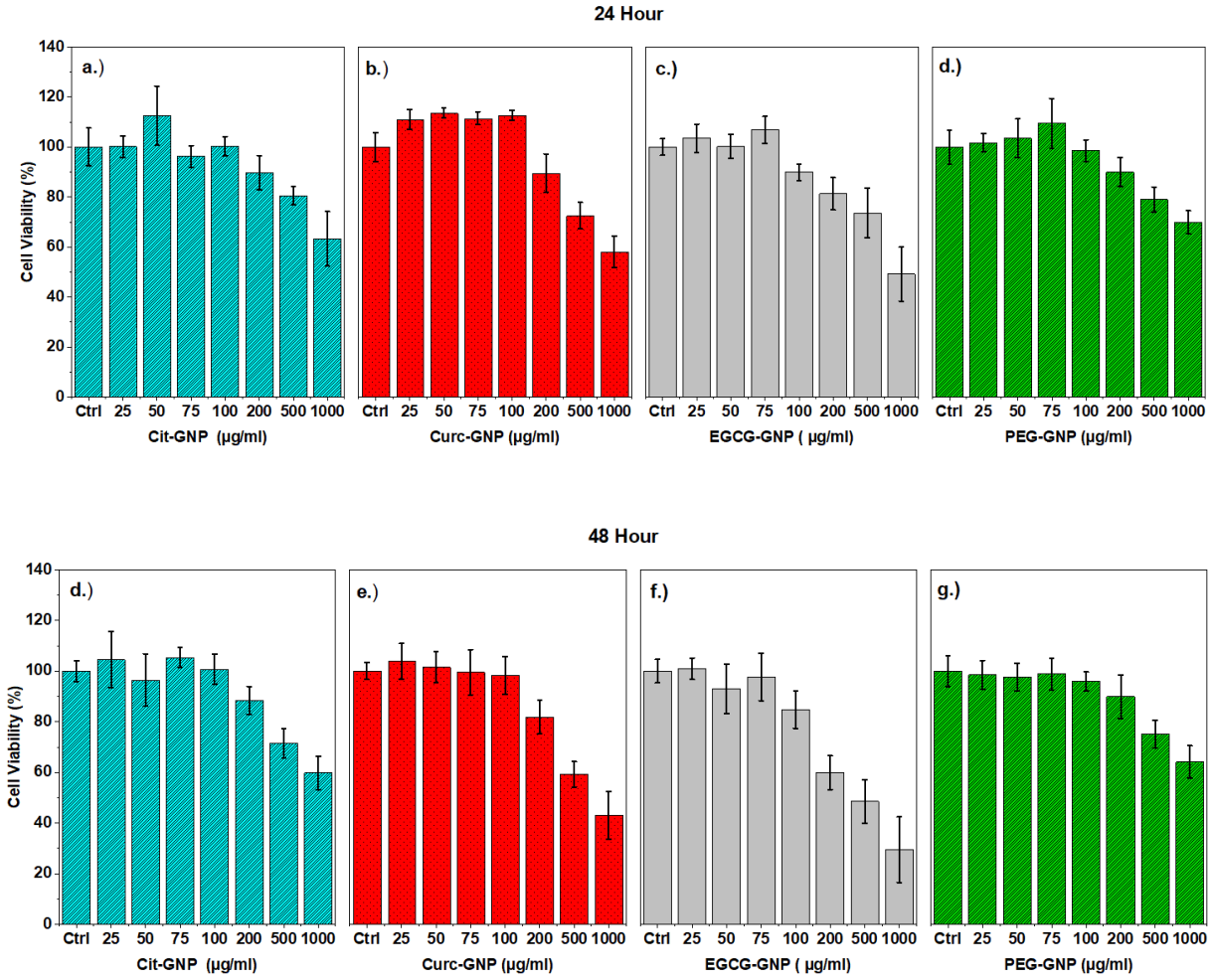


Figure 3.2: Cytotoxicity graphs demonstrate the relationship between increasing GNP concentration and toxicity. It is clear after 100 μg/mL there is a sharp increase in cytotoxicity regardless of GNP structure.

The trends observed in cytotoxicity highlighted a clear dose-response relationship for EGCG-GNP, Cit-GNP, and PEG-GNP. The concentration of GNP had a profound effect on cytotoxicity ($p < 0.01$), as cell viability consistently declined with increasing concentrations across these coatings. However, Curc-GNPs demonstrated a unique bi-phasic relationship, with cell viability remaining relatively higher across the 0 to 100 μg/mL range (for example, 112.75% at 100 μg/mL after 24 hours), but then viability decreased sharply between 100 μg/mL and 1000 μg/mL, dropping to 89.48% ($p < 0.05$) at 200 μg/mL, 72.58% ($p < 0.01$) at 500 μg/mL, and 58.06% ($p < 0.001$) at 1000 μg/mL (Figure 3.3 b). The type of GNP coating played a pivotal role in cytotoxicity, with EGCG-coated GNPs exhibiting the strongest cytotoxic effects, particularly at higher concentrations and extended time points. EGCG-GNP exhibited the highest cytotoxicity at concentrations above 100 μg/mL, particularly at 1000 μg/mL, where cell viability declined dramatically over time. At this concentration, viability decreased to 49.2% ($p < 0.01$) at 24 hours, 29.41% ($p < 0.01$) at 48 hours, and 16.93% ($p < 0.001$) at 72 hours, highlighting its potential as a potent

cytotoxic agent (Figure 3.3 d, g, i). These findings suggest that while PEG-GNP could serve as a safer platform for drug delivery due to its stability and inertness, EGCG-GNP may hold greater cytotoxic effects against PC-3 cells. Curc-GNP offers a unique dose-response relationship, with cytotoxicity sharply increasing above 100 μg/mL but remaining close to or above control cells at lower doses. The biphasic dose-response relationship to cells is not uncommon for phytochemical or plant-based molecules, as literature reports many phytochemicals exhibiting a hormetic effect on cells due to their antioxidant and ROS-quenching properties that can protect cells at low doses [13].



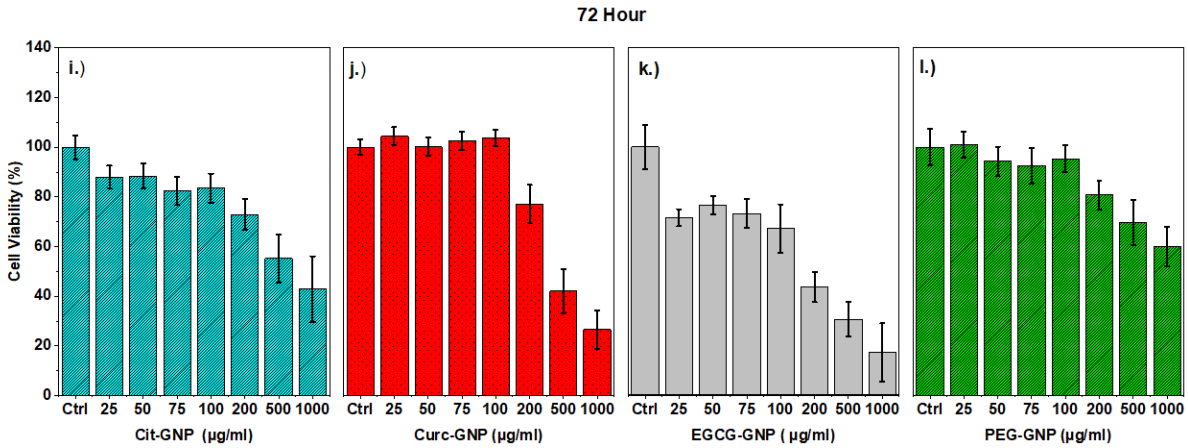


Figure 3.3: Cell viability graphs for all 4 typers of GNP structures ranging from 0-1000 μg/mL. Across all groups the highest cytotoxicity was reported for 1000 μg/mL GNP concentrations.

If we look at the literature, we see comparable results. Chavva *et al.* conducted a cytotoxicity assay using the WST-1 assay to evaluate EGCG-GNPs compared to Cit-GNPs in PC-3 prostate cancer cells [14]. EGCG-GNPs showed significantly higher cytotoxicity across all tested concentrations. For example, at 50 μg/mL, EGCG-GNPs reduced cell viability to 48%, compared to approximately 75% viability for Cit-GNPs after 96 hours. The IC50 (50% growth inhibition) for EGCG-GNPs was determined to be 24.9 μg/mL, while Cit-GNPs had a growth inhibition of only 2.9% at this same concentration, highlighting the superior antitumor efficacy of EGCG-GNPs. The authors reported the enhanced cytotoxicity was attributed to increased suppression of NF-κB activity, with a 65.5% reduction for EGCG-GNPs compared to 7.7% for Cit-GNPs [14].

The literature data on Curc-GNP is also similar to our findings. Nambiar *et al.* conducted a cytotoxicity study on Curc-GNPs with and without serum-supplemented medium using the MTT assay [15]. The size of the Curc-GNPs was 15 nm (core size), with a hydrodynamic size of 21.5 nm in water. The concentrations used were 14, 28, 56, 140, and 280 μg/mL, and the time points were 24 and 48 hours. In serum-free medium, cell viability dropped significantly, whereas in serum-supplemented medium, Curc-GNP-treated cells maintained very high viability even at the upper concentration ranges of 140 μg/mL and 280 μg/mL. After 48 hours, cell viability was reported to be 81 $\pm$ 6% for 140 μg/mL and 83 $\pm$ 7% for 280 μg/mL, relative to the positive control.

Soares *et al.* studied the cytotoxicity of different shaped PEG-GNPs (spherical, star-shaped, and rod-shaped) on prostate cancer cell lines (PC-3, DU145, and LNCaP) [16].

Cytotoxicity was assessed using the PrestoBlue assay at concentrations ranging from 0 to 1 mM after 24 hours of treatment. The size of the spherical GNPs was 146.73 ± 4.24 nm. The study found that at lower concentrations (up to 0.1 mM), all PEG-GNPs exhibited negligible cytotoxicity, maintaining approximately 80% cell viability across all cell lines. However, at the highest concentration tested (1 mM), cell viability decreased slightly, reaching approximately 75 to 80%, with rod-shaped PEG-GNPs (AuNPr-PEG) showing the most pronounced effects. Our findings support the notion that PEGylation can reduce the cytotoxicity of GNPs. Most GNP structures that use PEGylation utilize it for its stability and evasion from opsonin and typically incorporate a therapeutic molecule [16, 17, 18]. In other cases PEGylated GNPs are used in photothermal or imaging applications, so evasion from MPS system and biocompatibility are its main function in these applications [19, 20]. In our case, it is a long chain 6000 PEG coating with maximum coverage, so it is expected that our PEG-GNP will have low interaction and low uptake with PC-3 cells.

In the case of Curc-GNP, our results show that curcumin could be stimulating PC-3 cells at low doses and inducing apoptosis at high doses. This biphasic effect is well documented in literature for free curcumin [21, 22, 23]. For example, MDA-MB breast cancer cells exhibited increased glutathione (GSH) levels (138% $p<0.01$) at low curcumin concentrations, but strong inhibition (-56% $p<0.01$) at concentrations above 25 μg/mL [22]. Vashisht *et al.* treated buffalo granulosa cells with various concentrations of curcumin- loaded exosomes and observed increased expression of cell proliferation markers and anti-inflammatory signals at low concentrations (3.7 to 7.4 μg/mL) [21]. These included a reduction in pro-inflammatory cytokines such as IL-1β, IL-6, and TNF-α. Although these examples do not utilize GNP structures, the findings overlap greatly with our data, and based on the curcumin values calculated from the previous chapter (20.8 wt%), a 100 μg/mL GNP concentration correlates to 20.8 μg/mL of curcumin, which is in line with the concentrations used in these studies. We postulate that threshold-dependent events may determine whether curcumin acts protectively via antioxidant effects or triggers apoptosis. For example, the activation of caspase cascades or the loss of mitochondrial membrane potential may serve as critical thresholds that shift the cellular response from survival to cell death. Future work should examine cell signaling and gene expression to better understand the biphasic effects of Curc-GNPs on PC-3 cells.

3.4.2 Cellular Uptake

The uptake of GNPs was measured using ICP-MS, where PC-3 cells were exposed to two GNP concentrations (50 μg/mL and 100 μg/mL), two incubation periods (10 hours and 24 hours), three GNP surface coatings (EGCG-GNP, Curc-GNP, and Cit-GNP), and varying

medium serum conditions (serum supplemented and non-serum supplemented). Figure 3.4 displays the average Au pg uptake per cell for each study group. In all experiments, there was a clear dose dependent relationship between GNP uptake and incubation time ($p < 0.001$). Longer incubation times (24 hours) resulted in significantly higher uptake compared to shorter incubation times (10 hours), consistent across all GNP coatings and medium conditions.

There was also a linear relationship between GNP concentration and cellular uptake, with higher concentrations (100 μg/mL) leading to increased uptake compared to lower concentrations (50 μg/mL). This trend was statistically significant for all GNP coatings in both serum supplemented and non serum supplemented conditions ($p < 0.01$).

In terms of the effect of serum supplementation, lower GNP uptake was reported across all GNP surfaces and incubation times. This observation was most pronounced for Curc-GNPs after 24 hours, where cellular uptake of GNPs in non-serum supplemented medium was reported as 72.38 pg/cell, compared to 20.59 pg/cell in serum supplemented medium. This corresponds to a 3.52-fold increase in uptake for non-serum conditions ($p < 0.05$), suggesting that the absence of serum proteins may enhance nanoparticle cell interactions by preventing protein corona formation. EGCG-GNP also showed a large increase of 3.24 fold ($p < 0.05$), while Cit-GNP showed a smaller 1.97 fold ($p < 0.05$) increase between 24 hour serum supplemented and non-supplemented conditions.

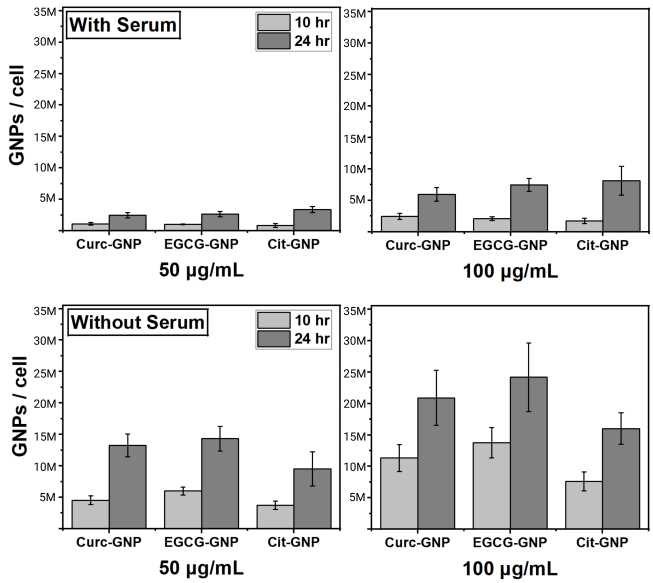


Figure 3.4: GNP uptake metrics between EGCG/CIT/Curc GNP coated NPs in millions(M)

Although pairwise comparisons ($p > 0.05$) indicated no strong correlation between the type of GNP coating and uptake in PC-3 cells under serum supplemented conditions, there was a significant difference for EGCG-GNP in the non-serum supplemented group compared to other coatings ($p < 0.05$). For example, the uptake for EGCG-GNP was 83.69 pg/cell, compared to 55.39 pg/cell for Cit-GNP and 72.38 pg/cell for Curc-GNP.

These findings demonstrate that non-serum conditions and longer incubation times optimize GNP uptake, with EGCG-GNP showing the highest overall uptake efficiency under these conditions. Our findings suggest that surface chemistry plays a critical role in cellular internalization, particularly when protein adherence from serum is reduced. It is also evident that EGCG's unique surface properties likely enhance its interaction with cell membranes.

Literature contains many studies on EGCG binding mechanisms with cell membranes and especially uptake in cancer cells [8,23]. This has been particularly studied in EGCG coated nanoparticles, showing higher uptake in prostate cancer cells. One of the main pioneers in this field is the Katti research group from the University of Missouri. Their study, titled "Laminin Receptor Specific Therapeutic Gold Nanoparticles Show Efficacy in Treating Prostate Cancer," was the first to demonstrate strong uptake of EGCG-GNPs in PC-3 cells and to identify Laminin67r as the membrane protein responsible for this interaction [24]. In a separate study, Chavva *et al.* investigated EGCG-GNP uptake and also found that these nanoparticles exhibited significantly higher internalization in cancer cells compared to normal cells [14]. After 24 hours of incubation, EGCG-GNPs demonstrated an uptake of 69.3% in PC-3 cells and 70.9% in MDA MB 231 cells, whereas non-cancerous cells RWPE1 and MCF 10A exhibited much lower uptake rates of 6.6% and 7.0%, respectively. In contrast, conventional Cit-GNPs showed slower and less efficient uptake, with a maximum internalization range of only 15.4% to 20.1% across all cell types after 24 hours. Furthermore, EGCG-GNP uptake by cancer cells was rapid, with over 50% internalized within the first 3 hours. Their study also revealed that the enhanced uptake of EGCG-GNPs in cancer cells was mediated by their binding to laminin receptors. Blocking the laminin receptors significantly reduced EGCG-GNP uptake in cancer cells especially prostate cancer cells, further supporting the role of receptor mediated mechanisms in selective nanoparticle internalization. It should be noted that the authors in this study used serum supplemented medium and still attained these results unlike our study. The correlation between surface coating and uptake in our experiment did not show strong links for 10 or 24 hour uptake in FBS supplemented medium. However, we observed a strong trend of increased EGCG-GNP uptake in the non-supplemented medium group. This could possibly be due to a variation in the extent of protein adherence to our GNP compared to those previously reported. It is evident that our EGCG-GNP structures had a high degree

of protein adherence that was effectively blocking the interaction between the EGCG and laminin receptors. GNP uptake across all GNP structures in the serum supplemented group was similar and within the margin of variance.

If we look at literature exploring other factors involved in GNP uptake, a very impactful study was conducted by Bilgi *et al.*, who created a machine learning model to predict cellular uptake of GNPs [25]. They identified key determinants of uptake with high accuracy. Using a dataset of 2,077 data points from 193 nanoparticles across 59 studies, the ensemble learning model was able to identify trends and predict uptake of GNPs. The study found that GNP concentration was the most significant factor influencing uptake, with a positive correlation between concentration and cellular internalization. Exposure duration also played a critical role, though prolonged exposure beyond 24 hours often showed no additional benefit, with saturation observed in some cell lines. GNP size was another important predictor, with particles under 90 nm demonstrating increased uptake, though this relationship plateaued for larger nanoparticles. Surface charge strongly influenced cellular adhesion and uptake, with positively charged particles typically showing higher interaction with negatively charged cell membranes. Surface coatings further modulated uptake, with functionalized GNPs such as EGCG, PVA, DMSA, and thiol enhancing internalization, while albumin coatings reduced uptake. Albumin is the highest protein component of our FBS component in the RPMI medium which could explain the drastically lower uptake concentrations in the serum supplemented studies. Shape effects revealed that spherical GNPs had high uptake efficiency compared to other geometries, though gold nanoshells achieved the highest uptake levels. These findings underscore the complex interplay of GNP properties and highlight the utility of machine learning in modeling and optimizing nanoparticle behavior in biological systems.

It is also noteworthy that Curc-GNP demonstrated uptake comparable to the levels to EGCG-GNP in our studies and significantly higher than Cit-GNP; however, very little literature was found specifically exploring the topic of Curcumin increasing cellular targeting or uptake. Some studies highlight curcumin's lipophilicity, which enhances its ability to integrate with lipid-rich cell membranes [26, 27]. Additionally, literature suggests that curcumin can bind to multiple cellular targets, such as heat shock proteins, cytoskeletal proteins, and NF-κB-related pathways. These interactions may contribute to Curc-GNP's enhanced ability to interact with cancer cells however, this needs further verification [28, 29, 30].

3.4.3 Clonogenic Assay

The analysis of EGCG-GNP's radiosensitizing effects demonstrated a clear dose-dependent enhancement in both SER and radiation-induced cell death. The D_{50} decreased with increasing GNP concentration, from 2.479 Gy at 25 μg/mL to 1.259 Gy at 500 μg/mL. This trend indicates that higher concentrations of EGCG-GNP significantly reduce the radiation dose required to achieve comparable therapeutic outcomes. The SER followed a similar pattern, increasing from 0.993 at 25 μg/mL to 1.995 at 500 μg/mL, confirming the nanoparticle's role as an effective radiosensitizer at higher doses.

The Linear Quadratic (LQ) model parameters, α and β, provided further insight into the biological mechanisms underlying EGCG-GNP's effects (Table 3.1). The α parameter, which represents the linear, dose dependent component of cell killing due to single track DNA damage, increased consistently with GNP concentration, from 0.1 at 0 μg/mL to 0.25 at 200 μg/mL. Single track damage refers to DNA damage caused by a single ionizing radiation event that is sufficient to kill a cell, such as a double strand break from one radiation track [31]. In contrast, double track damage refers to DNA damage that results from the interaction of two separate radiation tracks, where two independent events combine to produce a lethal lesion, often through the accumulation of sublethal damage [31]. Our study suggests that EGCG-GNP enhances the direct, radiation-induced damage to DNA as its concentration increases (Figure 3.5). The β parameter, reflecting the quadratic component associated with double-track DNA damage and complex lesion repair, also increased slightly with GNP concentration, but to a lesser extent. The higher α/β ratio observed at higher GNP concentrations indicates that the primary mode of cell killing shifts toward more linear, direct DNA damage as EGCG-GNP concentration increases, amplifying the radiosensitizing effect.

The effects of EGCG-GNP and Curc-GNP on the proliferation potential of PC-3 cells were evaluated under varying GNP concentrations and radiation doses (0, 2, 4, and 6 Gy). The goal of this in vitro study was to measure the radiosensitizing potential of green coated GNPs when introduced to PC-3 cell cultures. Figures 3.6 and 3.8 display the purple stained colonies for each treatment group, revealing distinct trends in cell proliferation. The colony images show a pronounced decrease in colony formation with increasing GNP concentration and radiation dose. This decrease was more evident left to right (increasing GNP concentration) than top to bottom (increasing radiation dose). Additionally, a change in colony morphology was observed with increasing radiation doses, where colonies at 0 Gy were large and circular, while colonies at 6 Gy were smaller, irregularly shaped, or reduced to faint specks. Notably, no significant changes in colony size or shape were reported with increasing GNP concentration alone.

The α constants for Curc-GNP were consistently higher than those for EGCG-GNP, ranging from 0.173 at 0 μg/mL to 0.579 at 500 μg/mL, compared to 0.103 at 0 μg/mL to 0.499 at 500 μg/mL for EGCG-GNP. In contrast, the β constants were higher for EGCG-GNP (0.072 to 0.041) than for Curc-GNP (0.04 to 0.032). These values suggest that EGCG-GNP is causing higher indirect DNA damage leading to apoptosis than Curc-GNP.

Interestingly, at 25 μg/mL, both EGCG-GNP and Curc-GNP showed a slight reduction in radiosensitization, with SER values of 0.993 and 0.979, respectively. This corresponds to a decrease of 0.7% and 2.1% in radiosensitization, possibly reflecting a transient radioprotective effect at low concentrations, consistent with findings from XTT cytotoxicity assays. Survival curves further demonstrate this trend, where cell survival at 25 μg/mL is equal to or slightly greater than in the non-radiation-treated cells.

At higher concentrations, both GNPs showed significant increases in sensitization. Expressing SER as a percentage increase over radiation alone, EGCG-GNP enhanced radiation damage by approximately 14% at 50 μg/mL, 20% at 100 μg/mL, 40% at 200 μg/mL, and 96% at 500 μg/mL. Similarly, Curc-GNP improved radiation damage by 10% at 50 μg/mL, 26% at 100 μg/mL, 32% at 200 μg/mL, and 82% at 500 μg/mL. These findings underscore the potential of green-coated GNPs as highly effective radiosensitizers, particularly at higher concentrations, where they significantly amplify the therapeutic impact of radiation treatment.

Table 3.1: *EGCG Radiosensitization:* Linear-quadratic model values (α and β), median lethal dose (D_{50}), sensitization enhancement ratio (SER), and α/β ratio for EGCG-GNP–treated PC-3 cells across increasing concentrations (0–500 μg/mL).

Concentration	α	β	D_{50}	SER	α/β
0 μg/ml	0.103	0.072	2.461	1.000	1.431
25 μg/ml	0.100	0.073	2.479	0.993	1.370
50 μg/ml	0.186	0.062	2.161	1.139	3.000
100 μg/ml	0.190	0.073	2.046	1.202	2.602
200 μg/ml	0.253	0.080	1.759	1.399	3.163
500 μg/ml	0.499	0.041	1.259	1.955	12.170

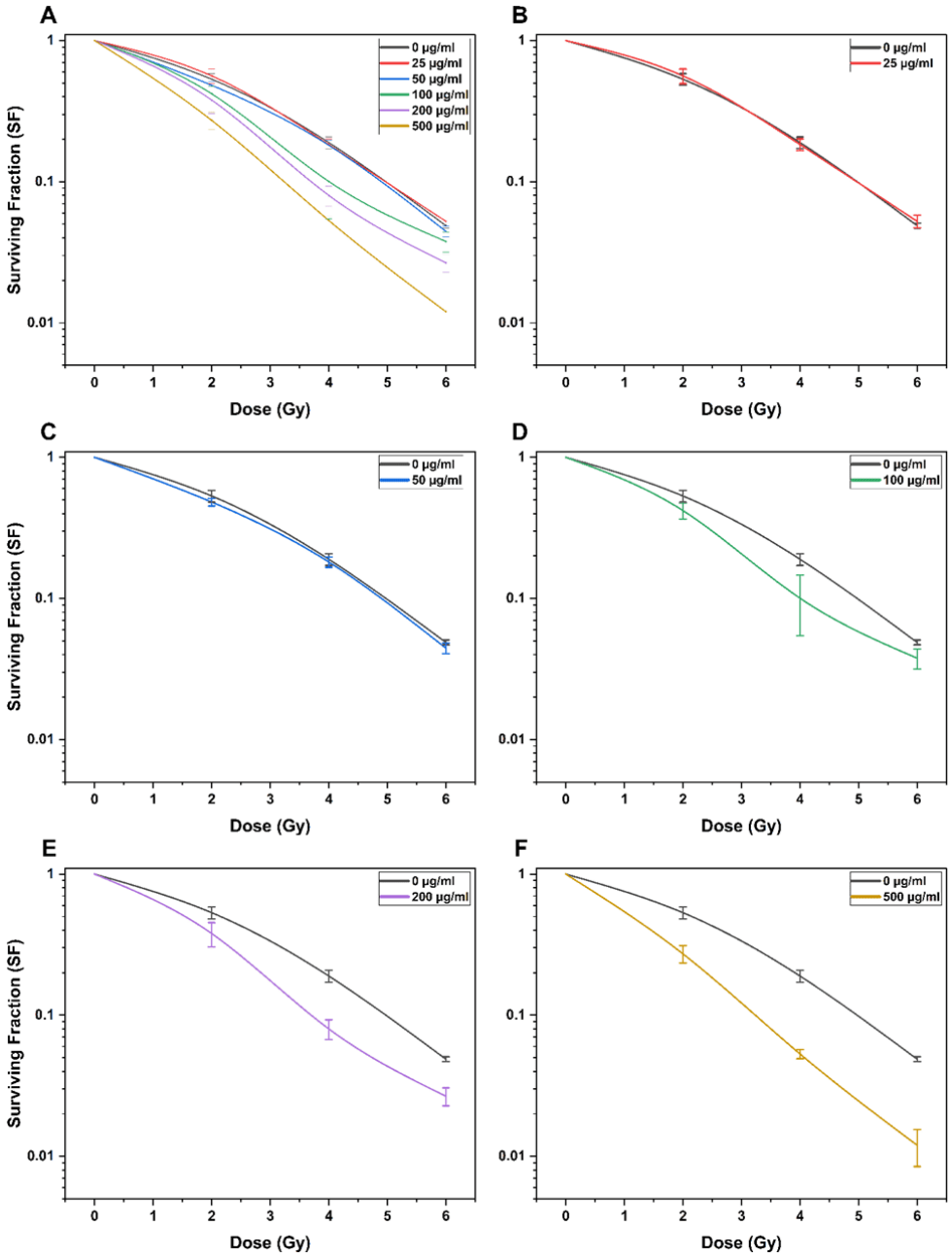


Figure 3.5: The cell survival curves illustrate the changes in surviving fraction due to the presence of GNPs. The greater the separation between the black line (control) and the colored lines (treatment), the higher the SER. Graph (F) shows a significant gap, corresponding to the 500 μg/mL concentration.

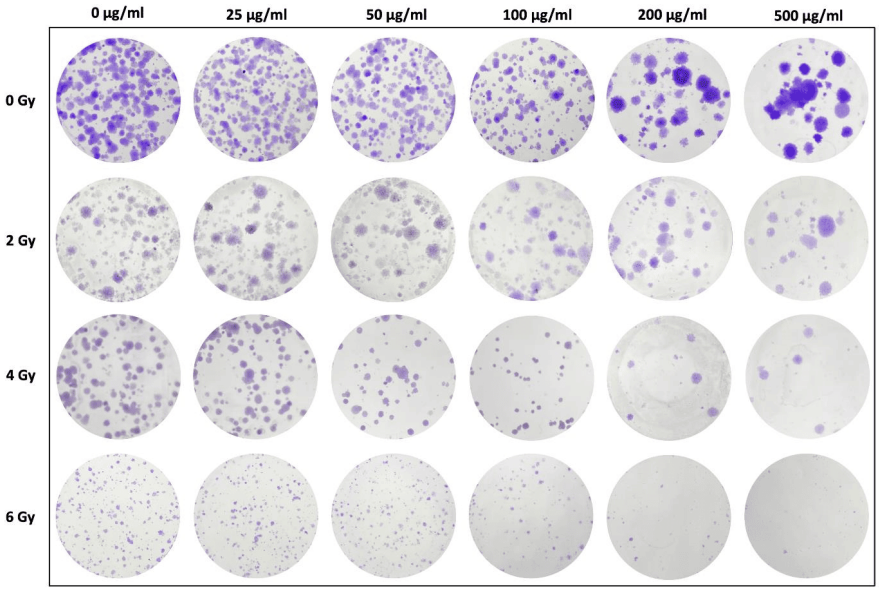


Figure 3.6: The image illustrates the clonogenic assay results with EGCG-GNP (0-500 μg/mL) concentrations increasing left-right and radiation doses increasing top to bottom (0-6 Gy).

The analysis of CURC-GNP's radiosensitizing effects revealed trends similar to those observed with EGCG- GNP (Table 3.2). There was a dose dependent reduction in D_{50} and an increase in SER across GNP concentrations. The D_{50} decreased from 2.05 Gy at 0 μg/mL to 1.127 Gy at 500 μg/mL, indicating a significant reduction in the radiation dose required to achieve 50% cell survival. The SER increased from 1.00 at 0 μg/mL to 1.82 at 500 μg/mL, highlighting the concentration dependent radiosensitizing potential of Curc-GNP.

The α parameter, representing the linear single track DNA damage component, increased from 0.24 at 25 μg/mL to 0.34 at 200 μg/mL, reflecting an enhanced direct damage effect as Curc-GNP concentration increased. The β parameter, associated with the quadratic double track DNA damage component, showed a slight increase from 0.04 at 25 μg/mL to 0.068 at 200 μg/mL but decreased to 0.032 at 500 μg/mL, suggesting a reduction in cumulative dose squared effects at higher concentrations. The α/β ratio increased substantially across concentrations, from 5.454 at 25 μg/mL to 18.093 at 500 μg/mL, indicating a growing predominance of single-track damage with increasing Curc-GNP levels. These results, analyzed using the LQ model, suggest that Curc-GNP enhances both direct and indirect

DNA damage at lower to intermediate concentrations but primarily amplifies linear effects at higher concentrations.

Lastly, Curc-GNP exhibited an SER value below 1 (0.98) at 25 μg/mL, suggesting slightly reduced efficacy at low concentrations compared to the control (Figure 3.7 B). This may be due to insufficient nanoparticle uptake or the antioxidant properties of curcumin, which could transiently scavenge radiation induced reactive oxygen species [21, 22, 23]. Together, these findings highlight Curc-GNP's potential as a concentration dependent radiosensitizer, with pronounced effects on linear damage pathways.

Table 3.2: *Curc-GNP Radiosensitization:* Linear-quadratic model values (α and β), median lethal dose (D_{50}), sensitization enhancement ratio (SER), and α/β ratio for Curc-GNP–treated PC-3 cells across increasing concentrations (0–500 μg/mL).

Concentration	α	β	D_{50}	SER	α/β
0 μg/ml	0.173	0.040	2.050	1.000	4.325
25 μg/ml	0.240	0.044	2.094	0.979	5.455
50 μg/ml	0.311	0.032	1.870	1.097	9.719
100 μg/ml	0.343	0.052	1.623	1.263	6.596
200 μg/ml	0.341	0.068	1.554	1.319	5.014
500 μg/ml	0.579	0.032	1.127	1.820	18.093

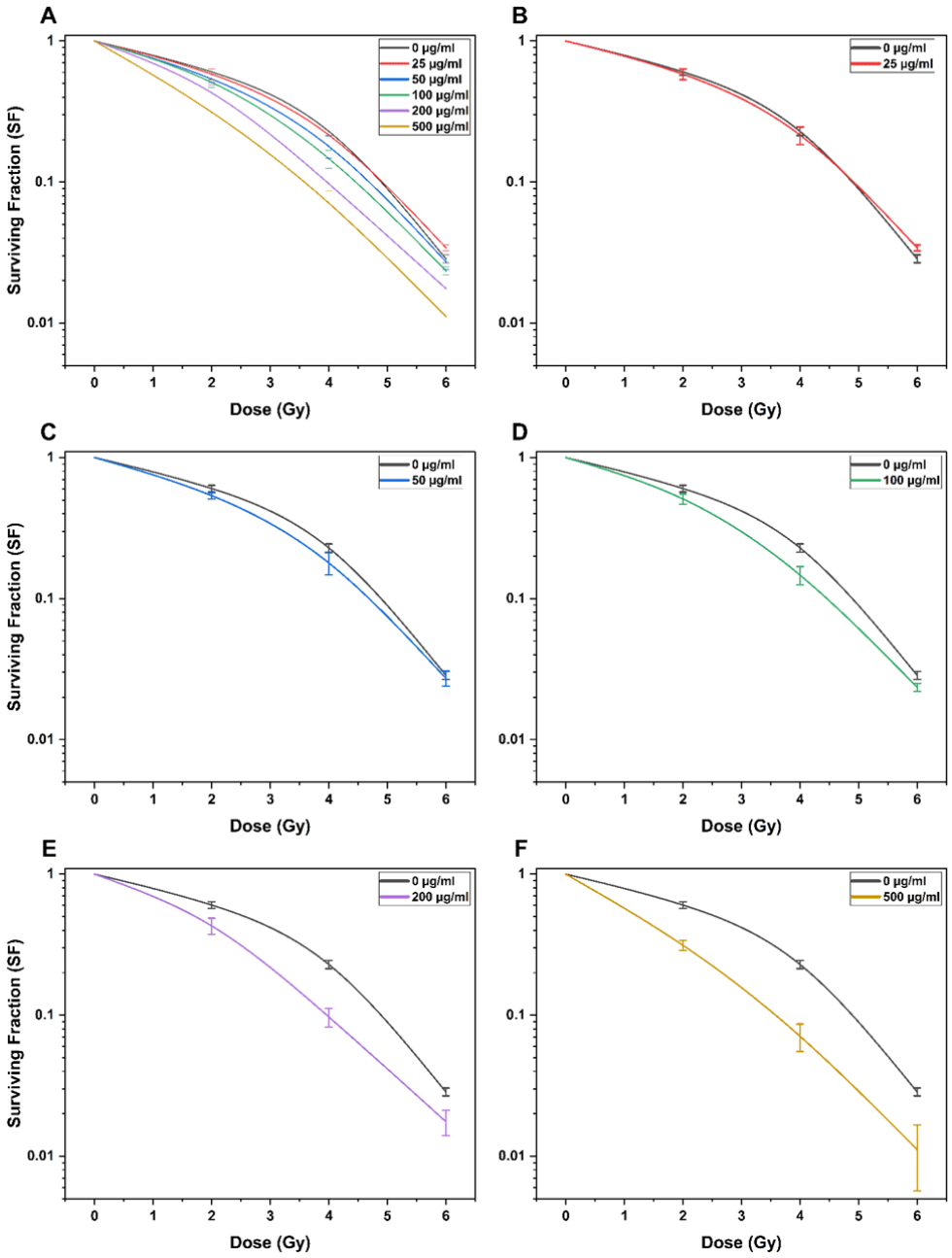


Figure 3.7: The cell survival curves illustrate the changes in surviving fraction due to the presence of GNPs. The greater the separation between the black line (control) and the colored lines (treatment), the higher the SER. Graph (B) shows overlap between lines signifying low SER.

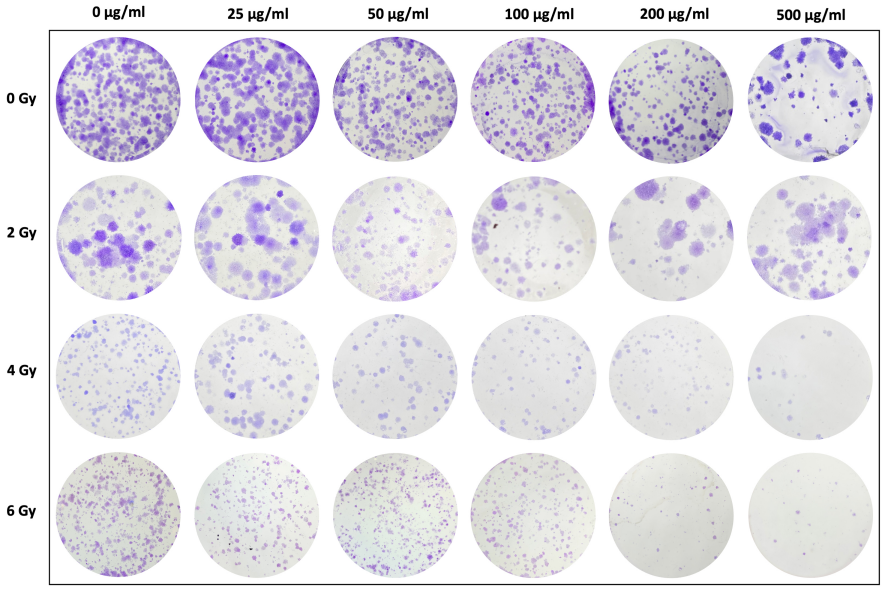


Figure 3.8: The image illustrates the clonogenic assay results with Curc-GNP (0-500 μg/mL) concentrations increasing left-right and radiation doses increasing top to bottom (0-6 Gy).

There have been various radiosensitization studies that have demonstrated the radio-enhancing effects of GNPs in prostate cancer [12, 32, 33, 34]. Zhang *et al.* from the University of Alberta demonstrated that glucose-coated gold nanoparticles (Glu-GNPs) at a concentration of 15 nM significantly enhance radiosensitivity in DU-145 prostate cancer cells [12]. Their results showed a 3-fold increase in nanoparticle uptake compared to neutral Cit-GNPs and a combination of Glu-GNPs with 2 Gy X-ray radiation led to a 45.97% inhibition in cell growth after 24 hours, compared to 15.88% with radiation alone. The inhibition by Cit-GNPs combined with 2 Gy X-ray radiation was 30.57% after 24 hours. Their use of the MTT assay, which primarily measures metabolic activity rather than clonogenic survival, limits direct comparison with our study, where clonogenic assays provided a more precise evaluation of radiation induced damage. [12]

Jain *et al.* investigated the cell-specific radiosensitizing effects of 1.9 nm GNPs at both kilovoltage (kV) and megavoltage (MV) photon energies, focusing on breast cancer (MDA-MB-231), prostate cancer (DU145), and normal lung epithelial (L132) cells [32]. The GNPs were used at a concentration of 12 μM (equivalent to 2.364 μg/mL). Their findings showed significant radiosensitization in MDA-MB-231 cells, with SER of 1.41 for 160 kVp X-rays, 1.29 for 6 MV photons, and 1.16 for 15 MV photons [32]. However, no significant

radiosensitization was observed in DU145 or L132 cells despite measurable GNP uptake in all cell lines. This was possibly due to the low GNP concentration used in their experiment. In contrast, our study utilized higher GNP concentrations of 25–500 μg/mL, which likely facilitated greater cellular uptake and interaction with radiation-induced damage pathways.

Shahhoseini *et al.* demonstrated the radiosensitizing potential of 15 nm spherical GNPs at a concentration of 1 mM (equivalent to 197 μg/mL) in prostate DU145 and lung A549 cancer cells [33]. The study showed that while GNPs alone were non-cytotoxic, their combination with 5 Gy X-ray irradiation resulted in an SER of 1.15. The GNP surface was not disclosed in the paper or supplementary file; the only description of the coating was "highly water-soluble thiol-based ligand" which hints that it may have been PEGylated GNPs used in this study.

Lastly, Tremi *et al.* conducted clonogenic assays in their study and reported significant radiosensitization effects of GNPs in PC-3 cancer cells, with PEG-GNPs (5 nm) at 100 μg/mL achieving a SER of 2.10 at 4 Gy [34]. The study emphasized the role of cellular localization, noting that nanoparticles distributed near the nucleus and within cytoplasmic structures contributed to enhanced DNA damage and impaired repair mechanisms. The findings of Tremi *et al.* provide the closest methodological parallel to our study, as they used clonogenic assays, comparable X-ray doses, and nanoparticle concentrations (up to 100 μg/mL) in PC-3 cells. However, their report of a maximum SER of 2.10 with PEG-GNPs at 100 μg/mL is considerably higher than our findings at similar concentrations, where EGCG-GNP and Curc-GNP achieved SER values of 1.202 and 1.263, respectively. This could be attributed to their use of 5 nm nanoparticles, which are more likely to localize within the nucleus. Nuclear uptake enhances radiosensitization due to proximity to DNA, as Auger electrons have a path length of only a few nanometers and can cause highly localized, severe DNA damage.

3.5 Conclusion

This study aimed to evaluate the in-vitro effects of green-coated GNPs, specifically EGCG-GNPs and Curc-GNPs, on prostate cancer PC-3 cells, comparing them with conventional GNPs, Cit-GNPs and PEG-GNPs. The results highlight the potential of these nanoparticles as effective radiosensitizers and their broader biological implications through a combination of cytotoxicity studies, cellular uptake analyses, and clonogenic assays. Key findings suggest that both EGCG-GNP and Curc-GNP demonstrate dose-dependent radiosensitization, with significant enhancements in SER and reductions in the radiation dose (D_{50}) required for therapeutic outcomes.

At 24 hours in serum-free conditions, the uptake of 100 μg/mL EGCG-GNP by PC-3 cells was 1.51-fold higher than Cit-GNP, highlighting the superior internalization efficiency of EGCG-GNP. At this concentration, EGCG-GNP achieved an SER of 1.202, while Curc-GNP achieved an SER of 1.263. EGCG-GNP demonstrated the highest radiosensitization effects overall, with an SER increasing up to 1.955 at 500 μg/mL. Its higher cytotoxicity, particularly at low concentrations, highlights its efficacy in inhibiting PC-3 cell viability. Conversely, Curc-GNP showed comparable radiosensitization potential, with an SER of 1.82 at 500 μg/mL, but exhibited lower cytotoxicity at equivalent concentrations according to XTT. Additionally, its potentially proliferative nature at low doses requires further investigation on identifying the dosing-window as we don't want to risk increasing cancer cell proliferation in vivo.

The implications of these findings are significant for designing GNP-based treatments in radiotherapy. Both EGCG-GNP and Curc-GNP enhanced radiation-induced damage in PC-3 cells, establishing a strong foundation for in vivo studies where dosage and surface coating can be further optimized to refine the therapeutic window.

While this study provides important insights into GNP effects on prostate cancer cells, several limitations merit consideration. First, the PEG-GNPs used were larger (45–70 nm) than the 15–25 nm range of other coatings, complicating direct comparisons. Future studies should use PEG-GNPs synthesized with lower molecular weight PEG (<6000 Da) to better evaluate cytotoxicity, antioxidant activity, and uptake. Additionally, although this study confirmed GNP uptake in PC-3 cells, it did not examine intracellular localization. As Jain *et al.* noted, nuclear-localized GNPs significantly enhance radiation-induced cell death, highlighting this as a critical avenue for further investigation [32]. Subcellular localization using fluorescence microscopy and flow cytometry could clarify how EGCG-GNP and Curc-GNP interact with organelles to enhance radiation effects.

The XTT assay was effective for assessing cytotoxicity but has limitations when comparing metabolic activity across nanoparticles with different physicochemical properties. Complementary methods such as impedance-based assays or apoptosis-specific assays may provide more mechanistic insight. Investigating cytokine responses and gene expression could also enhance understanding of the anticancer effects of GNPs.

References

[1] Catherine Carnovale et al. "Identifying trends in gold nanoparticle toxicity and uptake: size, shape, capping ligand, and biological corona". In: *ACS omega* 4.1 (2019), pp. 242–256.

[2] A Sani, C Cao, and D Cui. "Toxicity of gold nanoparticles (AuNPs): A review". In: *Biochemistry and biophysics reports* 26 (2021), p. 100991.

[3] Roche Diagnostics GmbH. *Cell Proliferation Kit II (XTT) - Product information sheet (Version 19)*. Roche. Retrieved from https://www.sigmaaldrich.com. 2021.

[4] Michael V Berridge, Patries M Herst, and An S Tan. "Tetrazolium dyes as tools in cell biology: new insights into their cellular reduction". In: *Biotechnology annual review* 11 (2005), pp. 127–152.

[5] Nicole A Schneck et al. "Current trends in magnetic particle enrichment for mass spectrometry-based analysis of cardiovascular protein biomarkers". In: *Nanomedicine* 10.3 (2015), pp. 433–446.

[6] Karl T. Butterworth et al. "A Mechanistic Overview of Gold Nanoparticle Radiosensitization: Is It All about DNA?" In: *Nanomedicine* 9.17 (2014), pp. 257–265.

[7] Laura E. Taggart et al. "The Role of Gold Nanoparticle Shape and Size in Radiosensitization of Cancer Cells". In: *Scientific Reports* 7 (2017), p. 40685.

[8] Ana Espinosa et al. "Impact of Gold Nanoparticle Size and Coating on Radiosensitization Mechanisms under Ionizing Radiation". In: *Nanoscale Advances* 6.5 (2025), pp. 1234–1247.

[9] M. Kumazoe et al. "Green Tea Polyphenol Epigallocatechin-3-gallate Inhibits the Growth and Metastasis of Human Prostate Cancer by Targeting the 67-kDa Laminin Receptor". In: *Cancer Letters* 261.2 (2008), pp. 227–234.

[10] Nicolaas AP Franken et al. "Clonogenic assay of cells in vitro". In: *Nature protocols* 1.5 (2006), pp. 2315–2319.

[11] Terry L Riss et al. "Cell viability assays". In: Eli Lilly & Company and the National Center for Advancing Translational Sciences, 2016.

[12] Xiaojing Zhang et al. "Enhanced radiation sensitivity in prostate cancer by gold-nanoparticles". In: *Clinical and Investigative Medicine* 31.3 (2008), E160–E167.

[13] Vittorio Calabrese et al. "Cellular stress responses, hormetic phytochemicals and vitagenes in aging and longevity". In: *Biochimica et Biophysica Acta (BBA)-Molecular Basis of Disease* 1822.5 (2012), pp. 753–783.

[14] X. Y. Su et al. "Enhancement of Radiosensitization by Metal-Based Nanoparticles in Cancer Radiation Therapy". In: *Cancer Biology & Medicine* 11.2 (2014), pp. 86–91.

[15] Suhash Reddy Chavva et al. "Epigallocatechin gallate-gold nanoparticles exhibit superior antitumor activity compared to conventional gold nanoparticles: potential synergistic interactions". In: *Nanomaterials* 9.3 (2019), p. 396.

[16] Shruti Nambiar et al. "Synthesis of curcumin-functionalized gold nanoparticles and cytotoxicity studies in human prostate cancer cell line". In: *Applied Nanoscience* 8 (2018), pp. 347–357.

[17] Sílvia Soares et al. "Metabolic disruption of gold nanospheres, nanostars and nanorods in human metastatic prostate cancer cells". In: *Cells* 12.5 (2023), p. 787.

[18] Steven K. Libutti et al. "Phase I and Pharmacokinetic Studies of CYT-6091, a Novel PEGylated Colloidal Gold–Tumor Necrosis Factor-α Nanomedicine". In: *Clinical Cancer Research* 16.24 (2010), pp. 6139–6149.

[19] Magdalena Kalinowska and et al. "Pegylated Gold Nanoparticles Conjugated with siRNA: Complexes with Improved Biophysical Properties and Biological Safety for Potential Use in Neurodegenerative Diseases". In: *International Journal of Nanomedicine* 18 (2023), pp. 2057–2073.

[20] J. M. Stern et al. "First-in-Human Evaluation of the Safety and Efficacy of AuroLase® Therapy for Ablation of Low- to Intermediate-Risk Prostate Cancer". In: *Proceedings of the National Academy of Sciences* 113.28 (2016), pp. 7760–7765.

[21] JF Hainfeld et al. "Gold nanoparticles: a new X-ray contrast agent". In: *The British journal of radiology* 79.939 (2006), pp. 248–253.

[22] Monika Vashisht et al. "Curcumin primed exosomes reverses LPS-induced pro-inflammatory gene expression in buffalo granulosa cells". In: *Journal of cellular biochemistry* 119.2 (2018), pp. 1488–1500.

[23] Mathilde Bayet-Robert and Daniel Morvan. "Metabolomics reveals metabolic targets and biphasic responses in breast cancer cells treated by curcumin alone and in association with docetaxel". In: *PloS one* 8.3 (2013), e57971.

[24] Ravi Shukla et al. "Laminin receptor specific therapeutic gold nanoparticles (198AuNP-EGCg) show efficacy in treating prostate cancer". In: *Proceedings of the National Academy of Sciences* 109.31 (2012), pp. 12426–12431. DOI: 10.1073/pnas.1121174109.

[25] V. H. Bilgi et al. "Identifying Factors Controlling Cellular Uptake of Gold Nanoparticles by Data-Driven Modeling". In: *Nano Today* 54 (2024), p. 102047.

[26] Wei-Chin Hung et al. "Membrane-thinning effect of curcumin". In: *Biophysical journal* 94.11 (2008), pp. 4331–4338.

[27] Jeffrey Barry et al. "Determining the effects of lipophilic drugs on membrane structure by solid-state NMR spectroscopy: the case of the antioxidant curcumin". In: *Journal of the American Chemical Society* 131.12 (2009), pp. 4490–4498.

[28] Chiara Giommarelli et al. "The enhancement of antiproliferative and proapoptotic activity of HDAC inhibitors by curcumin is mediated by Hsp90 inhibition". In: *Cellular and molecular life sciences* 67 (2010), pp. 995–1004.

[29] Steven JT Jackson et al. "Curcumin binds tubulin, induces mitotic catastrophe, and impedes normal endothelial cell proliferation". In: *Food and chemical toxicology* 60 (2013), pp. 431–438.

[30] Lan Li et al. "Nuclear factor-κB and IκB kinase are constitutively active in human pancreatic cells, and their down-regulation by curcumin (diferuloylmethane) is associated with the suppression of proliferation and the induction of apoptosis". In: *Cancer: Interdisciplinary International Journal of the American Cancer Society* 101.10 (2004), pp. 2351–2362.

[31] GW Barendsen. "The relationships between RBE and LET for different types of lethal damage in mammalian cells: biophysical and molecular mechanisms". In: *Radiation research* 139.3 (1994), pp. 257–270.

[32] S. Jain, D. G. Hirst, and J. M. O'Sullivan. "Cell-Specific Radiosensitization by Gold Nanoparticles at Megavoltage Radiation Energies". In: *International Journal of Radiation Oncology, Biology, Physics* 79.2 (2011), pp. 531–539.

[33] Elham Shahhoseini et al. "Combined effects of gold nanoparticles and ionizing radiation on human prostate and lung cancer cell migration". In: *International journal of molecular sciences* 20.18 (2019), p. 4488.

[34] Ioanna Tremi et al. "Biological response of human cancer cells to ionizing radiation in combination with gold nanoparticles". In: *Cancers* 14.20 (2022), p. 5086.

Chapter 4

In Vivo Studies

In vivo experimentation is crucial for drug-delivery research, assessing biodistribution, clearance, biocompatibility, immune response, and efficacy in complex biological systems. This study aimed to characterize the in vivo behavior of EGCG- and Curc-capped gold nanoparticles (GNPs) in mice and dogs, and to develop a PBPK model for predicting their pharmacokinetics and interspecies extrapolation. **Methods:** CD1 mice were administered EGCG-GNPs or Curc-GNPs (10 mg Au/kg IP) and monitored for biodistribution and toxicity via ICP-MS, organ weight analysis, and histopathology over 56 days. A PBPK model was developed using mouse data and extrapolated to rats using literature data. Canine pilot studies assessed the feasibility and safety of intra-arterial GNP delivery to the prostate, alone and combined with prostatic arterial embolization (PAE), in healthy beagles and one clinical prostate cancer case. **Results:** In mice, both GNP formulations predominantly accumulated in the liver and spleen, with significant time-dependent clearance from the liver via hepatobiliary excretion, while splenic retention persisted. Minimal renal accumulation was observed. Both EGCG-GNPs and Curc-GNPs demonstrated a favorable toxicity profile in mice, with no abnormal behavior, normal weight gain, and no overt histopathological changes in major organs. The PBPK model accurately predicted GNP biodistribution in mice (Absolute average fold error = 1.48) and successfully extrapolated to rats (AAFE = 2.18) across varying doses and administration routes. Canine studies confirmed the technical feasibility and systemic safety of intra-arterial GNP delivery and PAE in healthy beagles. The clinical case, however, experienced severe adverse events attributed primarily to carboplatin-induced myelosuppression and pre-existing comorbidities, confounding GNP-specific toxicity assessment. **Conclusion:** EGCG-GNPs and Curc-GNPs exhibit favorable biodistribution and toxicity profiles in mice, primarily accumulating in reticuloendothelial organs with significant hepatic clearance. The developed PBPK model effectively predicts

GNP pharmacokinetics and demonstrates interspecies extrapolation utility. While intra-arterial delivery in canines is feasible and safe in healthy subjects, challenges remain in long-term X-ray visualization and distinguishing GNP-specific toxicity in complex clinical settings, necessitating further development of radiotheranostic approaches and refined study designs.

4.1 Introduction

In vivo experimentation is a critical step in drug-delivery research, following in vitro assays. Whereas in vitro tests provide controlled settings to study cellular interactions, in vivo models capture the full complexity of vascular, immune, and metabolic systems that cannot be reproduced in vitro [1]. This realism justifies higher cost and ethical burden, letting researchers validate in vitro findings with biologically relevant data. In nanomedicine, such models assess biodistribution, clearance, biocompatibility, immune response, and efficacy. The immune response, largely governed by the reticuloendothelial system (RES), is a contentious and pivotal topic in nanomedicine. In vivo models allow for the assessment of blood circulation time, organ distribution, routes of clearance, and toxicity, all of which are critical for the development of safe and effective nanodrugs [1]. Such insights are crucial for understanding how GNPs interact with biological systems, including their potential for immune evasion, accumulation in target tissues, and overall therapeutic performance [1].

Among in vivo models, laboratory mice, are widely regarded as essential tools in biomedical research. Described by some as "miniature bioreactors in the palm of your hand," lab mice possess numerous physiological and anatomical similarities to humans, including comparable organ systems and immune pathways [2, 3]. These similarities make them highly suitable for preliminary in vivo studies, particularly for assessing biodistribution and clearance. Lab mice are also advantageous due to their small size, ease of handling, low genetic variance, and cost-effectiveness [3].

In our study, we utilize CD1 mice to investigate the biodistribution, clearance, and toxicity of EGCG-GNP and Curc-GNP formulations. These experiments are foundational for understanding the pharmacokinetics of GNPs and optimizing their design for maximum efficacy and safety. The pharmacokinetic data obtained from these experiments are used to construct a physiologically based pharmacokinetic (PBPK) model for our GNP formulations and we will test its extrapolation to rats.

The next stage of the project was to apply our EGCG-GNPs in canine subjects. The main reason we initially utilize a mouse model and then progress to canine testing is

that, while mice are invaluable for initial studies, their limitations in modeling certain human diseases necessitate the use of larger, more physiologically relevant models [2, 3]. For prostate cancer research, one challenge is the significant anatomical and pathological differences between the human and mouse prostate [3, 4]. For this reason, upon completion of mouse studies, we conducted pilot studies of EGCG-GNPs in laboratory dogs. Canine models provide a critical bridge for translational research, as their prostate is anatomically and histologically similar to the human prostate, including in size, vascularization, and response to hormones [4]. Canines are also one of the few animal species that naturally develop prostate cancer [4]. These similarities make dogs ideal models for studying the efficacy of EGCG-GNPs for prostate cancer. In collaboration with the Waterloo Regional Health Network (WRHN) and the Ontario Veterinary College (OVC), we developed a minimally invasive procedure to deliver nanodrug formulations directly to the prostate through CT-guided microcatheter intra-arterial delivery, that is then followed by prostatic arterial embolization (PAE).

PAE is a minimally invasive procedure primarily used to treat benign prostatic hyperplasia (BPH). BPH is a condition common among older men in which noncancerous enlargement of the prostate gland impinges on the urinary tract, causing difficulty urinating, pain or burning during urination, and discomfort that can disrupt quality of life [5, 6]. It is caused by an overgrowth of cells in the prostate, and although its root cause is not fully understood, hormonal changes as men age are considered a possible factor [6]. PAE addresses BPH by reducing blood flow to the prostate gland, which causes the prostate to shrink. The procedure is conducted by an interventional radiologist who selectively embolizes, or blocks, the main prostatic artery of both prostate lobes using microparticles (Figure 4.1)[5]. Many randomized controlled trials have demonstrated that PAE improves urinary flow, reduces lower urinary tract infections, enhances quality of life, and is safe, with very low rates of severe adverse events reported [7, 8]. The application of embolization beads to prostatic arteries is performed using X-ray angiography, where a microcatheter is guided through the pelvic arteries via a small puncture near the groin [5]. A contrast dye is administered through the catheter to help map the arteries and guide the radiologist to the prostate. Additionally, a vasodilator is applied to facilitate catheter advancement through the arteries. Once the arteries are mapped and the microcatheter reaches the prostate, microspheres (100–500 μm) are released, expand from their compressed state, and lodge into the artery, causing blockage and permanent reduction of blood flow [5, 6, 7, 8]. The process is then repeated on the other side to block blood flow to both the right and left prostate lobes. This blockage causes ischemia and tissue necrosis of the prostate, leading to shrinkage over time. It is important to note that not all blood flow to the prostate is blocked; literature sources indicate that 10–30% of blood flow is

preserved through smaller arteries and collateral vessels [9].

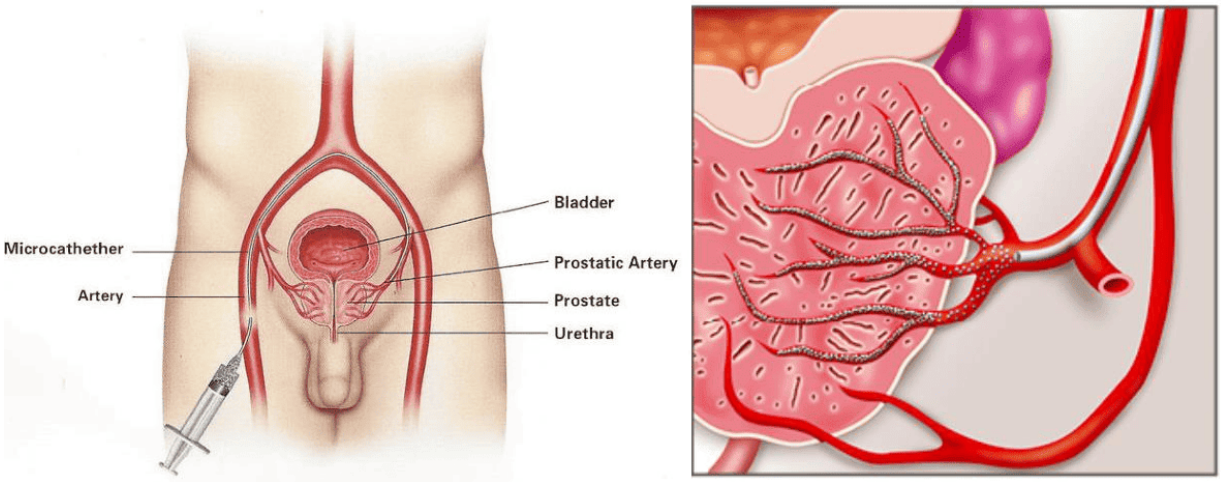


Figure 4.1: *Prostatic-artery embolization (PAE) as a platform for gold-nanoparticle delivery.* Left panel: A microcatheter is introduced through the femoral artery and navigated under fluoroscopy into each prostatic artery. Right panel (magnification): The embolic spheres lodge in terminal intraprostatic arterioles, blocking arterial inflow while simultaneously depositing GNPs throughout the surrounding prostatic parenchyma [10].

In our project, we aim to utilize microcatheter intraarterial delivery of EGCG-GNPs directly to the main artery of the left and right prostate gland, combined with arterial blockage using embospheres. In principle, this approach will reduce blood flow to the tumor, enhance exposure of our nanodrug formulation to the tumor, and reduce systemic exposure of EGCG-GNPs to nontarget organs. PAE alone has been tested for prostate cancer treatment however, there is limited and inconclusive evidence regarding its efficacy. Some studies have shown efficacy in partial tumor control; a systematic review by Burkhardt *et al.* explored 13 clinical studies and found only modest partial tumor reductions but no high-quality evidence of durable oncologic benefit [11]. PAE can have partial efficacy, but the prostate and its cancer will likely retain enough collateral blood flow to survive [11, 12]. Therefore, on its own, PAE embolization is not sufficient to treat prostate cancer, but it is believed to have potential when combined with other treatment modalities, but more research is needed in this field. To our knowledge, no one has utilized prostatic arterial embolization in combination with nanodrug delivery. Considering the challenge of systemic IV administration for many nano-cancer drugs, we believe this procedure could provide a solution by localizing the majority of drug exposure to the prostate organ [13]. Additionally,

in combination with adjuvant radiotherapy, the radiosensitizing properties of GNPs can further improve efficacy [14, 15].

Toxicity is one of the biggest challenges facing the clinical translation of all GNP biomedical projects, and it is one of the main components we wish to address in this chapter through our in vivo studies. This topic has sparked intense debate since GNPs were first considered for use in nanomedicine [16, 17]. One reason for this caution is the medical history of gold salts, which were once used to treat rheumatoid arthritis and were associated with numerous serious toxicity issues, including skin and mucous membrane reactions [18]. Some patients experienced permanent stains on their skin or eyes through photoreduction of circulating gold ions, which precipitated as nanogold in dermal and ocular tissues [18]. Other adverse events included renal toxicity, bone marrow suppression, hepatotoxicity, and allergic reactions ranging from mild to severe anaphylactic responses [18]. However, as mentioned in chapter 1, molecular gold and nanogold have very different properties. Proof of this difference in the context of toxicity is that auranofin, the gold salt treatment FDA approved in 1985, has an LD50 in mice of 6.55 mg Au/kg, whereas 15 nm Cit-GNPs exhibit an LD50 greater than 1000 mg Au/kg [19, 20]. In our project, we aim to explore the renal and hepatic toxicity of our GNPs through histopathology analysis of mice organs. Additionally, we aim to analyze toxicity in canine subjects by performing serial complete blood counts, serum chemistry panels (ALT, ALP, creatinine, urea, electrolytes, total protein, albumin), and urinalysis at baseline and multiple post-dose time points to capture any acute or evolving renal or hepatic dysfunction.

The last component of our project is designing a PBPK model for GNP biodistribution based on our EGCG-GNP and Curc-GNP murine biodistribution data. PBPK models are extensively used in pharmaceutical research to simulate and predict the absorption, distribution, metabolism, and excretion of drugs or molecules in the body using a mathematical framework [21]. The strength of PBPK models lies in their predictive power, making them particularly valuable for nanodrug research; as discussed in previous chapters, nanoparticles exhibit vastly different behaviors depending on factors such as size, shape, surface charge, and coating [14, 15, 16, 17, 20]. By incorporating these variables, PBPK models can provide detailed insights into mechanistic pathways, including the absorption, distribution, and metabolism of nanoparticles [21]. Additionally, they enable nanoparticle design optimization, allow extrapolation to other animals such as from mice to dogs or humans, and help in optimizing dosing regimens. For example, if we aim to achieve a specific concentration of GNP uptake in the prostate, the PBPK model can guide the necessary adjustments in dosing strategies [21]. Furthermore, these models can identify potential toxicity by assessing GNP accumulation in non-targeted organs or predicting off-target effects [21]. Another significant advantage of PBPK modeling is its ability to

reduce reliance on in vivo testing. It decreases the cost and time associated with animal testing while also addressing ethical concerns by reducing the number of sacrificed animals. Although numerous studies have explored the biocompatibility and biodistribution of GNPs in vivo, no such studies have been reported for phytochemical conjugated nanoparticles.

The procedure of combining IA delivery of EGCG-GNP to the prostate and PAE is a novel multistep procedure devised by the collaborative team at University of Waterloo, WRHN, and the University of Guelph. To our knowledge, the combination of nanodrug formulations and PAE to treat prostate cancer has never been proposed, and our research is the first to explore this modality. This multistep procedure is a product of the collaboration between different organizations, bringing together a range of specialties and skills, including medical physicists, oncologists, radiologists, veterinary experts, and nanomedicine experts.

Our in vivo project begins with biodistribution and toxicity studies in the murine model. Then, we expand on the murine data to build a PBPK model for our GNPs and predict their biodistribution through interspecies extrapolation to the rat model. Lastly, our canine pilot study will be broken down into two subgroups. One group consists of three purpose bred lab beagles that do not have prostate cancer, who will be utilized to serve as a test of proof of concept and to assess tolerability, safety, and toxicity in these exploratory studies. The other group will consist of our canine clinical trial subject, a client owned twelve-year-old Boston terrier with a prostate tumor diagnosis of plasmacytoid urothelial carcinoma that was localized to the prostate. The treatment plan for the clinical case was intraarterial (IA) delivery of 1 mL of 1.5 mg /mL EGCG-GNP in both lobes along with 5.5 mL carboplatin (10 mg/ mL). Toxicity, tolerability, and feasibility of nanodrug delivery through PAE are the primary insights we aim to obtain from the canine studies. Secondary insights include efficacy of our procedure in the clinical prostate cancer case and sustained CT-contrast enhancement in the prostate of dogs treated with EGCG-GNPs.

Our hypothesis for the murine study is that Curc-GNP and EGCG-GNPs with majority size range between 15-25 nm will primarily accumulate in the liver and spleen, with minimal accumulation in the bladder due to these GNPs exceeding the glomerular filtration size threshold of less than 10 nm. We expect excretion to occur via the hepatobiliary route, resulting in a decrease in gold (Au) concentration in the liver from day 1 to day 56. Toxicity will be low and assessed through monitoring body weight, organ-to-weight index, histopathological analysis of GNP exposed organs, and observation of mouse behavior. PAE-mediated delivery of 1.5 mg/mL EGCG-GNPs in laboratory beagles is expected to be well tolerated and to produce CT contrast enhancement in the prostate greater than 100 HU. Toxicity will also be low and assessed through urinalysis, blood analysis, and flagging of any biomarkers outside the normal range will be taken as signs of toxicity. Additionally,

toxicity will be assessed through adverse event reporting by veterinary specialists at the animal care facility. Finally, our hypothesis for the clinical trial case is that the procedure will again be well tolerated, and we expect to observe a decrease in tumor and prostate volume during follow-up evaluations post procedure.

4.2 Materials

Reagents for GNP synthesis were as follows: Curcumin (≥98% purity; Alexis Biochemicals, San Diego, CA, USA), gold(III) chloride trihydrate ($HAuCl_4 \cdot 3H_2O$, 520918; Sigma-Aldrich, St. Louis, MO, USA), epigallocatechin gallate (≤95% purity; E4143; Sigma-Aldrich, St. Louis, MO, USA). All GNP synthesis protocols utilized ultrapure Milli-Q water from a Millipore Gradient A10 water purification system (Merck Millipore, Burlington, MA, USA).

1000 ppm (μg/mL) gold standard for concentration measurements using ICP-MS was purchased from Inorganic Ventures and Sigma-Aldrich (38168–Aldrich, St. Louis, MO, USA).

10% neutral-buffered formalin (3.7–4% formaldehyde in 0.1 M phosphate buffer, pH 7.4; Sigma-Aldrich, HT501128, St. Louis, MO, USA) was used for fixation of harvested organs prior to paraffin embedding and histopathological analysis.

4.3 Methods

4.3.1 In vivo Mice studies

All murine experiments were approved by the Research Ethics and Animal Care Committee at the University of Waterloo (AUPP Number 17-14), and procedures were conducted in accordance with the wellbeing and ethics guidelines set forth by the Canadian Council on Animal Care (CCAC). The mice were housed and cared for at the animal research facility (CAF). A total of 122 three-week-old CD-1 mice were delivered to the facility, where they were cared for and acclimatized for 6 weeks before initiation of experiments. 30 mice were administered EGCG-GNPs by intraperitoneal (IP) injection at 10 mg of gold/kg of body weight (average injection volume = 371.04 μL); another 34 mice were administered Curc-GNPs by IP injection at 10 mg of gold/kg of body weight (average injection volume = 377.93 μL); and 58 more mice were used as control subjects and received 500 μL saline by IP injection (Table 4.1). The concentrations of the EGCG-GNPs and

Curc-GNPs from synthesis were 422.77 μg/mL and 391.43 μg/mL, respectively. However, the advised upper limit for IP injection volume was 0.5 mL, and the desired dose would require a larger injection volume. In order to meet this requirement, the GNP solutions were further concentrated by centrifugation to increase the gold concentration to 700 μg/mL. This resulted in an average injection volume of 0.38 mL per mouse. A single IP injection of the GNPs was administered 4 to 5 mm deep into the peritoneal cavity for all mice. After treatment, the weight of each mouse was recorded every three days. During weighing sessions, the mice were examined, and any changes in behavior or physical abnormalities were recorded. The time points for each group were 1, 7, 14, 28, and 56 days, after which the mice were euthanized. CO_2 inhalation was used for euthanasia. The CO_2 flow rate was approximately 2 L/min, and CO_2 flow was maintained in the cage for 10 min. The mice were then dissected, and tissues from the listed organs were extracted and placed in 50 mL polystyrene vials. All instruments and samples were thoroughly washed with water to minimize cross-contamination of GNPs between samples. In the treatment group, one mouse was set aside for histological analysis, and the remaining mice were included in the gold quantification study. From the control group, one set of mouse organs was included in the gold quantification study.

Table 4.1: Number of mice sacrificed for each time point and study group

Time Point (days)	**Number of mice in EGCG-AuNP arm**	**Number of mice in Curc-AuNP arm**
1	5C, 5T (10 total)	5C, 6T (11 total)
7	5C, 5T (10 total)	5C, 6T (11 total)
14	5C, 5T (10 total)	5C, 6T (11 total)
28	7C, 8T (15 total)	7C, 8T (15 total)
56	7C, 7T (14 total)	7C, 8T (15 total)

*T- Treatment group, C- Control group

4.3.1.1 Gold Quantification - Biodistribution

ICP-MS (Teledyne Leeman Labs) was used for accurately determining the gold concentration of the synthesized EGCG-GNPs and Curc-GNPs in the mouse organs. A calibration curve

for quantifying gold content in the organs was generated using a blank, and five standard products (1 to 25 parts per billion). Calibration curve correlation coefficients were all >0.995. The calibration curve was verified with a standard prepared using a different source of gold, and was considered acceptable when within ±10% of the expected value. The method detection limit (MDL) for gold in solution was 3 ppb, and the limit of quantitation (LOQ) for gold in solution provided was 10 ppb. The instrument analysis was performed on ^{197}Au, while ^{195}Pt and ^{205}Pt were used as internal standards to correct for varying plasma conditions. The impacts of the biological media on the MDL and LOQ of ICP-MS measurements were assumed negligible.

Organ digestion was done by an addition of 1.5 mL aqua regia (HNO3 + 3HCl) and 8.5 mL of MilliQ H2O to vials containing select organs, and placement upon a heat block to facilitate digestion. Each vial was left on the heat block for at least three hours, and the temperature on the heat block was set at 175 °C. The vials were then filtered using a vacuum filter pump with DigiFilter 0.45 micron tubes. The filtered liquid in the vials was labeled and sent to the University of Guelph (located in Guelph, Ontario, Canada) analytical laboratory for precise quantification of gold content using ICP-MS.

4.3.1.2 GNP Toxicity- Organ weight Analysis

Organ weight to body weight ratio is a method that is used in toxicology to indicate potential toxic effects by detecting hypertrophy (increase in weight) or atrophy (decrease in weight) [22]. It is especially useful to assess hepatotoxic effects caused by GNPs. In general, an increase in organ weight indicates compensatory hypertrophy such as inflammation and decrease in organ weight indicates tissue damage [22]. The test is the most sensitive for the liver and kidney as both are considered filtering organs [23, 24]. The liver is widely recognized as one of the most sensitive and informative organs for toxicity assessment using organ:body weight ratios [25, 23]. Liver weight changes (both absolute and relative) are strongly associated with histopathologic changes and are a standard endpoint in toxicity studies. Kidney weight is also a sensitive indicator of toxicity, as the kidneys are major sites for excretion and are commonly affected by xenobiotics [24]. The Society of Toxicologic Pathology (STP) recommends that liver, heart, kidneys, brain, and testes be weighed in all general toxicology studies, with spleen and thymus also recommended for rodents [26].

Table 4.2: Organ:Body Weight Ratio Utility in mouse IP injections.

Organ	**Sensitivity/Utility for Organ: Body Weight Ratio Toxicity Test**
Liver	High (very informative)
Kidneys	High
Heart	Moderate
Spleen	Moderate
Lungs	Low, unless respiratory toxicity suspected
Stomach	Low

In our study, the organ:body weight ratio of the treatment group will be compared to the control and statistical analyses of the data will be conducted to assess if the difference in weight due to GNP injection is statistically significant. Our primary target organs for this analysis are liver and kidney due to their higher utility and sensitivity to this method. Organ weights were first normalized to each animal's body weight and expressed as

$$\textit{Relative organ weight ratio} = \frac{\textit{organ weight (mg)}}{\textit{bodyweight}(g)} \tag{4.1}$$

Average organ weight/body weight ratios for liver, kidney, heart, spleen, lungs and heart for treatment group and control group are then compared based on t-test p-values to detect any statistically significant differences.

For each organ, the following procedure was carried out:

1. **Data Summary:** Organ-to-body weight ratios were calculated as mean ± standard deviation of the mean for each treatment group and the control group.

2. **Two-Sample t-Test:** For each organ, a t-test was used to compare the mean ratio in the treatment group versus the control group.

3. **Null hypothesis:** The Null hypothesis (H_0) stated that there was no difference in the true mean organ:body weight ratio between the groups, while the alternative hypothesis (H_1) stated that there was a true difference (two-tailed test). A p-value of < 0.05 was considered statistically significant.

4. **Reporting & Interpretation:** Results are presented as mean ± SD with the exact p-value denoted above the comparison bar chart columns. Any statistically significant difference in mean organ:body weight ratio was considered an indicator for potential organ enlargement (hypertrophy) or shrinkage (atrophy) and highlighted in red.

4.3.1.3 Histopathology of Organs

One set of organs from day 14, 28, and 56 treatment groups were sent to the histopathology lab for analysis. Day 1 and day 7 treatment groups were chosen not to be analyzed as structural changes caused by GNP toxicity if present would unlikely manifest within the short time frame. Histology analysis was carried out by Histovet Surgical Pathology (Guelph, Ontario) by Dr. Brian Wilcock, and the procedure was provided below.

Upon dissection, the six organs (kidney, liver, lung, stomach, spleen, and heart) were transferred to a vial and immediately immersed in 10% neutral-buffered formalin. The vials were then transferred to the pathology lab, where multiple serial sections were prepared from select tissues: two sections of kidney, one section of liver, and one section of spleen. After at least 24 hours of fixation, the specimens were dehydrated, cleared, and embedded in paraffin using standard histological protocols. Paraffin blocks were sectioned at 4–5 μm thickness, mounted onto glass slides, and stained with hematoxylin and eosin. Each slide was observed under light microscopy. Sections of kidney were examined for cortical tubule architecture, glomerular structure, and any signs of inflammation or injury. Liver samples were evaluated for hepatocellular architecture, cytoplasmic characteristics, and any leukocytic infiltrates or tissue damage. Spleen sections were inspected for relative distribution of red and white pulp, hematopoietic activity, and potential pigmentary changes. All observations were recorded in accordance with standard rodent histopathological evaluation criteria.

4.3.2 PBPK Model

Biodistribution data was collected for both EGCG-GNPs and Curc-GNPs, and used to inform the physiologically-based pharmacokinetic (PBPK) model for mice, which was then extrapolated to rat species using literature data [27]. Due to their similar physicochemical characteristics and biodistribution data, the two particles were considered equivalent entities in the model. The modeling workflow in Figure 4.2 was used to develop the PBPK model for the GNPs in mice using data from this study, and evaluate its utility for extrapolation to other species.

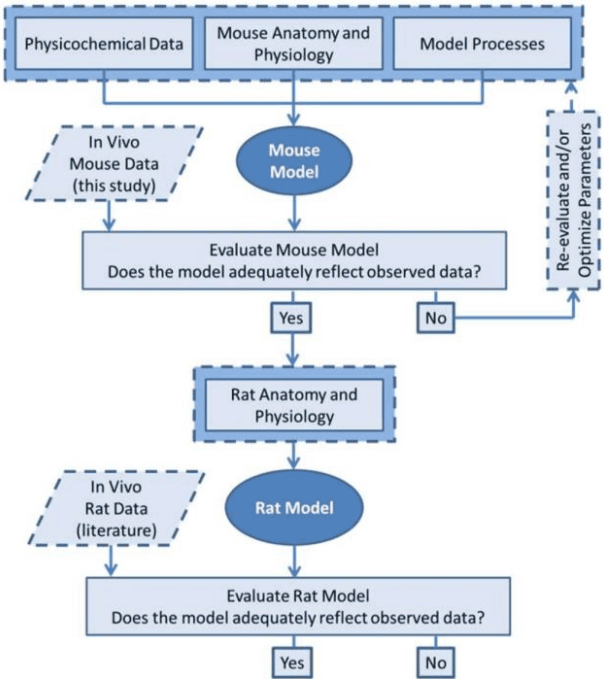


Figure 4.2: Physiologically based pharmacokinetic (PBPK) modeling workflow.

4.3.2.1 Software

The PBPK model was built and evaluated in MATLAB R2017a using the Intiquan toolbox (IQMTools v1.2.2.2) by Henning Schmidt. Experimental data from the literature was digitized using the PlotDigitizer v2.6.8 application by Joseph Huwaldt.

4.3.2.2 Model Structure

The whole-body PBPK model structure for large molecules and therapeutic proteins by Niederalt *et al.* [28] was adapted with features from recent NP PBPK models [29, 30, 31, 32]. Within the virtual body, fifteen organs were represented as mathematical compartments, and connected by plasma and lymph flows. The fifteen organs modeled were the heart, kidneys, muscle, skin, brain, adipose, gonads, liver, stomach, spleen, pancreas, small intestine, large intestine, bone and lungs. Each organ was divided into four sub-compartments: plasma, vascular endothelium, macrophages and interstitial space.

The model processes are described in Figure 4.3. Within organs, GNPs in the plasma sub-compartment moved across the endothelium into the interstitial space by extravasation or transcytosis. The interplay of convection and diffusion as it relates to extravasation was described by the two-pore model, which accounts for the hydrodynamic radius of the particle, and the dynamic fluid flux across large and small pores in the capillary wall [28, 33]. Transcytosis was mediated by pinocytosis into the vascular endothelium, and exocytosis to the opposite side.

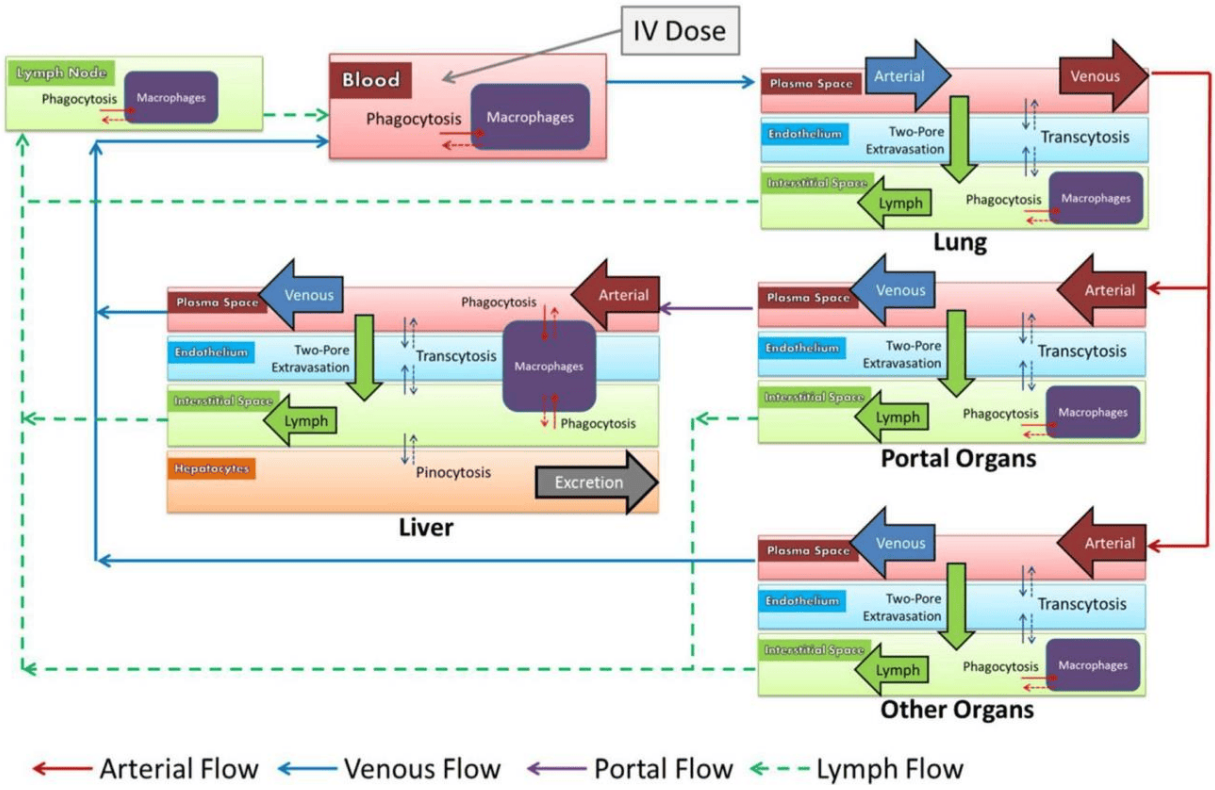


Figure 4.3: *Schematic of GNP biodistribution* - GNPs circulate throughout the body, as pictured. They may cross into the interstitial spaces of organs by extravasation or transcytosis across the endothelium. Phagocytic uptake into macrophages and pinocytic uptake into hepatocytes are key determinants of biodistribution. Lymph flow recycles GNPs from the interstitial space back into the venous blood. Particles are excreted from hepatocytes into the bile. Renal excretion is negligible for particles >10 nm in diameter. Aborig *et al.* [34]

In the interstitial space, GNPs were taken up into macrophages by phagocytosis. Fluid

in the interstitial space drained into the lymphatic system, which recycled GNPs back to the venous blood via the thoracic duct. In the liver, macrophages known as Kupffer cells lined the sinusoids and phagocytozed GNPs directly from the plasma. A unique sub-compartment in the liver described pinocytosis into hepatocytes, and subsequent excretion into the bile. Renal excretion was assumed negligible for GNPs larger than 10 nm in diameter [35]. IP administration was described as a bolus into an administration compartment from which GNPs diffused into the interstitial spaces and into lymph nodes surrounding the portal organs (stomach, spleen, pancreas, small intestine and large intestine). The model equations are presented in the Appendix C.

4.3.2.3 Model Parameterization

Anatomy:

Organ volumes, compositions, plasma flows and lymph flows for a 28 g mouse and a 280 g rat were obtained from PK-Sim (www.open-systems-pharmacology.org). Lymph node volumes were obtained from Shah and Betts [36].

Extravasation:

The two-pore model for extravasation was implemented as outlined by Niederalt *et al.* [28]. A lymph reflection coefficient (σ^{IS}) described the resistance to lymph flow in the interstitial space due to particle size and physical and electrostatic interactions with the extracellular matrix [36].

Vascular Endothelium:

The endothelial fraction of each organ (i) was derived from vascular surface area by:

$$F_i^E = k_e \times F_i^V \times d_e \tag{4.2}$$

Where k_e is a constant of proportionality (950 cm^2/mL), F_i^E is the vascular fraction of the organ, and d_e is the thickness of vascular endothelium ($3{\times}10^{-5}$ cm) [28]. These parameters are assumed species-independent in the absence of additional physiologic data. The rate of pinocytosis into the vascular endothelium ($CLup$) was set to 0.05 μL/h/μL endothelial cells in agreement with the majority of PBPK models for large molecules to

date [36, 37, 38]. The rate of exocytosis was assumed to be equal to the rate of pinocytosis to maintain fluid balance in endothelial cells.

Macrophages:

Macrophage volume in each organ (V_i^M) was calculated as a fraction of the cellular volume. The following factors were used as reference values to assign macrophage fractions to other organs:

1. Kupffer cells and stellate macrophages make up 10% of the cellular volume of the liver [39, 40]
2. Complete blood counts indicate that 1% of the blood volume is comprised of phagocytic cells, based on an average white blood cell volume of 1.25 pL [41]
3. White pulp macrophages make up 30% of the cellular volume of the spleen [42, 43, 44]

To quantify macrophages in other organs by these reference mediums, RNA expression data for 7 proteins that are largely specific to macrophage populations (CD14, CD40, CD11b, EMR1, CD68, CSF-1 and CSF-1R) and the macrophage volumes listed in two PBPK models were compiled [30, 38]. Based on these factors, the remaining organs were categorized as having prominent (4%) or low (2%) macrophage content. The macrophage fractions for all organs are listed in the Appendix C.

The maximum rate of phagocytosis (P_{up}) is drug-specific and required optimization in the absence of any in vitro data. A range between 0.075 and 40 μL/h/μL macrophages was reported in the PBPK study by Lin *et al.* [31], and these boundaries were used for the optimization. Exocytosis in macrophages was assumed to be the same as in endothelial cells (0.05 μL/h/μL macrophages). Phagocytosis of NPs is a saturable process. Therefore, a Michaelis-Menten approximation was implemented for the phagocytosis rate in each organ (i):

$$Pup_i = Pup \times V_i^M \times \left(1 - \frac{C_i^M}{K_M + C_i^M}\right) \tag{4.3}$$

where C_i^M is the concentration of GNPs in the macrophages, and K_M is the half-saturation concentration in the cells (5000 μg/mL) based on the maximum GNP capacity reported by Alkilany and Murphy [20]. In the liver, macrophages were present lining the sinusoidal capillaries. The fraction of phagocytic uptake (F_{up}^M) from plasma and the fraction

of exocytosis back to plasma (F_{rec}^{M}) were both set to 0.5 in the absence of any physiologic data. This ratio may represent the ratio of Kupffer cell volume to stellate macrophage volume in the liver.

Hepatocytes:

Hepatocyte volume in the liver (V_{Liver}^{H}) was calculated as 75% of the cellular volume [40]. The rates of pinocytosis and exocytosis in hepatocytes were assumed to be the same as the respective rates in the vascular endothelium. The rate of NP excretion into bile (K_{Bile}) is drug-specific and required optimization.

Intraperitoneal Administration:

GNPs diffused into the interstitial spaces of the portal organs (stomach, spleen, pancreas, small intestine and large intestine) and into the lymph, according to a first order rate constant (K_{Abs}) (Figure 4.4). An optimized bioavailability (F) was applied to the dose, based on the observation that a portion of the dose remained trapped in the intraperitoneal space upon dissection. The fraction of the bioavailable dose that diffused into the interstitial space of each portal organ (i) was proportional to the respective organ volume, while 10% was absorbed directly into the lymph.

$$F_{i}^{IP} = (1 - F) \times 0.9 \times \frac{V_i}{V_{portal}}; \quad F_{lymph}^{IP} = (1 - F) \times 0.1 \tag{4.4}$$

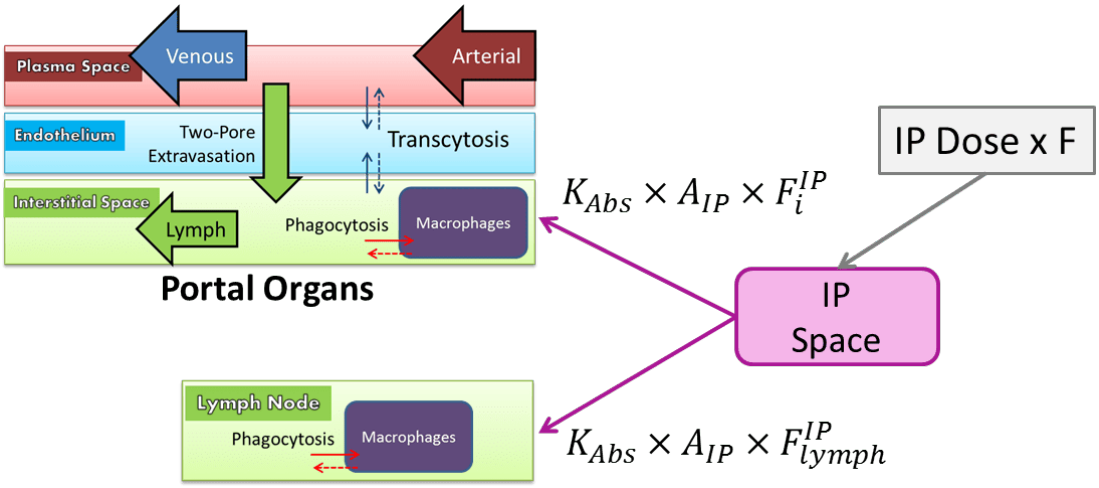


Figure 4.4: *IP Administration Pathway* - Schematic depicting the intraperitoneal (IP) injection route of administration. A fraction of NPs diffuses from the IP space into the interstitial portal organs and lymph node before reaching systemic circulation. Aborig *et al.* [34]

Optimization The maximum rate of phagocytosis (P_{up}), the rate of excretion into bile (K_{Bile}), the lymph reflection coefficient (γ_{IS}) and the IP bioavailability (F) were optimized to the experimental data in mice for the liver and spleen obtained from this study. Appropriate identifiability of the four parameters was confirmed prior to the optimization by assessing local sensitivity and parameter correlation with the *IQMidentifiability* function. A simulated annealing temperature-based algorithm was used for the optimization.

Model Evaluation:

The utility of the PBPK model for extrapolating biodistribution to other species was evaluated with two experimental datasets for non-PEGylated GNPs in rats from literature (Table 4.3) [27, 45]. Anatomical and physiological parameters in the mouse model were adapted to represent a mean rat with a weight of 280 g, while all other parameters and processes in the model were unchanged. The rat model was simulated, and the absolute average fold error across all data points was calculated to compare model predictions to observed values for each available organ in the literature datasets possessing measurements significantly different from controls.

Table 4.3: Experimental datasets from literature used for model evaluation

Dataset	Species	Particle[a]	Dose	Organ PK[b]	Meas. Time
Balasubramanian *et al.* [27]	Rat	20 nm Au with citrate	0.01 mg Au/kg IV	Liver, Spleen, Lung, Kidney, Stomach, Intestine	1, 7, 30 and 60 days
Fraga *et al.* [45]	Rat	16 nm Au with citrate	0.7 mg Au/kg IV	Liver, Spleen, Lung	30 min and 28 days

[a] Particle size is reported as the diameter measured by TEM visualization.

[b] PK data was extracted for organs with non-zero values that were different from controls and converted to amounts in organs (μg).

Sensitivity Analysis:

A local sensitivity analysis was performed to capture how each parameter may affect GNP exposure in the liver and spleen. For the analysis, each parameter was varied independently by $\pm$ 10% of the initial value and the resulting percent changes in the liver and spleen area-under-the-curve (AUC) outputs were reported.

4.3.3 Canine Studies

The canine studies were conducted at the University of Guelph through the Ontario Veterinary College (OVC), one of the leading institutions in Canada specializing in veterinary medicine. Procedures were approved by the University of Guelph Animal Care Committee (AUPP Number 4010). The canine pilot study was led by Dr. Anthony Mutsaers, and Charly McKenna conducted and collected the clinical data for this portion of the project. The study began with the first procedure, IA injection of EGCG-GNP in Beagle 1, which acted as the procedure control for EGCG-GNP administration. The following procedure was PAE in Beagle 2, serving as the embolization control. The purpose of both studies was to benchmark the independent safety and biodistribution profiles of EGCG-GNP infusion and embolization before combining them. Once this baseline was established, we progressed to the final stage of the pilot Beagle study by combining both procedures, IA of EGCG-GNP and PAE, in Beagle 3. This included IA delivery of 2 mL EGCG-GNP (1.5 mg/mL) into both right and left prostate lobes and IA delivery of 2 mL Embospheres, blocking only the right main artery. The average age of all three beagles was 6.98 years and an average weight of 12.9 kg. The dogs were housed at the Central Animal Facility at the OVC in kennels with trays underneath for urine collection.

The final stage of the pilot study involved applying our procedure to a clinical case of prostate cancer in a male neutered Boston terrier diagnosed with prostate cancer. The canine patient had previously received treatment at the OVC oncology department with mitoxantrone and carboplatin chemotherapy, showing low responsiveness; thus, alternative treatment was explored.

Table 4.4: Treatment protocols for the four different canine study groups.

Study Group	**Intervention Details**
Lab Beagle 1 (GNP control)	• IA injection of 2 mL EGCG-GNP into Right prostate lobe. • No IA injection into Left prostate lobe. • No embolization.
Lab Beagle 2 (PAE control)	• IA injection of 2 mL Embosphere beads (300-500 μm) into Right prostate lobe. • No IA injection into Left prostate lobe. • No EGCG-GNP application.
Lab Beagle 3 (Full Protocol)	• IA injection of 2 mL EGCG-GNP into Right prostate lobe. • IA injection of 2 mL EGCG-GNP into Left prostate lobe. • 2 mL Embosphere beads (300-500 μm) into Right prostate lobe only.
Canine clinical trial	• IA injection of 1 mL EGCG-GNP + 5.5 mL Carboplatin (10 mg/mL) into Right prostate lobe. • IA injection of 1 mL EGCG-GNP + 5.5 mL Carboplatin (10 mg/mL) into Left prostate lobe. • No Embolization.

4.3.3.1 Beagle 1: Intra-Arterial Injection of EGCG-GNP

IA injection of EGCG-GNP was first performed in Beagle 1 to assess the feasibility and tissue distribution of locally delivered nanoparticles. The preparation for the procedure involved sedation and/or general anesthesia, followed by placement of the dog in lateral recumbency. The ventral and lateral regions of the neck were clipped and prepared using sterile technique

to expose the carotid artery. An 18-gauge over-the-needle catheter was advanced into the artery and replaced with a hydrophilic guide wire, after which an introducer sheath was positioned and sutured in place.

Under fluoroscopic guidance, a Berenstein catheter was navigated into the prostatic arterial supply with the aid of a microcatheter and guide wire. A 50:50 mixture of saline and contrast medium (Isovue-300) was used to visualize the arterial anatomy. Once the prostatic artery was identified, 2 mL of EGCG-GNP (1.5 mg/mL) was delivered. This procedure was monitored closely through non-invasive blood pressure measurement and repeated contrast injections to confirm appropriate targeting. Post-procedural monitoring involved hourly assessments (temperature, pulse, respiration) for the first 8 hours, with subsequent daily examinations until study completion. Bloodwork and urinalysis was conducted prior to procedure, day 1, and day 7.

4.3.3.2 Beagle 2: Prostatic Arterial Embolization

PAE was conducted as a separate procedure in Beagle 2. Following the same approach to carotid artery access mentioned above for Beagle 1, a microcatheter was directed to the right prostatic lobe under fluoroscopic guidance. Embolic particles (Embosphere beads, 300–500 μm) suspended in a saline-contrast mixture were injected to occlude arterial blood flow within the prostatic vasculature. The volume of beads used was approximately 2 mL per lobe. Similar to the IA procedure described above, real-time fluoroscopy confirmed embolic distribution. Post-procedural imaging, including contrast-enhanced CT, was performed to evaluate the extent of the embolization, and the dog was monitored closely using the same post-procedure timeline. Bloodwork and urinalysis was conducted prior to procedure, day 1, day 2, and day 7.

4.3.3.3 Beagle 3: IA Injection of EGCG-GNP + Prostatic Arterial Embolization

In the final beagle study (Beagle 3), both interventions, IA administration of EGCG-GNP and PAE, were performed in a single session. After securing vascular access through the carotid artery, a microcatheter was navigated into the left prostatic artery, where Embosphere beads (2 mL) were mixed with EGCG-GNP (1.5 mg/mL) and injected. The catheter was then carefully repositioned to the right prostatic lobe for an injection of EGCG-GNP (1.5 mg/mL) alone. This approach enabled a controlled comparison of GNPs delivered both with and without concurrent embolization. CT-imaging comparison would

be used to observe the extent of EGCG-GNP accumulation between the embolized right and nonembolized left lobe. Beagle 3 underwent contrast-enhanced imaging approximately one hour later, followed by repeated CT-imaging on Days 1, 2, and 6, based on observed radiodense changes or other clinical indicators. Bloodwork was conducted prior to procedure, day 1, day 2, day 3 and day 7. Urinalysis was conducted at baseline, day 2 and day 3 post-procedure.

4.3.3.4 Clinical Case

A client-owned 12-year-old Boston Terrier (11.4 kg) served as the clinical case, presenting with confirmed prostatic tumors that had proven refractory to previous chemotherapy. Specifically, the prostate cancer diagnosis was prostate urothelial carcinoma localized to the prostate with bladder wall thickening. His prostate was enlarged and irregular with several mineral densities. Other medical conditions included intervertebral disk disease, suspect focal seizures and degenerative valvular disease. Additionally, he had signs consistent with urinary tract infection prior to procedure. Clinical signs of prostate cancer included urethra impingement or stranguria highlighted by slow and spasmodic urination.

General anesthesia was induced (fentanyl, midazolam, and propofol) and maintained with isoflurane. After carotid artery access was established (using the same approach described for the beagles), both prostatic lobes were infused with a combination of carboplatin (10 mg/kg, 10 mg/mL) and 1 mL of EGCG-GNP (1.5 mg/mL). The total carboplatin-GNP solution volume per lobe was approximately 6.5 mL. Following the procedure, the dog was observed in the Intensive Care Unit for at least 24 hours with vital signs (temperature, pulse, respiration, blood gases) recorded every 2 hours. Blood and urine were collected at intervals similar to the beagle studies, with additional samples taken as clinically warranted. If the dog remained stable beyond 48 hours, the jugular catheter would be removed, and the dog would be discharged to the owner's care. A follow-up exam, including advanced imaging (contrast-enhanced CT and Doppler ultrasound), was scheduled 7–10 days later to evaluate therapeutic response and catheter site healing.

4.4 Results & Discussion

4.4.1 Mice studies

The mouse studies were completed successfully with no major deviations from protocol. Only one procedural mishap occurred during IP injection of 122 mice, in which a mouse died

during the procedure. During monitoring, one mouse developed an eye injury attributed to trauma from other housed mice, resulting in degradation and blindness in that eye. Experienced veterinary technicians determined that neither incident was related to the GNPs. The death during IP injection was attributed to incorrect animal handling, specifically a grip that was too tight. The blind eye was caused by a scratch, likely from another mouse. Skin discoloration was observed at the injection site on the stomach, particularly in the 1- and 7- day groups (Appendix Figure C.1). This discoloration faded in groups monitored for longer periods and was linked to GNPs. GNP-related skin discoloration is commonly reported in clinical trials; for example, microneedle GNP injections for vaccines have shown persistent purple/blue discoloration at injection sites months post-procedure, and AuroLase gold nanoshell clinical trials for prostate cancer reported blue discoloration at IV puncture sites [46, 47]. No behavioral changes were noted.

4.4.1.1 GNP Biodistribution in Mice

Elemental Au was detected in most mouse organs. The highest amounts were found in the liver and spleen. The distribution pattern is shown in Figure 4.5. The greatest site for Au accumulation was the liver at all time points and for both Curc-GNPs and EGCG-GNPs. The secondary and tertiary accumulation sites were the spleen and stomach, respectively. These high levels detected in the liver and spleen were expected, as literature states that GNPs exhibit size-dependent biodistribution, with GNPs of diameters between 10–100 nm preferentially taken up by organs of the RES system (liver and spleen) [48]. Our GNP structures are approximately ~20-25 nm according to DLS measurements when EGCG/Curc-GNPs are in aqueous solution. However, we found size increases dramatically when GNP structures are in cell media, with the formation of a protein corona causing the size to increase to 30–40 nm. High Au stomach concentrations resulted from the intraperitoneal injection method, where GNP absorption in abdominal fat, intestines, and stomach lining occurred through diffusion and close proximity to the intraperitoneal cavity. Kidney concentrations were low but detectable at 1–14 days, while 28- and 56-day time points showed values close to zero. For smaller GNPs (<10 nm), it is reported that kidney accumulation is more pronounced and increases over time, especially for 5-10 nm GNPs where the glomerular filtration unit in mice is approximately 5 nm; larger particles experience more steric hindrance and thus prolonged GNP accumulation in kidney [35]. There were little signs of kidney accumulation in our study.

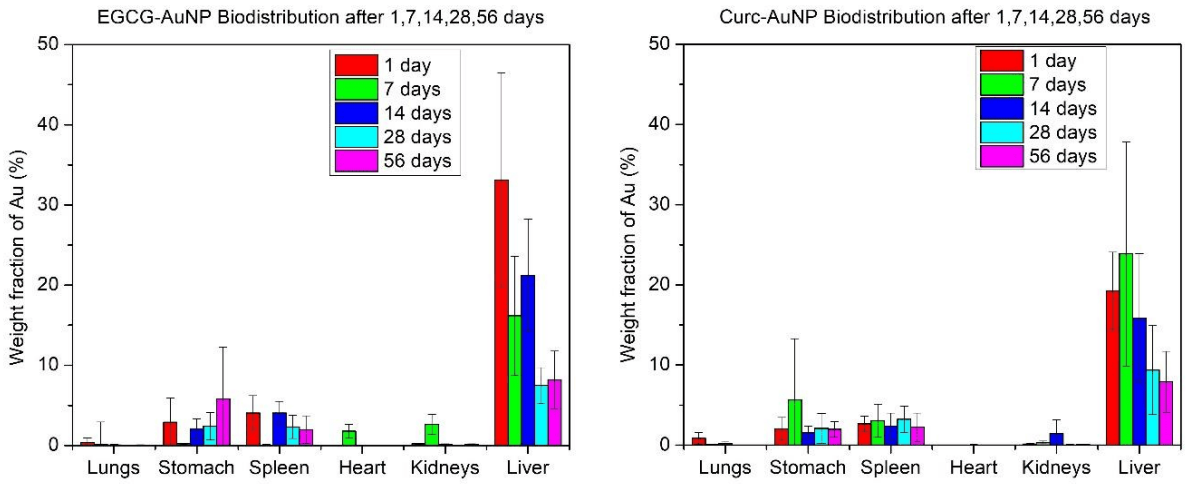


Figure 4.5: Weight fractions of injected AuNP dose found in select organs after acid digestion.

The excretion process of GNPs is a very complex and not fully elucidated in literature. More research is needed to fully understand the mechanisms and factors influencing GNP clearance. GNP's chemical inertness and stability mean it is not readily transformed into more excretable forms and can stay lodged in the lysosome of cells indefinitely [18]. In our study we report data that shows a significant clearance of our GNP structures from the liver through decrease in Au concentration as time increases with Au concentrations substantially lower than day1 and day 7 Au concentration levels (Table 4.5). For EGCG-GNP study group, Au concentration in the liver was 4 times lower on day 56 versus day 1 (33.11% vs 8.18% p <0.01). The correlation between Au concentration and time was graphed in a scatter plot in Figure 4.6 where adjusted R^2 values and slope were determined from the line of best fit. The slope for both studies is negative indicating a downward trend with EGCG-GNPs containing livers showing a steeper decline of -0.362 versus -0.255 for Curc-GNPs. The R^2 value for EGCG of 0.372 indicates a moderate trend while the R^2 value of 0.247 indicates a weaker trend. However, linear regression trend analysis showed the decrease of Au concentration from day1 to day 56 for both Curc-GNP and EGCG-GNP were statistically significant. P-value for the trend of decreasing Au weight fraction % in the liver as time passes is $p \approx 0.003$ for EGCG-GNP and $p \approx 0.006$ for Curc-GNP. There was no statistically significant difference in biodistribution between EGCG-GNP and Curc-GNP. One of the primary pathways for the excretion of GNPs from the liver is believed to occur through the hepatobiliary route. However, not all studies have shown clearance of GNPs in the liver after accumulation especially for GNPs >100 nm [49, 50]. GNPs

that agglomerate or aggregate in hepatic Kuppffer and endothelial cells of the liver tend to show long-term accumulation and impede their elimination [51]. For example, PEG-GNPs showed greater levels of elimination from the liver than CS-GNP (chitosan) and PEI-GNP (polyethyleneimine; cationic polymer) due to better stability according to the authors [51]. GNP size has also been related to clearance as reported by Sonavane *et al.* where they found that smaller GNPs exhibited more clearance from the liver to the small intestine and fecal Au concentration was higher for smaller GNPs [49]. AuroLase IV systemic application of 150 nm gold nanoshells in clinical trials showed persistent Au detection through elevated CT-imaging of liver and spleen. Liver X-ray contrast increased by an average of 28.9 HU, $p = 0.010$; spleen increased by an average of 63.7 HU, $p = 0.012$ and this persisted for the entire monitoring period (up to 3 years) with no signs of decreasing [50].

Table 4.5: The fraction of Au that was detected in the liver is relative to the initial GNP dose.

Time Point (days)	**Weight Fraction of Au in Liver (%)[a] (EGCG)**	**Weight Fraction of Au in Liver (%)[a] (CURC)**
1	33.11% ± 13.33	19.28% ± 4.78
7	16.18% ± 7.41	23.88% ± 13.99
14	21.23% ± 7.00	15.85% ± 8.07
28	7.49% ± 2.22	9.38% ± 5.55
56	8.18% ± 3.58	7.92% ± 3.78

[a] ± values are standard deviation values.

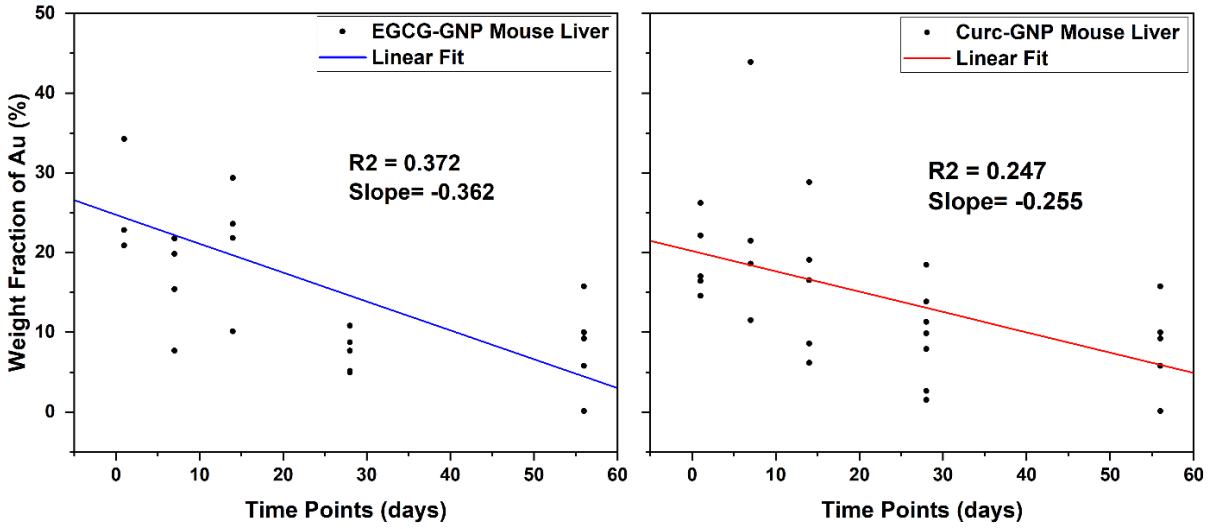


Figure 4.6: *Scatter plot of weight fraction of Au versus number of days in Liver* - Scatter plot of time versus weight fraction of Au % to assess clearance of GNPs from the Liver of mice. Linear fit was constructed on OriginPro through the linear fit function.

In our study, biodistribution data for the spleen showed no signs of elimination or clearance of GNPs in either Curc or EGCG study groups. The values of Au weight fraction % remained consistent across all time points, with minimal change in Au levels detected even after 56 days. The linear fit graph in Figure 4.7 shows no trend, with slope and R^2 values $\approx$0. Literature indicates clearance of GNPs from mouse spleen depends on recirculation of splenic macrophages [49]. Unlike the liver, the spleen lacks a direct biliary route; nanoparticulates must exit via recirculating macrophages and return to the liver for excretion. Current approaches to overcome splenic retention include using biodegradable gold clusters or surface chemistries that evade splenic capture [49].

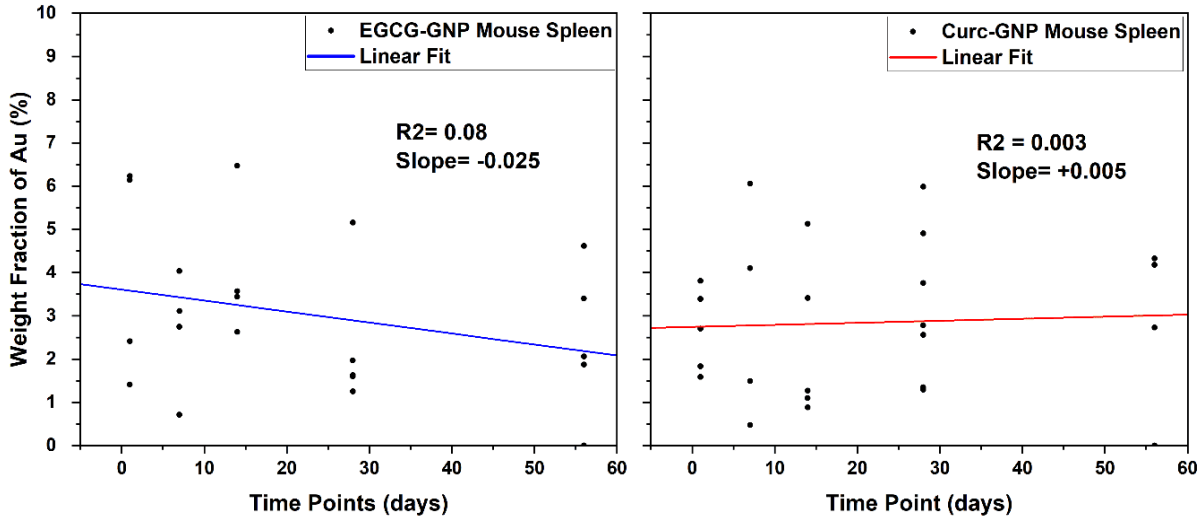


Figure 4.7: *Scatter plot of weight fraction of Au versus number of days in Spleen*: The line of best fit shows no trend towards decreasing Au content in the spleen inferring that there is long term accumulation in the spleen.

4.4.2 GNP Toxicity-Organ Weight Analysis

From an observational perspective there was no behavior observed that hinted at ailment of GNP injected mice. Behavior was observed the day after injection and every fourth day during weight measurements. Behaviors relating to activity level, feeding and drinking, pain or discomfort in movements, motor coordination or balance were all deemed normal. Weight measurements were taken every fourth day after injection to monitor for any signs of systemic toxicity. No weight loss greater than 10% was observed in any mouse within the treatment group. Instead, a steady increase in weight was reported for most mice in both treatment groups (EGCG-GNP and Curc-GNP), as shown in Figure 4.8. Body weight measurements are an important parameter to track as they could be an early indicator of health deterioration in mice.

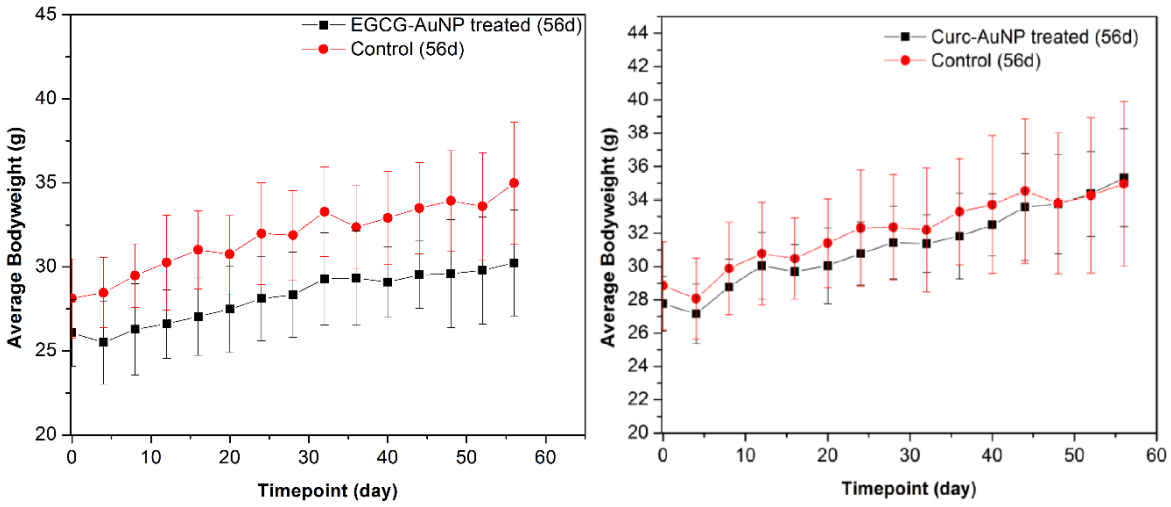


Figure 4.8: *Mouse weight was recorded every 4 days*: Both treatment groups showed a steady increase in weight that was in line with weight gain reported in the control groups.

Organ:body weight indices are valid and widely accepted endpoints for detecting potential toxicity in mouse studies following IV or IP injection, especially when interpreted alongside other pathological and clinical data [22, 23, 24, 25, 26]. As a toxicological evaluation, organ weight to body weight ratios should not be interpreted in isolation but corroborated with histopathological findings and clinical signs, as changes may result from factors unrelated to drug toxicity (illness, dehydration, nutrition, etc.) [22]. The liver is particularly prone to hypertrophy or inflammation due to its central role in metabolism and detoxification [25]. Increases or decreases in liver weight relative to body weight can be associated with hepatocellular hypertrophy, proliferative lesions, steatosis, or necrosis [25]. Renal or hepatic toxicity is usually indicated by an increase in weight, often suggesting swelling from inflammation, congestion, cellular proliferation, or accumulation of substances such as protein deposits or edema [23, 24, 25]. Only in cases of extreme toxicity is a decrease in weight typically observed, due to necrosis or irreversible organ injury [52].

In the EGCG-GNP study group, most organ-to-body-weight ratios in the treatment cohorts were closely aligned with, and indistinguishable from, those of the control group (Figure 4.9). The sole exception was the 7-day EGCG-GNP cohort: mice given a 10 mg/kg dose had livers roughly 14 % heavier than saline-treated controls ($p < 0.05$). Their mean liver organ-weight-to-body-weight ratio was 58.6 $\pm$ 5.2 mg/g, versus 51.3 $\pm$ 0.8 mg/g in controls. This increase may reflect hepatocellular hypertrophy, inflammation, or other

adaptive or adverse responses to EGCG-GNPs; detailed histopathology will be required to confirm the underlying cause.

High-dose EGCG alone can be hepatotoxic. Yan *et al.* reviewed clinical studies and case reports and found that intakes exceeding 400 mg day^{-1} can elevate ALT and AST [53]. Similarly, Yu Z *et al.*, in their study titled "Effect of Green Tea Supplements on Liver Enzyme Elevation: Results from a Randomized Intervention Study in the United States," administered catechin capsules containing 843 mg day^{-1} EGCG to 513 women for 12 months; 26 participants (5.1 %) developed aminotransferase elevations (ALT and/or AST) without concurrent increases in alkaline phosphatase or bilirubin, indicating hepatocellular drug-induced liver injury [54]. Enzyme levels normalized after stopping supplementation and rose again on rechallenge, confirming causality.

Within our study, liver hypertrophy was observed only at this single time point, and the majority of EGCG-GNP time points showed no significant liver-weight changes, suggesting limited toxicity. Nonetheless, comprehensive histopathological analysis remains necessary.

In the Curc-GNP treatment group, most organ-to-body-weight ratios of kidney or liver were virtually indistinguishable from those of the controls. The sole exception was the 1-day exposure cohort, which showed kidney hypertrophy: kidneys were 11 % heavier than those of saline-treated controls ($p < 0.05$) (Figure 4.10). This finding points to a transient, early renal response to Curc-GNPs rather than cumulative or progressive toxicity. All liver weights fell within the control range.

Curcumin's renal and hepatic safety profile mirrors that of EGCG: very high doses can provoke reversible organ injury in some individuals [55, 56, 57]. Case reports describe oxalate nephropathy after 2–5 g day^{-1} turmeric powder, yet most patients exhibited no lasting kidney damage and returned to normal oxalate levels once supplementation ceased [55]. A recent randomized controlled trial in chronic kidney disease (CKD) patients likewise found that curcumin did not raise the risk of CKD progression, kidney failure, or death compared with placebo, with similar rates of renal adverse events in both groups [56].

Regarding liver effects, a meta-analysis by Vajdi *et al.* covering 15 randomized controlled trials (905 nonalcoholic fatty liver disease patients) concluded that curcumin is largely hepatoprotective. ALT values continued to decline up to 160 mg day^{-1} and ALP up to 250 mg day^{-1}, after which the effect plateaued or reversed, with minimal evidence of hepatotoxicity [57]. If we consider the curcumin loading disclosed in Chapter 3 of our study, the curcumin dose administered to mice is 2.08 mg/kg (10.8 wt%). This value is well below the reported oral (>2 g/kg) and intraperitoneal(1.5 mg/kg) LD50 values for chronic exposure of curcumin in mice (PubChem) [58]. Additionally, curcumin-loaded nanocomplexes have been shown to be well tolerated at oral doses up to 50 mg/kg and 270

mg/kg [59].

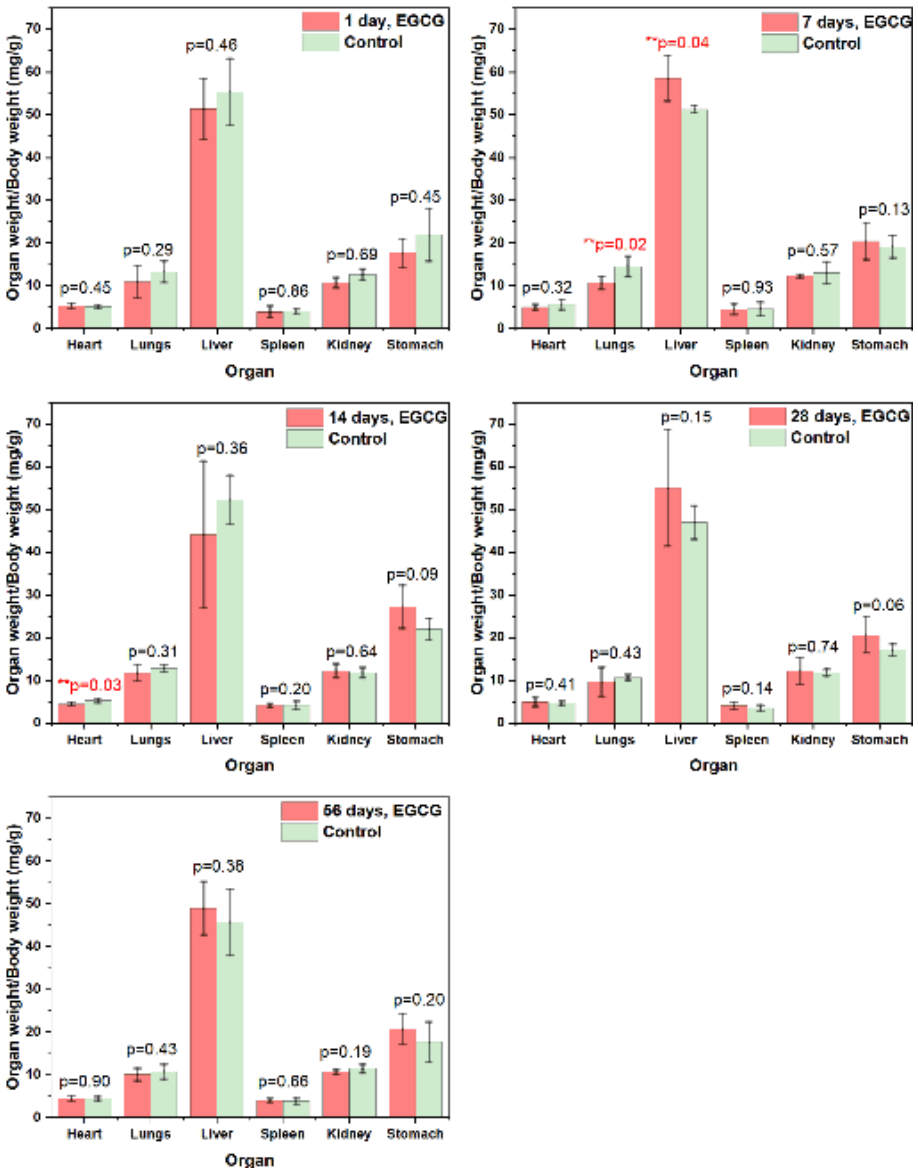


Figure 4.9: Organ:body weight ratios to assess liver or spleen atrophy or dystrophy for EGCG-GNPs

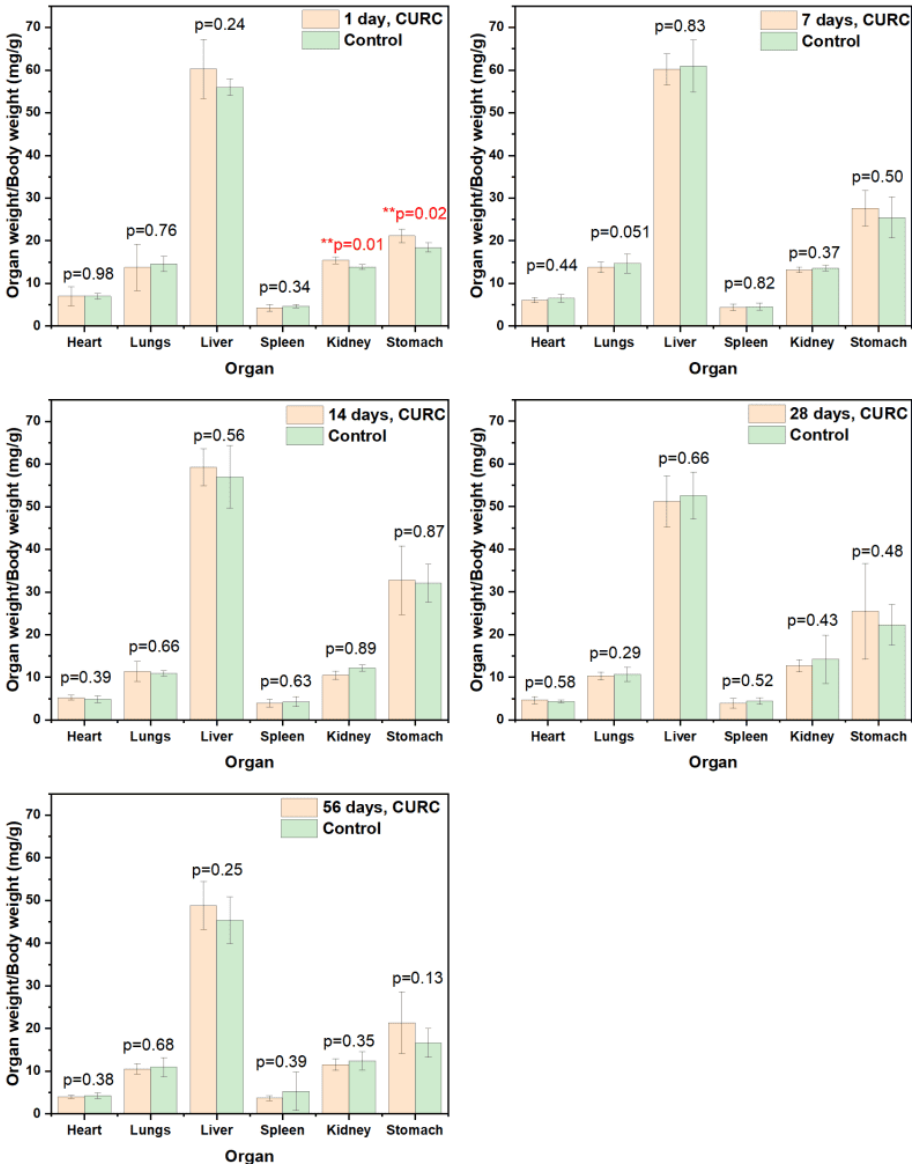


Figure 4.10: Organ:body weight ratios to assess liver or spleen atrophy or dystrophy for Curc-GNPs

4.4.2.1 GNP Toxicity- Histology

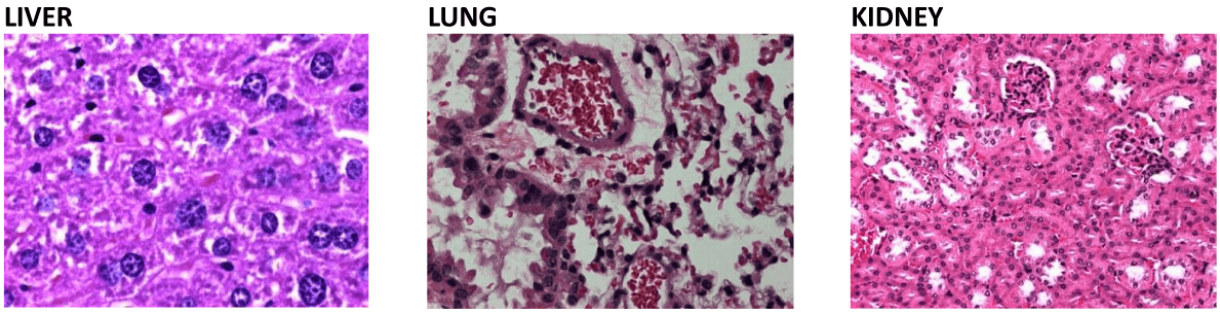


Figure 4.11: *GNP Toxicity*: Histological Examination of Liver, Lung, and Kidney Tissues.

Histological analysis allows us to observe microscopic changes in cells and tissues following EGCG-GNP or Curc-GNP administration in mice. This approach can reveal cell death (necrosis), inflammation, abnormal proliferation, and other pathological alterations in the liver, kidneys, spleen, lungs, stomach, and heart that may arise from nanoparticle exposure. Although organ-to-body-weight ratios, urinalysis, blood chemistry, and behavioral monitoring provide early indications of toxicity, histology pinpoints the exact cell types and tissue structures affected.

In this study, veterinary pathologist Dr Brian P. Wilcock examined organs from the 14-, and 28-day EGCG-GNP and Curc-GNP treatment groups, along with matched controls for each time point. Ten histopathology reports were generated, and none showed evidence of cellular toxicity in the liver, kidneys, spleen, lungs, stomach, or heart. A concise summary of the findings is presented in Table 4.6, while exact reports for the 14, and 28 day cohorts appear in the appendix section of this chapter. Representative hematoxylin and eosin micrographs of EGCG-GNP–treated liver, lung, and kidney tissues are displayed in Figure 4.11. Hematoxylin stains cell nuclei blue to purple, highlighting DNA and nuclear structures whereas the eosin stains the cytoplasm, extracellular matrix, and other tissue components pink to red.

Table 4.6: Summary of histopathology review for both EGCG-GNP and Curc-GNP treated organs.

Organ	General Microscopic findings	Interpretation for GNP toxicity
Liver	Normal lobular architecture. Only background two-fold nuclear size variation, mild glycogen-type vacuolation and very mild biliary pigment/retention; **no** inflammation, necrosis, fibrosis, sinusoidal leukocytosis or Kupffer-cell activation found in any liver samples	Hepatocytes and sinusoidal lining cells show no evidence of GNP-induced oxidative or inflammatory stress
Kidney	Cortical tubules tightly packed with intact epithelium; glomeruli normal in size and cellularity; **absent** interstitial edema, fibrosis, leukocyte infiltration or protein casts.	No tubular degeneration or glomerular injury, critical because kidneys are a common accumulation site for our smaller GNPs (<10nm).
Spleen	Balanced red- to white-pulp ratio; extramedullary hematopoiesis and lymphoid follicles within the expected range; no pigment overload, hyperplasia or necrosis.	Normal splenic turnover indicates that systemic immune or hemolytic responses to GNPs were not triggered at the doses tested.
Stomach	Intact squamous and glandular mucosa; mature gastric glands; occasional ingesta and sparse background mononuclear cells; no ulceration, edema or fibrosis.	Absence of mucosal erosion or inflammatory infiltrate suggests the GNP formulation is not locally irritating.
Heart	Ventricular myocardium and valves structurally normal; no myocyte necrosis, fibrosis or inflammatory infiltrates.	Cardiomyocytes remain uninjured, indicating no acute or chronic cardiotoxic effect.
Lungs	Bronchial/bronchiolar epithelium well preserved; alveolar walls thin with no hypercellularity; vasculature and pleura unremarkable; no edema, hemorrhage, leukocytes or fibrosis.	The respiratory tract shows no evidence of GNP-induced oxidative or inflammatory damage.

4.4.3 PBPK model

Optimization:

The optimized values for the maximum rate of phagocytosis (P_{up}), the rate of excretion into bile (K_{Bile}), the lymph reflection coefficient (σ^{IS}) and the IP bioavailability (F) were 0.995 mL/h/Ml macrophages, 0.0128/h, 0.64 and 0.76 respectively. Figure 4.12 shows the final mouse model simulations compared to the observed biodistribution data for Curc- and EGCG-capped GNPs in this study. Despite the wide variability in the data, an absolute average fold error of 1.48 was achieved between the model predictions and the observed mean values in all organs. All organ profiles after fitting to liver and spleen are available in the Appendix Materials. While the overall fit was acceptable, the model tended to over-predict amounts in organs with very low or near-zero exposure (heart, kidney and lung) and under-predict amounts in portal organs (spleen and stomach) after IP administration. The optimized model was then evaluated.

Model Evaluation:

The mouse model was successfully adapted to represent rats with anatomical and physiological parameters. Figure 4.13 demonstrates the utility of the PBPK model for extrapolation across particle sizes, doses (0.01, 0.7 and 10 mg Au/kg), routes of administration (IP vs. IV) and species (mouse vs rat). Liver profiles were approximated well at all doses. As with the original mouse model, there was a trend for an over-prediction in organs with very low exposures. Given the uncertainty in the data and the heterogeneity in the experiments, the model was proficient for rats with predictions across all organs achieving an absolute average fold error of 2.18. Much of the error was driven by an over-prediction of the Au content in the lung. All organ profiles for model evaluation are available in the Supplementary Materials.

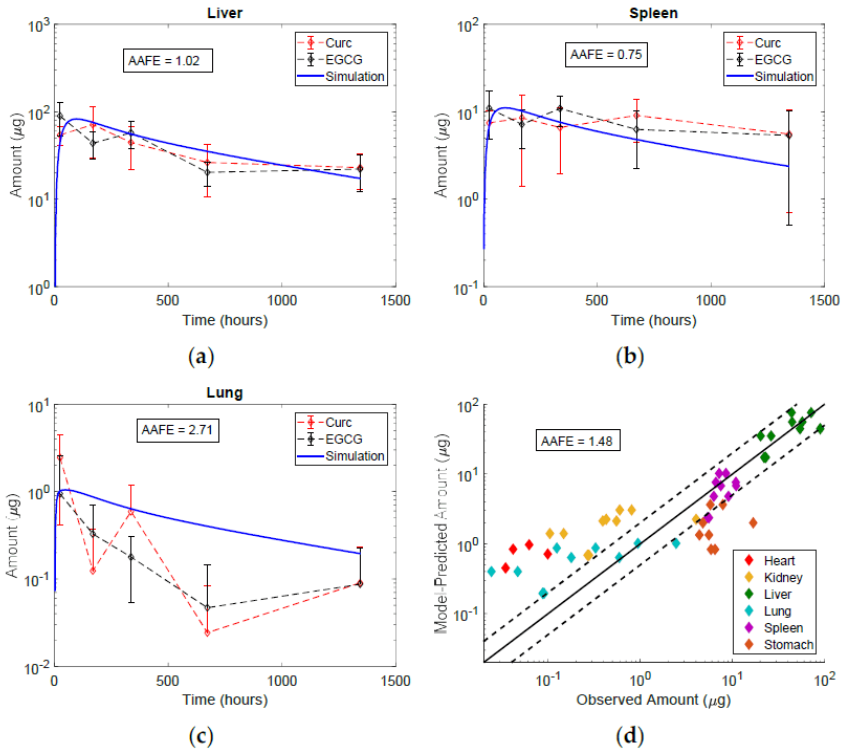


Figure 4.12: *Model Simulation vs Observed Biodistribution*: Final mouse model simulations compared to the observed biodistribution data for organs in this study: (a) liver (b) spleen and (c) lung. (d) shows the model-predicted vs. observed amounts in each organ with relation to the equality line achieving an absolute average fold error of 1.48. Aborig *et al.* [34]

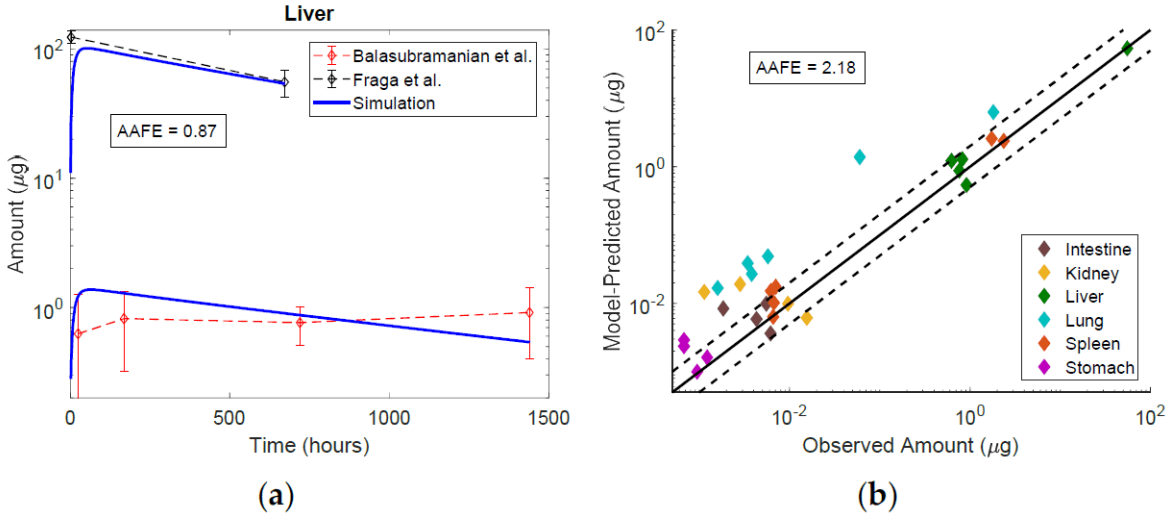


Figure 4.13: *Interspecies extrapolation from mouse to rat*: Rat model simulations compared to the observed biodistribution data in rats after IV administration from Balasubramanian *et al.* [45] and Fraga *et al.* [27] (a) shows the liver profiles and (b) shows the model-predicted vs. observed amounts in each organ with relation to the equality line achieving an absolute average fold error of 2.18. Aborig *et al.* [34]

Sensitivity Analysis:

To assess the relative importance of each process in the biodistribution of NPs after IV administration in mice, key parameters were perturbed by ±10%, and the resulting changes in liver and spleen AUC outputs are reported in Figure 4.14. When comparing the two, liver exposure is more sensitive to changes in extravasation (e.g., solute radius) and spleen exposure is more sensitive to changes in cellular uptake.

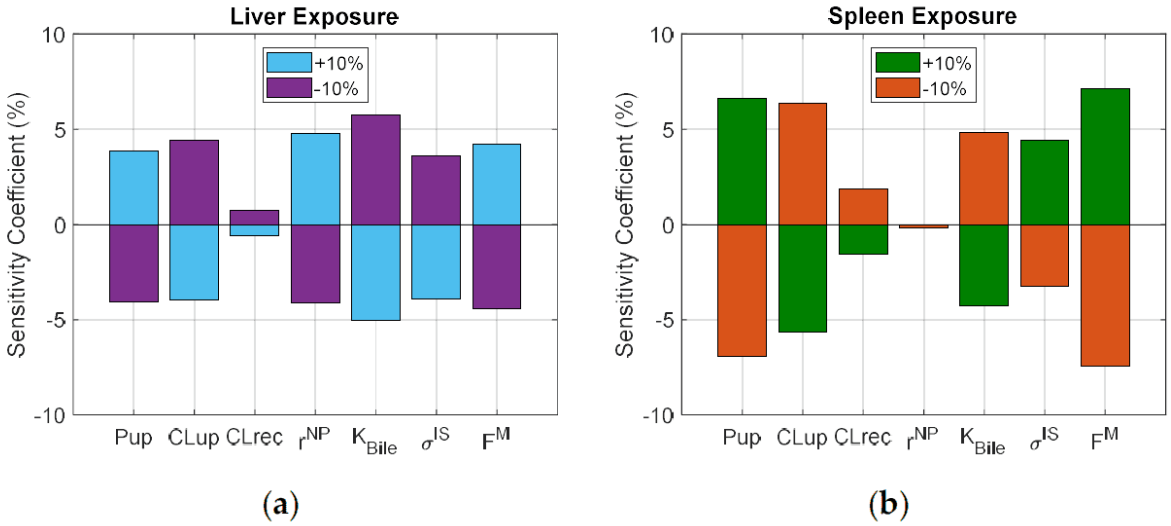


Figure 4.14: Sensitivity of liver (a) and spleen (b) exposures to relative perturbations in key parameters. Pup = maximum rate of phagocytosis; $CLup$ = rate of pinocytosis; $CLrec$ = rate of exocytosis; r^{Np} = nanoparticle hydrodynamic radius; K_{Bile} = rate of excretion into bile; σ^{IS} = lymph reflection coefficient; F^M = macrophage fraction of organ. Aborig *et al.* [34]

The PBPK model was designed and calibrated with the biodistribution data generated in this mouse study by IP administration of 10 mg/kg EGCG- and Curc-GNPs. Following optimization to the liver and spleen profiles for these entities, the model demonstrated convincing accuracy for describing Au amounts in each organ over time (liver, spleen, heart, kidney, lung and stomach), with an absolute average fold error of 1.48 (Figure 4.12). The model over-predicted Au amounts in organs with very low or near zero exposure. While the absolute difference is negligible, this phenomenon may be explained by the loss of blood or other organ fluid during sample preparation and transfer, or misspecification of convection and diffusion parameters in the two-pore model; as the convection-and-diffusion equations governing GNP escape from capillaries were originally validated for small molecules. There were notable uncertainties in the modeling of IP administration. High observed amounts in the stomach are not traditionally seen following IV administration of inorganic NPs, and thus the under-prediction of the model for this organ was attributed to this uncertainty.

The test for interspecies extrapolation to rats passed with reasonable accuracy, achieving an absolute average fold error of 2.18 (Figure 4.13). While most organs were within 2.5-fold error, there was a trend for over-prediction of Au amounts in organs with very low or

near-zero exposure, especially the lung (AAFE = 9.10 across the data from both studies). The lung organ composition is unique because it is made up of 80% extracellular fluid. If the over-prediction error is due to loss of organ fluid (blood, interstitial fluid) during sample obtainment and transfer, then it follows logically that the lung presents with the highest error. The overall accuracy in interspecies extrapolation is acceptable given the extrapolation not only across species, but also across doses, routes of administration, particle sizes and experimental designs. While the calibration data in this study was generated at a dose of 10 mg/kg IP in mice, the evaluation datasets were generated at doses of 0.01 and 0.07 mg/kg by IV administration in rats with GNPs of significantly larger hydrodynamic radii (median 12 nm in calibration vs. 23 nm in evaluation datasets) and using citrate as the alternative capping agent. Citrate maintains a similar negative charge to curcumin and EGCG, and in the absence of any in vitro studies comparing the various capping agents, the impact of this physicochemical alteration on biodistribution was not accounted for in the model. Further exploration of the impact of surface charge on phagocytic uptake may inform these features in the future.

4.4.4 Canine Study

Beagle studies:

Complete blood counts, serum biochemistry and urinalysis were obtained before IA injection of EGCG-GNPs and at all follow-up points. Baseline values lay within the established canine reference ranges and served as the comparator for post-procedure results. After injection, liver enzymes ALT, ALP and GGT, together with albumin, globulin and cholesterol, remained within or very close to their reference intervals; the brief, mild rises in ALP and creatine kinase seen at 24 hours in two dogs resolved by Day 7 and were attributed to the catheter procedure rather than to the GNPs (Table C.2). Creatinine, urea, electrolyte and phosphate concentrations were stable, and urine specific gravity, protein, blood and sediment showed no progressive abnormalities (Table C.3). Haematologic indices which included neutrophils, lymphocytes, monocytes, platelets and haematocrit, also fluctuated only minimally and without a consistent pattern (Table C.1). Taken together, these findings indicate that the EGCG-GNP administration produced no clinically significant hepatic, renal or haematological toxicity in any beagle. Detailed numerical data on CBC, serum biochemistry and urinalysis are provided in the appendix tables of this chapter (Table C.1, C.2, and C.3 respectively).

The temperature of all beagles remained within the normal range during and throughout the post- procedure monitoring period (average: 38.45 °C). The total time under anesthesia

for the procedure was approximately 2.92 ± 1.1 hours, and the total procedure time was on average 2.21 ± 0.57 hours. Pulse and respiration rates were within normal ranges (68–128 bpm; respiration: 16–40 breaths per minute). Physical behavior monitoring showed normal activity related to appetite, alertness, and perceived energy levels for Beagles 1 and 2, with only mild reductions in activity observed during recovery from the I.A./PAE procedure. However, Beagle 3 experienced adverse events, showing signs of lethargy and discomfort post-procedure. On Day 2, additional adverse events were reported, including signs of abdominal pain, constipation, excessive panting, and nausea. Beagle 3 was administered buprenorphine (0.3 mg/mL IV) and an anti-nausea medication (maropitant citrate, 10 mg/mL IV), and was monitored closely. Following a bowel movement on Day 3 post-procedure, Beagle 3's condition showed significant improvement.

A central objective of the canine study was to determine whether a 1.5 mg/mL EGCG-GNP suspension could reproduce, in vivo, the approximately 58 HU/mg Au signal observed in water phantom experiments. In the phantom studies of chapter 2, vials with concentrations ≥0.5 mg Au/mL produced clear and distinguishable contrast. However, in the dogs, 1-hour post-procedure scans were dominated by iodinated Isovue contrast used for microcatheter guidance; this resulted in marked enhancement of the kidneys and urethra in all animals, and the bladder and prostate in Beagles 2 and 3, making it impossible to isolate the EGCG-GNP signal at that early time point (Figure 4.15). After the iodine contrast cleared, only modest residual enhancement remained: Beagle 3's prostate reached a mean of about 609 HU at one hour but fell to 112 HU by 48 hours; Beagle 2 peaked at roughly 355 HU; Beagle 1 showed no discernible uptake. Several factors may explain this shortfall:

(i) Intra-arterial delivery may not have achieved durable GNP retention in prostatic tissue, allowing for rapid wash-out or systemic redistribution.

(ii) The 1.5 mg/mL GNP formulation could have been diluted by blood, interstitial fluid, or prostatic secretions immediately after injection, lowering the local gold concentration below the 0.5 mg/mL threshold identified in water phantom studies.

(iii) The pelvic environment of a live beagle, with surrounding bone, heterogeneous soft tissue, and motion artifact, may attenuate the X-ray beam and increase scatter, reducing apparent signal compared to the idealized setting of GNP vials in water.

Collectively, these factors help explain why post-procedural CT attenuation was lower than predicted from bench measurements. This is consistent with the challenges reported in translating nanoparticle-based imaging from controlled laboratory settings to the complex in

vivo environment. Figure 4.15 below illustrates this effect, showing the high CT attenuation observed in Beagle 3 at 1 hour post-procedure, followed by a gradual decline in signal over time, with no identifiable hyperdense areas remaining in the prostate lobe by Day 6 where EGCG-GNPs would be expected to accumulate due to Embosphere mediated bloackage.

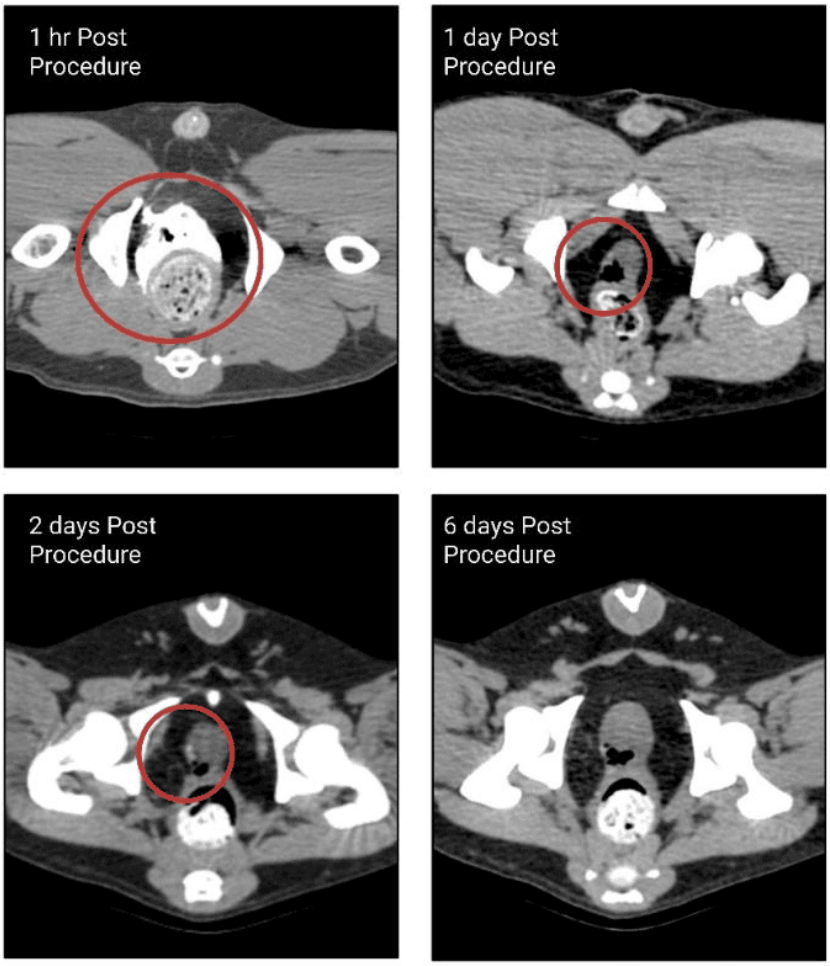


Figure 4.15: Axial CT of Beagle 3 (red circle). Strong intraprostatic/bladder contrast at 1 h post-procedure fades by 1 day, lessens further at 2 days, and is nearly absent by day 6. Image reproduced from McKenna, C. J. (2021). Investigating a novel approach to prostate tumour treatment in dogs (Master's thesis, University of Guelph). © Charly Jean McKenna.

Clinical Study:

The 12-year-old Boston Terrier tolerated catheter-directed infusion of carboplatin (10 mg/kg) admixed with 1 mL of 1.5 mg/mL EGCG-GNPs to each prostatic lobe without intra-operative complications. Within the first hour, contrast-enhanced ultrasound indicated loss of intraprostatic perfusion and the development of intraglandular gas, suggesting acute vascular stasis and possible interaction between the platinum drug and the GNP suspension. During the initial 24 h of intensive care, vital parameters were stable, but progressive leukocytosis ($24.5 \times 10^9\ L^{-1}$) and marked creatine-kinase, amylase, and lipase surges signalled systemic inflammatory and pancreatic injury. By the second day, deterioration was rapid : abrupt neutropenia ($0.59 \times 10^9\ L^{-1}$), severe thrombocytopenia ($99 \times 10^9\ L^{-1}$), rising azotaemia, and hypo-albuminaemia accompanied fever, hypotension, and ventricular arrhythmias unresponsive to vasopressors, culminating in cardiopulmonary arrest approximately 48 h post-procedure. Post-mortem imaging and necropsy demonstrated a large multinodular prostatic carcinoma, widespread fibrinous peritonitis, bladder vascular distension, biventricular myocardial degeneration and myxomatous atrioventricular valves, together with polymicrobial infection caused by the bacterial pathogens *Enterococcus faecium*, *Klebsiella pneumoniae* and *Pediococcus acidilactici* cultured from the bladder, filter organs and jugular catheter. The overall picture indicates that the fatal outcome was driven by pre-existing prostatic neoplasia complicated by urinary tract infection, systemic inflammatory response and cardiovascular compromise.

EGCG-GNP causality is difficult to assess in this case, as the nanoparticles were administered in conjunction with a highly toxic chemotherapeutic, carboplatin. Carboplatin's well-known dose-limiting toxicity is bone marrow suppression, which can sharply reduce blood cell production (myelosuppression) and thereby increase the risk of infection, anemia, and bleeding (Pfizer: Carboplatin Prescribing information) [60]. Notably, carboplatin frequently induces neutropenia in treated dogs, and in some instances this progresses to life-threatening neutropenic sepsis [61]. Additionally, the poor preexisting condition of the 12 year old dog, which included intervertebral disk disease, suspect focal seizures and degenerative valvular disease further complicate root-cause analysis. In the Boston Terrier, the sudden onset of severe neutropenia and thrombocytopenia by the second day post-infusion is consistent with acute carboplatin-induced myelosuppression, which would critically impair the dog's ability to fight infection. Smaller dogs are particularly susceptible to severe hematologic toxicity from carboplatin – one study found that dogs <10 kg had significantly higher odds of developing grade 3–4 neutropenia and thrombocytopenia compared to larger dogs [61]. This heightened vulnerability in a small patient may have further predisposed the Boston Terrier to overwhelming infection (and

even hemorrhagic complications like hematuria) following chemotherapy.

Another consideration is the possibility of an iatrogenic infection introduced during the intra-arterial EGCG-GNP/carboplatin treatment. If the EGCG-GNP solution or catheter apparatus was not completely sterile, it could have directly seeded bacteria into the bloodstream or urinary tract. The necropsy finding of polymicrobial infection (involving Enterococcus faecium, Klebsiella pneumoniae, and Pediococcus spp.) supports the presence of a systemic infection; this may have originated from the pre-existing urinary tract infection or from contaminants introduced during the procedure. However, any such infection became lethal largely because the dog's immune defenses were compromised, a consequence expected with carboplatin's immunosuppressive effect. Several factors appear to have converged to produce the fatal outcome, including advanced prostate carcinoma, a pre-existing urinary infection, degenerative cardiac disease, and procedural stress. In addition, the pronounced myelosuppression observed after treatment raises concern about a possible immunosuppressive effect from the combined use of carboplatin and EGCG-GNPs. Because these events unfolded amid many confounders, the precise role of each agent cannot be assigned with certainty; nevertheless, the rapid decline in neutrophil and platelet counts mirrors carboplatin's recognized toxicity and may have weakened host defenses, permitting infection and systemic inflammation to spiral out of control. Potential toxicity or contamination from the EGCG GNP suspension cannot be excluded, yet the formulation was prepared under strict aseptic conditions in a class II laminar flow hood, passed through a 0.22 μm sterile filter, and handled only with autoclaved glassware and single use syringes and catheters, which reduces the likelihood that EGCG-GNPs themselves introduced or amplified the infectious process. Moreover, most published studies have not linked GNPs to clinically significant myelosuppression; this effect has only been observed when GNPs are conjugated or loaded with immune suppressors such as chemotherapeutics (doxorubicin, gemcitabine, or paclitaxel) [62, 63]. Therefore, carboplatin remains the more plausible cause of the abrupt neutropenia and thrombocytopenia observed in this case.

4.5 Conclusion

In vivo studies in CD-1 mice revealed that both EGCG-GNPs and Curc-GNPs predominantly accumulate in reticuloendothelial organs. The liver was the principal site of gold deposition at all examined time points, followed by the spleen and, to a lesser extent, the stomach. This distribution aligns with expectations for ~20-25 nm GNPs, which are efficiently sequestered by hepatic Kupffer cells and splenic macrophages of the mononuclear phagocyte system. Minimal gold was detected in the kidneys, and by later time points (14-56 days)

renal gold levels declined to near zero, indicating that glomerular clearance was negligible for these ~20–40 nm (protein corona-enlarged) GNPs. Instead, clearance occurred via hepatobiliary excretion: gold content in the liver decreased significantly over the 56-day study period, with hepatic gold levels roughly four-fold lower by day 56 compared to day 1. Both EGCG-GNP and Curc-GNP exhibited this downward trend in hepatic gold burden, demonstrating time-dependent nanoparticle elimination from the liver. Notably, no statistically significant differences were observed between EGCG- and Curcumin-coated GNPs in their organ distribution or clearance profiles, suggesting that the capping agents did not markedly alter in vivo biodistribution under these conditions. The spleen, in contrast to the liver, showed persistent gold retention with no clear decrease over time, indicating that splenic sequestration may lead to longer-term EGCG-GNP/Curc-GNP deposition (a known behavior for nanoparticles that accumulate in splenic macrophages).

Crucially, the murine experiments demonstrated a favorable toxicity profile for both GNP formulations. No abnormal behavior or clinical signs of illness were noted in treated mice throughout the monitoring period. All animals gained weight normally after injection, with no instances of $>10\%$ body weight loss. In addition, organ weight analyses showed only few instances of differences between GNP-treated mice and controls, with liver and spleen weight-to-body weight ratios remaining in the normal range. The only notable findings were one case of kidney atrophy in the Curc-GNP group at 24 hours and one case of liver atrophy in the EGCG-GNP group at 7 days post-procedure. Histopathological examination of major organs (liver, spleen, kidneys, lungs, and stomach) revealed no overt lesions or tissue damage attributable to GNP accumulation. Consistent with the benign clinical observations, there were no signs of acute inflammation, necrosis, or degenerative changes in GNP-exposed tissues. These findings collectively indicate that at the tested dose (10 mg Au per kg, delivered intraperitoneally), EGCG-GNPs and Curc-GNPs were well tolerated in mice. This favorable biodistribution and toxicity profile in mice provided a critical foundation for advancing larger animal models.

The PBPK model effectively predicted GNP biodistribution in mice and successfully extrapolated to rats across various doses, routes, and particle sizes, especially for liver profiles. However, it consistently over-predicted GNP amounts in organs with very low exposure and showed some under-prediction in portal organs after IP administration. These discrepancies might stem from challenges in modeling IP administration or potential fluid loss during sample preparation. Despite these limitations, the model's overall accuracy for interspecies extrapolation is acceptable given the wide range of conditions it accounts for.

Encouraged by the murine results, a pilot study in canine subjects was conducted to assess the feasibility and safety of intra-arterial GNP delivery to the prostate, as well as the potential benefits of combining nanoparticle infusion with prostatic artery embolization.

The procedures were successfully carried out in 3 laboratory beagle dogs under image-guided catheterization, demonstrating the practical feasibility of targeted intra-arterial nanotherapy. All three dogs tolerated their respective procedures with no major immediate complications. Real-time imaging and post-procedure monitoring indicated that vital signs remained stable; there were no acute toxic reactions to the nanoparticles or the embolic agents. Serial bloodwork (hematology and serum chemistry) and urinalysis conducted from 1 day to 1 week post-procedure did not show significant abnormalities, suggesting that the EGCG-GNP infusion and PAE were both well tolerated systemically. CT-contrast in lab beagles did not present CT-attenuation as hypothesized with 24 hours showing high contrast but are confounded with iodine contrast agent administration, day 1, 2 and 6 days post-procedure showed little to no CT-attenuation. Despite this, the combination of IA nanodrug delivery with embolization proved technically feasible and safe in healthy canines.

The clinical case of a 12-year-old Boston Terrier with spontaneous plasmacytoid urothelial carcinoma confirmed the technical feasibility of bilateral IA delivery of 1 mL EGCG-GNP (1.5 mg Au/mL) plus 5.5 mL carboplatin (10 mg/mL) per lobe, yet highlighted important safety challenges. Although catheter placement and infusion were uneventful, the dog developed severe pancytopenia, sepsis and cardiovascular collapse within 48 h findings most consistent with acute carboplatin-induced myelosuppression compounded by pre-existing infection and comorbidities; EGCG-GNP specific toxicity could not be distinguished. This sentinel event underscores the need for cautious cytotoxic dosing, rigorous sterility controls and more sensitive, real-time methods to track nanoparticle distribution in diseased tissue.

A key limitation identified across experiments was inadequate long-term visualization of 1.5 mg/mL EGCG-GNPs by conventional CT, especially after iodine contrast dissipated. To address this, future work will focus on radiotheranostic EGCG-^{198}Au GNPs, whose γ-emission enables SPECT tracking while β- particles deliver a cytotoxic payload. Intrinsic contrast of EGCG-GNPs is important for verifying drug retention and facilitating treatment planning and dosimetry for radiotherapy. Additional priorities include reducing splenic retention through surface-chemistry optimization, refining embolization protocols to maximize intratumoral trapping, and expanding canine cohorts to prostate cancer patients without coadministration of toxic chemotherapeutics to better characterize efficacy and reduce confounding variables. Together, these steps will advance the EGCG-GNP platform toward a clinically viable, image- guided nanoradiotherapeutic for prostate cancer.

References

[1] E. Blanco, H. Shen, and M. Ferrari. "Principles of nanoparticle design for overcoming biological barriers to drug delivery". In: *Nature Biotechnology* 33.9 (2015), pp. 941–951. DOI: 10.1038/nbt.3330.

[2] N. Rosenthal and S. Brown. "The mouse ascending: perspectives for human-disease models". In: *Nature Cell Biology* 9.9 (2007), pp. 993–999. DOI: 10.1038/ncb437.

[3] Elizabeth C. Bryda. "The Mighty Mouse: The Impact of Rodents on Advances in Biomedical Research". In: *Missouri Medicine* 110.3 (May 2013), p. 207. URL: https://www.ncbi.nlm.nih.gov/pmc/articles/PMC3987984/.

[4] Bruce E. Leroy and Nicole Northrup. "Prostate cancer in dogs: comparative and clinical aspects". In: *The Veterinary Journal* 180.2 (May 2009), pp. 149–162. DOI: 10.1016/j.tvjl.2008.07.012.

[5] Francisco Cesar Carnevale and et al. "Prostatic Artery Embolization for the Treatment of Lower Urinary Tract Symptoms Due to Benign Prostatic Hyperplasia: 10 Years' Experience". In: *Radiology* 296.2 (Aug. 2020), pp. 444–451. DOI: 10.1148/radiol.2020191249.

[6] National Institute of Diabetes and Digestive and Kidney Diseases. *Enlarged Prostate (Benign Prostatic Hyperplasia)*. https://www.niddk.nih.gov/health-information/urologic-diseases/prostate-problems/enlarged-prostate-benign-prostatic-hyperplasia. Accessed 2 July 2025. 2025.

[7] Nicholas Brown and et al. "The 'Prostate Embolisation AS first-line therapY compAred to meDication in treatment naïVe men with prostAte eNlargement, a randomised ControllEd trial' (P-EASY ADVANCE): a randomised controlled trial of prostate embolisation vs medication for BPH". In: *BJU International* 134.Suppl 2 (Aug. 2024), p. 38. DOI: 10.1111/bju.16479.

[8] Xiao-Yan Wang and et al. "Prostate artery embolization on lower urinary tract symptoms related to benign prostatic hyperplasia: A systematic review and meta-analysis". In: *World Journal of Clinical Cases* 10.32 (Nov. 2022), pp. 11812–11826. DOI: 10.12998/wjcc.v10.i32.11812.

[9] Tiago Bilhim and et al. "Prostatic Arterial Supply: Anatomic and Imaging Findings Relevant for Selective Arterial Embolization". In: *Journal of Vascular and Interventional Radiology* 23.11 (Nov. 2012), pp. 1403–1415. DOI: 10.1016/j.jvir.2012.07.028.

[10] Sachin Modi and Mark Harris. "Prostate Artery Embolisation in the Treatment of Benign Prostatic Hyperplasia: A Multidisciplinary Approach". In: *EMJ* 10 (Apr. 2022), pp. 02–13. URL: https://www.emjreviews.com/en-us/amj/urology/article/prostate-artery-embolisation-in-the-treatment-of-benign-prostatic-hyperplasia-a-multidisciplinary-approach-s181022.

[11] Orlando Burkhardt and et al. "Prostatic Artery Embolization in Patients with Prostate Cancer: A Systematic Review". In: *European Urology Focus* 10.3 (May 2024), pp. 387–399. DOI: 10.1016/j.euf.2023.02.005.

[12] Livio Mordasini and et al. "Prostatic Artery Embolization in the Treatment of Localized Prostate Cancer: A Bicentric Prospective Proof-of-Concept Study of 12 Patients". In: *Journal of Vascular and Interventional Radiology* 29.5 (May 2018), pp. 589–597. DOI: 10.1016/j.jvir.2018.01.766.

[13] Dan Peer and et al. "Nanocarriers as an emerging platform for cancer therapy". In: *Nature Nanotechnology* 2.12 (Dec. 2007), pp. 751–760. DOI: 10.1038/nnano.2007.387.

[14] Karl T. Butterworth et al. "A Mechanistic Overview of Gold Nanoparticle Radiosensitization: Is It All about DNA?" In: *Nanomedicine* 9.17 (2014), pp. 257–265.

[15] Laura E. Taggart et al. "The Role of Gold Nanoparticle Shape and Size in Radiosensitization of Cancer Cells". In: *Scientific Reports* 7 (2017), p. 40685.

[16] Catherine Carnovale et al. "Identifying trends in gold nanoparticle toxicity and uptake: size, shape, capping ligand, and biological corona". In: *ACS omega* 4.1 (2019), pp. 242–256.

[17] Yan-Peng Jia and et al. "The in vitro and in vivo toxicity of gold nanoparticles". In: *Chinese Chemical Letters* 28.4 (2017), pp. 691–702.

[18] Alice Balfourier and et al. "Gold-based therapy: From past to present". In: *Proceedings of the National Academy of Sciences of the United States of America* 117.37 (Sept. 2020), pp. 22639–22648. DOI: 10.1073/pnas.2007285117.

[19] I. Kenkyu. "Data on auranofin toxicity in mice". In: *Iyakuhin Kenkyu* 17 (1986), pp. 1106–1112.

[20] Alaaldin M. Alkilany and Catherine J. Murphy. "Toxicity and cellular uptake of gold nanoparticles: What we have learned so far?" In: *Journal of Nanoparticle Research* 12.7 (2010), pp. 2313–2333.

[21] Hm Jones and K. Rowland-Yeo. "Basic concepts in physiologically based pharmacokinetic modeling in drug discovery and development". In: *CPT: Pharmacometrics & Systems Pharmacology* 2.8 (Aug. 2013), e63. DOI: 10.1038/psp.2013.41.

[22] Steven A. Bailey and et al. "Relationships between organ weight and body/brain weight in the rat: what is the best analytical endpoint?" In: *Toxicologic Pathology* 32.4 (July 2004), pp. 448–466. DOI: 10.1080/01926230490465874.

[23] Stanley E. Lazic and et al. "Determining organ weight toxicity with Bayesian causal models: Improving on the analysis of relative organ weights". In: *Scientific Reports* 10.6625 (Apr. 2020), pp. 1–12. DOI: 10.1038/s41598-020-63465-y.

[24] Evisabel A. Craig and et al. "The relationship between chemical-induced kidney weight increases and kidney histopathology in rats". In: *Journal of Applied Toxicology* 35.7 (July 2015), pp. 729–736. DOI: 10.1002/jat.3036.

[25] Roman Mezencev and et al. "The association between histopathologic effects and liver weight changes induced in mice and rats by chemical exposures: an analysis of the data from Toxicity Reference Database (ToxRefDB)". In: *Toxicological Sciences* 200.2 (Aug. 2024), pp. 404–413. DOI: 10.1093/toxsci/kfae056.

[26] Rani S. Sellers and et al. "Society of Toxicologic Pathology position paper: organ weight recommendations for toxicology studies". In: *Toxicologic Pathology* 35.5 (Aug. 2007), pp. 751–755. DOI: 10.1080/01926230701595300.

[27] Sónia Fraga et al. "Short-and long-term distribution and toxicity of gold nanoparticles in the rat after a single-dose intravenous administration". In: *Nanomedicine: Nanotechnology, Biology and Medicine* 10.8 (2014), pp. 1757–1766.

[28] C. Niederalt et al. "A generic whole body physiologically based pharmacokinetic model for therapeutic proteins in PK-Sim". In: *Journal of Pharmacokinetics and Pharmacodynamics* 45 (2018), pp. 235–257. DOI: 10.1007/s10928-018-9576-5.

[29] D.E. Mager et al. "Physiologically based pharmacokinetic model for composite nanodevices: Effect of charge and size on in vivo disposition". In: *Pharmaceutical Research* 29 (2012), pp. 2534–2542. DOI: 10.1007/s11095-012-0785-1.

[30] U. Carlander et al. "Toward a general physiologically-based pharmacokinetic model for intravenously injected nanoparticles". In: *International Journal of Nanomedicine* 11 (2016), pp. 625–640. DOI: 10.2147/IJN.S100046.

[31] Z. Lin, N.A. Monteiro-Riviere, and J.E. Riviere. "A physiologically based pharmacokinetic model for polyethylene glycol-coated gold nanoparticles of different sizes in adult mice". In: *Nanotoxicology* 10 (2016), pp. 162–172. DOI: 10.3109/17435390.2015.1039060.

[32] G. Bachler, N. von Goetz, and K. Hungerbühler. "A physiologically based pharmacokinetic model for ionic silver and silver nanoparticles". In: *International Journal of Nanomedicine* 8 (2013), pp. 3365–3382. DOI: 10.2147/IJN.S49785.

[33] B. Rippe and B. Haraldsson. "Transport of macromolecules across microvascular walls: The two-pore theory". In: *Physiological Reviews* 74 (1994), pp. 163–219. DOI: 10.1152/physrev.1994.74.1.163.

[34] Mohamed Aborig et al. "Biodistribution and Physiologically-Based Pharmacokinetic Modeling of Gold Nanoparticles in Mice with Interspecies Extrapolation". In: *Pharmaceutics* 11.4 (Apr. 2019), p. 179. ISSN: 1999-4923. DOI: 10.3390/pharmaceutics11040179.

[35] M. Longmire, P.L. Choyke, and H. Kobayashi. "Clearance properties of nano-sized particles and molecules as imaging agents: Considerations and caveats". In: *Nanomedicine* 3 (2008), pp. 703–717. DOI: 10.2217/17435889.3.5.703.

[36] D.K. Shah and A.M. Betts. "Towards a platform PBPK model to characterize the plasma and tissue disposition of monoclonal antibodies in preclinical species and human". In: *Journal of Pharmacokinetics and Pharmacodynamics* 39 (2012), pp. 67–86. DOI: 10.1007/s10928-011-9232-2.

[37] Yang Chen and Joseph P. Balthasar. "Evaluation of a catenary PBPK model for predicting the in vivo disposition of mAbs engineered for high-affinity binding to FcRn". In: *AAPS Journal* 14.4 (Dec. 2012), pp. 850–859. DOI: 10.1208/s12248-012-9395-9.

[38] T. Li and J.P. Balthasar. "Application of Physiologically Based Pharmacokinetic Modeling to Predict the Effects of FcRn Inhibitors in Mice, Rats, and Monkeys". In: *Journal of Pharmaceutical Sciences* 108 (2019), pp. 701–713. DOI: 10.1016/j.xphs.2018.11.015.

[39] H. Morales-Navarrete et al. "A versatile pipeline for the multi-scale digital reconstruction and quantitative analysis of 3D tissue architecture". In: *eLife* 4 (2015), e11214. DOI: 10.7554/eLife.11214.

[40] Janie L. Baratta et al. "Cellular organization of normal mouse liver: a histological, quantitative immunocytochemical, and fine structural analysis". In: *Histochemistry and Cell Biology* 131.6 (June 2009), pp. 713–726. DOI: 10.1007/s00418-009-0577-1.

[41] *Blood Basics*. https://www.hematology.org/Patients/Basics/. Accessed 1 February 2019.

[42] A. J. P. Veerman and W. van Ewijk. "White pulp compartments in the spleen of rats and mice". In: *Cell and Tissue Research* 156.4 (Mar. 1975), pp. 417–441. DOI: 10.1007/BF00225103.

[43] Arnold M. Markoe and James P. Okunewick. "Changes in Spleen Cellularity and Erythrocyte Accumulation Following Rauscher Virus Infection in the Mouse". In: *Scandinavian Journal of Haematology* 10.4 (Apr. 1973), pp. 273–281. DOI: 10.1111/j.1600-0609.1973.tb00072.x.

[44] M. Beran and B. Tribukait. "The Quantitative Bone Marrow and Spleen Composition in Male NMRI and CBA Mice". In: *Acta Haematologica* 45.1 (Mar. 2009), pp. 55–64. DOI: 10.1159/000208607.

[45] Suresh K. Balasubramanian and et al. "Biodistribution of gold nanoparticles and gene expression changes in the liver and spleen after intravenous administration in rats". In: *Biomaterials* 31.8 (Mar. 2010), pp. 2034–2042. DOI: 10.1016/j.biomaterials.2009.11.079.

[46] A. Miauton et al. "Safety and immunogenicity of a synthetic nanoparticle-based t-cell-priming peptide vaccine against dengue in healthy adults in Switzerland: A double-blind, randomized, vehicle-controlled, phase-1 study". In: *eBioMedicine* 99 (2024), p. 104922.

[47] A. R. Rastinehad et al. "Gold nanoshell-localized photothermal ablation of prostate tumors in a clinical pilot device study". In: *Proceedings of the National Academy of Sciences* 116.37 (2019), pp. 18590–18596.

[48] Wim H. De Jong and et al. "Particle size-dependent organ distribution of gold nanoparticles after intravenous administration". In: *Biomaterials* 29.12 (Apr. 2008), pp. 1912–1919. DOI: 10.1016/j.biomaterials.2007.12.037.

[49] Ganeshchandra Sonavane and et al. "Biodistribution of Colloidal Gold Nanoparticles After Intravenous Administration: Effect of Particle Size". In: *Colloids and Surfaces B: Biointerfaces* 66 (Nov. 2008), pp. 274–280. DOI: 10.1016/j.colsurfb.2008.07.004.

[50] Sonia Gaur and et al. "Gold nanoshells for prostate cancer treatment: evidence for deposition in abdominal organs". In: *Abdominal Radiology* 49.6 (June 2024), pp. 1929–1939. DOI: 10.1007/s00261-024-04184-0.

[51] Xue Li et al. "Surface chemistry governs the sub-organ transfer, clearance and toxicity of functional gold nanoparticles in the liver and kidney". In: *Journal of nanobiotechnology* 18 (2020), pp. 1–16.

[52] Bindhu Michael and et al. "Evaluation of Organ Weights for Rodent and Non-Rodent Toxicity Studies: A Review of Regulatory Guidelines and a Survey of Current Practices". In: *Toxicologic Pathology* 35.5 (Aug. 2007), pp. 742–750. DOI: 10.1080/01926230701595292.

[53] Ruike Yan and Yanli Cao. "The Safety and Efficacy of Dietary Epigallocatechin Gallate Supplementation for the Management of Obesity and Non-Alcoholic Fatty Liver Disease: Recent Updates". In: *Biomedicines* 13.1 (Jan. 2025), p. 206. DOI: 10.3390/biomedicines13010206.

[54] Zheming Yu and et al. "Effect of Green Tea Supplements on Liver Enzyme Elevation: Results from a Randomized Intervention Study in the United States". In: *Cancer Prevention Research* 10.10 (Oct. 2017), pp. 571–579. DOI: 10.1158/1940-6207.CAPR-17-0160.

[55] Onica Washington and et al. "Oxalate nephropathy and chronic turmeric supplementation: a case report". In: *Jornal Brasileiro de Nefrologia* 46.1 (Jan. 2024), p. 99. DOI: 10.1590/2175-8239-JBN-2023-0079en.

[56] Matthew A. Weir and et al. "The effect of micro-particle curcumin on chronic kidney disease progression: the MPAC-CKD randomized clinical trial". In: *Nephrology Dialysis Transplantation* 38.10 (Feb. 2023), p. 2192. DOI: 10.1093/ndt/gfad037.

[57] Mahdi Vajdi and et al. "Curcumin supplementation effect on liver enzymes in patients with nonalcoholic fatty liver disease: a GRADE-assessed systematic review and dose-response meta-analysis of randomized controlled trials". In: *Nutrition Reviews* 83.1 (Jan. 2025), pp. 1–12. DOI: 10.1093/nutrit/nuad166.

[58] National Center for Biotechnology Information. *Curcumin. PubChem Compound Summary for CID 969516*. Accessed July 2025. 2025. URL: https://pubchem.ncbi.nlm.nih.gov/compound/Curcumin#section=Acute-Effects.

[59] C. Jantawong et al. *Curcumin-loaded nanocomplexes: Acute and chronic toxicity studies in mice and hamsters*. 2021.

[60] Inc. Hospira. *Carboplatin injection: Prescribing information*. Pfizer. Accessed July 2025. 2023. URL: https://labeling.pfizer.com/ShowLabeling.aspx?id=17160.

[61] Calli Coffee and et al. "Carboplatin-induced myelosuppression as related to body weight in dogs". In: *Veterinary and Comparative Oncology* 18.4 (Dec. 2020), pp. 804–810. DOI: 10.1111/vco.12622.

[62] Behrooz Yahyaei and Parastoo Pourali. "One step conjugation of some chemotherapeutic drugs to the biologically produced gold nanoparticles and assessment of their anticancer effects". In: *Scientific Reports* 9.10242 (July 2019), pp. 1–15. DOI: 10.1038/s41598-019-46602-0.

[63] Karol P. Steckiewicz and et al. "Assessment of Anti-Tumor potential and safety of application of Glutathione stabilized Gold Nanoparticles conjugated with Chemotherapeutics". In: *International Journal of Medical Sciences* 17.6 (Mar. 2020), p. 824. DOI: 10.7150/ijms.40827.

Chapter 5

Conclusions & Future Directions

5.1 Conclusions

The research presented in this thesis provided comprehensive insights into the synthesis, characterization, biological evaluation, and translational potential of phytochemical-coated gold nanoparticles, specifically EGCG-GNPs and Curc-GNPs, as promising tools for prostate cancer therapy. The overarching aim was to develop and assess these nanoparticles for their suitability as radiosensitizers, with subsequent evaluation of biodistribution and safety profiles to inform their clinical potential.

In Chapter 2, titled "Synthesis and Characterization of EGCG-GNPs & Curc-GNPs," four distinct gold nanoparticle formulations, EGCG-GNPs, Curc-GNPs, Cit-GNPs, and PEG-GNPs were successfully synthesized and thoroughly characterized. The eco-friendly, single-step green synthesis method employed for EGCG-GNPs and Curc-GNPs resulted in nanoparticles exhibiting superior stability, higher yields, and advantageous physicochemical properties compared to traditional Cit/PEG-GNPs. Rigorous characterization through Dynamic Light Scattering (DLS) and Transmission Electron Microscopy (TEM) revealed monodisperse, spherical nanoparticles with consistent core diameters ($\sim$10 nm) and controlled hydrodynamic diameters (20-25 nm). Colloidal analysis indicated negative zeta potentials, notably lower for PEG-GNPs due to their polymeric coating. UV-Vis spectroscopy highlighted the enhanced stability of Curc-GNPs in biological media, particularly in serum-supplemented RPMI, underscoring their lipophilic protein affinity. Functional characterization confirmed significant antioxidant activity for both EGCG- and Curc-GNPs, surpassing the capabilities of Cit- and PEG-GNPs. The robust attachment of curcumin was validated using FTIR spectroscopy and HPLC, with drug loading quantified

at 20.8 wt%. CT imaging experiments demonstrated a linear relationship between EGCG-GNP concentration and imaging contrast (57.56 HU per mg/mL Au), confirming their potential for clinical imaging applications.

Chapter 3, "In Vitro Studies," established the therapeutic potential of EGCG-GNPs and Curc-GNPs as radiosensitizers in prostate cancer PC-3 cells. Cytotoxicity studies using the XTT assay identified significant dose- and time-dependent toxicity for all GNP formulations at concentrations above 100 μg/mL. EGCG-GNPs displayed the highest cytotoxicity, with viability dropping as low as 16.93% at high concentrations after 72 hours. Curc-GNPs uniquely exhibited a biphasic hormetic response, promoting modest proliferation at low concentrations (0-100 μg/mL) but causing marked toxicity above this threshold. Cellular uptake experiments quantified via ICP-MS highlighted greater internalization of GNPs under serum-free conditions, suggesting protein corona formation impeded nanoparticle uptake in serum-supplemented media. EGCG-GNPs demonstrated the highest cellular uptake, likely due to receptor-mediated interactions such as those involving Laminin67r, with Curc-GNPs also showing significantly superior uptake compared to Cit-GNPs. Crucially, clonogenic assays confirmed the strong radiosensitization potential of both EGCG- and Curc-GNPs, with EGCG-GNPs achieving the highest Sensitization Enhancement Ratio (SER) of 1.955 at 500 μg/mL, substantially reducing the radiation dose required for inducing cancer cell apoptosis. The analysis of linear-quadratic model parameters indicated EGCG-GNPs predominantly enhanced single-track DNA damage. Interestingly, radiosensitization slightly decreased at the lowest tested concentration (25 μg/mL), possibly indicating transient radioprotective effects or inadequate uptake at lower doses. These findings emphasized EGCG-GNPs as the most effective radiosensitizer, with Curc-GNPs holding comparable potential, meriting further optimization to define the optimal therapeutic window.

Chapter 4, "In Vivo Studies," demonstrated favorable biodistribution and toxicity profiles of EGCG-GNPs and Curc-GNPs in murine models. Predominant accumulation occurred in reticuloendothelial organs, primarily the liver, followed by the spleen and stomach, aligning with expected macrophage-driven biodistribution patterns. Significant hepatobiliary clearance of gold was observed over 56 days, while spleen retention remained persistent, reflecting macrophage entrapment. Minimal renal clearance validated size-based renal exclusion. Crucially, the GNPs exhibited benign toxicity profiles, indicated by normal physiological behavior, weight gain, and absence of histopathological abnormalities in major organs. A Physiologically Based Pharmacokinetic (PBPK) model, successfully calibrated to these biodistribution data, reliably predicted GNP pharmacokinetics across different rat models, although slight deviations were noted in specific organs due to methodological factors. The pilot canine study established the technical feasibility and systemic safety of intra-arterial GNP delivery to the prostate, both alone and combined with embolization.

However, visualization challenges arose post iodine-contrast dissipation, highlighting the need for advanced imaging modalities. A clinical case in a Boston Terrier underscored the complexity of combining EGCG-GNPs with chemotherapy, as severe myelosuppression from carboplatin confounded safety evaluations.

Collectively, this thesis demonstrated the robust synthesis, characterization, and in vitro validation of EGCG- and Curc-GNPs as potent radiosensitizers. The promising in vivo biodistribution, safety data, and translational potential pave the way for future studies to optimize dosing strategies, surface functionalization, and combination with radiotherapy, thereby facilitating their clinical development for prostate cancer therapy.

5.2 Challenges and Future Directions

Based on the results presented in the previous chapters, a new set of hypotheses and lines of inquiry have emerged. These will guide the future direction of this research project and help advance the clinical application of phytochemical GNPs in prostate cancer therapy. Several challenges have been identified throughout the study, including issues related to physicochemical properties, in vitro tests, in vivo animal studies, and, notably, our clinical case involving the application of PAE+GNP therapy in naturally occurring canine prostate cancer. Each of these challenges offers valuable insights that will inform the next iteration of our PAE-mediated nanoparticle treatment. By addressing these obstacles, we aim to refine our approach and bring our proposed therapy one step closer to clinical human trials.

5.2.1 GNP stability in vivo relating to serum adsorption and aggregation in ionic solutions

One of the main challenges observed with three out of the four GNPs tested, EGCG-GNP, Curc-GNP, and Cit-GNP, is their tendency to aggregate in ionic solutions and their high affinity for serum proteins. These issues were highlighted in Chapter 2.4.1 (UV-Vis Spectroscopic Analysis), where both Curc-GNPs and Cit-GNPs demonstrated aggregation in non-serum supplemented RPMI (see Figure 2.5). In the context of oncology, aggregation is particularly problematic in the protein-poor, acidic tumor microenvironment. For optimal GNP uptake, it is essential that these nanoparticles remain stable under such physiological conditions.

Additionally, the implications of protein adsorption in serum-rich environments were discussed in Chapter 3.4.2 (Cellular Uptake). Here, protein adherence to GNPs led to

significantly reduced uptake by PC-3 cells, with all GNPs exhibiting similar uptake levels despite their different surface coatings (Figure 3.4). The formation of a protein corona can sterically hinder direct ligand-receptor interactions or alter cell signaling, ultimately reducing cellular recognition and internalization. Notably, the expected laminin67r-mediated uptake of EGCG-GNPs was not observed, presenting a further challenge.

To address these issues, future work should focus on surface engineering strategies, such as incorporating stealth polymers such as PEG. PEGylation can inhibit protein binding and phytochemical desorption, potentially maintaining high uptake of EGCG-GNP or Curc-GNP in PC-3 cells, even in the presence of serum [142]. Achieving the optimal balance between PEG and ligand coverage will require systematic engineering and testing. I propose that future studies develop EGCG-GNP structures with both EGCG and PEG on the surface, testing initial PEG:EGCG weight ratios of 5:95, 10:90, 15:85, and 20:80. This approach will help identify which PEGylated EGCG-GNP formulation offers the best stability in ionic solutions while minimizing protein adsorption. These optimized nanoparticles should then be reevaluated in serum-supplemented cellular uptake studies to compare their performance to serum-free conditions and determine if PEGylation enable higher PC-3 cell uptake. Additionally, the new Pegylated EGCG-GNP can be retested in CD-1 mice to see if splenic uptake is reduced as this was also identified as a challenge in section 4.4.1.1 GNP Biodistribution in Mice where GNP concentrations in spleen showed consistent Au concentration up to 56 days with no signs of elimination (Figure 4.7).

5.2.2 Investigating the Biphasic Effects of Curc-GNPs

The next challenge is the need for greater clarity on the biphasic behavior of Curc-GNPs. Our objective is to develop a nanotherapeutic that enhances, rather than diminishes, the efficacy of radiotherapy; we do not want our formulation to inadvertently promote cancer cell growth. Therefore, further research is required to systematically investigate the biphasic effects of Curc-GNPs, particularly to identify the dose ranges at which they may shift from being potentially cytoprotective to cytotoxic. Although EGCG-GNPs exhibited high cytotoxicity in PC-3 cells, they should not be excluded from further study. Many phytochemicals, including curcumin and EGCG, are known to exhibit hormetic responses, acting as cell promoters at low doses and cell inhibitors at higher doses [143]. This phenomenon is thought to be linked to their antioxidant properties and ability to scavenge reactive oxygen species, which can contribute to cytoprotective effects at certain concentrations [143]. However, the precise mechanisms underlying these biphasic, hormetic responses remain unclear. Further research is needed to elucidate these pathways, particularly by examining the expression of

pro-survival genes such as BCL2 and GPX1. This will help characterize the dual effects of Curc-GNPs in PC-3 prostate cancer cells.

One experimental approach, called RT-qPCR, involves incubating PC-3 cells with Curc-GNP or EGCG-GNP formulations containing 10-50 μM phytochemical-equivalent doses for 6, 12, or 24 hours. After treatment, total RNA can be extracted from the lysed cells, and reverse transcription can be performed to synthesize corresponding complementary DNA. Quantitative PCR using primers specific for BCL2 and GPX1 would then be used to amplify and assess changes in gene expression. Expression levels can be compared to control cells to determine whether the nanoparticles upregulate or down-regulate pro-survival gene pathways [144].

5.2.3 Ct-Imaging Challenges Following PAE Procedure

A key advantage of intra-arterial administration of GNPs to the prostate is the potential for a theranostic agent that enables both imaging and treatment of prostate cancer. In our study, a concentration of 1.5 mg/mL EGCG-GNP was not visible on CT in canine models, presenting a significant challenge: without clear visualization of GNP uptake, neither accurate dosimetry nor enhancement analysis can be performed. One potential solution is to increase the EGCG-GNP concentration. However, higher concentrations may lead to nanoparticle aggregation and increased viscosity, which can hinder microcatheter delivery and compromise the homogeneity of the EGCG-GNP suspension. These changes may also raise the risk of toxicity to healthy prostate tissue and unintended embolization in non-target organs. Alternatively, increasing the injection volume could enhance visibility. In our canine clinical study, only 1 mL of EGCG-GNP per lobe was used, along with 5 mL carboplatin, which may have diluted the GNPs and reduced CT contrast. Future studies could explore IA injection of up to 6 mL EGCG- GNP per lobe to assess potential improvements in CT contrast. However, larger volumes carry risks such as reflux into adjacent organs, tissue over-distension, inflammation, and increased patient discomfort [145]. A more promising approach for tracking GNP retention and distribution in the prostate may be to convert EGCG-GNPs into radionuclide-labeled EGCG-^{198}AuNPs via neutron irradiation. Exposing GNPs to neutron flux in a nuclear reactor converts stable gold nuclei (^{197}Au) into radioactive ^{198}Au, enabling sensitive SPECT imaging of nanoparticle prostate distribution and tumor localization. The nuclear reactions for neutron activation of stable gold ($^{197}_{79}$Au) into unstable ($^{198}_{79}$Au) and its subsequent decay are below [146].

Neutron Activation:

$$^{197}_{79}Au + ^{1}_{0}n \rightarrow ^{198}_{79}Au + \gamma$$

Decay:

$$^{198}_{79}Au \rightarrow ^{198}_{80}Hg + e^{-} + \bar{\nu}_e$$

This process does not alter the size, shape, or surface chemistry of the nanoparticles. ^{198}Au emits gamma photons at 412 keV and has a half-life of 2.7 days, making it well- suited for Single Photon Emission Computed Tomography (SPECT) imaging [147]. SPECT is a widely used nuclear imaging modality for tumor detection and staging, offering spatial resolutions of 4-7 mm and high sensitivity, capable of detecting tumors as small as 7 mm [148]. For SPECT imaging of prostate tumors, radiotracer concentrations in the low nanomolar range (approximately 0.1-1 nM) have been reported as sufficient for lesion detection. However, this sensitivity depends on both the radiotracer's affinity and the level of PSMA expression in the tumor [148]. EGCG-^{198}AuNPs have demonstrated high affinity for prostate cancer cells, and incorporating SPECT imaging can help address the challenge of quantifying GNP uptake in the prostate and visualizing their dispersion or migration from the target tissue [51]. Additionally, ^{198}Au emits β^- particles with a maximum energy of approximately 0.96 MeV, corresponding to a tissue penetration range of about 0.4 mm which is enough to affect multiple cell layers [148]. This range of particle energies enables effective irradiation of cancer cells throughout the tumor, not just those adjacent to the EGCG-^{198}AuNPs.

5.2.4 Canine Clinical Trials

One of the major limitations of our study is the small number of canine patients used to implement the GNP PAE procedure. While the procedure was successfully conducted in three laboratory Beagles, only one cancer patient was recruited, and future studies should aim to apply EGCG-GNP + PAE exclusively in dogs with naturally occurring prostate cancer. This could be achieved by expanding the recruitment network to include veterinary centres across Canada. Although the Ontario Veterinary College is regarded as one of the top animal medical centres in the country, increasing the number of canine prostate cancer patients may require establishing partnerships with other institutions, such as the Atlantic Veterinary College at the University of Prince Edward Island or the Western College of Veterinary Medicine at the University of Saskatchewan, which also have a history of conducting oncologic clinical trials. Such collaborations would enhance recruitment opportunities and provide broader insights, allowing for a more incremental and robust research approach. A key challenge is that the PAE procedure is highly specialized, relying

heavily on the expertise and experience of veterinary radiologists. The availability of such skilled professionals may be limited outside leading centres like the Ontario Veterinary College.

Another important limitation of our canine clinical trial is the coadministration of chemoembolization agents with EGCG-GNPs. It is recommended that future trials avoid the use of additional chemotherapeutic agents that could confound the interpretation of therapeutic outcomes. Recruiting dogs with naturally occurring prostate cancer is inherently challenging, and it may not always be possible to maintain exclusivity in treatment protocols. Nevertheless, to obtain clear and meaningful conclusions, future canine trials should be conducted exclusively with EGCG-GNPs. If PAE with intra-arterial EGCG-GNP administration is successfully established, subsequent studies should consider incorporating radiotherapy to fully assess the efficacy of the proposed treatment strategy.

References

[1] Freddie Bray et al. "Global cancer statistics 2018: GLOBOCAN estimates of incidence and mortality worldwide for 36 cancers in 185 countries". In: *CA: a cancer journal for clinicians* 68.6 (2018), pp. 394–424.

[2] Darren R Brenner et al. "Projected estimates of cancer in Canada in 2022". In: *Cmaj* 194.17 (2022), E601–E607.

[3] Anupam Saini et al. "Cancer causes and treatments". In: *Int J Pharm Sci Res* 11.7 (2020), pp. 3121–3134.

[4] Akulapalli Sudhakar. "History of cancer, ancient and modern treatment methods". In: *Cancer Science & Therapy* 1.02 (2009), pp. i–iv.

[5] Mark S Litwin and Hung-Jui Tan. "The diagnosis and treatment of prostate cancer: a review". In: *Jama* 317.24 (2017), pp. 2532–2542.

[6] Peter H Gann. "Risk factors for prostate cancer". In: *Reviews in urology* 4.Suppl 5 (2002), S3.

[7] Rebecca L Siegel et al. "Cancer statistics, 2023". In: *CA: a cancer journal for clinicians* 73.1 (2023), pp. 17–48.

[8] A Discacciati, N Orsini, and A Wolk. "Body mass index and incidence of localized and advanced prostate cancer—a dose–response meta-analysis of prospective studies". In: *Annals of oncology* 23.7 (2012), pp. 1665–1671.

[9] Claire H Pernar et al. "The epidemiology of prostate cancer". In: *Cold Spring Harbor perspectives in medicine* 8.12 (2018), a030361.

[10] Beatrice S Knudsen and Valera Vasioukhin. "Mechanisms of prostate cancer initiation and progression". In: *Advances in cancer research* 109 (2010), pp. 1–50.

[11] Joaquin Mateo et al. "DNA repair in prostate cancer: biology and clinical implications". In: *European urology* 71.3 (2017), pp. 417–425.

[12] Rebecca L Siegel et al. "Cancer statistics, 2021". In: *CA: a cancer journal for clinicians* 71.1 (2021), pp. 7–33.

[13] Theodoros Karantanos, Paul G Corn, and Timothy C Thompson. "Prostate cancer progression after androgen deprivation therapy: mechanisms of castrate resistance and novel therapeutic approaches". In: *Oncogene* 32.49 (2013), pp. 5501–5511.

[14] Matthew R Cooperberg et al. "Contemporary trends in low risk prostate cancer: risk assessment and treatment". In: *The Journal of urology* 178.3S (2007), S14–S19.

[15] Georgi Pirtskhalaishvili, Ronald L Hrebinko, and Joel B Nelson. "The treatment of prostate cancer. An overview of current options". In: *Cancer practice* 9.6 (2001), pp. 295–306.

[16] Christopher JD Wallis et al. "Survival and complications following surgery and radiation for localized prostate cancer: an international collaborative review". In: *European urology* 73.1 (2018), pp. 11–20.

[17] Fritz Schröder et al. "Androgen deprivation therapy: past, present and future". In: *BJU international* 109 (2012), pp. 1–12.

[18] Rajamanickam Baskar et al. "Cancer and radiation therapy: current advances and future directions". In: *International journal of medical sciences* 9.3 (2012), p. 193.

[19] Vincent T DeVita Jr and Edward Chu. "A history of cancer chemotherapy". In: *Cancer research* 68.21 (2008), pp. 8643–8653.

[20] Emad Rajih et al. "Efficacy of Androgen Deprivation Therapy (ADT) in Combination with Radiation Therapy, compared to ADT alone in Patients with High-Risk Prostate Cancer: a meta-analysis". In: *Research Square* (Apr. 2025).

[21] Hongcheng Zhu et al. "Global radiotherapy demands and corresponding radiotherapy-professional workforce requirements in 2022 and predicted to 2050: a population-based study". In: *The Lancet Global Health* 12.12 (2024), e1945–e1953.

[22] Freddie C Hamdy et al. "10-year outcomes after monitoring, surgery, or radiotherapy for localized prostate cancer". In: *New England Journal of Medicine* 375.15 (2016), pp. 1415–1424.

[23] P. Care. "Radiation Therapy". In: *Quality Assurance* 10.4 (2019).

[24] Cheng Chen et al. "Comparisons of health-related quality of life among surgery and radiotherapy for localized prostate cancer: a systematic review and meta-analysis". In: *Oncotarget* 8.58 (2017), p. 99057.

[25] Nicholas G Zaorsky et al. "Causes of death among cancer patients". In: *Annals of oncology* 28.2 (2017), pp. 400–407.

[26] Yong Bae Kim and Chang-Ok Suh. "Evolution of radiotherapy: high-precision radiotherapy". In: *Journal of the Korean Medical Association* 51.7 (2008), pp. 604–611.

[27] Anthony L Zietman et al. "The treatment of prostate cancer by conventional radiation therapy: an analysis of long-term outcome." In: *International journal of radiation oncology, biology, physics* 32.2 (1995), pp. 287–292.

[28] Cyrus Chargari et al. "Brachytherapy: An overview for clinicians". In: *CA: a cancer journal for clinicians* 69.5 (2019), pp. 386–401.

[29] Albert Jang, Ayse T Kendi, and Oliver Sartor. "Status of PSMA-targeted radioligand therapy in prostate cancer: current data and future trials". In: *Therapeutic Advances in Medical Oncology* 15 (2023), p. 17588359231157632.

[30] Maja Benković. "Introduction to nutraceuticals and pharmaceuticals". In: *Nutraceuticals and natural product Pharmaceuticals*. Elsevier, 2019, pp. 1–31.

[31] Mariam Abotaleb et al. "Therapeutic potential of plant phenolic acids in the treatment of cancer". In: *Biomolecules* 10.2 (2020), p. 221.

[32] Cijo George Vazhappilly et al. "Current methodologies to refine bioavailability, delivery, and therapeutic efficacy of plant flavonoids in cancer treatment". In: *The Journal of Nutritional Biochemistry* 94 (2021), p. 108623.

[33] Samir Ali Abd El-Kaream. "Biochemical and biophysical study of chemopreventive and chemotherapeutic anti-tumor potential of some Egyptian plant extracts". In: *Biochemistry and biophysics reports* 18 (2019), p. 100637.

[34] Leewanshi Chakrawarti et al. "Therapeutic effects of EGCG: a patent review". In: *Expert opinion on therapeutic patents* 26.8 (2016), pp. 907–916.

[35] Zihao Wei et al. "Evaluation of structural and functional properties of protein–EGCG complexes and their ability of stabilizing a model β-carotene emulsion". In: *Food Hydrocolloids* 45 (2015), pp. 337–350.

[36] Giusy Rita Caponio et al. "Nutraceuticals: Focus on anti-inflammatory, anti-cancer, antioxidant properties in gastrointestinal tract". In: *Antioxidants* 11.7 (2022), p. 1274.

[37] Ahmad Salami, Enayatollah Seydi, and Jalal Pourahmad. "Use of nutraceuticals for prevention and treatment of cancer". In: *Iranian journal of pharmaceutical research: IJPR* 12.3 (2013), p. 219.

[38] Aroosa Fazal Illahi, Faqir Muhammad, and Bushra Akhtar. "Nanoformulations of nutraceuticals for cancer treatment". In: *Critical Reviews™ in Eukaryotic Gene Expression* 29.5 (2019).

[39] Leila Gholami et al. "Selective cellular uptake and cytotoxicity of curcumin-encapsulated SPC and HSPC liposome nanoparticles on human bladder cancer cells". In: *Current Pharmaceutical Design* 29.13 (2023), pp. 1046–1058.

[40] Hibah M Aldawsari et al. "Preparation and characterization of chitosan coated plga nanoparticles of resveratrol: Improved stability, antioxidant and apoptotic activities in H1299 lung cancer cells". In: *Coatings* 10.5 (2020), p. 439.

[41] Gabriela Corrêa Carvalho et al. "Cetyltrimethylammonium bromide in the synthesis of mesoporous silica nanoparticles: General aspects and in vitro toxicity". In: *Advances in Colloid and Interface Science* 307 (2022), p. 102746.

[42] Moniba Rahim et al. "Nutratherapeutics approach against cancer: tomato-mediated synthesised gold nanoparticles". In: *IET Nanobiotechnology* 12.1 (2018), pp. 1–5.

[43] Ramachandran Rajan et al. "Plant extract synthesized silver nanoparticles: An ongoing source of novel biocompatible materials". In: *Industrial Crops and Products* 70 (2015), pp. 356–373.

[44] Harjeet Singh et al. "Revisiting the green synthesis of nanoparticles: uncovering influences of plant extracts as reducing agents for enhanced synthesis efficiency and its biomedical applications". In: *International journal of nanomedicine* (2023), pp. 4727–4750.

[45] Motofumi Kumazoe and Hirofumi Tachibana. "Anti-cancer effect of EGCG and its mechanisms". In: *Functional Foods in Health and Disease* 6.2 (2016), pp. 70–78.

[46] Juan Miguel Lopez del Amo et al. "Structural properties of EGCG-induced, nontoxic Alzheimer's disease Aβ oligomers". In: *Journal of molecular biology* 421.4-5 (2012), pp. 517–524.

[47] Emma C Stuart, Marissa J Scandlyn, and Rhonda J Rosengren. "Role of epigallocatechin gallate (EGCG) in the treatment of breast and prostate cancer". In: *Life sciences* 79.25 (2006), pp. 2329–2336.

[48] Takeshi Hirayama. "Epidemiology of pancreatic cancer in Japan". In: *Japanese Journal of Clinical Oncology* 19.3 (1989), pp. 208–215.

[49] Norie Kurahashi et al. "Green tea consumption and prostate cancer risk in Japanese men: a prospective study". In: *American journal of epidemiology* 167.1 (2008), pp. 71–77.

[50] Changhwan Yeo et al. "Epigallocatechin-3-gallate suppresses vasculogenic mimicry through inhibiting the twist/VE-cadherin/AKT pathway in human prostate cancer PC-3 cells". In: *International journal of molecular sciences* 21.2 (2020), p. 439.

[51] Ravi Shukla et al. "Laminin receptor specific therapeutic gold nanoparticles (198AuNP-EGCg) show efficacy in treating prostate cancer". In: *Proceedings of the National Academy of Sciences* 109.31 (2012), pp. 12426–12431. DOI: 10.1073/pnas.1121174109.

[52] Fajun Yang et al. "The green tea polyphenol (-)-epigallocatechin-3-gallate blocks nuclear factor-κB activation by inhibiting IκB kinase activity in the intestinal epithelial cell line IEC-6". In: *Molecular Pharmacology* 60.3 (2001), pp. 528–533.

[53] Andrew C Schroeder et al. "A potential role for green tea as a radiation sensitizer for prostate cancer". In: *Pathology & Oncology Research* 25 (2019), pp. 263–268.

[54] Shivkanya Fuloria et al. "A comprehensive review on the therapeutic potential of Curcuma longa Linn. in relation to its major active constituent curcumin". In: *Frontiers in Pharmacology* 13 (2022), p. 820806.

[55] Young-Joon Surh and Hye-Kyung Na. "NF-κB and Nrf2 as prime molecular targets for chemoprevention and cytoprotection with anti-inflammatory and antioxidant phytochemicals". In: *Genes & nutrition* 2 (2008), pp. 313–317.

[56] Stephany J Veuger, Jill E Hunter, and Barbara W Durkacz. "Ionizing radiation-induced NF-κB activation requires PARP-1 function to confer radioresistance". In: *Oncogene* 28.6 (2009), pp. 832–842.

[57] Vivek Verma. "Relationship and interactions of curcumin with radiation therapy". In: *World journal of clinical oncology* 7.3 (2016), p. 275.

[58] Vasiliki Zoi et al. "Radiosensitization and radioprotection by curcumin in glioblastoma and other cancers". In: *Biomedicines* 10.2 (2022), p. 312.

[59] Santosh K Sandur et al. "Curcumin modulates the radiosensitivity of colorectal cancer cells by suppressing constitutive and inducible NF-κB activity". In: *International Journal of Radiation Oncology* Biology* Physics* 75.2 (2009), pp. 534–542.

[60] Ajaikumar B Kunnumakkara et al. "Curcumin sensitizes human colorectal cancer xenografts in nude mice to γ-radiation by targeting nuclear factor-κB–regulated gene products". In: *Clinical Cancer Research* 14.7 (2008), pp. 2128–2136.

[61] Mohammad Moniruzzaman and Taesun Min. "Curcumin, curcumin nanoparticles and curcumin nanospheres: A review on their pharmacodynamics based on monogastric farm animal, poultry and fish nutrition". In: *Pharmaceutics* 12.5 (2020), p. 447.

[62] Murali M Yallapu et al. "Curcumin-loaded magnetic nanoparticles for breast cancer therapeutics and imaging applications". In: *International journal of nanomedicine* (2012), pp. 1761–1779.

[63] Shruti Nambiar et al. “Synthesis of curcumin-functionalized gold nanoparticles and cytotoxicity studies in human prostate cancer cell line”. In: *Applied Nanoscience* 8 (2018), pp. 347–357.

[64] Anindita Mukerjee and Jamboor K Vishwanatha. “Formulation, characterization and evaluation of curcumin-loaded PLGA nanospheres for cancer therapy”. In: *Anticancer research* 29.10 (2009), pp. 3867–3875.

[65] Hareesh B Nair et al. “Delivery of antiinflammatory nutraceuticals by nanoparticles for the prevention and treatment of cancer”. In: *Biochemical pharmacology* 80.12 (2010), pp. 1833–1843.

[66] Peter A Williams and Glyn O Phillips. “Gum arabic”. In: *Handbook of hydrocolloids*. Elsevier, 2021, pp. 627–652.

[67] Nripen Chanda et al. “Radioactive gold nanoparticles in cancer therapy: therapeutic efficacy studies of GA-198AuNP nanoconstruct in prostate tumor-bearing mice”. In: *Nanomedicine in Cancer*. Jenny Stanford Publishing, 2017, pp. 753–774.

[68] Fuchsia Gold-Smith, Alyssa Fernandez, and Karen Bishop. “Mangiferin and cancer: Mechanisms of action”. In: *Nutrients* 8.7 (2016), p. 396.

[69] KV Katti et al. “Prostate tumor therapy advances in nuclear medicine: green nanotechnology toward the design of tumor specific radioactive gold nanoparticles”. In: *Journal of Radioanalytical and Nuclear Chemistry* 318 (2018), pp. 1737–1747.

[70] Menka Khoobchandani et al. “New approaches in breast cancer therapy through green nanotechnology and nano-ayurvedic medicine–pre-clinical and pilot human clinical investigations”. In: *International journal of nanomedicine* (2020), pp. 181–197.

[71] YANG Yan-Hua, MAO Jia-Wang, and TAN Xiao-Li. “Research progress on the source, production, and anti-cancer mechanisms of paclitaxel”. In: *Chinese journal of natural medicines* 18.12 (2020), pp. 890–897.

[72] AD Alate et al. “A new anti-cancer principle isolated from Gymnosporia rothiana Laws, and its use in attaining cures in L1210 leukaemia in combination with" S" phase sensitive drugs.” In: *Biomedicine/[publiee Pour l’AAICIG]* 28.5 (1978), pp. 270–273.

[73] Denise A Yardley. “nab-Paclitaxel mechanisms of action and delivery”. In: *Journal of Controlled Release* 170.3 (2013), pp. 365–372.

[74] Sruthi Sritharan and Nageswaran Sivalingam. “A comprehensive review on time-tested anticancer drug doxorubicin”. In: *Life sciences* 278 (2021), p. 119527.

[75] Peter Schwerdtfeger. "Relativistic effects in properties of gold". In: *Heteroatom Chemistry: An International Journal of Main Group Elements* 13.6 (2002), pp. 578–584.

[76] Julien Engel, Samantha Francis, and Alberto Roldan. "The influence of support materials on the structural and electronic properties of gold nanoparticles–a DFT study". In: *Physical Chemistry Chemical Physics* 21.35 (2019), pp. 19011–19025.

[77] Vincenzo Amendola et al. "Surface plasmon resonance in gold nanoparticles: a review". In: *Journal of physics: Condensed matter* 29.20 (2017), p. 203002.

[78] HS Zhou et al. "Controlled synthesis and quantum-size effect in gold-coated nanoparticles". In: *Physical Review B* 50.16 (1994), p. 12052.

[79] NG Khlebtsov and LA Dykman. "Biodistribution and toxicity of gold nanoparticles". In: *Nanotechnologies in Russia* 6.1 (2011), pp. 17–42.

[80] Stephanie Hirn et al. "Particle size-dependent and surface charge-dependent biodistribution of gold nanoparticles after intravenous administration". In: *European journal of pharmaceutics and biopharmaceutics* 77.3 (2011), pp. 407–416.

[81] Na Li, Pengxiang Zhao, and Didier Astruc. "Anisotropic gold nanoparticles: synthesis, properties, applications, and toxicity". In: *Angewandte Chemie International Edition* 53.7 (2014), pp. 1756–1789.

[82] Oshra Betzer et al. "The effect of nanoparticle size on the ability to cross the blood–brain barrier: an in vivo study". In: *Nanomedicine* 12.13 (2017), pp. 1533–1546.

[83] Wim H De Jong et al. "Particle size-dependent organ distribution of gold nanoparticles after intravenous administration". In: *Biomaterials* 29.12 (2008), pp. 1912–1919.

[84] Pallavi Vedantam, George Huang, and TR Jeremy Tzeng. "Size-dependent cellular toxicity and uptake of commercial colloidal gold nanoparticles in DU-145 cells". In: *Cancer nanotechnology* 4 (2013), pp. 13–20.

[85] Anil K Suresh and Anil K Suresh. "Biocompatibility and Inertness of Gold Nanocrystallites". In: *Metallic Nanocrystallites and their Interaction with Microbial Systems* (2012), pp. 47–54.

[86] Ihsan A Mohammed and Fatima J Al-Gawhari. "Gold Nanoparticle: Synthesis, Functionalization, Enhancement, Drug Delivery and Therapy: A Review." In: *Systematic Reviews in Pharmacy* 11.6 (2020).

[87] Wilson Roa et al. "Gold nanoparticle sensitize radiotherapy of prostate cancer cells by regulation of the cellcycle". In: *Nanotechnology* 20.37 (2009), p. 375101.

[88] Dong Luo et al. “Prostate-specific membrane antigen targeted gold nanoparticles for prostate cancer radiotherapy: does size matter for targeted particles?” In: *Chemical science* 10.35 (2019), pp. 8119–8128.

[89] Sílvia Soares et al. “Application of gold nanoparticles as radiosensitizer for metastatic prostate cancer cell lines”. In: *International Journal of Molecular Sciences* 24.4 (2023), p. 4122.

[90] Weichong Zhao et al. “Green synthesis, characterization and determination of anti-prostate cancer, cytotoxicity and antioxidant effects of gold nanoparticles synthesized using Alhagi maurorum”. In: *Inorganic Chemistry Communications* 141 (2022), p. 109525.

[91] Roya Herizchi et al. “Current methods for synthesis of gold nanoparticles”. In: *Artificial cells, nanomedicine, and biotechnology* 44.2 (2016), pp. 596–602.

[92] Ana Elisa F Oliveira et al. “Gold nanoparticles: a didactic step-by-step of the synthesis using the turkevich method, mechanisms, and characterizations”. In: *Analytica* 4.2 (2023), pp. 250–263.

[93] Jakub W Trzciński et al. “Synthetic guidelines for the precision engineering of gold nanoparticles”. In: *Current Opinion in Chemical Engineering* 29 (2020), pp. 59–66.

[94] Adamu Ibrahim Usman, Azlan Abdul Aziz, and Osama Abu Noqta. “Application of green synthesis of gold nanoparticles: A review”. In: *Jurnal Teknologi (Sciences & Engineering)* 81.1 (2019).

[95] Alaa AA Aljabali et al. “Synthesis of gold nanoparticles using leaf extract of Ziziphus zizyphus and their antimicrobial activity”. In: *Nanomaterials* 8.3 (2018), p. 174.

[96] Inès Hammami, Nadiyah M Alabdallah, et al. “Gold nanoparticles: Synthesis properties and applications”. In: *Journal of king Saud university-science* 33.7 (2021), p. 101560.

[97] Manu M Joseph and Thankappan T Sreelekha. “Gold nanoparticles-synthesis and applications in cancer management”. In: *Recent Patents on Materials Science* 7.1 (2014), pp. 8–25.

[98] Eun Jung Kim, Jeong Hyun Yeum, and Jin Hyun Choi. “Effects of polymeric stabilizers on the synthesis of gold nanoparticles”. In: *Journal of Materials Science & Technology* 30.2 (2014), pp. 107–111.

[99] Staci Adams et al. “Key factors affecting the reproducibility of synthesis and growth mechanism of near-infrared absorbing hollow gold nanospheres”. In: *Chemistry of Materials* 26.23 (2014), pp. 6805–6810.

[100] Howard Reiss, Dean C Marvin, and Richard H Heist. "The use of nucleation and growth as a tool in chemical physics". In: *Journal of Colloid and Interface Science* 58.1 (1977), pp. 125–141.

[101] Amirah Adlia et al. "Antifibrotic activity and in Ovo toxicity study of liver-targeted curcumin-gold nanoparticle". In: *Scientia pharmaceutica* 86.4 (2018), p. 41.

[102] Asghar Mesbahi. "A review on gold nanoparticles radiosensitization effect in radiation therapy of cancer". In: *Reports of Practical Oncology & Radiotherapy* 15.6 (2010), pp. 176–180.

[103] James F Hainfeld et al. "Gold nanoparticles enhance the radiation therapy of a murine squamous cell carcinoma". In: *Physics in Medicine & Biology* 55.11 (2010), p. 3045.

[104] Catherine Carnovale et al. "Identifying trends in gold nanoparticle toxicity and uptake: size, shape, capping ligand, and biological corona". In: *ACS omega* 4.1 (2019), pp. 242–256.

[105] Xinlong Wang et al. "Influence of cell size on cellular uptake of gold nanoparticles". In: *Biomaterials science* 4.6 (2016), pp. 970–978.

[106] Erik C Dreaden et al. "Size matters: gold nanoparticles in targeted cancer drug delivery". In: *Therapeutic delivery* 3.4 (2012), pp. 457–478.

[107] Arnida, Alexander Malugin, and Hamidreza Ghandehari. "Cellular uptake and toxicity of gold nanoparticles in prostate cancer cells: a comparative study of rods and spheres". In: *Journal of Applied Toxicology: An International Journal* 30.3 (2010), pp. 212–217.

[108] Kun Song et al. "Smart gold nanoparticles enhance killing effect on cancer cells". In: *International journal of oncology* 42.2 (2013), pp. 597–608.

[109] Qiyue Xia et al. "Size-and cell type-dependent cellular uptake, cytotoxicity and in vivo distribution of gold nanoparticles". In: *International journal of nanomedicine* (2019), pp. 6957–6970.

[110] Paola Nativo, Ian A Prior, and Mathias Brust. "Uptake and intracellular fate of surface-modified gold nanoparticles". In: *ACS nano* 2.8 (2008), pp. 1639–1644.

[111] PJCO Wardman. "Chemical radiosensitizers for use in radiotherapy". In: *Clinical oncology* 19.6 (2007), pp. 397–417.

[112] Sohyoung Her, David A Jaffray, and Christine Allen. "Gold nanoparticles for applications in cancer radiotherapy: Mechanisms and recent advancements". In: *Advanced drug delivery reviews* 109 (2017), pp. 84–101.

[113] Ivan Kempson. "Mechanisms of nanoparticle radiosensitization". In: *Wiley Interdisciplinary Reviews: Nanomedicine and Nanobiotechnology* 13.1 (2021), e1656.

[114] JHL Mott and JM Daniel. *Interactions of electromagnetic radiation and subatomic particles with matter-part 1*. 2021.

[115] Karl T Butterworth et al. "Physical basis and biological mechanisms of gold nanoparticle radiosensitization". In: *Nanoscale* 4.16 (2012), pp. 4830–4838.

[116] F Moradi et al. "Metallic nanoparticle radiosensitization: The role of Monte Carlo simulations towards progress". In: *Radiation Physics and Chemistry* 180 (2021), p. 109294.

[117] Douglas Howard et al. "Chemical mechanisms of nanoparticle radiosensitization and radioprotection: a review of structure-function relationships influencing reactive oxygen species". In: *International Journal of Molecular Sciences* 21.2 (2020), p. 579.

[118] Angélica Bueno Barbezan et al. "Radioactive gold nanoparticles coated with BSA: A promising approach for prostate cancer treatment". In: *Nanotheranostics* 8.1 (2024), p. 112.

[119] Hyukjin Lee et al. "Fluorescent gold nanoprobe sensitive to intracellular reactive oxygen species". In: *Advanced Functional Materials* 19.12 (2009), pp. 1884–1890.

[120] Soraia Rosa et al. "Biological mechanisms of gold nanoparticle radiosensitization". In: *Cancer nanotechnology* 8 (2017), pp. 1–25.

[121] Mingyang He et al. "MicroRNAs, DNA damage response, and cancer treatment". In: *International Journal of Molecular Sciences* 17.12 (2016), p. 2087.

[122] Sébastien Penninckx et al. "Thioredoxin reductase activity predicts gold nanoparticle radiosensitization effect". In: *Nanomaterials* 9.2 (2019), p. 295.

[123] Theodore S. Lawrence and Jonathan Maybaum. "Fluoropyrimidines as radiation sensitizers". In: *Seminars in Radiation Oncology* 3.1 (1993). Adjuvant Therapy for Colon and Rectal Cancer, pp. 20–28. ISSN: 1053-4296.

[124] Sabine Schmid et al. "Activity of platinum-based chemotherapy in patients with advanced prostate cancer with and without DNA repair gene aberrations". In: *JAMA network open* 3.10 (2020), e2021692–e2021692.

[125] Xue Li et al. "Surface chemistry governs the sub-organ transfer, clearance and toxicity of functional gold nanoparticles in the liver and kidney". In: *Journal of nanobiotechnology* 18 (2020), pp. 1–16.

[126] Yan-Peng Jia et al. "The in vitro and in vivo toxicity of gold nanoparticles". In: *Chinese Chemical Letters* 28.4 (2017), pp. 691–702.

[127] Luan NM Nguyen et al. “The exit of nanoparticles from solid tumours”. In: *Nature Materials* 22.10 (2023), pp. 1261–1272.

[128] Tatsuhiko Nakasato et al. “Superselective continuous arterial infusion chemotherapy through the superficial temporal artery for oral cavity tumors”. In: *American journal of neuroradiology* 21.10 (2000), pp. 1917–1922.

[129] Badri Bhattarai, Yeakub Zaker, and Terry P Bigioni. “Green synthesis of gold and silver nanoparticles: Challenges and opportunities”. In: *Current Opinion in Green and Sustainable Chemistry* 12 (2018), pp. 91–100.

[130] Nikolai Khlebtsov and Lev Dykman. “Biodistribution and toxicity of engineered gold nanoparticles: a review of in vitro and in vivo studies”. In: *Chemical Society Reviews* 40.3 (2011), pp. 1647–1671.

[131] Jiaqi Lin et al. “PEGylation on mixed monolayer gold nanoparticles: Effect of grafting density, chain length, and surface curvature”. In: *Journal of colloid and interface science* 504 (2017), pp. 325–333.

[132] Sjoerd Hak et al. “The effect of nanoparticle polyethylene glycol surface density on ligand-directed tumor targeting studied in vivo by dual modality imaging”. In: *ACS nano* 6.6 (2012), pp. 5648–5658.

[133] Khursheed Ali et al. “Moist Heat Synthesis of Magnetic EGCG-Cappedα-Fe2O3 Nanoparticles and Their In Vitro and In Silico Interactions with Pristine HSA-and NDM-1-Producing Bacteria”. In: *ACS omega* 8.51 (2023), pp. 48775–48786.

[134] John Turkevich, Peter Cooper Stevenson, and James Hillier. “A study of the nucleation and growth processes in the synthesis of colloidal gold”. In: *Discussions of the faraday society* 11 (1951), pp. 55–75.

[135] Joanne Manson et al. “Polyethylene glycol functionalized gold nanoparticles: the influence of capping density on stability in various media”. In: *Gold bulletin* 44 (2011), pp. 99–105.

[136] Ilhami Gülçin. “Antioxidant and antiradical activities of L-carnitine”. In: *Life sciences* 78.8 (2006), pp. 803–811.

[137] Johanna-Gabriela Walter et al. “SPR biosensor based on polymer multi-mode optical waveguide and nanoparticle signal enhancement”. In: *Sensors* 20.10 (2020), p. 2889.

[138] Karol P Steckiewicz et al. “Impact of gold nanoparticles shape on their cytotoxicity against human osteoblast and osteosarcoma in in vitro model. Evaluation of the safety of use and anti-cancer potential”. In: *Journal of Materials Science: Materials in Medicine* 30 (2019), pp. 1–15.

[139] Hilde Jans et al. “Dynamic light scattering as a powerful tool for gold nanoparticle bioconjugation and biomolecular binding studies”. In: *Analytical chemistry* 81.22 (2009), pp. 9425–9432.

[140] Jiaqi Dong et al. “Synthesis of precision gold nanoparticles using Turkevich method”. In: *KONA Powder and Particle Journal* 37 (2020), pp. 224–232.

[141] Vanna Sanna et al. “Single-step green synthesis and characterization of gold-conjugated polyphenol nanoparticles with antioxidant and biological activities”. In: *International journal of nanomedicine* (2014), pp. 4935–4951.

[142] Shehab Al Shehab, Riham El Kurdi, and Digambara Patra. “Curcumin mediated PEG thiol acid conjugated gold nanoparticles for the determination of melamine”. In: *Microchemical Journal* 153 (Mar. 2020), p. 104382. ISSN: 0026-265X. DOI: 10.1016/j.microc.2019.104382. URL: http://dx.doi.org/10.1016/j.microc.2019.104382.

[143] Edward J. Calabrese et al. “Does Green Tea Induce Hormesis?” In: *Dose-Response* 18.3 (July 2020). ISSN: 1559-3258. DOI: 10.1177/1559325820936170. URL: http://dx.doi.org/10.1177/1559325820936170.

[144] Ukjin Kim et al. “Phloretin Inhibits the Human Prostate Cancer Cells Through the Generation of Reactive Oxygen Species”. In: *Pathology & Oncology Research* 26.2 (Apr. 2019), pp. 977–984. ISSN: 1532-2807. DOI: 10.1007/s12253-019-00643-y. URL: http://dx.doi.org/10.1007/s12253-019-00643-y.

[145] Michele Andreucci, Richard Solomon, and Adis Tasanarong. “Side Effects of Radiographic Contrast Media: Pathogenesis, Risk Factors, and Prevention”. In: *BioMed Research International* 2014 (2014), pp. 1–20. ISSN: 2314-6141. DOI: 10.1155/2014/741018. URL: http://dx.doi.org/10.1155/2014/741018.

[146] Vibha Vansola et al. “Measurement of 197Au (n, γ) 198gAu reaction cross-section at the neutron energies of 1.12, 2.12, 3.12 and 4.12 MeV”. In: *Radiochimica Acta* 103.12 (Sept. 2015), pp. 817–823. ISSN: 0033-8230. DOI: 10.1515/ract-2015-2431. URL: http://dx.doi.org/10.1515/ract-2015-2431.

[147] N. Koshikawa et al. “Activation imaging of gold nanoparticles for versatile drug visualization: An in vivo demonstration”. In: *Applied Physics Letters* 126.10 (Mar. 2025). ISSN: 1077-3118. DOI: 10.1063/5.0251048. URL: http://dx.doi.org/10.1063/5.0251048.

[148] Vincenzo Cuccurullo, Giuseppe Di Stasio, and Luigi Mansi. “Nuclear medicine in prostate cancer: A new era for radiotracers”. In: *World Journal of Nuclear Medicine* 17.02 (Apr. 2018), pp. 70–78. ISSN: 1607-3312. DOI: 10.4103/wjnm.wjnm_54_17. URL: http://dx.doi.org/10.4103/wjnm.WJNM_54_17.

Appendices

Appendix A

Table A.1: ICP-MS measurements. Each reading was carried out in triplicates and each group was preceded by blank and a 10 ppm measurement to compare accuracy.

Sample ID	Line	Conc.	Units
10 ppm - 1	Au 242.795 r	99.22% 9.92240	mg/L
10 ppm - 2	Au 242.795 r	100.01% 9.99922	mg/L
10 ppm - 3	Au 242.795 r	99.79% 9.96994	mg/L
blank - 1	Au 242.795 r	0.0209	mg/L
blank - 2	Au 242.795 r	0.0269	mg/L
blank - 3	Au 242.795 r	0.0356	mg/L
0.5 ml CURCAuNP - 1	Au 242.795 r	15.8286	mg/L
0.5 ml CURCAuNP - 2	Au 242.795 r	15.2101	mg/L
0.5 ml CURCAuNP - 3	Au 242.795 r	16.5153	mg/L
1.0 ml CURCAuNP - 1	Au 242.795 r	34.1096	mg/L
1.0 ml CURCAuNP - 2	Au 242.795 r	33.5521	mg/L
1.0 ml CURCAuNP - 3	Au 242.795 r	34.206	mg/L
1.5 ml CURCAuNP - 1	Au 242.795 r	49.9118	mg/L

Continued on next page

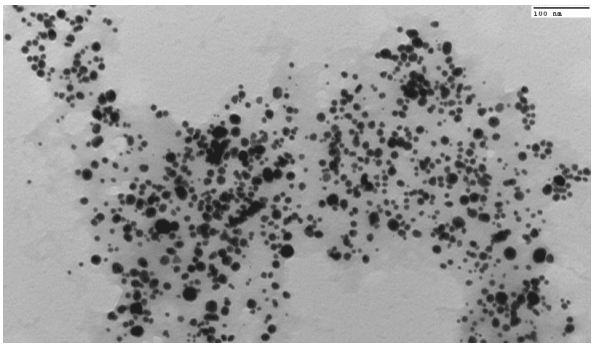
(*Table A.1 – continued from previous page*)

1.5 ml CURCAuNP - 2	Au 242.795 r	48.7352	mg/L
1.5 ml CURCAuNP - 3	Au 242.795 r	50.8097	mg/L
10 ppm - 1	Au 242.795 r	96.53% 9.65253	mg/L
10 ppm - 2	Au 242.795 r	97.59% 9.75857	mg/L
10 ppm - 3	Au 242.795 r	97.67% 9.76655	mg/L
blank - 1	Au 242.795 r	0.0291	mg/L
blank - 2	Au 242.795 r	0.0268	mg/L
blank - 3	Au 242.795 r	0.0131	mg/L
0.5 ml EGCGAuNP - 1	Au 242.795 r	21.2465	mg/L
0.5 ml EGCGAuNP - 2	Au 242.795 r	21.6929	mg/L
0.5 ml EGCGAuNP - 3	Au 242.795 r	21.6695	mg/L
1.0 ml EGCGAuNP - 1	Au 242.795 r	42.6147	mg/L
1.0 ml EGCGAuNP - 2	Au 242.795 r	43.0675	mg/L
1.0 ml EGCGAuNP - 3	Au 242.795 r	43.0508	mg/L
1.5 ml EGCGAuNP - 1	Au 242.795 r	61.2857	mg/L
1.5 ml EGCGAuNP - 2	Au 242.795 r	62.4977	mg/L
1.5 ml EGCGAuNP - 3	Au 242.795 r	62.6045	mg/L
10 ppm - 1	Au 242.795 r	98.11% 9.81128	mg/L
10 ppm - 2	Au 242.795 r	98.37% 9.83684	mg/L
10 ppm - 3	Au 242.795 r	98.68% 9.86711	mg/L
blank - 1	Au 242.795 r	0.0316	mg/L
blank - 2	Au 242.795 r	0.0613	mg/L
blank - 3	Au 242.795 r	0.0458	mg/L
0.5 ml CITAuNP - 1	Au 242.795 r	4.4115	mg/L
0.5 ml CITAuNP - 2	Au 242.795 r	4.5518	mg/L
0.5 ml CITAuNP - 3	Au 242.795 r	4.6437	mg/L
1.0 ml CITAuNP - 1	Au 242.795 r	8.5358	mg/L

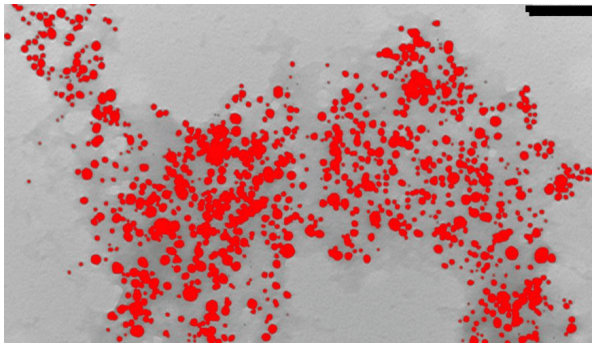
Continued on next page

(*Table A.1 – continued from previous page*)

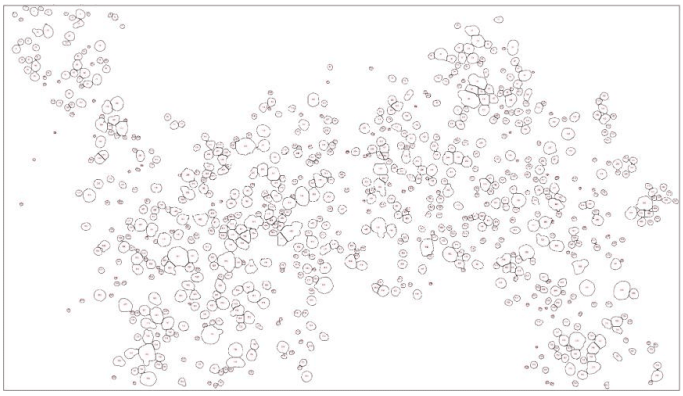
1.0 ml CITAuNP - 2	Au 242.795 r	8.9729	mg/L
1.0 ml CITAuNP - 3	Au 242.795 r	9.4086	mg/L
1.5 ml CITAuNP - 1	Au 242.795 r	12.697	mg/L
1.5 ml CITAuNP - 2	Au 242.795 r	12.0205	mg/L
1.5 ml CITAuNP - 3	Au 242.795 r	12.6631	mg/L
10 ppm - 1	Au 242.795 r	97.98% 9.79752	mg/L
10 ppm - 2	Au 242.795 r	98.01% 9.80102	mg/L
10 ppm - 3	Au 242.795 r	98.71% 9.87134	mg/L
blank - 1	Au 242.795 r	0.0505	mg/L
blank - 2	Au 242.795 r	0.0227	mg/L
blank - 3	Au 242.795 r	0.0487	mg/L
0.5 ml PEGAuNP - 1	Au 242.795 r	3.7115	mg/L
0.5 ml PEGAuNP - 2	Au 242.795 r	3.5518	mg/L
0.5 ml PEGAuNP - 3	Au 242.795 r	3.6437	mg/L
1.0 ml PEGAuNP - 1	Au 242.795 r	7.5358	mg/L
1.0 ml PEGAuNP - 2	Au 242.795 r	7.9729	mg/L
1.0 ml PEGAuNP - 3	Au 242.795 r	7.4086	mg/L
1.5 ml PEGAuNP - 1	Au 242.795 r	11.697	mg/L
1.5 ml PEGAuNP - 2	Au 242.795 r	11.0205	mg/L
1.5 ml PEGAuNP - 3	Au 242.795 r	11.9631	mg/L
10 ppm - 1	Au 242.795 r	98.31% 9.831	mg/L
10 ppm - 2	Au 242.795 r	97.62% 9.762	mg/L
10 ppm - 3	Au 242.795 r	98.86% 9.886	mg/L
blank - 1	Au 242.795 r	0.0168	mg/L
blank - 2	Au 242.795 r	0.0268	mg/L
blank - 3	Au 242.795 r	0.0179	mg/L



(A) Adjust scale using size bar



(B) Threshold to select only GNPs



(C) Apply size and circularity thresholds to improve accuracy.

Figure A.1: Stepwise process of ImageJ Particle Size Analysis

Thresholds applied: Size range: 5-500 nm^2 & Circularity: 0.60-1.00

$$Circularity = 4\pi \left(\frac{Area}{Perimeter^2} \right)$$

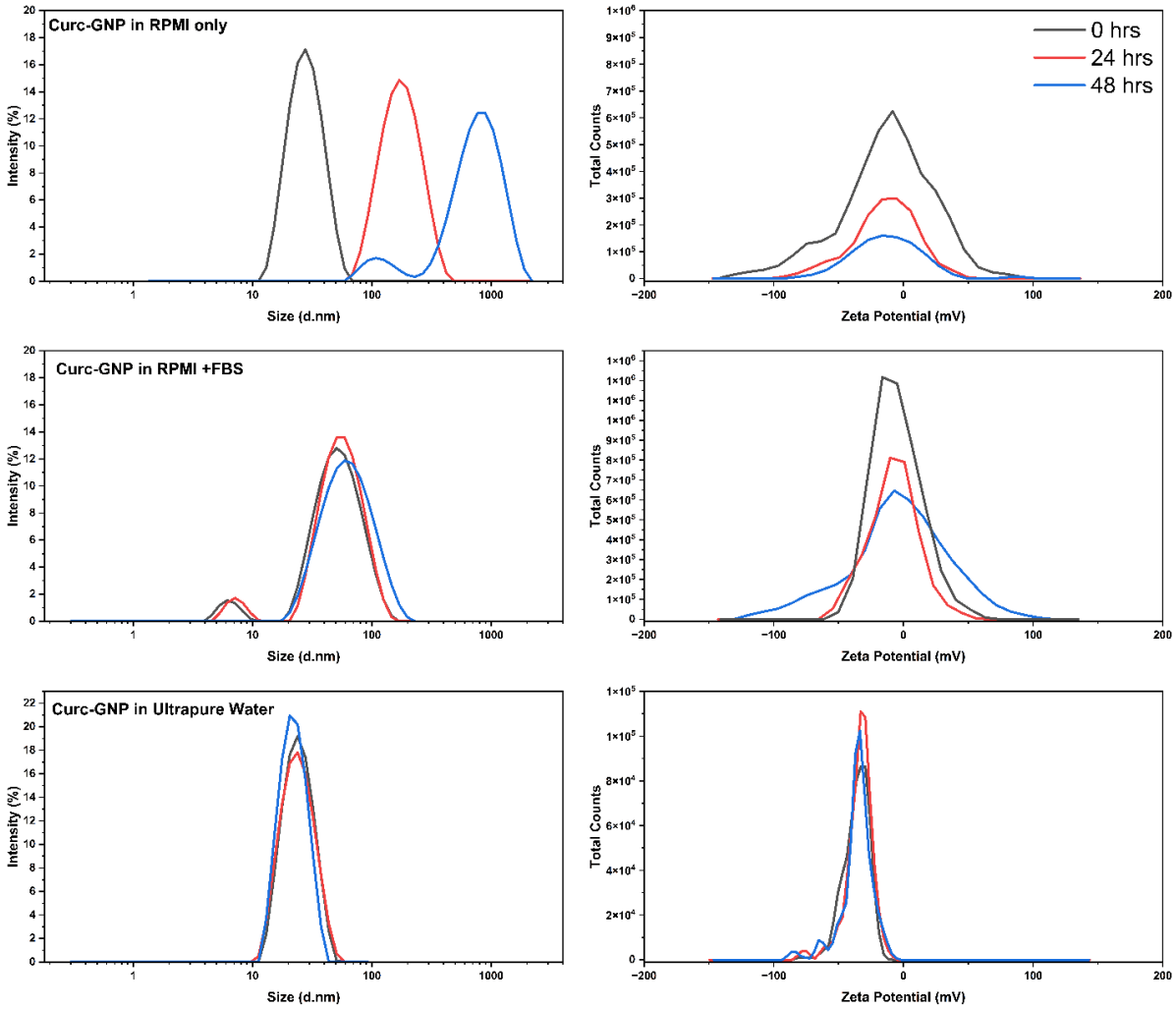


Figure A.2: DLS graphs for size distribution (intensity%) and zeta potential of Curc-GNPs at 0, 24 and 48 hours in three different media.

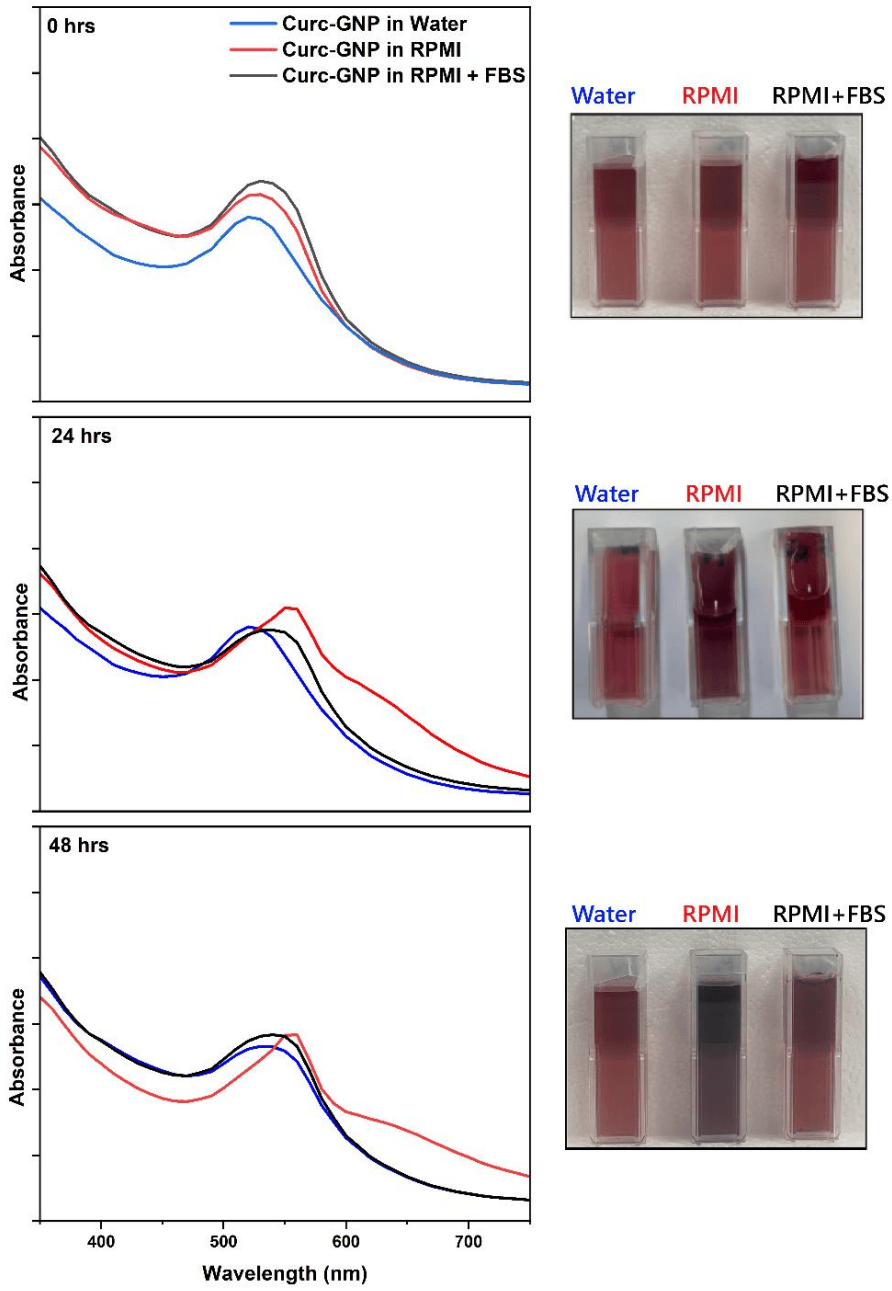


Figure A.3: UV-Vis spectra and image of Curc-GNPs incubated in three different media for 24 hours.

Table A.2: The HPLC responses, calculated concentrations, and percent deviations for curcumin standards (0.1–50 ppm) used to derive the calibration equation (y = 1.17×10^5x + 3.04×10^4; $R^2 = 0.998$).

Sample Name	Result Id	Peak Name	X Value (ppm)	Response	Calc. Value (ppm)	% Deviation
0.1ppm	3433	Curcumin	0.109	10424.501	-0.17	-257.02
0.1ppm	3436	Curcumin	0.109	12131	-0.156	-243.58
1ppm	3437	Curcumin	1.085	120839.001	0.773	-28.77
1ppm	3438	Curcumin	1.085	117898.999	0.748	-31.09
5ppm	3439	Curcumin	5.425	657772	5.36	-1.21
5ppm	3440	Curcumin	5.425	650118.003	5.294	-2.41
10ppm	3441	Curcumin	10.85	1349715.005	11.27	3.87
10ppm	3442	Curcumin	10.85	1355459.506	11.319	4.33
20ppm	3443	Curcumin	21.7	2635523.026	22.254	2.55
20ppm	3444	Curcumin	21.7	2631325.017	22.218	2.39
50ppm	3445	Curcumin	54.25	6385318.98	54.286	0.07
50ppm	3446	Curcumin	54.25	6309739.093	53.641	-1.12

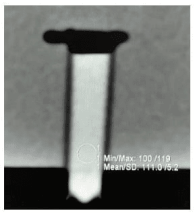
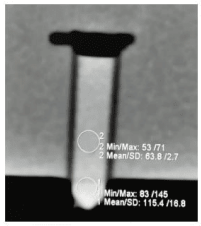
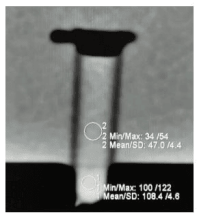
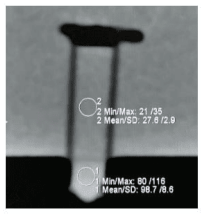
The Limit of Quantitation (LOQ) was determined using the calibration curve method, based on the equation:

$$LOQ = \frac{10 \times \sigma}{S}$$

Where σ represents the standard deviation of the response, S represents the slope of the calibration curve.

$$LOQ = \frac{10 \times 42165.7}{117000}$$
$$LOQ = 3.603\ ppm$$

Table A.3: The CT-Images and Mean HU Contrast for Different EGCG-GNPs Concentrations.

EGCG-GNPS Concentration	**Mean HU Contrast**	**Graphics**
1500 μg/mL	111.0 HU $\pm$ 5.2	
1000 μg/mL	91.7 HU $\pm$ 5.4	
500 μg/mL	63.8 HU $\pm$ 2.7	
250 μg/mL	47.0 HU $\pm$ 4.4	
Tap Water	27.6 HU $\pm$ 2.9	

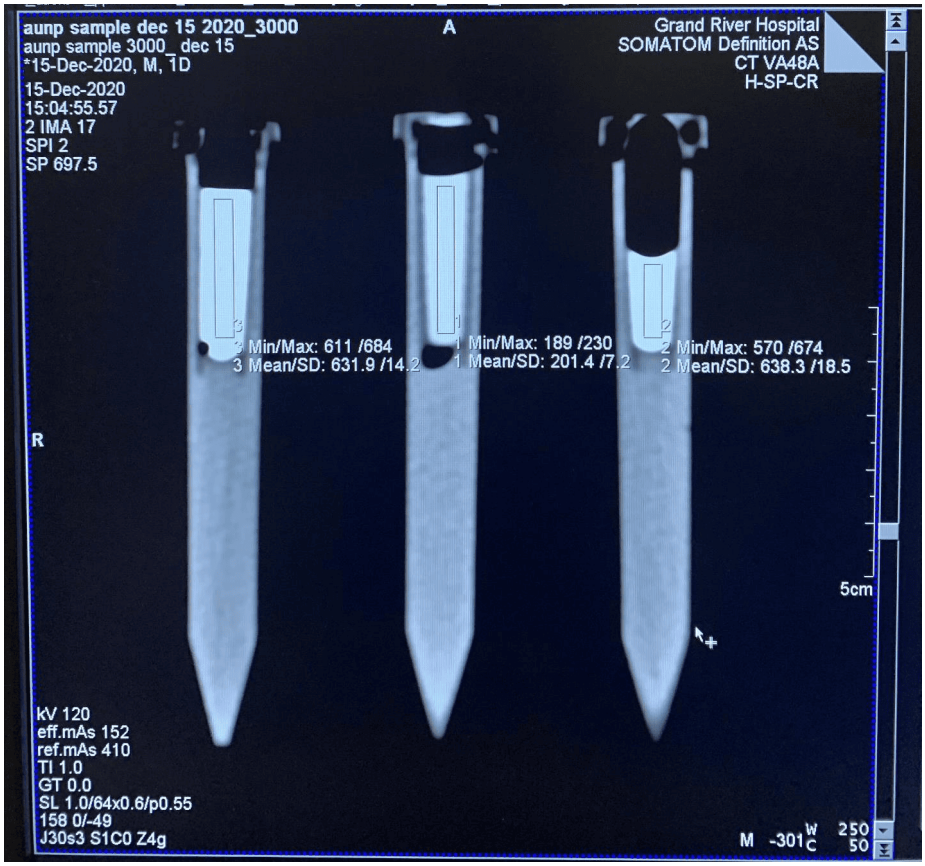


Figure A.4: (Left) Image of ultra concentrated EGCG-GNP (approx. 10 mg/mL), (Centre) 1.5 mg/mL EGCG-GNP, and (Right) 200 mM $HAuCl_4$ stock solution as a comparison.

Appendix B

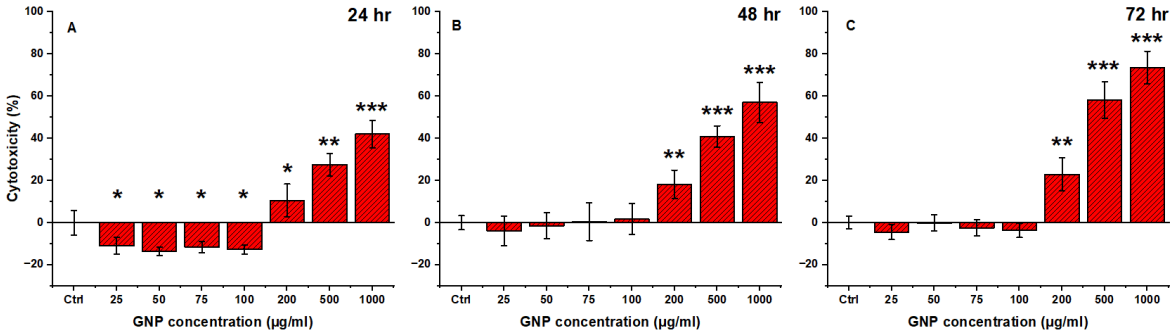


Figure B.1: *XTT results exploring the biphasic dose of Curc-GNP.* Cytotoxicity of Curc-GNPs in RPMI+FBS with PC-3 cells. The statistical significance was indicated by $^{*}p < 0.05$, $^{**}p < 0.01$, and $^{***}p < 0.001$.

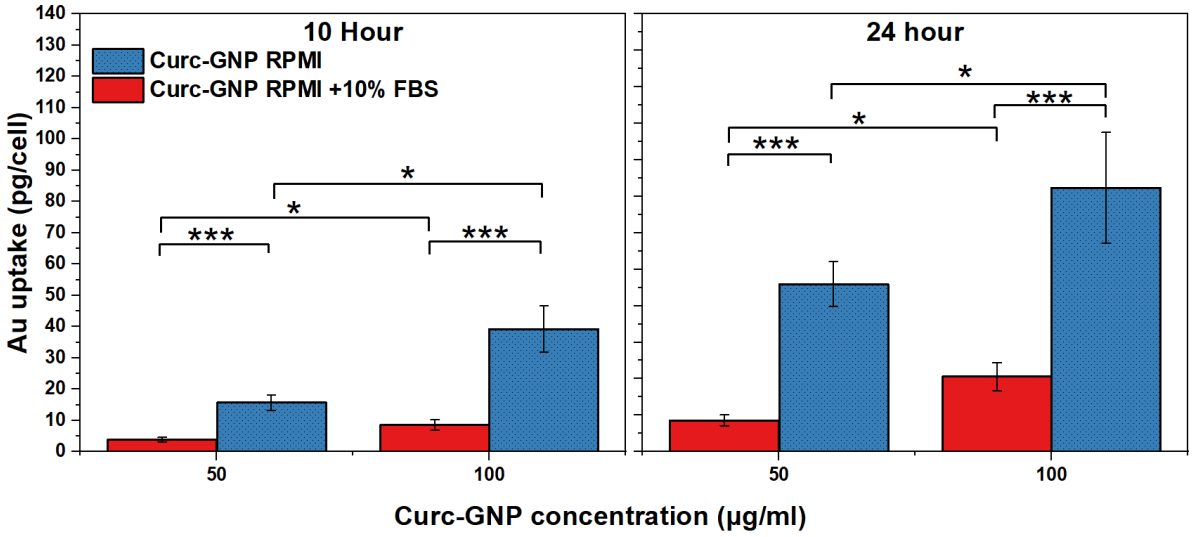


Figure B.2: *Cellular uptake of Curc-GNPs.* Showing the differences in uptake for serum vs non serum, 10 vs 24 hr, and 50 μg/mL vs 100 μg/mL for Curc-GNPs treated to PC-3 cells ($^{*}p < 0.05$, $^{**}p < 0.01$, and $^{***}p < 0.001$).

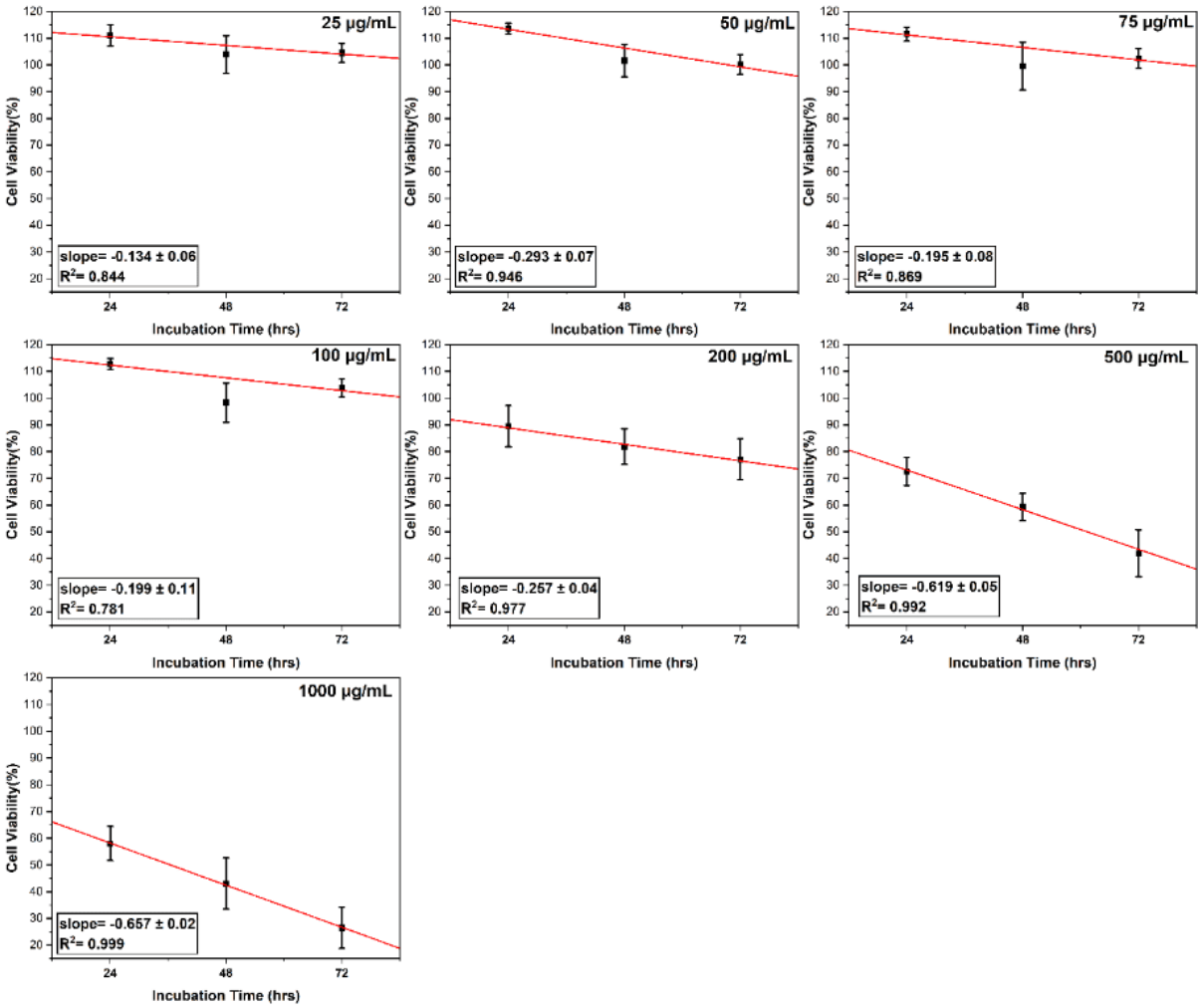


Figure B.3: Curc-GNP time-dependent change in cell viability (%) of PC3 cells incubated with varying concentrations (25-1,000 μg/mL) of for 24, 48, 72 hours.

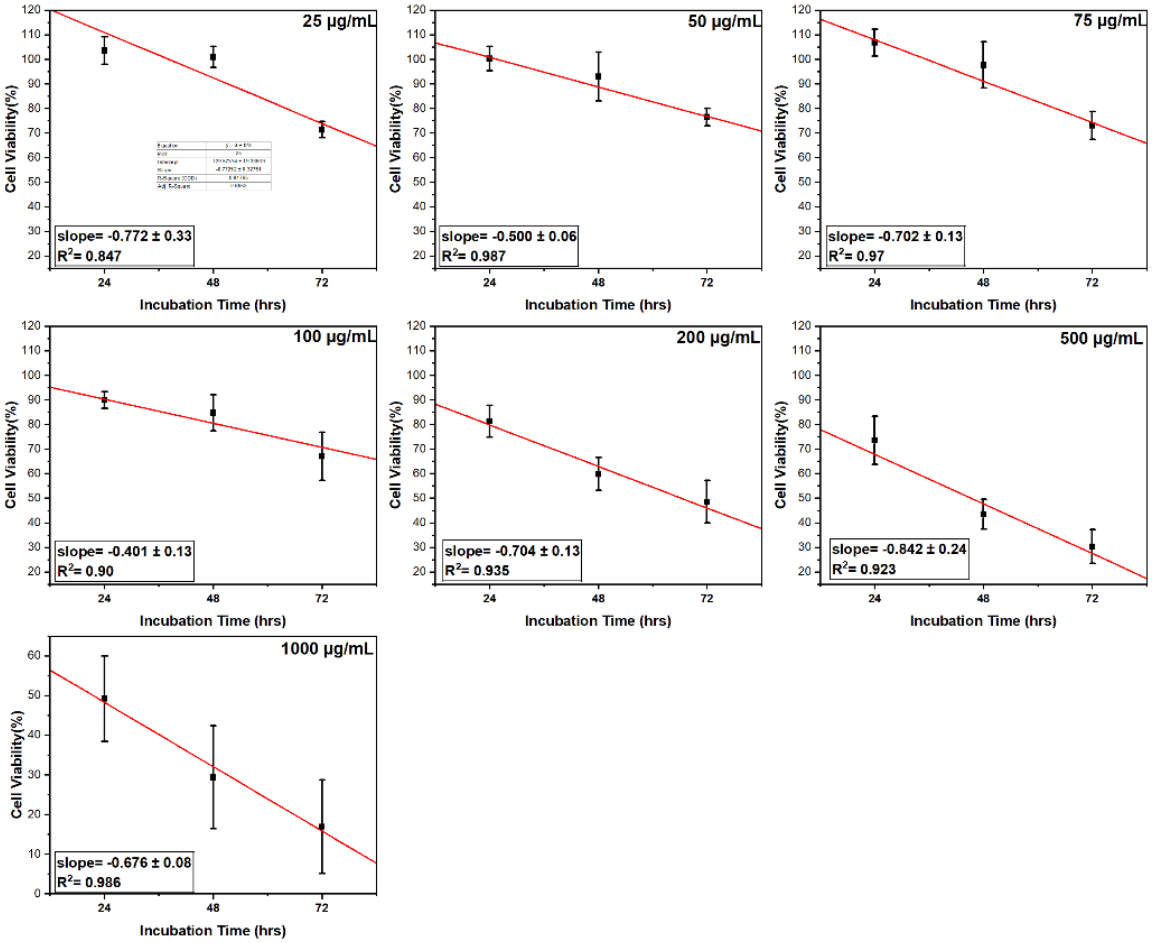


Figure B.4: EGCG-GNP time-dependent change in cell viability (%) of PC3 cells incubated with varying concentrations (25-1,000 μg/mL) of for 24, 48, 72 hours.

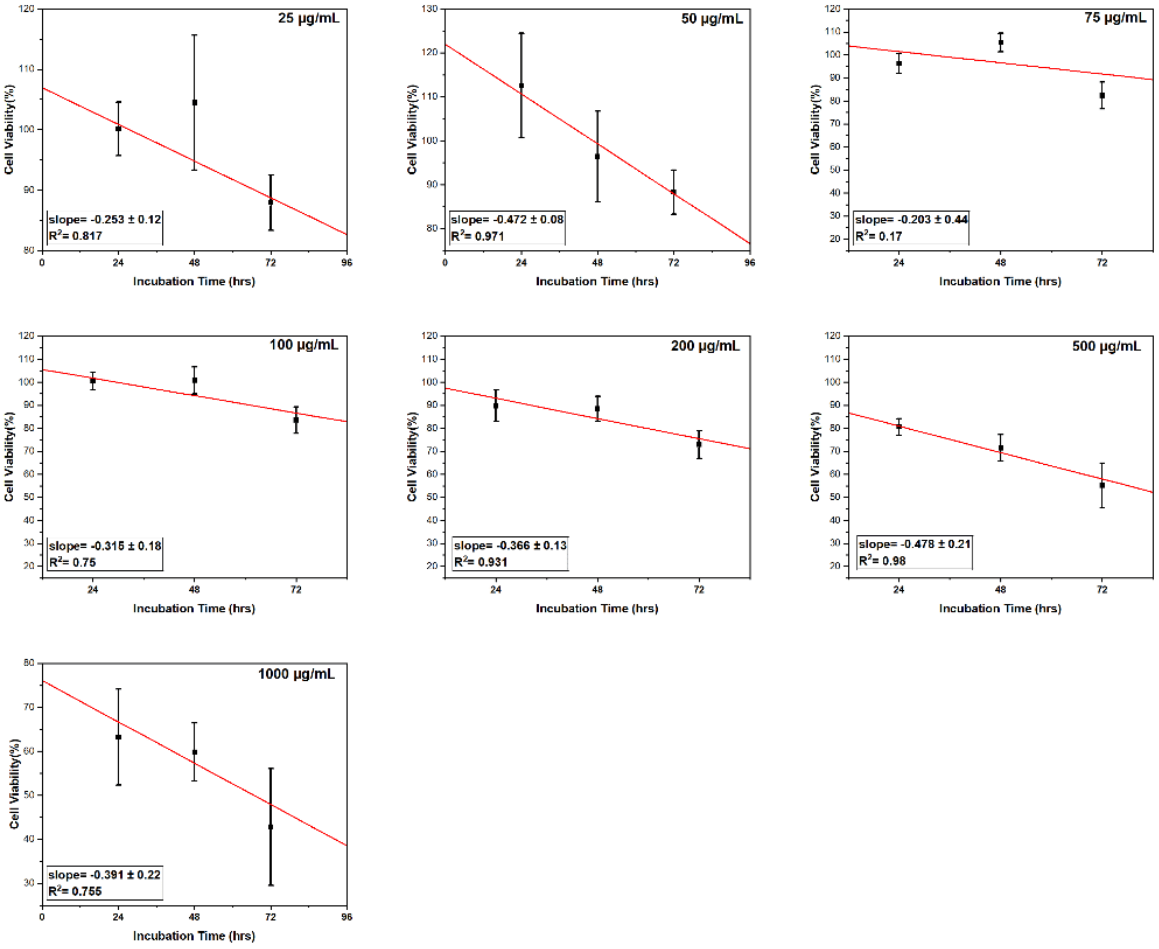


Figure B.5: Cit-GNP time-dependent change in cell viability (%) of PC3 cells incubated with varying concentrations (25-1,000 μg/mL) of for 24, 48, 72 hours.

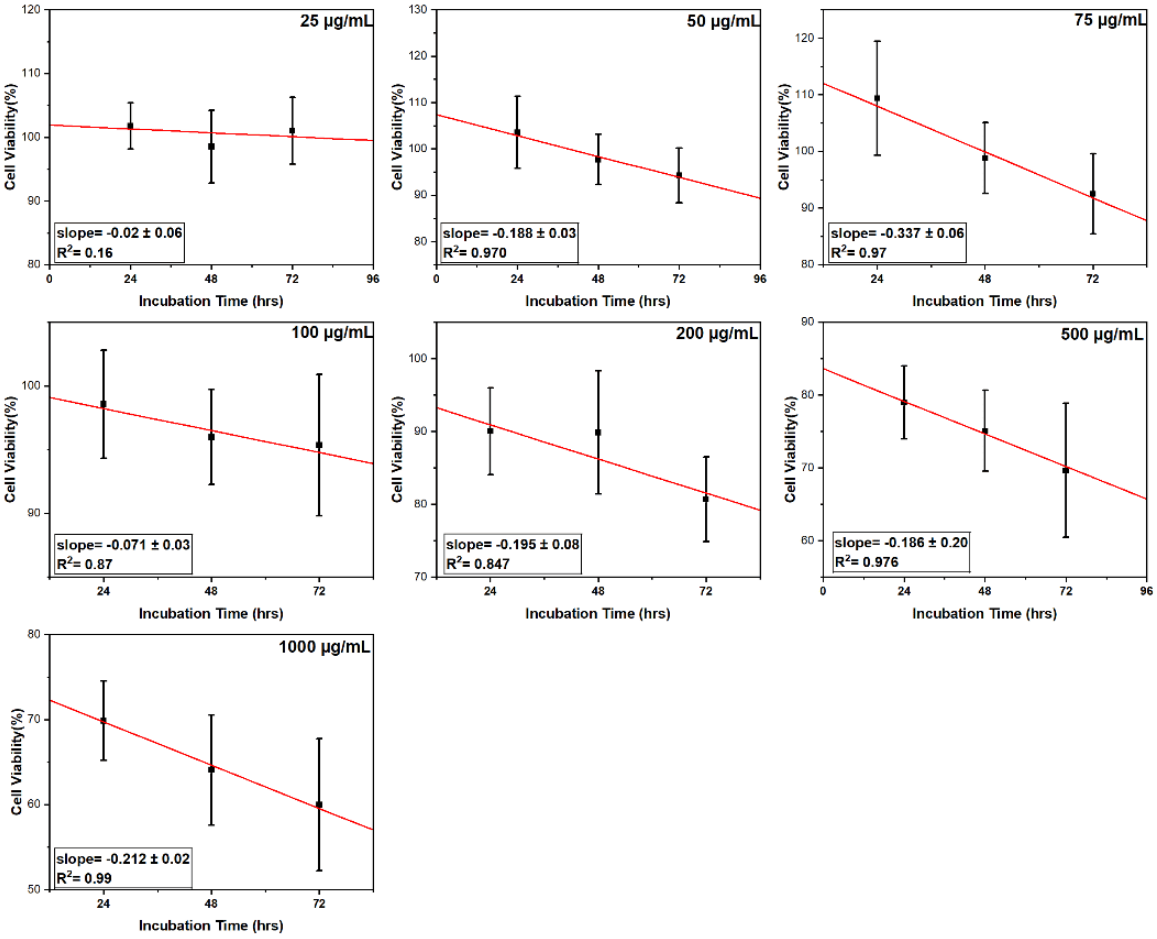


Figure B.6: PEG-GNP time-dependent change in cell viability (%) of PC3 cells incubated with varying concentrations (25-1,000 μg/mL) of for 24, 48, 72 hours.

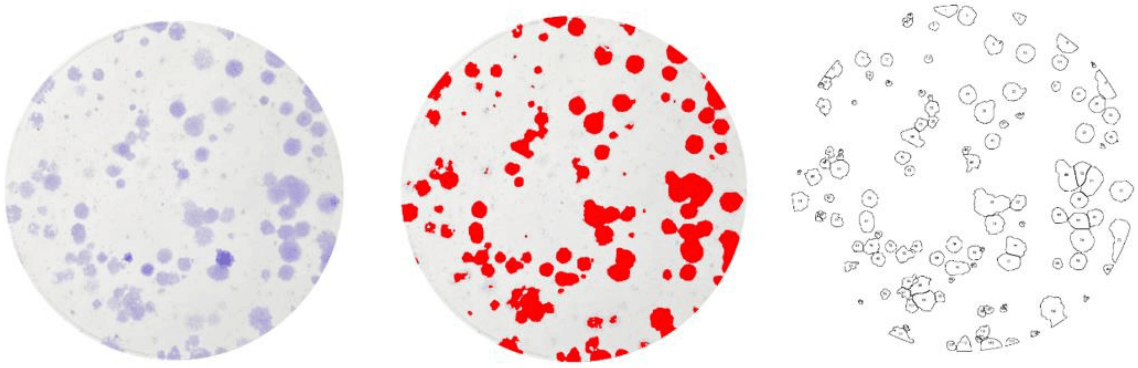


Figure B.7: Image processing for colony count analysis. Minimum size cut-off for colony count was 0.044 mm^2.

Python Script for Linear–Quadratic Model Fitting of Clonogenic Survival Data

```python
import numpy as np
import pandas as pd
from scipy.optimize import curve_fit

def lq(d, a, b):
    return np.exp(-(a*d + b*d*d))

def r2(obs, pred):
    ss_res = np.sum((obs - pred)**2)
    ss_tot = np.sum((obs - np.mean(obs))**2)
    return 1 - ss_res/ss_tot

def d50(a, b):
    disc = b*b - 4*a*(-np.log(2))
    if disc < 0:
        return np.nan
    root1 = (-a + np.sqrt(disc)) / (2*b)
    root2 = (-a - np.sqrt(disc)) / (2*b)
    pos = [r for r in [root1, root2] if r > 0]
    return pos[0] if pos else np.nan

def fit_lq(dose, sf, sf_err=None):
    guess = [0.2, 0.02]
    if sf_err is not None:
        popt, pcov = curve_fit(lq, dose, sf, p0=guess, sigma=sf_err, absolute_sigma=True)
    else:
        popt, pcov = curve_fit(lq, dose, sf, p0=guess)
    a, b = popt
    sa, sb = np.sqrt(np.diag(pcov))
    pred = lq(dose, a, b)
    return a, b, sa, sb, r2(sf, pred), d50(a, b)
```

```python

if __name__ == "__main__":
    df = pd.read_csv("Curc_GNP_clonogenic_data.csv")
    groups = ["ctrl", "25ug", "50ug", "75ug", "100ug", "200ug", "500ug"]
    results = {}
    ctrl_d50 = None

    for g in groups:
        e_col = f"{g}_err"
        errors = df[e_col].values if e_col in df.columns else None
        a, b, sa, sb, rsq, dv = fit_lq(df["dose"], df[g], errors)
        results[g] = {"a": a, "b": b, "sa": sa, "sb": sb, "rsq": rsq, "dv": dv}
        if g == "ctrl":
            ctrl_d50 = dv

    for g in groups:
        r = results[g]
        if g != "ctrl" and r["dv"] > 0 and ctrl_d50 and ctrl_d50 > 0:
            ser = ctrl_d50 / r["dv"]
        else:
            ser = np.nan

        print(f"\nGroup: {g}")
        print(f" Alpha (±SE): {r['a']:.4f} ± {r['sa']:.4f}")
        print(f" Beta (±SE): {r['b']:.4f} ± {r['sb']:.4f}")
        print(f" R²: {r['rsq']:.3f}")
        print(f" D50: {r['dv']:.3f} Gy")
        print(f" SER vs Ctrl: {ser:.3f}")
```

Appendix C

Table C.1: *CBC Results* - Beagle Study (McKenna, C. J. (2021))

Parameter	Unit	Reference Range	B1 Day0	B1 24h	B1 Day7	B2 Day0	B2 24h	B2 Day7	B3 Day0	B3 24h	B3 72h	B3 Day7
Plateletcrit	%	0.14-0.47	0.06	0.10	0.47	0.27	0.19	0.36	0.21	0.16	0.16	0.28
TS Protein	g/L	55-75	68	51	68	72	72	66	66	63	56	65
Absolute lymphs	$\times 10^9$/L	0.8-5.1	1.20	1.04	0.85	0.88	1.12	0.74	1.03	1.32	1.44	0.85
Absolute monos	$\times 10^9$/L	0.0-1.1	0.57	0.48	0.94	0.39	0.61	0.40	0.43	0.56	0.46	0.37
Absolute neuts	$\times 10^9$/L	2.9-10.6	4.47	5.24	6.38	3.91	8.36	4.28	3.83	7.52	5.55	4.82
Hct	L/L	0.39-0.56	0.44	0.23	0.41	0.50	0.53	0.43	0.45	0.43	0.38	0.43
MCH	pg	21-25	23	23	23	24	23	23	23	23	22	23
MCHC	g/L	321-360	345	337	319	344	326	325	340	333	326	329
MCV	fL	66-75	68	68	71	69	71	72	67	69	69	69
MPV	fL	7-14	14.9	11.6	15.9	11.2	10.3	10.4	9	9.2	9.3	9
Plts	$\times 10^9$/L	117-418	41	88	294	237	188	350	229	168	168	309
RBC	$\times 10^{12}$/L	5.8-8.5	6.4	3.4	5.9	7.3	7.4	6.1	6.7	6.2	5.6	6.2
WBC	$\times 10^9$/L	4.9-15.4	6.3	6.9	8.5	5.5	10.2	5.7	5.4	9.4	7.6	6.1

Table C.2: *Serum Biochemistry* - Beagle Study (McKenna, C. J. (2021))

Parameter	Unit	Reference Range	B1 Day0	B1 24h	B1 Day7	B2 Day0	B2 24h	B2 48h	B2 Day7	B3 Day0	B3 24h	B3 48h	B3 72h	B3 Day7
AG ratio		0.7-1.8	1.81	1.69	1.46	1.41	1.50	1.18	1.27	1.80	1.35	1.17	1.32	1.20
ALP	U/L	22-143	41	164	81	50	313	196	114	37	131	120	84	66
ALT	U/L	19-107	47	38	31	31	64	39	28	20	20	19	13	19
Steroid induced ALP	U/L	0-84	0	6	3	0	17	10	7	8	11	11	7	7
Amylase	U/L	299-947	528	890	1008	462	484	471	503	381	514	646	506	410
Anion	mmol/L	13-24	23	18	20	20	24	29	23	21	23	22	18	23
CK	U/L	40-255	244	712	151	317	316	355	216	118	269	219	122	95
Ca	mmol/L	2.50-3.00	2.42	2.19	2.43	2.18	2.31	1.98	2.07	2.47	2.20	2.34	2.22	2.00
CalOsmo	mmol/L		291	287	290	286	287	286	291	290	288	287	281	290
Cholesterol	mmol/L	3.60-10.20	5.39	3.89	5.23	5.08	6.16	4.98	5.79	4.31	3.93	4.64	3.71	4.34
Cl	mmol/L	104-119	112	112	110	114	108	108	111	110	109	110	106	109
Co2	mmol/L	15-25	16	20	20	16	18	13	19	19	18	17	23	20
Conjugated Bilirubin	μmol/L	0-1	1	1	1	0	1	0	1	0	0	0	1	0
Creatinine	μmol/L	20-150	49	42	47	7	58	35	24	52	48	52	36	39
Free Bilirubin	μmol/L	0-3	1	0	1	1	0	0	0	1	0	0	0	1
GGT	U/L	0-7	0	1	2	0	4	0	1	3	0	1	3	3
Globulin	g/L	21-42	21	16	24	22	22	22	26	20	23	29	22	25

Continued on next page

(Table C.2 – continued from previous page)

Glucose	mmol/L	3.3-7.3	4.8	6.4	5.2	4.6	5.0	4.5	3.9	5.4	4.8	5.1	5.1	4.2
Hemolysis			Mild	NEG	NEG	Mod.	NEG	Mild	Mild	NEG	Mild	Mild	NEG	NEG
K	mmol/L	3.8-5.4	4.2	3.8	4.4	4.0	4.6	4.6	4.7	4.2	4.2	4.2	3.7	4.6
Lipase	U/L	25-353	43	55	51	128	51	38	73	39	46	64	67	40
Lipemia			NEG	NEG	NEG	NEG	NEG	NEG	Mild	NEG	NEG	Mild	NEG	NEG
Mg	mmol/L	0.7-1.0	0.8	0.7	0.8	0.7	0.8	0.9	0.7	0.7	0.8	0.8	0.8	0.6
Na	mmol/L	140-154	147	146	146	146	145	145	148	146	146	145	143	147
NaK ratio		29-37	35	39	34	37	32	32	31	34	35	35	39	32
Phos	mmol/L	0.90-1.85	1.30	1.15	1.55	1.01	0.65	1.12	1.15	1.25	0.96	1.47	1.38	1.27
Total Bilirubin	μmol/L	0-4	2	1	2	1	1	0	1	1	0	0	1	1
Total Protein	g/L	55-74	59	43	59	53	55	48	59	56	54	63	51	55
Urea	mmol/L	3.5-9.0	4.5	2.1	4.9	2.9	3.6	3.0	3.5	5.4	3.4	4.2	2.9	3.8
Albumin	g/L	29-43	38	27	35	31	33	26	33	36	31	34	29	30

Table C.3: *Urinalysis Results* - Beagle Study (McKenna, C. J. (2021))

Parameter	**Unit**	**B1 Baseline**	**B2 Baseline**	**B3 Baseline**	**B3 Day2 (48h)**	**B3 Day3 (72h)**
Clarity		Slightly cloudy	Clear	Slightly cloudy	Slightly cloudy	Slightly cloudy
Colour		Yellow	Yellow	Yellow	Yellow	Yellow
Glucose		Negative	Negative	Negative	Negative	Negative
Ketones		Negative	Negative	Negative	Negative	Negative
Multistix protein	/100×	1+	Negative	Negative	Negative	Negative
RBCs	/100×	>100	Occasional	1-4	occasional	30-50
WBCs		6-10	None Seen	occasional	2-5	1-3
Amorphous			Occasional			
Bacteria				Occasional		
Bilirubin	/100×	1+	Negative	Negative	Negative	Negative
Blood	/100×	2+	Negative	Negative	Trace	1+
Fat	/100×			Occasional		2+
Fine granular cast				occasional		Occasional
pH		7.0	7.0	6.0	7.0	6.5
Source	/400×	Free flow	Other	Free flow		Other
Specific gravity	/400×	1.058	1.019	1.044	1.015	1.024
Squamous epi		1-3	0-1	1-2		Occasional
Urobilinogen	/100×	3.2	3.2	3.2	3.2	3.2
Vol (mL)		8.5	6.5	70.0	11.0	40
Squamous epi		1-3	0-1	1-2		Occasional
Urobilinogen	/100×	3.2	3.2	3.2	3.2	3.2
Vol (mL)		8.5	6.5	70.0	11.0	40



Figure C.1: Stomach purple discoloration caused by GNP injection in the intraperitoneal cavity.

Curc-GNP Histology Reports by Dr. Wilcock for Curc-GNP 14 & 28-day treatment groups.

DIAGNOSIS: 1. FOR MOUSE T5.14, HISTOLOGICALLY NORMAL TISSUES

The slide is labeled T5.14 and contains eight sections prepared from seven pieces of tissue in the formalin bottle. All of these appear histologically normal. Specifically, this includes normal myocardium, normal liver, and normal spleen. The spleen shows the usual mixture of hematopoiesis and lymphoid nodules, both well within the normal range for the age and species.

The liver displays mild, diffuse twofold variation in nuclear size, which is normal for this species. The hepatocytes exhibit mild biliary retention, also considered normal, with no evidence of inflammation, necrosis, or fibrosis. There are no cytoplasmic inclusions other than the normal background of yellow- green bile pigment and glycogen vacuolation. There is no activation of sinusoidal macrophages, and all vasculature is absolutely normal.

In the kidney, all tubules are histologically normal, with absolutely no degenerative changes within the tubular epithelium. There is no separation of tubules by edema or fibrosis, and there are no leukocytes present. The glomeruli are perfect.

Large sections of lung display normal bronchial and bronchiolar epithelium, as well as normal blood vessels. The alveoli show no hypercellularity, and there is no inflammation, necrosis, fibrosis, or any other abnormal change.

The myocardium is free of necrosis, fibrosis, or leukocytic infiltration.

The section of stomach is perfect, including the presence of abundant ingesta. There is no evidence of active or recent ulceration, and leukocytes are well within the normal range.

DIAGNOSIS: 2. FOR MOUSE T8.28, HISTOLOGICALLY NORMAL TISSUES

There are seven pieces of tissue on a slide labeled T8.28. One by one, I am examining histologically normal sections from six different organs. In none of them do I observe any inflammation, necrosis, fibrosis, hyperplasia, or any type of intracellular inclusions.

More specifically, the liver shows only normal mild anisokaryosis. The sinusoidal macrophages remain inconspicuous, and there is no sinusoidal leukocytosis. The hepatocytes themselves have mild feathery vacuolation typical of moderate glycogen storage, along with very mild intracellular cholestasis. I consider all of this to be perfectly normal. I see no intracellular inclusions, and there is absolutely no degenerative change.

In the kidney, I observe normal tubules with no degenerative changes. They are packed closely together with no interstitial edema, fibrosis, or leukocytosis. The glomeruli are perfect.

The myocardium shows no fibrosis, necrosis, or inflammation.

The lung is histologically normal in terms of bronchial and bronchiolar epithelium, alveolar morphology, and there is an absence of edema or cellular infiltration, with no changes to the pleura or blood vessels.

The spleen has normal lymphoid follicular activity and hematopoiesis, and the stomach is absolutely normal with no inflammation, ulceration, or fibrosis.

This slide does not include pancreas.

EGCG-GNP Histology Reports by Dr. Wilcox for EGCG-GNP 14 & 28-day treatment groups.

DIAGNOSIS: 1. FOR MOUSE T6.14D, HISTOLOGICALLY NORMAL TISSUES

Kidney: The two sections of kidney are both histologically normal. The cortical tubules are mature and closely packed, with no interstitial edema or fibrosis to indicate previous tubular injury. There is no increase in leukocytes, and the tubules themselves show no evidence of active or recent injury. The glomeruli are structurally normal, and the tubules contain no cellular debris or protein. By all measurable histologic parameters, this kidney is normal.

Liver: The single section of liver is histologically normal in all parameters assessed. There is widespread twofold variation in nuclear size, which is well within the normal range for this species. There is no hepatocellular necrosis, no influx of leukocytes, and no fibrosis. Hepatic architecture remains absolutely normal. The hepatocellular cytoplasm shows moderate feathery vacuolation, likely due to glycogen loading. I can detect no qualitative or quantitative difference between this liver and that of the normal control mouse.

Lung: The large section of lung displays normal bronchioles and bronchi with mature epithelium, normal alveoli with no increase in cellularity, no evidence of alveolar injury, no increase in leukocytes, and normal pulmonary blood vessels. The visceral pleura is also normal.

Stomach: The stomach contains abundant ingesta. The section includes the junction between the squamous and glandular stomach, both of which are histologically normal. The glandular stomach, in particular, has an intact and mature surface epithelium, mature glands with no increased spacing, no fibrosis, and only a small accumulation of mixed mononuclear leukocytes, especially around the base of the gastric glands. The submucosa and tunica muscularis are perfect.

Spleen: The spleen section shows a normal ratio of red pulp to white pulp, a normal amount of hematopoiesis, and no abnormal pigmentary accumulations. The surface mesothelium has no reactive changes and remains normal.

DIAGNOSIS: 2. FOR MOUSE C7.28D, HISTOLOGICALLY NORMAL TISSUES

I am examining eight sections from six tissues on a slide labeled C7.28. These tissues include single sections from normal liver, stomach, myocardium, pancreas, spleen, and lung. There are also two sections of histologically normal kidney. There is no pancreas or esophagus present on this slide. No lesions are observed in any tissueâĂŤthere is no evidence of necrosis, fibrosis, inflammation, hyperplasia, or abnormal intracellular accumulations.

DIAGNOSIS:

1. HISTOLOGICALLY NORMAL TISSUES

PBPK Supplementary Materials:

Model Building PK:	This Study
Particles:	EGCG and Curcumin-capped Gold Nanoparticles
Hydrodynamic Radius:	20 nm
Dose:	10 mg Au/kg IP
Animal:	Mouse

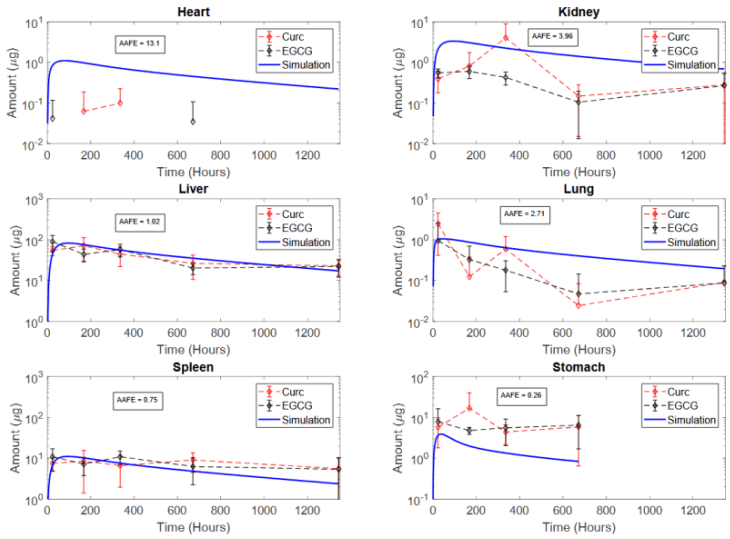


Figure C.2: Comparison of Model Simulations to Mouse Biodistribution Data from this Study.

Model Evaluation PK: Balasubramanian *et al.*
Particles: Citrate-capped Gold Nanoparticles
Hydrodynamic Radius: 30 nm
Dose: 0.01 mg Au/kg IV
Animal: Rat

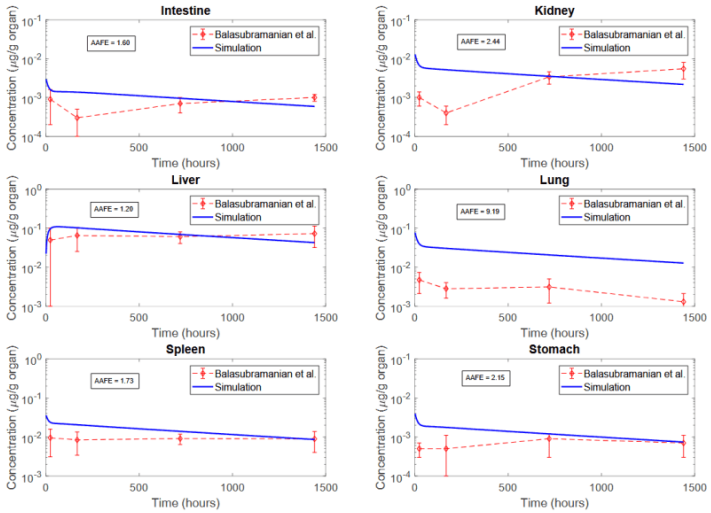


Figure C.3: Comparison of Model Simulations to Rat Biodistribution Data from Balasubramanian *et al.*

Model Evaluation PK: Fraga *et al.*
Particles: Citrate-capped Gold Nanoparticles
Hydrodynamic Radius: 23 nm
Dose: 0.7 mg Au/kg IV
Animal: Rat

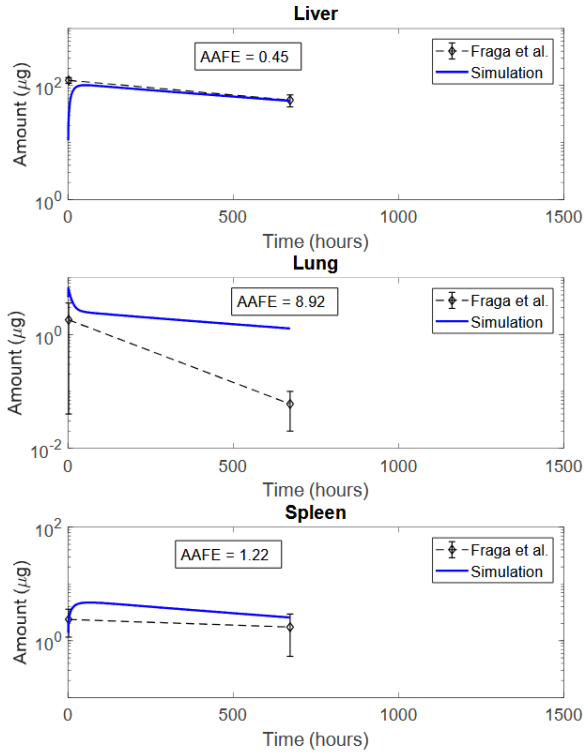


Figure C.4: Comparison of Model Simulations to Rat Biodistribution Data from Fraga *et al.*

Table C.4: State, Variable and Parameter Notation

Term	Units	Definition
PLQ_{Lung}	mL/h	Total body plasma flow
$L_{lymphNode}$	mL/h	Total body lymph flow
PLQ_i	mL/h	Plasma flow into and out of each organ
L_i	mL/h	Lymph flow into and out of each organ
C_{plasma}	μg/mL	Concentration of NP in plasma
$C_{lymphNode}$	μg/mL	Concentration of NP in lymph
C_iP	μg/mL	Concentration of NP in organ plasma space
C_iE	μg/mL	Concentration of NP in organ endothelium
C_iM	μg/mL	Concentration of NP in organ macrophages
C_iIS	μg/mL	Concentration of NP in organ interstitial space
C^H_{Liver}	μg/mL	Concentration of NP in liver hepatocytes
F^V_i	-	Vascular space fraction (plasma and blood)
F^P_i	-	Plasma space fraction
F^E_i	-	Endothelium fraction
F^M_I	-	Fraction of cellular volume attributed to macrophages
F^{IS}_i	-	Interstitial fraction
F^C_i	-	Cellular fraction
F^H_{Liver}	-	Fraction of cellular volume attributed to hepatocytes
V_{Plasma}	mL	Volume of plasma
$V_{lymphNode}$	mL	Volume of lymphatic system components
V_i	mL	Volume of organ
$V_{i_{mouse}}$	mL	Volume of organ in a 21g mouse
V^P_i	mL	Volume of organ plasma space
V_iE	mL	Volume of organ endothelium
V_iM	mL	Volume of organ macrophages
V_iIS	mL	Volume of organ interstitial space

Continued on next page

(*Table C.4 – continued from previous page*)

V_{Liver}^{H}	mL	Volume of liver hepatocytes
P_{up}	mL/h/mL	Rate of phagocytosis per mL of macrophages
K_M	μg/mL	Michaelis-Menten constant for saturable phagocytosis
F_{up}^{M}	-	Fraction of phagocytic uptake from liver plasma
F_{rec}^{M}	-	Fraction of exocytosis from liver macrophages into plasma
$CLup$	mL/h/mL	Rate of pinocytosis and exocytosis per mL of endothelium, macrophages and hepatocytes
F_{up}^{E}	-	Fraction of pinocytic uptake from organ plasma space
F_{rec}^{E}	-	Fraction of exocytosis into organ plasma space
K_{Bile}	1/h	Rate of excretion into bile from liver hepatocytes
A_{IP}	μg	Amount of NP in the intraperitoneal space
K_{Abs}	1/h	Rate of absorption from the intraperitoneal space
F	-	Intraperitoneal bioavailability
F_{portal}^{IP}	-	Fraction absorbed into the portal system
J_i^L	mL/h	Fluid flux across large pores
J_i^S	mL/h	Fluid flux across small pores
$Jiso_i$	mL/h	Fluid recirculation flow rate
P_i^L	cm/h	Permeability across large pores
P_i^S	cm/h	Permeability across small pores
Pe_i^L	-	Peclet number for large pores
Pe_i^S	-	Peclet number for small pores
S_i	cm^2	Surface area of vascular endothelium
γ_i^L	-	Ratio of NP hydrodynamic radius to organ large pore radius
γ_i^S	-	Ratio of NP hydrodynamic radius to organ small pore radius
r_i^L	nm	Organ large pore radius
r_i^S	nm	Organ small pore radius
r_i^{NP}	nm	NP hydrodynamic radius
α_i^L	-	Fraction of flow via large pores in organ
α_i^S	-	Fraction of flow via small pores in organ
K_{IP}	-	Interstitial:Plasma partition coefficient

Continued on next page

(Table C.4 – continued from previous page)

Lp_i	mL/h/N	Hydraulic conductivity in organ
RT	NÂůcm/mol	Gas constant at body temperature (37°C)
N_a	1/mol	AvogadroâĂŹs number
k_e	cm^2/mL	Proportionality constant for vascular endothelium
d_e	cm	Thickness of vascular endothelium
F_i^{Jiso}	-	Fluid recirculation fraction
F_i^{lymph}	-	Lymph flow fraction

Table C.5: Anatomical Values for Mouse

Parameter	**Notation**	**Value**	**Unit**
Body Mass	BM	28	g
Hematocrit	HCT	0.45	
Plasma Cardiac Output	CO_{Plasma}	240.7	mL/h

Table C.6: Organ Volumes and Composition for Mouse

	V_i (mL)	V_i^P (mL)	V_i^E (mL)	V_i^{IS} (mL)	V_i^C (mL)	V_i^M (mL)	V_i^H (mL)	SA_i (cm^2)
Heart	0.1266	0.018243	0.000945	0.01266	0.079825	0.001597	-	31.51074
Kidney	0.4531	0.026167	0.001356	0.09062	0.313549	0.006271	-	45.196725
Muscle	13.326	0.190562	0.009875	1.59912	11.37053	0.227411	-	329.1522
Skin	3.865	0.040389	0.002093	1.16723	2.622242	0.052445	-	69.76325
Brain	0.227	0.004619	0.000239	0.000908	0.217454	0.008698	-	7.97905
Adipose	1.33	0.007315	0.000379	0.17955	1.136771	0.045471	-	12.635
Gonads	0.333	0.025641	0.001329	0.022977	0.262074	0.010483	-	44.289
Liver	1.73	0.109423	0.00567	0.28199	1.24339	0.124339	0.9325	189.0025
Stomach	0.1466	0.00258	0.000134	0.01466	0.127115	0.005085	-	4.45664
Spleen	0.133	0.020628	0.001069	0.01995	0.074475	0.022343	-	35.6307
Pancreas	0.173	0.017127	0.000887	0.02076	0.120213	0.004809	-	29.583
S. Intestine	1.874	0.024737	0.001282	0.176156	1.651586	0.066063	-	42.7272
L. Intestine	0.836	0.011035	0.000572	0.078584	0.73678	0.029471	-	19.0608
Bone	2.11	0.047581	0.002466	0.211	1.810024	0.072401	-	82.1845
Lung	0.133	0.045792	0.002373	0.025004	0.022365	0.000895	-	79.0951
Plasma	0.55	-	-	-	-	0.011	-	-
Lymph	0.113	-	-	-	-	0.00452	-	-

Table C.7: Fluid Flow Rates for Mouse

	$\boldsymbol{PLQ_i}$ (mL/h)	$\boldsymbol{L_i}$ (mL/h)	$\boldsymbol{Jiso_i}$ (mL/h)	$\boldsymbol{J_i^L}$ (mL/h)	$\boldsymbol{J_i^S}$ (mL/h)	$\boldsymbol{F_i^{lymph}}$	$\boldsymbol{F_i^{Jiso}}$
Heart	12.31365	0.018101	0.015001	0.015906	0.002195	0.00147	0.96
Kidney	57.17012	0.040534	0.026629	0.028655	0.011878	0.000709	0.761
Muscle	40.01798	0.080436	0.020276	0.024298	0.056138	0.00201	0.292
Skin	18.03486	0.063483	0.033813	0.036987	0.026496	0.00352	0.617
Brain	5.728368	0.000416	0.000145	0.000166	0.00025	0.0000727	0.404
Adipose	1.7556	0.013237	0.004082	0.004103	0.008493	0.00754	0.357
Gonads	2.109888	0.02342	0.019412	0.020583	0.002837	0.0111	0.96
Liver	15.36863	0.307373	0.053654	0.299552	0.007821	0.02	0.96
Stomach	4.8378	0.009676	0.008018	0.008502	0.001173	0.002	0.96
Spleen	3.9501	0.078607	0.000143	0.063029	0.015578	0.0199	0.01
Pancreas	2.2836	0.069193	0.000598	0.004057	0.065136	0.0303	0.01
S. Intestine	43.98203	0.085765	0.013252	0.017541	0.068224	0.00195	0.179
L. Intestine	21.99867	0.316781	0.048943	0.064782	0.251999	0.0144	0.179
Bone	11.1408	0.007375	0.006108	0.006477	0.000899	0.000662	0.96
Lung	240.7	0.008562	0.000074	0.000502	0.00806	-	0.01
Plasma	240.7	-	-	-	-	-	-
Lymph	-	1.122958	-	-	-	-	-

Table C.8: Extravasation Parameters

	r^L (nm)	r^S (nm)	α_i^L	LP_i (mL/h/N)
Heart	25	4.5	0.05	0.03096
Kidney	25	4.5	0.05	0.27
Muscle	25	4.5	0.05	0.01944
Skin	25	4.5	0.05	0.04206
Brain	25	4.5	0.05	0.000108
Adipose	25	4.5	0.05	0.01944
Gonads	25	4.5	0.05	0.01944
Liver	33	9	0.8	0.084
Stomach	25	4.5	0.05	0.0858
Spleen	33	9	0.80	0.084
Pancreas	25	4.5	0.05	0.0696
S. Intestine	25	4.5	0.05	0.3324
L. Intestine	25	4.5	0.05	0.4038
Bone	25	4.5	0.05	0.01944
Lung	25	4.5	0.05	0.01224

Table C.9: Macrophage Content

	F_i^M
Heart	0.02
Kidney	0.02
Muscle	0.02
Skin	0.02
Brain	0.04
Adipose	0.04
Gonads	0.04
Liver	0.1
Stomach	0.04
Spleen	0.30
Pancreas	0.04
S. Intestine	0.04
L. Intestine	0.04
Bone	0.04
Lung	0.04
Plasma	0.02
Lymph	0.04

Table C.10: Model Constants

Parameter	Notation	Value	Unit
Gas constant at body temperature 37°C	RT	$2.58E+05$	NÂůcm/mol
Proportionality constant for vascular endothelium	k_e	950	cm^2/mL
Thickness of vascular endothelium	d_e	$3.00E-05$	cm
AvogadroâĂŹs number	N_a	$6.02E+23$	1/mol
Interstitial:Plasma partition coefficient	K_{IP}	0.96	-
Rate of pinocytosis and exocytosis per mL of endothelium, macrophages and hepatocytes	$CLup$	$5.00E-02$	L/h/L
Fraction of pinocytic uptake from organ plasma space	F_{up}^{E}	0.5	-
Fraction of exocytosis into organ plasma space	F_{rec}^{E}	0.5	-
Rate of phagocytosis per mL of macrophages	Pup	0.995	L/h/L
Michaelis-Menten constant for saturable phagocytosis	K_M	5000	μg/mL
Fraction of phagocytic uptake from liver plasma	F_{up}^{M}	0.5	-
Fraction of exocytosis from liver macrophages into plasma	F_{rec}^{M}	0.5	-
Lymphatic reflection coefficient	σ^{IS}	0.64	-
Rate of excretion into bile from liver hepatocytes	K_{Bile}	0.0128	1/h
Intraperitoneal bioavailability	F	0.76	-
Fraction absorbed into the portal system	F_{Portal}	0.9	-
Rate of absorption from the intraperitoneal space	K_{Abs}	0.05	1/h

Table C.11: Anatomical Values for Rat

Parameter	Notation	Value	Unit
Body Mass	BM	280	g
Hematocrit	HCT	0.45	
Plasma Cardiac Output	CO_{Plasma}	1747.762	mL/h

Table C.12: Organ Volumes and Composition for Rat

	V_i (mL)	V_i^P (mL)	V_i^E (mL)	V_i^{IS} (mL)	V_i^C (mL)	V_i^M (mL)	V_i^H (mL)	SA_i (cm^2)
Heart	0.983	0.14165	0.00734	0.0983	0.619814	0.012396	-	244.6687
Kidney	2.827	0.163259	0.00846	0.5654	1.956305	0.039126	-	281.9933
Muscle	149.97	2.144571	0.111128	17.9964	127.9633	2.559265	-	3704.259
Skin	49.17	0.513827	0.026626	14.84934	33.3598	0.667196	-	887.5185
Brain	2.089	0.042511	0.002203	0.008356	2.001148	0.080046	-	73.42835
Adipose	12.292	0.067606	0.003503	1.65942	10.50616	0.420246	-	116.774
Gonads	3.073	0.236621	0.012261	0.212037	2.418482	0.096739	-	408.709
Liver	12.6615	0.80084	0.041498	2.063825	9.100105	0.91001	6.825079	1383.269
Stomach	1.352	0.023795	0.001233	0.1352	1.172303	0.046892	-	41.1008
Spleen	0.73756	0.114396	0.005928	0.110634	0.413006	0.123902	-	197.5923
Pancreas	1.598	0.158202	0.008198	0.19176	1.110402	0.044416	-	273.258
S. Intestine	6.146	0.081127	0.004204	0.577724	5.416568	0.216663	-	140.1288
L. Intestine	2.676	0.035323	0.00183	0.251544	2.358402	0.094336	-	61.0128
Bone	19.422	0.437966	0.022695	1.9422	16.6608	0.666432	-	756.4869
Lung	1.229	0.423145	0.021927	0.231052	0.206667	0.008267	-	730.8863
Plasma	6.56	-	-	-	-	0.1312	-	-
Lymph	1.15	-	-	-	-	0.046	-	-

Table C.13: Fluid Flow Rates for Rat

	$\boldsymbol{PLQ_i}$ (mL/h)	$\boldsymbol{L_i}$ (mL/h)	$\boldsymbol{Jiso_i}$ (mL/h)	$\boldsymbol{J_i^L}$ (mL/h)	$\boldsymbol{J_i^S}$ (mL/h)	$\boldsymbol{F_i^{lymph}}$	$\boldsymbol{F_i^{Jiso}}$
Heart	161.7344	0.23775	0.099503	0.111391	0.126359	0.00147	0.96
Kidney	374.5167	0.265532	0.094757	0.108033	0.157499	0.000709	0.761
Muscle	304.3641	0.611772	0.068817	0.099405	0.512366	0.00201	0.292
Skin	236.5765	0.832749	0.190001	0.231638	0.601111	0.00352	0.617
Brain	54.06729	0.003931	0.000654	0.00085	0.00308	0.0000727	0.404
Adipose	16.22544	0.12234	0.017978	0.018175	0.098244	0.00754	0.357
Gonads	19.47053	0.216123	0.085406	0.096212	0.119911	0.0111	0.96
Liver	81.14249	1.622850	0.145903	1.444183	0.178666	0.02	0.96
Stomach	45.96786	0.091936	0.036332	0.040928	0.051007	0.002	0.96
Spleen	25.69276	0.511286	0.000525	0.409554	0.101732	0.0199	0.01
Pancreas	20.95649	0.634982	0.002614	0.034363	0.600619	0.0303	0.01
S. Intestine	101.409	0.197748	0.020566	0.030453	0.167294	0.00195	0.179
L. Intestine	202.817	2.920565	0.306176	0.452204	2.468361	0.0144	0.179
Bone	102.7597	0.068027	0.026882	0.030283	0.037743	0.000662	0.96
Lung	1747.762	0.062118	0.000256	0.003362	0.058756	-	0.01
Plasma	1747.762	-	-	-	-	-	-
Lymph	-	8.399707	-	-	-	-	-

Blood Compartment: Plasma

Equation C1: Amount of NP in Plasma

$$
\begin{aligned}
V_{Plasma} \times & \frac{dC_{Plasma}}{dt} \\
& = (PLQ_{Heart} - L_{Heart}) \times C^P_{Heart} + (PLQ_{Kidney} - L_{Kidney}) \times C^P_{Kidney} \\
& + (PLQ_{Muscle} - L_{Muscle}) \times C^P_{Muscle} + (PLQ_{Skin} - L_{Skin}) \times C^P_{Skin} \\
& + (PLQ_{Brain} - L_{Brain}) \times C^P_{Brain} + (PLQ_{Adipose} - L_{Adipose}) \times C^P_{Adipose} \\
& + (PLQ_{Gonads} - L_{Gonads}) \times C^P_{Gonads} \\
& + (PLQ_{Liver} - L_{Liver} + PLQ_{Stomach} - L_{Stomach} + PLQ_{Spleen} - L_{Spleen} \\
& + PLQ_{Pancreas} - L_{Pancreas} + PLQ_{SInt} - L_{SInt} + PLQ_{LInt} - L_{LInt}) \times C^P_{Liver} \\
& + (PLQ_{Bone} - L_{Bone}) \times C^P_{Bone} + L_{LymphNode} \times C_{LymphNode} \\
& - PLQ_{Lung} \times C_{Plasma} - Pup \times V^M_{Plasma} \times \left(1 - \frac{C^M_{Plasma}}{K_M + C^M_{Plasma}}\right) \times C_{Plasma} \\
& + CLup \times V^M_{Plasma} \times C^M_{Plasma}
\end{aligned}
$$

Equation C2: Concentration of NP in Plasma Macrophages

$$
\frac{dC^M_{Plasma}}{dt} = Pup \times \left(1 - \frac{C^M_{Plasma}}{K_M + C^M_{Plasma}}\right) \times C_{Plasma} - CLup \times C^M_{Plasma}
$$

Lymph Node Compartment

Equation C3: Amount of NP in Lymphatic System

$$
\begin{aligned}
V_{LymphNode} \times \frac{dC_{LymphNode}}{dt} & \\
&= K_{Abs} \times A_{IP} \times \left(1 - F^{IP}_{Portal}\right) + \left(1 - \sigma^{IS}_{Heart}\right) \times L_{Heart} \times C^{IS}_{Heart} \\
&+ \left(1 - \sigma^{IS}_{Kidney}\right) \times L_{Kidney} \times C^{IS}_{Kidney} + \left(1 - \sigma^{IS}_{Muscle}\right) \times L_{Muscle} \times C^{IS}_{Muscle} \\
&+ \left(1 - \sigma^{IS}_{Skin}\right) \times L_{Skin} \times C^{IS}_{Skin} + \left(1 - \sigma^{IS}_{Brain}\right) \times L_{Brain} \times C^{IS}_{Brain} \\
&+ \left(1 - \sigma^{IS}_{Adipose}\right) \times L_{Adipose} \times C^{IS}_{Adipose} \\
&+ \left(1 - \sigma^{IS}_{Gonads}\right) \times L_{Gonads} \times C^{IS}_{Gonads} + \left(1 - \sigma^{IS}_{Liver}\right) \times L_{Liver} \times C^{IS}_{Liver} \\
&+ \left(1 - \sigma^{IS}_{Stomach}\right) \times L_{Stomach} \times C^{IS}_{Stomach} \\
&+ \left(1 - \sigma^{IS}_{Spleen}\right) \times L_{Spleen} \times C^{IS}_{Spleen} \\
&+ \left(1 - \sigma^{IS}_{Pancreas}\right) \times L_{Pancreas} \times C^{IS}_{Pancreas} + \left(1 - \sigma^{IS}_{SInt}\right) \times L_{SInt} \times C^{IS}_{SInt} \\
&+ \left(1 - \sigma^{IS}_{LInt}\right) \times L_{LInt} \times C^{IS}_{LInt} + \left(1 - \sigma^{IS}_{Bone}\right) \times L_{Bone} \times C^{IS}_{Bone} \\
&+ \left(1 - \sigma^{IS}_{Lung}\right) \times L_{Lung} \times C^{IS}_{Lung} - L_{LymphNode} \times C_{LymphNode} \\
&+ Pup \times V^{M}_{LymphNode} \times \left(1 - \frac{C^{M}_{LymphNode}}{K_M + C^{M}_{LymphNode}}\right) \times C_{LymphNode} \\
&+ CLup \times V^{M}_{LymphNode} \times C^{M}_{LymphNode}
\end{aligned}
$$

Equation C4: Concentration of NP in Lymphatic System Macrophages

$$
\frac{dC^{M}_{LymphNode}}{dt} = Pup \times \left(1 - \frac{C^{M}_{LymphNode}}{K_M + C^{M}_{LymphNode}}\right) \times C_{LymphNode} - CLup \times C^{M}_{LymphNode}
$$

Organ Sub-Compartment: Plasma Space

Equation C5: Amount of NP in Plasma Space of Organs (i = all organs except the Lungs and Liver)

$$\begin{aligned} V_i^P \times \frac{dC_i^P}{dt} =& PLQ_i \times C_{Lung}^P - (PLQ_i - L_i) \times C_i^P \\ & - \left(J_i^L \times \left(1 - \sigma_i^L\right) \times C_i^P + P_i^L \times S_i \times \left(C_i^P - \frac{C_i^{IS}}{K_{IP}} \right) \times \frac{Pe_i^L}{e^{Pe_i^L - 1}} \right. \\ & \left. + J_i^S \times \left(1 - \sigma_i^S\right) \times C_i^P + P_i^S \times S_i \times \left(C_i^P - \frac{C_i^{IS}}{K_{IP}} \right) \times \frac{Pe_i^S}{e^{Pe_i^S - 1}} \right) \\ & - CLup \times V_i^E \times C_i^P \times F_{up}^E + CLup \times V_i^E \times C_i^E \times F_{rec}^E \end{aligned}$$

Equation C6: Amount of NP in Plasma Space of Lung (i = Lung)

$$\begin{aligned} V_i^P \times \frac{dC_i^P}{dt} =& PLQ_i \times C_{Plasma}^P - (PLQ_i - L_i) \times C_i^P \\ & - \left(J_i^L \times \left(1 - \sigma_i^L\right) \times C_i^P + P_i^L \times S_i \times \left(C_i^P - \frac{C_i^{IS}}{K_{IP}} \right) \times \frac{Pe_i^L}{e^{Pe_i^L} - 1} \right. \\ & \left. + J_i^S \times \left(1 - \sigma_i^S\right) \times C_i^P + P_i^S \times S_i \times \left(C_i^P - \frac{C_i^{IS}}{K_{IP}} \right) \times \frac{Pe_i^S}{e^{Pe_i^S} - 1} \right) \\ & - CLup \times V_i^E \times C_i^P \times F_{up}^E + CLup \times V_i^E \times C_i^E \times F_{rec}^E \end{aligned}$$

Equation C7: Amount of NP in Plasma Space of Liver (i = Liver)

$$
\begin{aligned}
V_i^P \times \frac{dC_i^P}{dt} =& PLQ_i \times C_{Lung}^P + (PLQ_{Stomach} - L_{Stomach}) \times C_{Stomach}^P \\
&+ (PLQ_{Spleen} - L_{Spleen}) \times C_{Spleen}^P \\
&+ (PLQ_{Pancreas} - L_{Pancreas}) \times C_{Pancreas}^P + (PLQ_{SInt} - L_{SInt}) \times C_{SInt}^P \\
&+ (PLQ_{LInt} - L_{Lint}) \times C_{LInt}^P \\
&- (PLQ_i - L_i + PLQ_{Stomach} - L_{Stomach} + PLQ_{Spleen} - L_{Spleen} \\
&+ PLQ_{Pancreas} - L_{Pancreas} + PLQ_{SInt} - L_{SInt} + PLQ_{LInt} - L_{LInt}) \times C_i^P \\
&- \left(J_i^L \times \left(1 - \sigma_i^L\right) \times C_i^P + P_i^L \times S_i \times \left(C_i^P - \frac{C_i^{IS}}{K_{IP}} \right) \times \frac{Pe_i^L}{e^{Pe_i^L} - 1} \right. \\
&\left. + J_i^S \times \left(1 - \sigma_i^S\right) \times C_i^P + P_i^S \times S_i \times \left(C_i^P - \frac{C_i^{IS}}{K_{IP}} \right) \times \frac{Pe_i^S}{e^{Pe_i^S} - 1} \right) \\
&- CLup \times V_i^E \times C_i^P \times F_{up}^E + CLup \times V_i^E \times C_i^E \times F_{rec}^E \\
&- Pup \times \left(1 - \frac{C_i^M}{K_M + C_i^M} \right) \times V_i^M \times C_i^P \times F_{up}^M + CLup \times V_i^M \times C_i^M \times F_{rec}^M
\end{aligned}
$$

Organ Sub-Compartment: Macrophages

Equation C8: Concentration of NP in Organ Macrophages (i = all organs except the Liver)

$$\frac{dC_i^M}{dt} = Pup \times \left(1 - \frac{C_i^M}{K_M + C_i^M} \right) \times C_i^{IS} - CLup \times C_i^M$$

Equation C9: Concentration of NP in Organ Macrophages in Liver (i = Liver)

$$\frac{dC_i^M}{dt} = Pup \times \left(1 - \frac{C_i^M}{K_M + C_i^M} \right) \times \left(C_i^P \times F_{up}^M + C_i^{IS} \times \left(1 - F_{up}^M\right) \right) - CLup \times C_i^M$$

Organ Sub-Compartment: Vascular Endothelium

Equation C10: Concentration of NP in Vascular Endothelium

$$\frac{dC_i^E}{dt} = CLup \times \left(C_i^P \times F_{up}^E + C_i^{IS} \times \left(1 - F_{up}^E\right) \right) - CLup \times C_i^E$$

Liver Sub-Compartment: Hepatocytes

Equation C11: Concentration of NP in Hepatocytes in Liver

$$\frac{dC^H_{Liver}}{dt} = CLup \times C^{IS}_{Liver} - CLup \times C^H_{Liver} - K_{Bile} \times C^H_{Liver}$$

Organ Sub-Compartment: Interstitial Space

Equation C12: Amount of NP in Interstitial Space of Organs (i = all organs except the Liver, Stomach, Spleen, Pancreas, Small Intestine and Large Intestine)

$$\begin{aligned} V_i^{IS} \times \frac{dC_i^{IS}}{dt} = &\left(J_i^L \times \left(1-\sigma_i^L\right) \times C_i^P + P_i^L \times S_i \times \left(C_i^P - \frac{C_i^{IS}}{K_{IP}} \right) \times \frac{Pe_i^L}{e^{Pe_i^L}-1} \right. \\ &\left. + J_i^S \times \left(1-\sigma_i^S\right) \times C_i^P + P_i^S \times S_i \times \left(C_i^P - \frac{C_i^{IS}}{K_{IP}} \right) \times \frac{Pe_i^S}{e^{Pe_i^S-1}} \right) \\ &- \left(1-\sigma_i^{IS}\right) \times L_i \times C_i^{IS} - CLup \times V_i^E \times C_i^{IS} \times \left(1-F_{up}^E\right) \\ &+ CLup \times V_i^E \times C_i^E \times \left(1-F_{rec}^E\right) - Pup \times \left(1 - \frac{C_i^M}{K_M + C_i^M}\right) \times V_i^M \times C_i^{IS} \\ &+ CLup \times V_i^M \times C_i^M \end{aligned}$$

Equation C13: Amount of NP in Interstitial Space of Portal Organs (i = Stomach, Spleen, Pancreas, Small Intestine and Large Intestine)

$$\begin{aligned} V_i^{IS} \times \frac{dC_i^{IS}}{dt} = &K_{Abs} \times A_{IP} \times F_{Portal}^{IP} \times \frac{V_i}{V_{Portal}} \\ &+ \left(J_i^L \times \left(1-\sigma_i^L\right) \times C_i^P + P_i^L \times S_i \times \left(C_i^P - \frac{C_i^{IS}}{K_{IP}} \right) \times \frac{Pe_i^L}{e^{Pe_i^L}-1} \right. \\ &\left. + J_i^S \times \left(1-\sigma_i^S\right) \times C_i^P + P_i^S \times S_i \times \left(C_i^P - \frac{C_i^{IS}}{K_{IP}} \right) \times \frac{Pe_i^S}{e^{Pe_i^S-1}} \right) \\ &- \left(1-\sigma_i^{IS}\right) \times L_i \times C_i^{IS} - CLup \times V_i^E \times C_i^{IS} \times \left(1-F_{up}^E\right) \\ &+ CLup \times V_i^E \times C_i^E \times \left(1-F_{rec}^E\right) - Pup \times \left(1 - \frac{C_i^M}{K_M + C_i^M}\right) \times V_i^M \times C_i^{IS} \\ &+ CLup \times V_i^M \times C_i^M \end{aligned}$$

Equation C14: Amount of NP in the Interstitial Space of Liver (i = Liver)

$$\begin{aligned} V_i^{IS} \times \frac{dC_i^{IS}}{dt} = & \left(J_i^L \times \left(1-\sigma_i^L\right) \times C_i^P + P_i^L \times S_i \times \left(C_i^P - \frac{C_i^{IS}}{K_{IP}} \right) \times \frac{Pe_i^L}{e^{Pe_i^L}-1} \right. \\ & \left. + J_i^S \times \left(1-\sigma_i^S\right) \times C_i^P + P_i^S \times S_i \times \left(C_i^P - \frac{C_i^{IS}}{K_{IP}} \right) \times \frac{Pe_i^S}{e^{Pe_i^S-1}} \right) \\ & - \left(1-\sigma_i^{IS}\right) \times L_i \times C_i^{IS} - CLup \times V_i^E \times C_i^{IS} \times \left(1-F_{up}^E\right) \\ & + CLup \times V_i^E \times C_{Liver}^E \times \left(1-F_{rec}^E\right) \\ & - Pup \times \left(1 - \frac{C_i^M}{K_M + C_i^M} \right) \times V_i^M \times C_i^{IS} \times \left(1-F_{up}^M\right) \\ & + CLup \times V_i^M \times C_i^M \times \left(1-F_{rec}^M\right) - CLup \times V_{Liver}^H \times C_i^{IS} \\ & + CLup \times V_{Liver}^H \times C_{Liver}^H \end{aligned}$$

Miscellaneous Equations: Pores

Equation C15: Vascular Reflection Coefficient across Large Pores

$$\sigma_i^L = \begin{cases} 1 - \dfrac{\left(1-\gamma_i^L\right)^2 \times \left[2 - \left(1-\gamma_i^L\right)^2\right] \times \left(1 - \dfrac{\gamma_i^L}{3}\right)}{1 - \dfrac{\gamma_i^L}{3} + \dfrac{2 \times \left(\gamma_i^L\right)^2}{3}} & , \gamma_i^L < 1 \\ 0.999 & , \gamma_i^L \geq 1 \end{cases}$$

Equation C16: Vascular Reflection Coefficient across Small Pores

$$\sigma_i^S = \begin{cases} 1 - \dfrac{\left(1-\gamma_i^S\right)^2 \times \left[2 - \left(1-\gamma_i^S\right)^2\right] \times \left(1 - \dfrac{\gamma_i^S}{3}\right)}{1 - \dfrac{\gamma_i^S}{3} + \dfrac{2 \times \left(\gamma_i^S\right)^2}{3}} & , \gamma_i^S \leq 1 \\ 0.999 & , \gamma_i^S \leq 1 \end{cases}$$

Equation C17: Permeability across Large Pores

$$P_i^L = \begin{cases} \dfrac{\left(1-\gamma_i^L\right)^{\frac{9}{2}}}{1 - 0.3956 \times \gamma_i^L + 1.0616 \times \left(\gamma_i^L\right)^2} \times \dfrac{RT \times \alpha_i^L \times 4 \times Lp_i}{3 \times \pi \times N_a \times r^{NP} \times \left(r_i^L\right)^2} & , \gamma_i^L < 1 \\ 1 \cdot 10^{-21} & , \gamma_i^L \geq 1 \end{cases}$$

Equation C18: Permeability across Small Pores

$$P_i^S = \begin{cases} \dfrac{\left(1-\gamma_i^S\right)^{\frac{9}{2}}}{1-0.3956\times\gamma_i^S+1.0616\times\left(\gamma_i^S\right)^2} \times \dfrac{RT\times\left(1-\alpha_i^L\right)\times 4\times Lp_i}{3\times\pi\times N_a\times r^{NP}\times\left(r_i^S\right)^2} & ,\gamma_i^S<1 \\ 1\cdot 10^{-21} & ,\gamma_i^S\geq 1 \end{cases}$$

Miscellaneous Equations: Fluid Flux

Equation C19: Lymph Flow Rate

$$L_i = PLQ_i \times F_i^{lymph}$$

Equation C20: Fluid Flux Rate across Large Pores

$$J_i^L = \alpha_i^L \times L_i + F_i^{Jiso} \times \left(1-\alpha_i^L\right) \times L_i \times \left(\frac{V_i}{V_{i_{mouse}}}\right)^{-\frac{1}{3}}$$

Equation C21: Fluid Flux Rate across Small Pores

$$J_i^S = \left(1-\alpha_i^L\right) \times L_i - F_i^{Jiso} \times \left(1-\alpha_i^L\right) \times L_i \times \left(\frac{V_i}{V_{i_{mouse}}}\right)^{-\frac{1}{3}}$$

Miscellaneous Equations: Endothelium

Equation C22: Vascular Endothelial Surface Area

$$S_i = k_e \times F_i^V \times V_i$$

Equation C23: Vascular Endothelial Volume

$$V_i^E = S_i \times d_e$$

Miscellaneous Equations: Intraperitoneal Space

Equation C24: Amount of NP in the Intraperitoneal Space

$$A^{IP} = F \times Ro - K_{Abs} \times A^{IP}$$

Equation C25: Total Volume of Portal Organs

$$V_{Portal} = V_{Stomach} + V_{Spleen} + V_{Pancreas} + V_{SInt} + V_{LInt}$$